Simulations of Radiatively Driven Convection and Spatially Heterogeneous Solar Radiation Intensity in Ice-Covered Lakes

by

Donovan James McMurrich Allum

A thesis
presented to the University of Waterloo
in fulfillment of the
thesis requirement for the degree of
Doctor of Philosophy
in
Applied Mathematics

Waterloo, Ontario, Canada, 2023

Examining Committee Membership

The following served on the Examining Committee for this thesis. The decision of the Examining Committee is by majority vote.

External Examiner:	Jay Austin Professor, Swenson College of Science and Engineering, University of Minnesota Duluth
Supervisor:	Marek Stastna Professor, Dept. of Applied Mathematics, University of Waterloo
Internal Member:	Francis Poulin Professor, Dept. of Applied Mathematics, University of Waterloo
Internal Member:	Matthew Scott Associate Professor, Dept. of Applied Mathematics, University of Waterloo
Internal-External Member:	Andrea Scott Associate Professor, Dept. of Systems Design Engineering, University of Waterloo

Author's Declaration

I hereby declare that I am the sole author of this thesis. This is a true copy of the thesis, including any required final revisions, as accepted by my examiners.

I understand that my thesis may be made electronically available to the public.

Abstract

At the end of winter as sunlight and increasing air temperatures melt the snow layer above the ice, allowing significant radiation from the sun to enter the water column. In the cold water regime ($T < 4$ °C, where 4 °C is the freshwater temperature of maximum density) increasing the temperature also increases the density, contrary to warm water settings. Therefore, adding heat near the surface results in radiatively driven convection. This process under ice has received a lot of attention recently from fluid dynamicists and limnologists in part due to its uniqueness (solar radiation driving convection, shielding from wind), and its sensitivity to global warming due to its very narrow temperature range. Previous simulations have mostly focused on two dimensions (2D) and ignored spatial heterogeneity of the solar radiation intensity. In this thesis, I use direct numerical simulations to compare radiatively driven convection in two and three dimensions - with and without a background stratification - and the impact of spatially varying solar radiation intensity in cold water in both two and three dimensions (3D). The simulations presented here are in idealized and simplified systems to isolate the dynamics of interest.

The findings in Chapter 3 demonstrate that radiatively driven convection lead to a Rayleigh-Taylor-like instability whereby heat is exchanged with a motionless ambient below. 2D simulations have significantly less viscous dissipation and larger convective velocities, compared to 3D simulations, but the depth of the convective layer grows at a similar rate. Upwelling plumes are largely irrotational, contribution to most - but not all - of the difference in viscous dissipation between 2D and 3D. In 3D, large convective plumes persist but the features are significantly smaller scale and upwelling plumes are rotational and dissipative. By adding a background stratification, it was shown that in both 2D and 3D, convective plumes penetrate into the background stratification by reflecting off the stratification when the stratification is warmer and entraining the warmer fluid into the interior of the convective layer.

Chapter 4 and 5 both use direct numerical simulations to analyze the effect of spatially heterogeneous solar radiation intensity. These simulations show that spatial variations in solar radiation results in a robust, cool, buoyant intrusion which propagates along the surface, originating from the 'shadowed' region where the solar radiation is damped. Chapter 4 consists of a process study in 2D where the albedo change, initial temperature and attenuation length are varied. The Albedo change only affects the development of the intrusion, whereas the initial temperature and attenuation length both affect the development of the intrusion and the radiatively driven convection away from the shadowed region. A non-dimensionalization scheme was presented which collapsed the front speed of the intrusion for all parameter variations except the albedo. Chapter 5 examines the impact of geomet-

ric differences of the shadowed region in 3D. One shadow is rectangular and the other is circular. The rectangular shadow results in a deeper intrusion which is able to propagate further than the circular shadow. The intrusion is eventually arrested by a large vortex generated by the Kelvin-Helmholtz instability at the shear layer between the intrusion and the return flow.

Acknowledgements

I would like to start by thanking my supervisor, Marek Stastna. I have come a long way as a scientist, teacher and academic under your supervision. It would not have been possible without the guidance, mentorship and humanity of my friend and mentor, Marek.

I would like to also thank and acknowledge the contributions of the members of my committee, Francis Poulin and Matthew Scott, for their time and energy spent reading my initial research proposal and this thesis. Thank you to the internal-external and external examiners, Andrea Scott and Jay Austin who dedicated significant amount of time to this process. Thank you to the University of Waterloo, the Math faculty and Applied Mathematics department for supporting me throughout that last four years.

Thank you to my many fellow students over the years who have provided valuable scientific discussions and friendships that have not only made this experience possible but also a fun, enriching period of my life. This thank you goes out to Andrew Grace, Nico Castro-Folker, Sierra Legare, as well as many others I have encountered through my undergraduate, master's and PhD.

Thank you to both my parents for their full support since they drove me from Winnipeg, Manitoba to Peterborough, Ontario in the summer of 2012 to pursue my undergraduate degree at Trent University in mathematical physics. I was neither hardworking, studious, nor punctual in high school and they still managed to support me at the beginning and continue that support through the completion of my PhD.

Thank you to both of my older sisters who provided significant emotional support despite living a province apart these last 11 years. Without the many late night, weekend chats, I would not have had the confidence to continue pushing forward.

A final thank you to my partner Michaela Jennings who has been with me through this wild journey the last 10 years. You've watched me grow as a person and supported me like nobody else, even when I struggled the most. You celebrated for me when I was unable, and celebrated with me when I had the energy. Thank you for putting up with me as I challenged myself to reach this goal and it would have been impossible without you.

Dedication

This thesis is dedicated to my partner, Michaela Jennings, who has essentially earned co-authorship on this thesis through her many years of support. I also dedicate this thesis to our dog Kingsley who is the daily light in my life.

Table of Contents

List of Figures

List of Tables

List of Abbreviations

CML Convective Mixed Layer

List of Symbols

ϕ Random vector: a location in n-dimensional Cartesian space, where each dimensional component is determined by a random process

Chapter 1

Introduction

The content of this thesis is concerned with the motion of fluids due to differences in the mass of a fluid compared to its volume, also known as density or buoyancy. This type of fluid motion is called density or buoyancy driven flows. Density differences are a necessary but insufficient condition for buoyancy driven flows. Motion can spontaneously arise only under certain density configurations. The type of density - limiting our discussion to only incompressible fluids - configuration that will not lead to spontaneous motion, is one where the density decreases in the upwards direction. Such a configuration is called a stable stratification, where a stratified fluid is one where the density varies in the vertical direction. If a single fluid particle[1] flows upwards, the surrounding density will be lower and the fluid particle will be less buoyant than its surroundings, causing it to sink downwards, in the direction of gravity. An unstable stratification is when the density increases in the upwards direction. If another small perturbation in an unstable stratification causes a fluid particle to flow downwards, it will be more dense and less buoyant than its surroundings and continue to fall. An unstable stratification leading to spontaneous fluid motion is called convection.

Temperature is one fluid dynamical variable that changes the density of water. Other examples include pressure (relevant in the deep ocean and deep lakes) and salinity. For this thesis, the focus is primarily on temperature differences. Most laypersons are at least

[1] A fluid particle is the smallest possible size of a collection of water molecules that is sufficiently large so that the fluid obeys the continuum hypothesis. This hypothesis assumes that a fluid is a continuum. This hypothesis holds as long as the length scales of interest in a fluid flow are much greater than the average distance between water molecules (Kundu and Cohen, 1990). There are 18 ml of water in a single mole, which has an Avogadro's number of water molecules (6.022×10^{23}) at standard temperature and pressure. This fact further emphasizes the strength of the continuum hypothesis.

passively familiar with a change in temperature leading to a change in buoyancy. For example, when one adds an ice cube to cool a glass of water. By construction, the water in the glass is warmer than the ice cube, which floats due to its lower density. This change of density due to temperature is also possible without changing the state of matter. Indeed, changing the temperature of liquid water changes its density, and this change continues past changes of state. If a shallow body of water is stratified in temperature, is it also stratified in density[2].

One fact that is unique about water is that there exists a temperature in which its density is maximized. Deviations from this temperature always result in a decrease in density for fresh water. The temperature of maximum density, T_{MD}, is approximately 4 °C (Leppäranta, 2014). As a consequence of the existence of T_{MD}, a stratification that consists of water that increase in temperature in the vertical direction can be stable or unstable depending on whether the temperatures are above or below T_{MD}.

In this chapter, the basic principles that are relevant to this research are discussed. Starting first with a summary of the key dynamical processes in inland lakes in Section 1.1.

1.1 Small lake dynamics

There are five main mechanisms to induced motion in lakes:

1. Solar radiation,
2. Surface cooling or warming,
3. Differential heating/cooling,
4. River inflow, and
5. Wind.

Each of these are depicted in Figure 1.1.

Solar radiation heats water near the surface of a lake. In tropical lakes year round, and ice-free temperate and arctic lakes in the summer with temperatures exceeding T_{MD},

[2]It is actually technically possible to have a fluid be stratified in temperature but have no change in density if another variable, like salinity cancels out a change in density. As we are primarily focused on fresh water where temperature changes are most relevant, this statement generally holds true.

increasing temperature decreases density and resists convection. However, in ice-covered lakes the opposite is true and solar radiation destabilizes the stratification and drives convection (Leppäranta, 2014). This is discussed further in Section 1.2. Surface cooling can drive motion in a very similar way to solar radiation but only under ice-free and warmer conditions[3]. Unlike solar radiation, however, it is thought of as a process that is mostly confined to the surface, whereas, solar radiation can penetrate much deeper into the water column. Surface cooling under these conditions drives convection (Curry and Webster, 1998; Bouffard and Wüest, 2019). Examples of causes of surface cooling include evaporation, precipitation and conduction (Curry and Webster, 1998; Bouffard and Wüest, 2019).

Not all heating and cooling has the same potential to drive motion. Cooling and heating occurs more rapidly in shallow regions (Ulloa et al., 2019; Bouffard and Wüest, 2019; Ramón et al., 2021). This process is known as differential heating or differential cooling. Differential heating in cold lakes and differential cooling in warm lakes both lead to a class of buoyancy driven flows called gravity currents. A gravity current is any current that is driven by density differences between two or more fluids (e.g., oil on top of water) or by density differences in a single fluid. The most common way that a gravity current is generated is by a sharp, lateral difference in density. This is clearly not standard convection as it was defined above. Gravity currents are discussed in more detail in Section 4.1.2. Differential heating and cooling generates these lateral density differences through temperature and the resulting gravity current transports the heated or cooled fluid downslope, distributing nutrients and other quantities to the deeper regions of a lake (Bouffard and Wüest, 2019).

River inflows can introduce water that is heavier or lighter than the lake water, leading to currents that propagate along the surface or at the bottom (Legg, 2012; Bouffard and Wüest, 2019). Occasionally, the river water can be colder than T_{MD} while the lake water can be warmer (and vice versa). The resulting mixing between these two temperatures creates denser fluid and further drives motion in a process known as cabbeling (Bouffard and Wüest, 2019; Grace et al., 2023b,a).

The last main mechanism that can drive motion is wind. While wind is typically weaker in inland bodies of water compared to the ocean, it still dominates mechanical energy input in open water. Wind is also significantly more complicated physically because wind drives surface waves at the free surface, and these have their own complex dynamics (Wüest and Lorke, 2003). Momentum from the wind is transferred to water by a shear-stress at the

[3]The idea of cold and warm waters responding very differently to warming and cooling is central to the topic of this thesis. This difference is fully explained in Section 1.2.

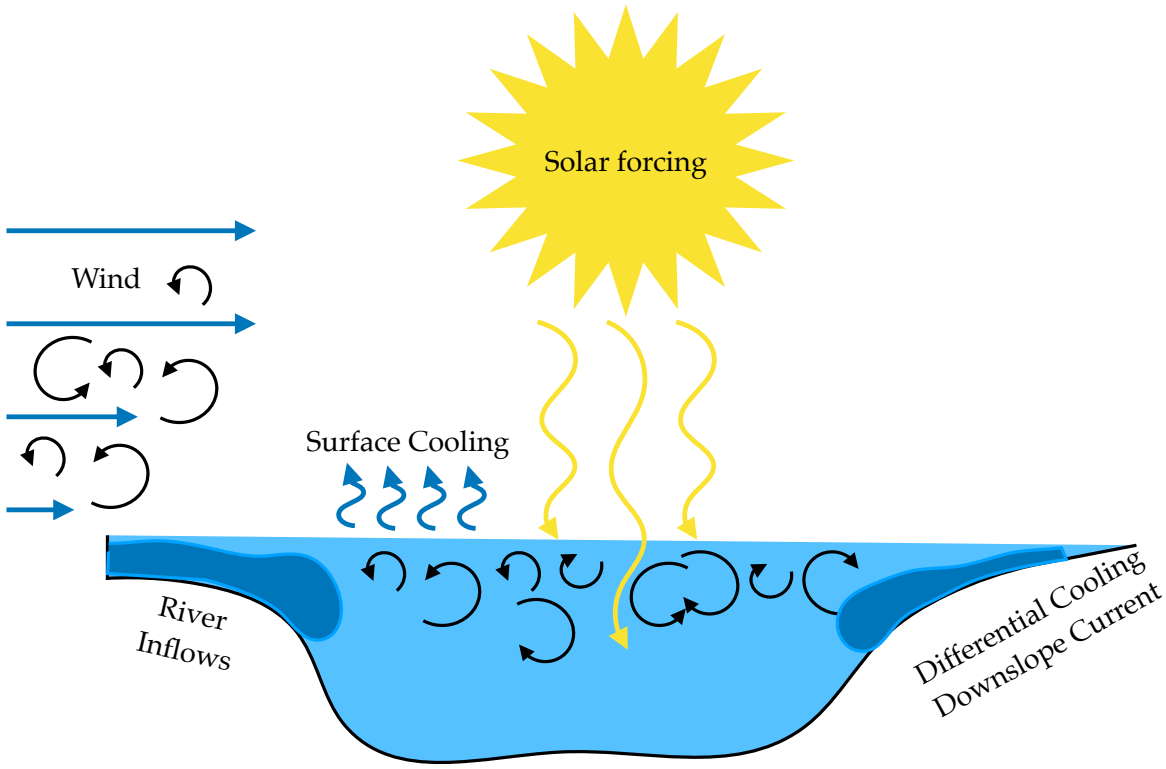

Figure 1.1: Cartoon of a small lake and the main mechanisms that lead to motion.

surface, which can generate waves, vertical mixing and cross-shore transport (Wüest and Lorke, 2003).

For the remainder of this thesis, the focus will be entirely on the impact of solar radiation. Mechanisms like river inflows, differential heating and cooling are neglected for simplicity. The former requires accounting for the influx of large amounts of water and the latter requires variations in bathymetry. Wind and surface cooling are neglected on physical grounds due to the fact that they are largely absent in the type of lake studied in this thesis, ice-covered lakes.

1.2 Ice-covered lakes

Ice-covered lakes are inland bodies of water with some degree of ice coverage, typically present in the winter season. Most ice-covered lakes have annual ice-coverage that melts in the spring and refreezes in the fall (Magnuson et al., 2000; Leppäranta, 2014; Karetnikov et al., 2017; Hewer and Gough, 2019); multi-year ice coverage is rare (Leppäranta, 2014). Ice-covered lakes are unique for two main reasons.

First, the ice layer shields the water body from wind at the surface (as well as other surface effects like evaporation or precipitation[4]), ceasing the transfer of momentum that can drive motion (Leppäranta, 2014). Ice-free lakes hit by powerful wind at the surface generate waves and can sometimes induce motion on the scale of the entire basin, called a seiche (Kundu and Cohen, 1990). Wind can also induce circulation in the basin as well (Ulloa et al., 2020). Due to the ice-cover, any circulation must be driven by another mechanism.

Second, water temperatures in ice-covered lakes are typically found between 0 and 4 °C (Leppäranta, 2014). This temperature range is unique when compared to most other lakes because a stable stratification occurs when the temperature decreases towards the surface. When ice-cover melts in the summer, temperatures exceed T_{MD}, as it does year round in tropical lakes. For these temperatures, a stratification is stable if the temperature increases towards the surface. This difference is significant because certain processes have a near-surface warming effect, which would be stabilizing in warmer lakes but destabilizing in ice-covered lakes. One such process that is central to the dynamics presented in this thesis, is sunlight.

Incoming sunlight that heats the water near the surface in a warm lake (temperatures above 4 °C) decreases its density and is stable. However, in ice-covered lakes with temperatures less than 4 °C, the result is heavier water sitting atop cool water that is unstable to any kind of perturbation to the water. The key statement is that in ice-covered lakes, sunlight drives motion, while in warmer lakes, sunlight arrests motion.

Lakes with ice-coverage are typically found at the high latitudes, although many temperate lakes (including the Great Lakes in Canada and the U.S.A) grow some form of ice-cover during the winter season (Leppäranta, 2014). The higher the latitude, the less sunlight the lake received in the winter and the more it receives in the summer. Most lakes

[4]Evaporation and precipitation are examples of latent heat fluxes that are generated by a change in state. While these latent fluxes are no longer possible in an ice-covered lake, the exchange of heat with the ice is still a form of a latent heat flux in which water is frozen or melted at the interface.

- in abundance and total area - are found in the high latitudes (Verpoorter et al., 2014) and hence many have a period with some degree of ice-cover.

1.3 Phases of winter

The winter season is typically thought of as consisting of two phases. The division of these phases is best reviewed in (Kirillin et al., 2012), so I will only go into some detail here.

The first is labeled Winter I and corresponds to the early part of the winter. In Winter I, there is typically a layer of snow that sits on top of the ice. This snow layer blocks most of the incoming sunlight. Snow is much more effective, compared with ice, at reflecting and absorbing sunlight with an albedo - the fraction of sunlight reflected at the air interface - ranging from 0.4 to 0.9 in snow and 0.2 to 0.6 in ice (Leppäranta, 2014; Bouffard et al., 2016). The range of albedo overlap occurs in the driest ice and the wettest snow. Liquid water is the least reflective state and, hence, the dryness of ice increases its albedo and the wetness of snow decreases it. Typical drivers of motion in Winter I include heat flow from sediments in shallow regions, river inflows, and Coriolis force (Kirillin et al., 2012).

The second period, which is most relevant for this thesis, is labeled Winter II and corresponds to the time period after the snow layer has melted. Due to the lower albedo of ice, a significant amount of solar radiation is able to enter the water column (Farmer, 1975; Bouffard et al., 2016), destabilizing it and generating motion in what generally referred to as penetrative convection (Deardorff et al., 1969; Farmer, 1975). In the context of solar radiation, this process is called radiatively driven convection (Mironov et al., 2002; Bouillaut et al., 2019; Austin, 2019). This process continues until ice melts at the surface and temperatures exceed T_{MD} and sunlight begins to stabilize the water column. After some time, a turbulent mixing layer forms underneath a thin thermal boundary layer. The turbulent mixing layer, which is typically uniform in temperature, is called the convective mixed layer (CML), or sometimes just the convective layer (CL). Beneath the CML is either the bottom of the lake or a stably stratified background, sometimes called a quiescent layer.

1.3.1 Sunlight absorption

Up to this point, any description of the manner in which solar radiation supplies heat and increases the temperature of the water column has been vague. Unlike temperature changes due to temperature differences between the air and water, or the ice and water at the surface of the water column, which is implemented as a boundary condition, solar

radiation is a volumetric heating source (Leppäranta, 2014). Detailed descriptions of solar radiation and how it introduces heat into the water column can be found in Ref. Curry and Webster (1998); Kantha and Clayson (2000); Leppäranta (2014). The level of detail and rigor presented in both textbooks goes beyond what is necessary for this thesis. In the remainder of this section, the heating introduced by solar radiation is presented in a more intuitive (author's opinion) manner with less rigor than the textbooks mentioned above, but still follows the same basic logic.

Start by recalling that sunlight can be thought of as a collection of particles, or photons, and the water as particles, or H_2O molecules. As depicted in Figure 1.2, photons enter the water column and travel until they interact with water molecules. Treating the molecules as particles or solid, tiny spheres is called Mie theory (Curry and Webster, 1998; Wallace and Hobbs, 2006), the details of which go well beyond the scope of this thesis. To summarize, using Maxwell's equations, a cross section is estimated whereby if the photon passing within this cross section it might be absorbed or scattered, where a unique cross-section is given for absorption and scattering. The photon can either be absorbed by the water molecule, increasing the energy of one of its electrons and causing the molecule to vibrate. The average vibration and motion of molecules in medium is precisely its temperature (Wallace and Hobbs, 2006; Smith and Dent, 2019), hence, a main mechanism for increasing temperature is absorption. Scattering causes the photon to change direction and retain its momentum[5]. The photon will continue to travel until it interacts with a new molecule, where it is possibly absorbed or re-scattered. The net effect is to increase the rate of heating in each layer.

Due to the random orientations of the water molecules, and massive number of molecules and photons, absorption and scattering is essentially a probabilistic process. The number of photons per square metre is so massive that assuming constant absorption, and hence, constant heating at fixed depth is a reasonable model. A mathematical formalism for this idea is to assume that the change in the intensity of light – proportional to the number of photons – with depth is proportional to the intensity of light (i.e., if there are more photons, there are more photons that will be absorbed). This is written mathematically as

$$\frac{\partial I}{\partial p} = -CI, \tag{1.1}$$

[5]It is possible for a scattered photon to transfer some of its momentum - and therefore change its energy and wavelength - to the water molecule, thereby increasing its kinetic energy and the temperature of the medium. This is a type of scattering called Raman scattering (Smith and Dent, 2019) and is neglected in the discussion here.

where p is the penetration distance, I is the intensity of light, C is the proportionality constant and typically referred to as attenuation coefficient and has units of inverse length (typically m^{-1}) (Curry and Webster, 1998; Leppäranta, 2014). This model ignores possible reflection at the bottom of the domain. This assumption is appropriate if most of the radiation is absorbed above the bottom of the domain. The research presented in this thesis can safely rely on this assumption.

The attenuation coefficient can be decomposed into scattering, s, and absorption, a, coefficients as

$$C = s + a.$$

Implicitly, by summing s and a into a total attenuation coefficient, C, we are treating them as equivalent processes on the change in temperature. For the remainder of this thesis, the distinction is unimportant. Further, a more useful representation of the attentuation coefficient is to use its inverse, the attenuation length, λ. This quantity is equivalent but more intuitive because of its units of length defining a natural decay scale for absorption. Eq. 1.1 can therefore be rewritten as

$$\frac{\partial I}{\partial p} = -\frac{I}{\lambda}. \tag{1.2}$$

The attenuation length describes the clarity of the water. A larger attenuation length implies a higher water clarity and less absorption per unit penetration distance. The negative sign on the right-hand side reflects the fact that the intensity of light is decreasing with penetration depth. A change of variables from p, which is positive downwards, to z, the standard upward pointing Cartesian coordinate, results in a new equation written as follows

$$\frac{\partial I}{\partial z} = \frac{I}{\lambda} \tag{1.3}$$

In this new equation, I, is a function of $z = -p$. The negative sign is gone from the right-hand side because light from the sun is traveling downwards and, hence, its intensity is decreasing with decreasing z, and vice versa. The solution to this equation is

$$I = A \exp\left(\frac{z}{\lambda}\right), \tag{1.4}$$

Where A is an arbitrary constant. Using the boundary condition, defined at the water surface, $I(L_z) = I_0$, where L_z is the height of the water above the bottom, and I_0 is

the intensity of solar radiation after it passes through the ice in units of watts per metre squared, we obtain the following equation for light intensity as a function of depth

$$I = I_0 \exp\Big(- \frac{(L_z - z)}{\lambda} \Big) \tag{1.5}$$

This is known as the Beer-Lambert Law (Leppäranta, 2014). This form of Eq. 1.5, assumes that the rate of absorption is the same for all wavelengths of light. This is naturally an approximation. An improvement on this approximation is to divide light into short and longwave radiation and assign a unique attenuation length for both (Kantha and Clayson, 2000; Leppäranta, 2014). Longwave radiation (e.g., infrared) is mostly absorbed in the first few centimetres, whereas shortwave radiation (visible and ultraviolet) can penetrate much deeper (Defant, 1960). Further divisions into different sections of the electromagnetic spectrum is possible and sometimes required for certain studies with biological implications. An exact treatment assumes that λ continuously varies with wavelength. This level of detail is not necessary for the work described in this thesis. In each chapter, 1.5 is used to model sunlight absorption in the systems of interest. In chapters 3 and 4, this equation is slightly modified to introduce lateral variations, more on this later.

However, this equation just tells us about how the intensity of the sunlight changes with penetration distance into the water column. Instead, we require the fraction of intensity lost as the sun light penetrates further into the water column to determine its effect on temperature. This is captured by taking the derivative of 1.5 with respect to z, as follows

$$\frac{\partial I}{\partial z} = \frac{I_0}{\lambda} \exp\Big(- \frac{(L_z - z)}{\lambda} \Big) \tag{1.6}$$

One may notice that this equation clearly does not have the units of temperature, but instead Watts per square metre, per metre. The change in temperature is instead proportional to Eq. 1.6, to be discussed further in Section 2.1.3.

1.4 Thesis summary

The main topic of this thesis is how radiatively driven convection is modified by sharp, lateral changes in solar radiation intensity. A large set of numerical simulations are used to study these systems. Lateral temperature differences are generated by the lateral changes in solar radiation intensity and, as a result, gravity currents are possible. First, in Chapter 2 is the technical background (mathematical and numerical) necessary for the subsequent results chapters. The first results chapter is a comparison of radiatively driven convection in

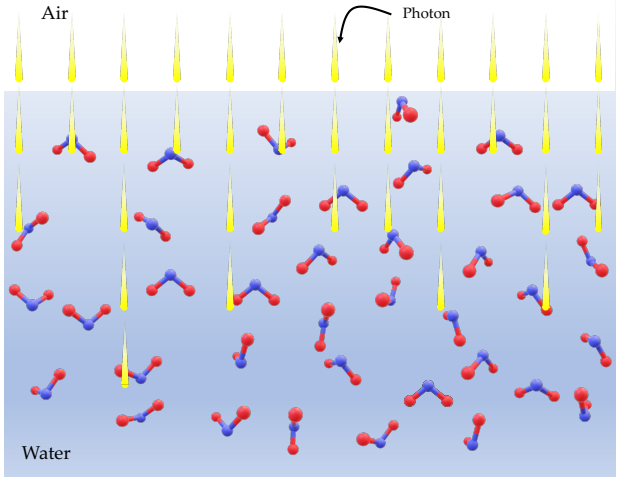

Figure 1.2: Schematic demonstrating how photons are absorbed in a body of water by water molecules. Water molecules are represented by the band chain of particles. Hydrogen atoms are coloured red and oxygen in blue. The yellow shapes are photons that are absorbed if they interact with a water molecule.

two dimensions (2D) and three dimensions (3D) with homogeneous solar radiation intensity at the surface in Chapter 3. The purpose of this comparison is that radiatively driven convection differs between 2D and 3D and naturally will affect the motion induced by sharp, lateral changes in solar radiation intensity. Chapter 4 is a process study analyzing heterogeneous solar radiation in 2D and Chapter 5 revisits heterogeneous solar radiation in 3D, by considering different geometries that are not possible in 2D. The results of each chapter are concluded separately in Section 3.6, 4.8 and 5.9, with a short synthesis of these conclusions in Chapter 6. This thesis is concluded by discussion possible future research on this topic that extends the work presented here, in 6.2.

Chapter 2

Technical Background

2.1 Equations of motion

In order to derive the relevant equations of motion, we must first start with the Reynolds Transport Theorem, also known as the Leibniz rule. Reynolds Transport Theorem states that the time derivative of an integral over a *material volume* of a scalar quantity, $F(\vec{x}, t)$, is written as follows:

$$\frac{d}{dt}\int_{V(t)} F(\vec{x}, t)dV = \int_{V(t)} \frac{\partial F(\vec{x}, t)}{\partial t}dV + \int_{A(t)} F(\vec{x}, t)\vec{u} \cdot d\vec{A}. \tag{2.1}$$

$\vec{x} = (x, y, z)$ is a point in space in Cartesian coordinates, $\vec{u} = (u, v, w)$ is the fluid velocity and $d\vec{A}$ is the outward pointing normal of an infinitesimal element on the orientable boundary, $A(t)$, of a connected volume $V(t)$. A material volume is a volume that follows the motion of a specific collection of fluid particles. The total mass inside a material volume is conserved, a differential equation for this statement will be defined later. A material volume can expand, contract, and change shape with the fluid particles (a strange sentence given all we do is incompressible fluids, but technically correct). In (Vallis, 2017), it is shown using Eq. 2.1 that a material volume only changes due to nonzero velocities normal to the boundary and is written explicitly as,

$$\frac{d}{dt}\int_{V(t)} dV = \int_{A(t)} \vec{u} \cdot d\vec{A}. \tag{2.2}$$

The validity of Eq. 2.1 can be motivated in one-dimension by first writing

$$\Phi(a(t), b(t), t) = \int_{a(t)}^{b(t)} F(x, t)dx,$$

and taking its time derivative

$$\frac{d}{dt}\Phi(a(t),b(t),t) = \frac{\partial\Phi}{\partial a}\frac{\partial a}{\partial t} + \frac{\partial\Phi}{\partial b}\frac{\partial b}{\partial t} + \frac{\partial\Phi}{\partial t}. \tag{2.3}$$

Through repeated applications of the fundamental theorem of calculus it can be shown that

$$\frac{d}{dt}\int_{a(t)}^{b(t)} F(x,t)dx = \int_{a(t)}^{b(t)} \frac{\partial F(x,t)}{\partial t}dx + F(b(t),t)\frac{\partial b}{\partial t} - F(a(t),t)\frac{\partial a}{\partial t}. \tag{2.4}$$

The calculation of the first term is shown in Ref. Flanders (1973) and represents the time dependence of the integrand. The second and third term are contributions due to the velocity of the boundaries of the domain, $a(t)$ and $b(t)$ - described in (Kundu and Cohen, 1990) with the aid of a useful diagram - and is analogous to the last term in Eq. 2.1.

2.1.1 Conservation of mass

There are several ways to derive a continuity equation as outlined in (Vallis, 2017). In (Kundu and Cohen, 1990) and (Batchelor and Batchelor, 1967), the derivation is conducted using a fixed volume. Here, I will briefly give the derivation using a material volume. By definition of a material volume - described in the previous section - the total mass, M, is conserved. This is written in equation form as

$$\frac{dM}{dt} = \frac{d}{dt}\int_{V(t)} \rho(\vec{x},t)dV = 0.$$

Since $V(t)$ is a material volume, we can use Eq. 2.1 to rewrite the above equation as

$$\frac{d}{dt}\int_{V(t)} \rho(\vec{x},t)dV = \int_{V(t)} \frac{\partial\rho}{\partial t}dV + \int_{A(t)} \rho\vec{u}\cdot d\vec{A}.$$

Using the divergence theorem, the last term can be written in term of a volume integral and we arrive at

$$\int_{V(t)} \left[\frac{\partial\rho}{\partial t} + \nabla\cdot(\rho\vec{u})\right]dV = 0.$$

The material volume, $V(t)$, is arbitrary and since the above is true as an integral over the volume, the integrand must also vanish - this is called the Dubois-Reymond lemma. This idea allows us to arrive at the conservation of mass in differential form:

$$\frac{\partial\rho}{\partial t} + \nabla\cdot(\rho\vec{u}) = 0. \tag{2.5}$$

This can be rewritten further by applying the product rule for the divergence to the second term and defining the material derivative,

$$\frac{D}{Dt} = \frac{\partial}{\partial t} + (\vec{u} \cdot \nabla).$$

The final version of the conservation of mass in differential form is thus

$$\frac{1}{\rho}\frac{D\rho}{Dt} + \nabla \cdot \vec{u} = 0. \tag{2.6}$$

Incompressible fluids

As we've just shown, Eq. 2.6, in a compressible fluid a nonzero velocity divergence must be balanced by a change in density. An incompressible fluid cannot change its density, as a result, the conservation of mass becomes

$$\nabla \cdot \vec{u} = 0. \tag{2.7}$$

In reality, no fluid is completely incompressible. However, it can be treated as one under certain conditions. Specifically, in order for Eq. 2.7 to be accurate, we require

$$\left|\frac{1}{\rho}\frac{D\rho}{Dt}\right| \ll \nabla \cdot \vec{u}.$$

This shows that simply "small" variations in density are insufficient to make the assumption of incompressibility. Instead it is the ratio of the density variations to the mean density that must be vanishingly small. This condition is often written as

$$\frac{\delta\rho}{\rho_0} \ll 1,$$

where $\delta\rho$ represents the density variations within the flow and ρ_0 is some constant reference density. In (Vallis, 2017), this condition is taken a step further to show that the Mach number - the ratio of the typical velocities within the flow to the speed of sound - must be much less than 1 for the incompressibility condition to hold. As we shall see later, in Section 2.4, a consequence of this condition is that changes in pressure are instantaneous and the speed of sound is effectively infinite.

2.1.2 Conservation of momentum

We can derive the conservation of momentum by starting from the familiar Newton's second law,

$$\vec{F}_{net} = \frac{d}{dt}\vec{p}, \tag{2.8}$$

where $\vec{F}_{net}$ is the net force and $\vec{p} = M\vec{v}$ is the momentum. We are going to derive the momentum equations for a Newtonian fluid contained within a material volume, $V(t)$. The total momentum of $V(t)$ is

$$\vec{p} = \int_{V(t)} \rho\vec{u}dV$$

and Eq. 2.8 becomes

$$\vec{F}_{net} = \frac{d}{dt}\int_{V(t)} \rho\vec{u}dV. \tag{2.9}$$

Since $V(t)$ is a material volume, it can be shown that

$$\frac{d}{dt}\int_{V(t)} \rho\vec{u}dV = \int_{V(t)} \rho\frac{D\vec{u}}{Dt}dV,$$

using the Reynolds Transport Theorem (Eq. 2.1) and the conservation of mass (Eq. 2.6). This is shown in more detail in (Kundu and Cohen, 1990) and (Vallis, 2017). As a result, Eq. 2.9 bcomes

$$\vec{F}_{net} = \int_{V(t)} \rho\frac{D\vec{u}}{Dt}dV. \tag{2.10}$$

The next step is to consider the forces acting on the fluid, $\vec{F}_{net}$. In this thesis, we will only consider surface forces and body forces. The only body force that is relevant to the work in this thesis is the gravitational force. The total gravitational force applied to a material volume, $V(t)$, with density $\rho(\vec{x}, t)$ and gravitational acceleration, $g\hat{k}$, is

$$-\int_{V(t)} \rho g\hat{k}dV,$$

where $\hat{k}$ is the unit vector in the positive (upwards) z direction.

Unlike the body force, which is nonessential to the study of fluid motion - although essential to geophysical flows - the surface forces describes the effect of direct contact, both in the interior of the fluid and at the boundary of the fluid, at either a solid boundary or at the interface with another fluid (e.g., wind at the air-water interface on a lake). These surface forces can be described with the stress tensor, τ_{ij}. In three dimensions, the stress tensor is a 9 component, square, symmetric matrix. Its diagonal components describe the normal stresses - a force per unit area acting in the direction perpendicular to the surface - such as compression or tensile forces. The off diagonal components describe the shear stresses, a force per unit area acting parallel to a surface. A more detailed description of the components of the stress tensor can be found in (Kundu and Cohen, 1990).

The total of the surface forces in a material volume, $V(t)$, is obtained by adding up the surface forces along its boundary, $A(t)$ (Kundu and Cohen, 1990). This is written in integral form as

$$\int_{A(t)} \tau_{ij} dA_j,$$

where dA_j is the unit vector normal to the surface of the material volume. Applying the divergence theorem to this integral, adding it and the body force term to Eq. 2.10, we arrive at the following equation

$$\int_{V(t)} \Big[\rho \frac{D\vec{u}}{Dt} + g\rho\hat{k} - \nabla \cdot \tau\Big] dV = 0.$$

Since this is true over the arbitrary volume, it must also be true point wise, hence

$$\rho \frac{D\vec{u}}{Dt} = -g\rho\hat{k} + \nabla \cdot \tau. \tag{2.11}$$

This is known as the Cauchy equation. While named, this is not the final form of the momentum equation. To complete the derivation, we must introduce the stress-strain relationship, the relationship between the forces acting on the fluid (stress) and how the fluid is deformed by the forces (strain). For a Newtonian fluid, the relationship - known as a constitutive equation - is (Kundu and Cohen, 1990)

$$\tau_{ij} = -(p + \frac{2}{3}\mu\nabla \cdot \vec{u})\delta_{ij} + 2\mu e_{ij}, \tag{2.12}$$

where p is the pressure, μ is the dynamic viscosity, $\delta_i j$ is the identity matrix, and e_{ij} is the rate of strain tensor and is equal to

$$e_{ij} = \frac{1}{2}\Big(\frac{\partial u_i}{\partial x_j} + \frac{\partial u_j}{\partial x_i}\Big).$$

One should note that the trace of e_{ij} reduces exactly to $\nabla \cdot \vec{u}$. Up to this point, we have not assumed anything about the compressibility of the fluid described by these equations. From this point on, we will assume incompressibility, which is described briefly in Section 2.1.1. Using that result, the constitutive equation for an incompressible fluid is

$$\tau_{ij} = -p\delta_{ij} + 2\mu e_{ij}. \tag{2.13}$$

With this assumption, and plugging in Eq. 2.13 into Eq. 2.11, we arrive at the Navier-Stokes Equations for an incompressible fluid.

$$\rho \frac{D\vec{u}}{Dt} = -\nabla p - g\rho\hat{k} + \mu\nabla^2\vec{u} \tag{2.14}$$

This derivation is contained in (Kundu and Cohen, 1990) and (Vallis, 2017) in considerably more detail.

2.1.3 The Boussinesq approximation

While Eq. 2.14 are indeed the incompressible Navier-Stokes equations, even with Eq. 2.7, these equations are not yet closed. Currently, we have five unknowns ($\vec{u} = (u, v, w)$, p and ρ) but only four equations. The final equation is the internal energy, e, evolution equation. This equation will not be presented here - a derivation of this equation can be found in (Kundu and Cohen, 1990) - but instead its successor, the temperature, T, evolution equation. The internal energy equation becomes the temperature equation under what is known as the Boussinesq approximation.

In this section, I don't intend to present the full derivation of the Boussinesq approximation. Many textbooks have done this effectively[1]. In (Kundu and Cohen, 1990), the equations are derived by treating the fluid as an ideal gas. A perhaps naive assumption is successful at deriving the equations. Ref. Müller (2006) does not make the simplifying-but-naive ideal gas assumption but arrives at the same set of equations. Ref. Vallis (2017) takes a similar but perhaps more direct approach.

Ref. Müller (2006) states two basic assumptions: (1) the density does not vary significantly from its reference density, ρ_0 (this could be thought of as a mean density). (2)

[1] An interested reader should take a look at Andrew Grace's PhD Thesis (Grace, 2022), which provides a detailed summary of the derivation and justification of the Boussinesq approximation

The reference density does not vary significantly with depth. With these two assumptions, along with an infinite speed of sound, (Müller, 2006) shows that mass conservation becomes volume conservation (Eq. 2.7) and the density can be taken as constant in the momentum equations except in the buoyancy term. The incompressible Navier-Stokes equations under the Boussinesq approximation are therefore written as follows,

$$\frac{D\vec{u}}{Dt} = -\frac{1}{\rho_0}\nabla p + \nu\nabla^2\vec{u} - g\frac{\rho}{\rho_0}\hat{k}, \tag{2.15a}$$

$$\nabla \cdot \vec{u} = 0. \tag{2.15b}$$

$$\frac{DT}{Dt} = \kappa\nabla^2 T - \frac{1}{\rho_0 c_p}\nabla \cdot \vec{q}_{ext}, \tag{2.15c}$$

where c_p is the heat capacity, $\kappa = k/\rho_0 c_p$ is the thermal diffusivity and k is the thermal conductivity, $\nu = \mu/\rho_0$ is the momentum diffusivity, and $\vec{q}_{ext}$ is the external heat flux. In the previous set of equations, ρ represented the absolute density of the fluid. Here, it represents a perturbation of the absolute density from the reference density, ρ_0.

In this thesis, the only external source of heat is solar radiation, which obeys the Beer Lambert Law, Eq. 1.5. Since the solar radiation is from the sun and points downwards, vector form Eq. 1.5 is

$$\vec{q}_{ext} = -I_0 \exp\Big(-\frac{(L_z - z)}{\lambda}\Big)F(x,y)\hat{k}, \tag{2.16}$$

where $\hat{k}$ is the unit vector pointing in the z direction, and $F(x,y)$ is a smoothly varying function that describes the horizontal variations in solar radiation intensity. In Chapters 4 and 5, there will be horizontal variations and some radiation intensity. The exact form of these equations are given in the method sections for each chapter (4.2.1 and 5.2.1, in Chapters 4 and 5, respectively). In Chapter 3, there are no horizontal variations in solar radiation intensity and as a result $F(x,y) = 1$.

Taking the divergence of Eq. 2.16, we arrive at the form of the temperature equation that is used in each chapter

$$\frac{DT}{Dt} = \kappa\nabla^2 T + \frac{Q_0}{\lambda}\exp\Big(-\frac{(L_z - z)}{\lambda}\Big)F(x,y), \tag{2.17}$$

where $Q_0/\lambda = I_0/(\rho_0 c_p \lambda)$, is the magnitude of the temperature forcing in units of Celsius per second.

Equation of state

The density perturbation, ρ, (henceforth referred to as just as the density) is often determined from the temperature via an equation of state. In this thesis, we use the approximation to the UNESCO equation of state (Brydon et al., 1999), shifted so that the maximum temperature coincides with the temperature of maximum density for water, $T_{MD} = 4$ °C. This shifted equation of state has been previously applied to simulations of cold water convection (Grace et al., 2021; Allum et al., 2022). Figure 2.1 compares the shifted equation of state (used in this thesis) and unshifted equation of state, to the equation of state used by the MIT Global Circulation Model (MITgcm) (McDougall et al., 2003).

The fact that the temperature of maximum density does not coincide with 4 °C is a result of the equation of state in Ref. Brydon et al. (1999) not being properly calibrated for freshwater conditions. Nonetheless, as shown by 2.1, the shape is adequately captured by the equation of state in Ref. Brydon et al. (1999). The shifted and unshifted Brydon equations are cubic in temperature, with only three terms (in cases with no salinity, as is the entirety of this thesis). The original UNESCO equation (Millero et al., 1980) is quadratic in temperature and includes 26 terms. The reason for finding this approximation, as stated in Ref. Brydon et al. (1999), is because of the "high computational burden" of the original UNESCO equation of state. In the simulations presented in this thesis, determining the density from the temperature is not the most computationally expensive calculation, a title typically reserved for determining the pressure (see Section 2.4). Nonetheless, as shown in Figure 2.1, the differences between the Bryden, shifted, equation of state and the more accurate (and more complex) MITgcm equation of state is not significant.

2.2 Secondary equations

In order to aid in the analysis of the results presented in this thesis, we can derive secondary equations, starting from Eq. 2.15. In this section, we will look at the kinetic energy equation and the vorticity equation.

2.2.1 Kinetic energy

The evolution equation for the kinetic energy is important because it describes how energy stored in the motion of the fluid changes. The derivation, found in (Kundu and Cohen, 1990), relies on starting with the Cauchy equation (Eq. 2.11) and taking its dot product

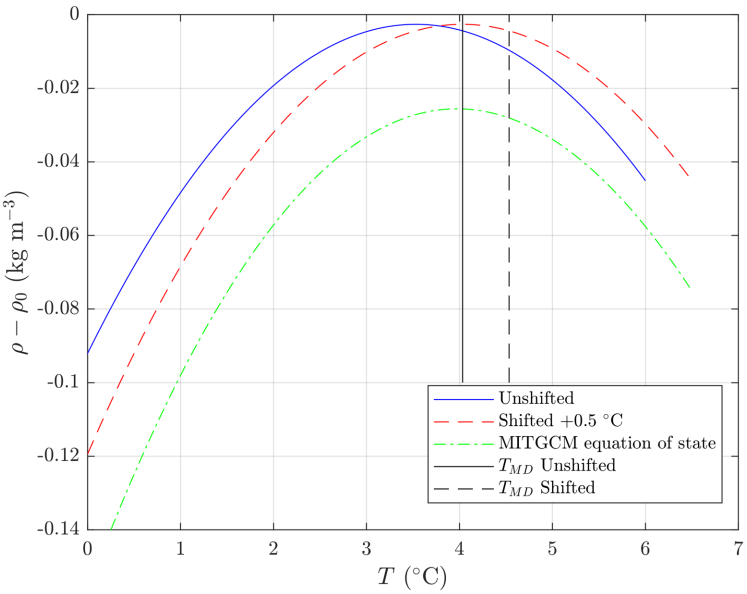

Figure 2.1: Brydon equation of state (Brydon et al., 1999) (solid, blue) shifted by 0.5 °C to the right (dashed, red). The MITGCM equation of state (McDougall et al., 2003) is included for comparison (dot-dashed, green). T_{MD} for each curve is indicated by the vertical lines. For each curve $\rho_0 = 1000$ kg m^{-3}.

with the fluid velocity, $\vec{u}$, and rewriting the stress divergence term using the product rule for divergence[2] as

$$\vec{u} \cdot (\nabla \cdot \tau) = \nabla \cdot (\vec{u} \cdot \tau) - \tau \nabla \vec{u}. \tag{2.18}$$

The left-hand side of Eq. 2.18 is the total increase in kinetic energy due to stresses and appears immediately upon taking the dot product with Eq. 2.11. The first term on the right-hand side of Eq. 2.18 is total work done on a fluid element. The last term is the work done due to deformation of the fluid element and reduces to τe (Kundu and Cohen, 1990), where e is the rate of strain tensor. Eq. 2.18 is effectively stating that the kinetic energy added to a fluid element is equal to the total work done on the fluid element, minus the deformation work. After deformation is accounted for, all the remaining energy is kinetic. Substituting in the constitutive equation for an incompressible Newtonian fluid, Eq. 2.13,

[2]The following equations are written using vector notation, which can be ambiguous at times. Using index notation, $\nabla \vec{u} = u_{i,j}$ and $\vec{u} \cdot \tau = u_i \tau_{ij}$. The former constructs a tensor and the later is a vector.

we arrive at

$$\rho_0 \frac{D}{Dt}\left(\frac{1}{2}\vec{u}\cdot\vec{u}\right) = \rho g w + \nabla\cdot(\vec{u}\cdot\tau) - \phi. \tag{2.19}$$

The last term is the viscous dissipation and is equal to $2\mu e^2$. This quantifies the transfer of kinetic energy to thermal energy via viscous effects. This quantity will be referenced occasionally in later chapters of this thesis, especially Chapter 3.

2.2.2 Vorticity

The next secondary equation that is important in this thesis is the vorticity, which is defined as $\nabla\times\vec{u}$. An evolution equation is obtained by taking the curl of Eq. 2.15a. Before we delve into the equation itself, its worthwhile spending a shorting time discussing the definition of the curl.

In 3D Cartesian coordinates, the curl of the vector is defined using the cross product of the ∇ operator and a vector. For a vector $\vec{F} = \big(F_1(x,y,z), F_2(x,y,z), F_3(x,y,z)\big)$, the curl of $\vec{F}$ is

$$\nabla\times\vec{F} = \Big(\frac{\partial F_3}{\partial y} - \frac{\partial F_2}{\partial z}, \frac{\partial F_1}{\partial z} - \frac{\partial F_3}{\partial x}, \frac{\partial F_2}{\partial x} - \frac{\partial F_1}{\partial y}\Big). \tag{2.20}$$

The full derivation (see (Kundu and Cohen, 1990), without the buoyancy term) is not worth including here as it requires the application of several involved vector calculus identities. However, we will include the derivation of the curl of the buoyancy term in Eq. 2.15a.

The buoyancy term can be written in vector form as

$$\vec{b} = -\frac{g}{\rho_0}(0,0,\rho(T(x,y,z))),$$

where $\vec{b}$ is the buoyancy. The curl of the buoyancy term is then

$$\nabla\times\vec{b} = \frac{g}{\rho_0}\Big(-\frac{\partial\rho}{\partial y}, \frac{\partial\rho}{\partial x}, 0\Big)$$

and is confined to the horizontal. This shows that horizontal density gradients generate rotation in the velocity field. This term is especially relevant to this thesis and any work related to gravity currents. The full vorticity equation is

$$\frac{D\vec{\omega}}{Dt} = (\vec{\omega}\cdot\nabla)\vec{u} + \frac{g}{\rho_0}\Big(-\frac{\partial\rho}{\partial y}, \frac{\partial\rho}{\partial x}, 0\Big) + \nu\nabla^2\vec{\omega}. \tag{2.21}$$

The first term is called the vortex stretching and tilting term and is nonzero when the vorticity field aligns with the velocity gradients. There is an excellent discussion in (Kundu and Cohen, 1990) that describes the physical meaning of this term. To summarize: stretching and tilting occur when the velocity changes along vortex lines. If the velocity gradient is parallel to the vortex lines, then stretching occurs. If the velocity gradient is perpendicular to the vortex lines, tilting occurs. The second term is called the baroclinic term and the final term is the viscosity term.

In this thesis, we will be considering both 2D and 3D simulations and the vorticity equation is most affected by a change between 2D and 3D. Typically we think of the cross product as being undefined in 2D, but if we restrict ourselves to a vector confined to the xz-plane, $\vec{F} = (F_1(x,z), 0, F_3(x,z))$, all terms in the curl that depend on F_2 or are derivatives with respect to y are now zero and hence the curl in 2D is written as

$$\nabla \times \vec{F} = \left(0, \frac{\partial F_1}{\partial z} - \frac{\partial F_3}{\partial x}, 0\right).$$

As a result, in 2D the vorticity is a scalar field $\vec{\omega} = (0, \omega, 0)$. Eq. 2.21 becomes

$$\frac{D\omega}{Dt} = \frac{g}{\rho_0}\frac{\partial \rho}{\partial x} + \nu \nabla^2 \omega. \tag{2.22}$$

In 2D, $(\vec{\omega}\cdot\nabla)\vec{u} = 0$ because $\vec{\omega}$ points in the y-direction and velocity gradients are confined to the xz-plane. As we will see in Chapter 3, the stretching and tilting of vortices - captured by $(\vec{\omega} \cdot \nabla)\vec{u}$ - is essential for the breakdown of vortices and enhanced dissipation. One way this can be visualized is explained in (Lesieur, 2008). A vortex tube - a collection of parallel vortex lines - which undergoes some vortex stretching, will decrease in diameter and increase its vorticity, by conservation of angular momentum. An increase in vorticity over a smaller region will also result in an increase in dissipative effects. Vortex tubes and lines do not exist in 2D and hence there is a missing mechanism to increase vorticity and dissipation compared to 3D.

2.3 Averaging notation

In this thesis, several forms of averaging (Horizontal, vertical, azimuthal, and domain averaging) will be used to present the results in each chapter.

For averages computed in the horizontal in Cartesian coordinates we will use the following notation

$$\langle f \rangle = \frac{1}{L_x L_y}\int_0^{L_x}\int_0^{L_y} f dy dx, \tag{2.23}$$

using the arbitrary scalar function f. In two dimensions, there is no y dimension and as a result Eq. 2.23 reduces to a single integral over x. If a horizontal mean is computed using only the x or only the y-direction in 3D, we will use $\langle f \rangle_x$ or $\langle f \rangle_y$ to denote this average.

For averages computed in the vertical we will use the following notation

$$\bar{f} = \frac{1}{L_z} \int_0^{L_z} f dz. \tag{2.24}$$

In Chapter 5, averaging in the azimuthal direction in cylindrical coordinates will be useful. Consider a cylindrical region or arbitrary height and radius R. Set the origin at the centre of this region with the z-axis aligned with the cylinder. An azimuthal average over this cylinder at height z is computed by taking the integral over a cylindrical shell of thickness Δr at radius r. The average is computed as

$$\langle f \rangle_\theta = \frac{\int_0^{\pi/2} \int_r^{r+\Delta r} f(r\cos(\theta), r\sin(\theta), z) r dr d\theta}{\int_0^{\pi/2} \int_r^{r+\Delta r} r dr d\theta}. \tag{2.25}$$

In Chapter 5, when we make use of an azimuthal average, they are computed numerically by defining a shell thickness, Δr, and summing the scalar quantity inside the shell at each z and dividing by the approximate area in the region.

In some cases an average will be computed over the domain and presented as a time series. In this case, the average will use the following notation

$$f_{avg} = \frac{1}{L_x L_y L_z} \int_0^{L_x} \int_0^{L_y} \int_0^{L_z} f dz dy dx. \tag{2.26}$$

Occasionally, the vertical, horizontal and domain averaging will be restricted to a subset of the horizontal, vertical or the domain. In which case, the region included in the averaging will be indicated in the relevant caption and the text.

In Chapters 3 and 4, the components of the horizontally average of the temperature equation will be used. It is obtained by taking the horizontal average (Eq. 2.23) of the temperature equation (Eq. 2.17)

$$\frac{\partial}{\partial t}\langle T \rangle = \kappa \frac{\partial^2}{\partial z^2}\langle T \rangle - \frac{\partial}{\partial z}\langle wT \rangle - \langle \nabla \cdot \vec{q}_{ext} \rangle. \tag{2.27}$$

In this thesis, $\nabla \cdot \vec{q}_{ext}$ will be independent of time, hence, it is possible to combine it with the left-hand side in order to define an evolution equation for the difference between the mean temperature profile and the mean forcing. We write this equation as follows

$$\frac{\partial}{\partial t}\Delta\langle T\rangle = \kappa\frac{\partial^2}{\partial z^2}\langle T\rangle - \frac{\partial}{\partial z}\langle wT\rangle, \tag{2.28}$$

where

$$\Delta\langle T\rangle = \langle T + \nabla \cdot \vec{q}_{ext}t + T_0(z)\rangle, \tag{2.29}$$

and $T_0(z)$ represents the initial temperature profile. Eq. 2.28 shows how convection and diffusion modulate $\langle T\rangle$ from the forcing. In the simulations presented in this thesis, convection is typically orders of magnitude stronger than diffusion except at the smallest length scales. As a result, the quantity $\langle wT\rangle$ appears repeatedly - especially in 3 - to describe how temperature is distributed by convection.

2.4 SPINS

The research presented in this thesis is comprised of a collection of numerical simulations, typically on the scale of metres. These simulations will be described in more detail in the respective chapters. To carry out these simulations, we use the non-hydrostatic pseudo spectral model, SPINS[3], described in the paper (Subich et al., 2013) and with further details in the PhD thesis (Subich, 2013). This model solves the Navier-Stokes equations under the Boussinesq approximation, specifically equations Eq. 2.15a and 2.15b. The model can be run under constant density conditions, but is often run with a varying density. Tracers can also be added, which by default obey an advection diffusion equation but source or sink terms can also be added. Tracers can be passive or active tracers. A passive tracer does not interact with the fluid flow, except to flow with it, an example is a dye. An active tracer interacts with the fluid flow - examples include temperature, salt or density - each of which would change the buoyancy term in the momentum equations (Eq. 2.15a).

In certain aspects, SPINS is a highly adaptable model that is easy to use and run for a physicist with only introductory C++ experience. SPINS is capable of applying periodic, no slip and free slip boundary conditions in velocity and Neumann boundary conditions for the tracers (typically temperature or density). It is also possible to apply an arbitrary - smoothly varying - mapping to the bottom boundary, which has been used to study flows

[3]Stands for **Sp**ectral Solver of the **I**ncompressible **N**avier-**S**tokes Equations

over bumps (Soontiens et al., 2015; Harnanan et al., 2017; Deepwell et al., 2017, 2021). Further, one can add arbitrary forcings - again, assumed to be smoothly varying due to the spectral nature of the model - to each of the momentum equations (Eq. 2.15a) or a tracer equation (often temperature or density, Eq. 2.17).

In other aspects, SPINS has some clear restrictions. The domain must be rectangular[4] and the boundary conditions of parallel walls must be of the same type.

In addition to applications to systems with curved boundaries, briefly discussed above, SPINS has been applied to a wide variety of domains. Including, but not limited to, internal waves interacting with sloped boundaries (Hartharn-Evans et al., 2022), convection generated by surface cooling (Olsthoorn et al., 2021), double-diffusive instabilities (Legare et al., 2021) and internal solitary waves (Deepwell et al., 2017). More recently, the focus has been on shear flows and gravity currents in the so-called cold water regime (Hanson et al., 2021; Grace, 2022; Grace et al., 2023b; Allum et al., 2022), discussed in more detail in the previous chapter. The cold-water regime is also of primary interest for this thesis.

SPINS, like any numerical model resolved on a grid, might produce what is known as aliasing (Flannery et al., 1992). This is a phenomenon that occurs in solutions to nonlinear systems computed used pseudospectral methods (Boyd, 2000). Once a grid with N points is set between $x = 0,\ L_x$, there is a maximum wavenumber that is possible to resolve on this grid using the trigonometric basis of a Fourier transform (Boyd, 2000; Flannery et al., 1992). The maximum wavenumber is

$$K = \frac{\pi}{\Delta x},$$

where Δx is the grid spacing. K is the shortest wavenumber sinusoid that is uniquely represented on a grid of N points between $x = 0,\ L_x$ with grid spacing Δx. A sinusoidal wave with wavenumber greater than K will appear the same as some other wavenumber on the interval $[-K, K]$ (Flannery et al., 1992; Boyd, 2000). This shift to resolvable wavenumber is precisely aliasing. Wavenumbers in a Fourier Transform outside of the interval $[-K, K]$ are reflected back into $[-K, K]$. Figure 12.1.1 of Ref. Flannery et al. (1992) perfectly depicts this reflection. The reflection coupled with the typical decay of a Fourier transform towards large wavenumbers implies that aliasing is most apparent at $k = \pm K$ with a smaller contribution at smaller k.

One way to deal with aliasing is to filter out some of the larger wavenumbers near the grid scale. Simple filters involve erasing the information at wavenumbers above a cut-off but more complex filters, like the ones SPINS uses, increasing the damping intensity

[4]Other than a mapped region, which is doable but does slow down computation time

smoothly towards the grid scale past a cut-off. A filter, regardless of type, has a different effect on the dynamics at small scales in 2D and 3D simulations. As you increase the number of dimensions, the fraction of the total wavenumbers dampened or removed by the filter increases. This is schematically represented in Figure 2.2. This effect is exaggerated even further in 3D. As a result of this effect, perturbations grow into instabilities more quickly in 2D compared to 3D [5], as the filter has a more dramatic effect on the small scales (large wavenumbers).

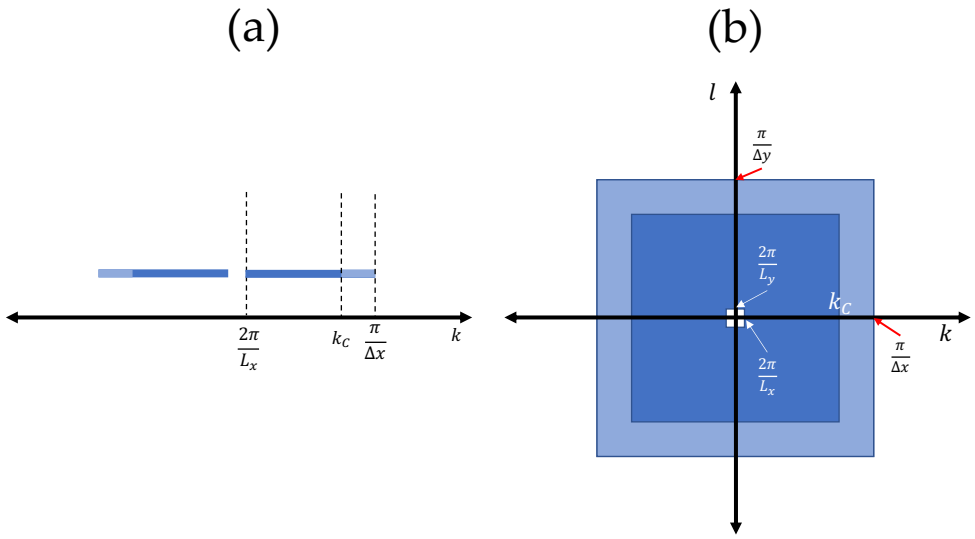

Figure 2.2: Schematic of the wavenumber space subjected to a uniform filter to wavenumbers larger than a cutoff frequency, k_C, in (a) one dimension and (b) 2D. The filter used by SPINS is exponential above the cutoff, this schematic is only meant to depict the idea of filtering above a cutoff.

SPINS is capable of direct numerical simulations, which is when all the important physics relevant to a simulation is resolved. Analytical solutions to the Navier-Stokes equations are not possible for the vast majority of flows and as a result, simulations at high resolution are the closest we can get to solutions to the Navier-Stokes equations. A filter applied to the smallest of scales might remove real physics from a simulation if too low of a resolution is used. However, this is still considered direct numerical simulations by some standards because (a) the filtering exists to remove unphysical, but typical consequences

[5]This is only true if the fastest growing mode as estimated by stability theory is below the cut-off. This might be true for early times with very small density differences due to low intensity solar forcing.

of numerical modelling, and (b) more importantly, no parameterization or model is used to estimate the effects of the smaller scales as it typical for large eddy simulations or the Reynold's Averaged Navier-Stokes equations (Moin and Mahesh, 1998).

2.4.1 Storage and memory challenges

Some of the simulations presented in this thesis are quite intensive as far as parallelization, storage and memory requirements, particularly the 3D simulations in Chapters 3 and 5.

The 3D simulations presented in this thesis required heavy parallelization, dividing the system onto 512 cores made available by the Digital Research Alliance of Canada via a Resource Allocation Competition award. We define the efficiency, E_N, with N cores as

$$E_N = \frac{t_1}{N t_N},$$

where t_i is the duration of the simulation in clock time. If a simulation is perfectly efficient, then $t_1 = N t_N$ and $E_N = 1$. However, some time will be lost via communication between cores during each time step. Figure 2.3 compares the efficiency of large 3D simulations on whole nodes and any number of nodes. A node is a single CPU that has typically many cores. It is expected that by spreading the cores across a larger number of nodes (as in any# of nodes), however, Figure 2.3 shows that this is negligible. Applying 512 cores to these simulations results in an efficiency of ≈ 0.6. The theoretical minimum where a single core is more efficient that N cores, is when $t_1 = t_N$, or when $E_N = \frac{1}{N}$. For $N = 512$, $\frac{1}{N} \approx 2 \times 10^{-3}$, showing that indeed SPINS scales quite well.

Figure 2.3 also shows that by doubling the number of cores in the second dimension does not have a large impact on efficiency, in fact, the simulation with twice as many points in the second dimension is the most efficient. This is likely due to general variability in efficiency that can be encountered when using a system like the Digital Research Alliance clusters. Doubling the number of cores, doubles the memory requirements and appears to have a low impact on the efficiency of these simulations. Naturally, doubling the number of points does increase the raw computation time.

The issue with storage from these large simulations typically comes from trying to access the data to analyze the simulations. The individual output files of the temperature field and all three velocity components ranged from 4 GB to 16 GB at each time step. The sizes of these data files, particularly the later, changed the ways that one can analyze SPINS output. The data files and the simulations are so large because the systems we

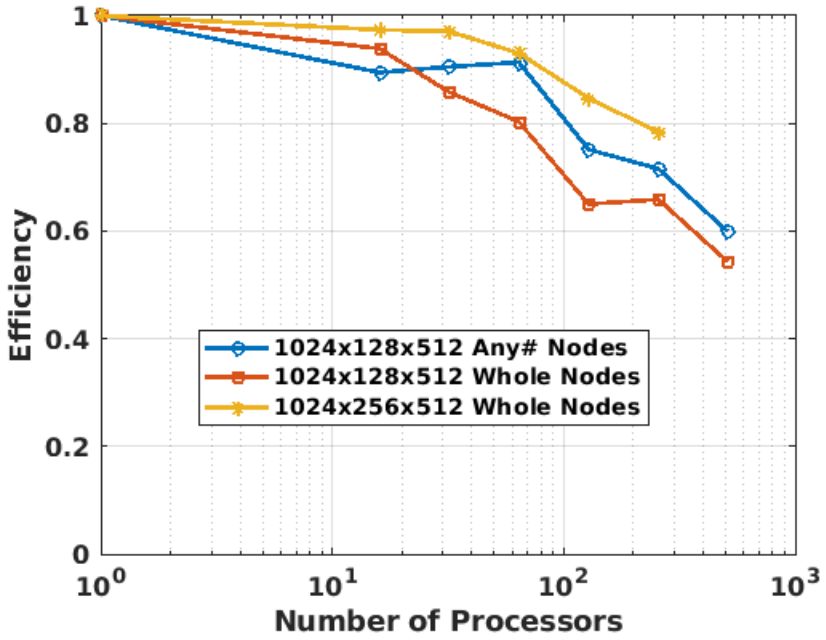

Figure 2.3: Efficiency, defined in the text, for 1, 16, 32, 64, 128, 256 and 512 CPUs for two systems with (N_x, N_y, N_z) given in the legend. These 3D simulations were run on the Graham Digital Research Alliance cluster. This figure was used in our successful application for a Resource Allocation Competition award.

study require three things that increase the size of the simulation: (a) high resolution, (b) space for motion in the vertical, and (c) space for motion in the horizontal.

We required high resolution to resolve the various scales of motion, space in the vertical to allow room for the development of vertical convection and space in the horizontal to allow space for the propagation of lateral gravity currents, an unusual combination.

The vast majority of analysis using data from the simulations in this thesis was done in Paraview, a visualization software ideal for 3D data, and MATLAB, a programming software optimized for linear algebra of reasonably sized matrices and plotting data. Paraview is ideal for visualizing data no more than a few hundreds of MB. For these visualizations, we were required to truncate the data and interpolate it onto a coarser grid. Of course, some care had to be given to ensure that the new grid was not so coarse as to distort the data.

The problem for MATLAB lies in opening the files. For files as large as those in

this thesis this is drastically slower. Moreover, as the memory requirements required to complete most standard computations is large, a memory allocation is required to run an M-file as a batch script, with the output produced only after several hours. On smaller data sets, it is possible to redo calculations (like a horizontal average) live when remaking a figure. This is not possible for files of 4 GB or larger. Instead, the practice was to create the data and save it in a .mat file to be accessed later for making a figure. This process has the drawback of requiring significantly more precision when writing MATLAB scripts as errors in the code or incorrect parameters could require a rerun that could take another day to complete.

Future work should be taken to update some of the default SPINS programs to make them more efficient. For example, the most common MATLAB function written for SPINS is called spins_reader. It reads the output files into MATLAB as an array. As of right now, it is completely serial and future researchers considering using SPINS to output very large data sets should consider designing a parallelized version.

2.5 Thesis layout

The rest of this thesis is layed out as follows: Chapters 3, 4, and 5 are the three results chapters and 6 is the conclusion chapter.

Chapter 3 presents the results of simulations of radiatively driven convection in both 2D and 3D and with and without a background stratification. The main focus of this thesis is on heterogeneous solar radiation intensity and its effect on buoyancy driven flows. Chapter 3, which contains no such variations, is a precursor to Chapter 4 and 5, which present simulations with heterogeneous solar radiation intensity in 2D and 3D, respectively. Hence, it is reasonable to start with a chapter comparing radiatively driven convection (Chapter 3), which is important dynamics in each chapter of this thesis.

The results chapters are formatted quite similarly. Each starts with an introduction where context for this research is presented. It is followed by a methods section where the systems of interest are defined, as well as any quantities that are used in that chapter that are not used in the results of other chapters.

The next section is a results preamble section that aims to briefly set the stage for the results. The results are then presented across several sections, the number of results sections varies between chapters depending on what best serves the narrative. The last section of each chapter is a conclusion section.

The final chapter of this thesis, Chapter 6, is the conclusion and future work chapter. The work of this thesis is briefly concluded and several avenues for future work are listed, where a small subset are discussed in more detail. Chapter 6 does not include a detailed conclusion and only aims to summarize the main points of each results chapter. A more complete conclusion is given at the end of each results chapter, in the conclusion section.

Chapter 3

Radiatively Driven Convection: A comparison between two- and three-dimensions

3.1 Introduction

Certain natural phenomenon can be reliably modelled in two-dimensions; for example, the initial stages of shear instabilities for which the fastest growing perturbation is two-dimensional. This result is known as Squire's theorem (Kundu and Cohen, 1990). In this case, it is possible to reproduce some behaviour of the natural phenomenon without increasing the cost of your simulation to that of a fully three dimensional one. However, all natural water bodies - lakes, rivers, oceans etc. - are three dimensional, and hence three dimensions are required for accurate simulations and especially direct numerical simulations.

There are some advantages to using high-resolution, two-dimensional simulations, such as faster run times, and lower memory requirements and lower storage size of outputs. Due to these advantages, two-dimensional simulations are often preferred, especially when doing parameter explorations, because more frequent runs are possible enabling a more complete survey of the parameter space.

The focus of this chapter is on radiatively driven convection at temperatures below the temperature of maximum density. As it was discussed in Chapter 1, the change in

temperature due to solar radiation is proportional to

$$\exp(-(L_z - z)/\lambda),$$

with the full equation given in Eq. 1.6. The resulting temperature profile is an unstable stratification with the warmest temperatures near the surface. This scenario is a more complicated version of a well researched set-up where a heavy fluid rests on top of a light fluid with a thin pycnocline layer between them. This unstable configuration and the resulting motion is called the Rayleigh-Taylor (with the acronym RT) instability (Rayleigh, 1882; Chandrasekhar, 2013).

A review of Rayleigh-Taylor instabilities is given in Ref. Sharp (1984) with a more recent review focused on theoretical advancements in Ref. Abarzhi (2010). The Rayleigh-Taylor instability grows from small perturbations in the flow or density at or near the pycnocline. The heavy fluid penetrates downwards as the light fluid penetrates upwards. Linear stability theory shows that the growth rate is related to the Atwood number,

$$A = \frac{\rho_H - \rho_L}{\rho_H + \rho_L},$$

where ρ_H (ρ_L) is the density of the heavy (light) fluid. Rayleigh-Taylor experiments that consider small A typically use values on the range of $\mathcal{O}(10^{-3})$ to $\mathcal{O}(10^{-1})$ (Dalziel, 1993; Dalziel et al., 1999; Andrews and Dalziel, 2010; Taghavi et al., 2012). In this chapter, and the remainder of this thesis, the maximum density differences result in an Atwood number that is $\mathcal{O}(10^{-5})$. This work and any related work in the cold water regime (Grace et al., 2021, 2022; Allum et al., 2022; Castro-Folker et al., 2023) probes this Atwood number regime, overall unexplored in the Rayleigh-Taylor instability and gravity current literature due to its narrow applicability to cold, freshwater lakes and the associated difficulty in studying these systems.

Once nonlinear terms become important and the features at the interface grow, the following nomenclature is used. The upwelling, light fluid are called bubbles and the downwelling, heavy fluid are called spikes (Sharp, 1984; Young et al., 2001; Cabot, 2006; Abarzhi, 2010). The names of these features are derived from the shape itself at the early stages of the nonlinear regime. The bubble is typically rounded and the spike more narrow and pointed (See Figure 1 in Ref. Abarzhi (2010)). After some time, the spike and bubbles are similar in shape. Shear forces at the boundary between the bubble and spikes produce vortices that give the developing instability its mushroom-like shape (Sharp, 1984; Abarzhi, 2010). This shape is especially apparent in 2D as it will be shown in Section 3.3. These features are present in 3D but breakdown more rapidly (Young et al., 2001; Cabot,

2006). The final stage, as described by (Sharp, 1984) is a breakdown of these features into turbulence.

There are two key differences between the stratification introduced by Eq. 1.6 and the classical Rayleigh-Taylor instability. First, the densities of the two, miscible, fluids are fixed in time (neglecting any mixing), whereas Eq. 1.6 introduces a time dependence of the upper layer. Second, the thin boundary layer is much smaller than the depth of either fluid. In fact, in theory the depth of both fluids are often assumed to be infinite (Kundu and Cohen, 1990; Chandrasekhar, 2013). Thirdly, the stratification introduced by Eq. 1.6 is varying across all depths, rather than constant density above and below the interface. Eq. 1.6 approaches zero rather quickly and, assuming $L_z/\lambda \ll 1$, there is an effective lower layer but no clear upper layer. As a result, the resulting instability can only generate mixing downwards, starting at or near the surface.

There is existing literature that compares the motion of Rayleigh-Taylor instabilities in 2D and 3D (Young et al., 2001; Cabot, 2006), but typically this involves a two-layer stratification, rather than the continuous, time varying stratification introduced by Eq. 1.6. At the same time, there are several examples of using two dimensional simulations to study the motion of water in lakes subjected to solar radiation in the cold water regime ($T < T_{MD}$) (Ulloa et al., 2019; Ramón et al., 2021; Grace et al., 2021; Allum et al., 2022) and one in three-dimensions (Grace et al., 2022). Vertical convection driven by the inverse stratification induced by the solar radiation is central to the analysis of each of these papers. In this chapter, we compare and contrast radiatively driven convection in both two- and three-dimensional simulations in order to show the differences between two and three dimensions.

3.1.1 Chapter overview

In this chapter, penetrative convection and radiatively driven convection are compared and contrasted in 2D and 3D. The analysis provides the highest resolution simulations to date of radiatively driven convection with and without a background stratification. Section 3.2 is the methods section where the system of interest is defined, the cases and relevant parameters are presented, and several quantities that are used in the results are defined. A summary of the results is given in Section 3.3. The 2D and 3D comparison without a background stratification is presented in Section 3.4 and with a background stratification in Section 3.4.

3.2 Methods preamble

3.2.1 System of interest

To analyze the differences between 2D and 3D convection driven by solar radiation, we consider four cases, listed in Table 3.1. In each case, the domain is rectangular and wider in the horizontal direction. Further, the length of the x dimension is equal to the length of the y dimensions for the 3D cases. We have two unstratified and two stratified cases, one in 2D and one in 3D for each. The stratification present in the initial conditions for the 2D and 3D stratified cases is discussed further below in Section 3.2.3. The 2D and 3D unstratified cases have constant temperature initial conditions. The only difference between the 2D and 3D cases with the same initial conditions is that the 2D case does not have a y-dimension and the motion is restricted to the xz-plane.

Case Name	ΔT (°C)
2D Unstratified	0
3D Unstratified	0
2D Stratified	0.5
3D Stratified	0.5

Table 3.1: Table of cases. For unchanged parameters between cases see Table 3.2. ΔT is the temperature change from the bottom to the top of the domain in the initial conditions.

The unchanged parameters are listed in Table 3.2. These parameters are used repeatedly throughout this thesis, and some are varied in Chapter 4. A more detailed discussion for the values given in Table 3.2 is given in Section 4.2.1[1]. For the 2D cases, L_y is not given and N_y is equal to one. A side view of the xz plane for all the cases considered in this chapter is given in Figure 3.1. The dotted line in the centre gives the vertical structure of the solar radiation intensity as a function of depth, where the purely vertical portion near the bottom indicates a value near zero. At the surface, the change in temperature per second due to solar radiation is Q_0/λ, as in Eq. 2.17, indicated by the rightward curve of the dotted line. This value for Q_0 is used for this chapter and the rest of this thesis.

In this chapter, there is no horizontal structure to the forcing term. The final term in

[1]Traditionally, a discussion of this type is done the first time parameters are mentioned. However, here it is kept for Chapter 4, as it was included in the published version of that chapter in Ref. Allum et al. (2022).

Eq. 2.17 is therefore

$$\frac{Q_0}{\lambda}\exp\Big(-\frac{(L_z-z)}{\lambda}\Big). \tag{3.1}$$

The schematic in Figure 3.1 shows that most of the body forcing is injected in the layer near the surface with depth λ. The y dimension is not shown but is present in the 3D cases, both stratified and unstratified. The length of this dimension, L_y, is equal to the length of the x dimension, L_x.

The aspect ratio $L_x/L_z = 2$ is unusual for a study entirely concerned with motion in the vertical. Motion in the horizontal is confined to the horizontal length scale of convective plumes, which grow due to the vertical temperature gradient. However, as we will see in Section 3.3, the size of these convective cells increases with time due to the constant solar radiation intensity increasing the vertical temperature gradient. If, say, the initial conditions started with an unstable stratification with the same structure as the dotted line in Figure 3.1 and no temperature forcing, normal development of instabilities would lead to an increase in the horizontal length scales of convective cells. However, over time due to a combination of mixing and a net downwards buoyancy flux, motion in the fluid would gradually slow and the length scale of these plumes would cease growing and also decrease. It is the constant supply of heat which continues the growth of the convective cells. It should be noted that due to the nonlinear equation of state, Figure 2.1, eventually temperatures will exceed a temperature of maximum density and the supply of heat will begin to suppress motion. However, in this thesis, simulations will end before temperatures exceed the temperature of maximum density.

As a result, a wide domain is required to accurately resolve the horizontal length scales of this problem at all times. In addition, in Chapters 4 and 5, there will be significant lateral and vertical motion simultaneously.

3.2.2 Depth of the convective layer

In this thesis, we will refer to the layer of fluid with active convection as the convective layer (CL), not to be confused with the CML present in ice-covered lakes and oceans (Bouffard and Wüest, 2019; Ulloa et al., 2019). In fresh water lakes at the end of winter, the CML is a quasi-steady state induced by diurnal forcing in fresh water lakes under ice. It is characterized by active convection which gradually penetrates into a stable stratification below and constant temperature with depth. The CL instead corresponds to the layer of active convection in the simulations presented in this thesis but prior to the development

Parameter	Description	Value
L_x	Lake Width	5.12 m
L_y	Lake Length	5.12 m
L_z	Lake Depth	2.56 m
N_x	X Grid Points	1024
N_y	Y Grid Points	1024
N_z	Z Grid Points	512
T_0	Initial Temperature	2.5 °C
λ	Attenuation Coefficient	0.4 m
ρ_0	Reference Density	1000 kg m^{-3}
ν	Kinematic Viscosity	10^{-6} m^2s^{-1}
κ	Temperature Diffusivity	1.43×10^{-7} m^2s^{-1}
Q_0	Magnitude of Solar Forcing	7.17×10^{-5} °Cms^{-1}

Table 3.2: System parameters used in this chapter which are unchanged between simulations.

of a CML. The CL can be thought of as the convection that leads to the development of the CML. Here we are studying the initial development of convection due to a Beer-Lambert law body forcing in the cold water regime in under-ice scenarios in the simplest configuration. As described in 3.2.1, we will consider a system with constant temperature initial conditions and one with a background stratification. The former is not typical of an ice-covered lake prior to ice-off (Kirillin et al., 2012; Bouffard and Wüest, 2019; Yang et al., 2017). Typically, prior to the introduction of solar radiation, the water column is stably stratified with T held at 0 °C at the surface. Nonetheless, the depth of the CL is a feature of interest. In this chapter, we track the depth of the CL, h_{CL}, which is equal to the height of the CL, z_{CL}, subtracted from the height of the domain, L_z.

In this chapter, we use $\langle wT \rangle$ (Eq. 2.28) to estimate h_{CL}. z_{CL} is defined by,

$$\langle wT \rangle (z_{CL}) = \delta_{CL}, \tag{3.2}$$

where δ_{CL} is an arbitrary cut off value which is determined through trial and error and with reference to the data. h_{CL} is easily determined through z_{CL} as defined above. For the unstratified cases, δ_{CL} is set at -10^{-5} ms^{-1} °C. For the stratified cases, δ_{CL} is set at -4×10^{-6} ms^{-1} °C.

The definition in Eq. 3.2 is a natural choice for the unstratified cases because beneath the CL, $\langle wT \rangle \approx 0$. However, it is slightly complicated for the stratified cases. The approximate equality holds for the stratified cases as long as temperatures in the CL

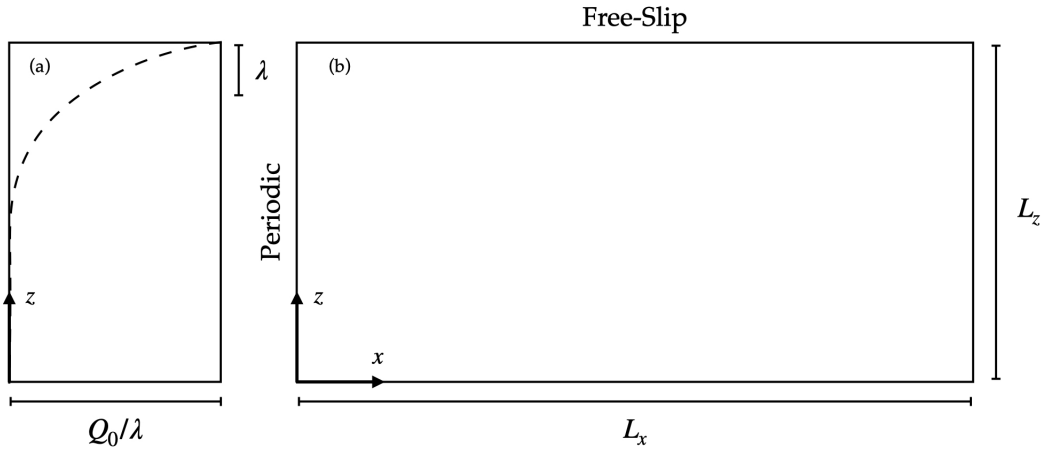

Figure 3.1: Schematic of the system used for the simulations in this chapter (Table 3.1). (a) Shape of the solar forcing according to Eq. 3.1. (b) Side view of the xz domain. Velocity boundary conditions listed along the respective boundaries. The 3D cases have a third dimension in and out of the page with $L_y = L_x$. The boundary conditions at the y boundaries match those at the x boundaries. See Table 3.2 and 3.1 for parameter definitions.

exceed temperatures in the background stratification immediately below the CL. Once the temperatures in the background stratification exceed the temperatures in the CL, $\langle wT \rangle$ will exceed zero, indicating an average upwards flux of warm fluid. For consistency, Eq. 3.2 is still used for the stratified case, however, it effectively is defined as the height where $\langle wT \rangle = 0$. This differs to the unstratified case because $\langle wT \rangle$ approaches zero but never crosses it.

In Ref. Kirillin et al. (2012) it is reported that

$$\frac{dh_{CML}}{dt} = -0.2(h_{CML}\Delta b)^{-1} w_*^3, \tag{3.3}$$

where h_{CML} is the depth of the CML, Δb is the buoyancy difference between the bottom of the CML and the stratified layer below, and w_* is a convective velocity scale for motions within the CML proposed by Ref. Mironov et al. (2002) and reported by Ref. Bouffard and Wüest (2019). w^* is related to the root-mean squared velocity, u_{rms} within the CML, defined as

$$u_{rms} = \sqrt{\langle u_i u_i \rangle}, \tag{3.4}$$

where the repeated index implies a sum over $i = 1, 3$ in 2D and $i = 1, 2, 3$ in 3D. u_{rms} is estimated as approximately $0.5w_*$ via measurements in Ref. Farmer (1975) and $0.7w_*$ via large eddy simulations in Ref. Mironov et al. (2002). u_{rms} is used in the analysis and comparison of 2D to 3D in Section 3.3.

3.2.3 Stratification

Ice covered lakes are typically stratified when solar radiation first begins to drive convection in the late winter (Kirillin et al., 2012; Bouffard and Wüest, 2019; Yang et al., 2017) The constant temperature case provides a baseline, and would be easier to implement in a physical laboratory, hence we start there in Section 3.4. The stratified initial conditions are more consistent with measurements in small lakes under ice-cover in the early part of the winter. The stratification we use is linear in temperature and due to density increasing with temperature for $T < T_{MD}$ is stably stratified. It can be written as follows

$$T(z) = \frac{\Delta T}{L_z}(L_z - z) + T_0. \tag{3.5}$$

The temperature change in the stratification, ΔT, is given for each stratified case in Table 3.1. This temperature profile results in a density profile that is increasing with depth, and a density gradient that is decreasing with depth. This is similar to Ref. Ulloa et al. (2019), which uses a smaller ΔT but the same form of the temperature stratification as Eq. 3.5. A linear temperature stratification is also observed in the early winter - prior to convective motion driven by solar radiation - see for example Ref. Kirillin et al. (2012). The temperature stratification and the resulting density stratification from the shifted equation of state (Brydon et al., 1999) are compared in Figure 3.2. While the nonlinearity of the equation of state is clear in Figure 3.2, it is also nearly linear over this narrow temperature range. Figure 3.2 also shows that the stratification is strongest near the surface and weakens near the bottom where the temperature is closer to T_{MD}. A cautious reader would be careful to not misinterpret the slopes on Figure 3.2. The dependent variable is on the horizontal axis, this is commonly done to aid in a visualization of the z axis as a vertical component of the system. This approach of putting the dependent variable on the horizontal axis when the independent variable is the z axis will be used repeatedly throughout this thesis.

In the simulations with no initial stratification, the solar radiation immediately creates an unstable stratification that takes some time to generate significant motion in the vertical. However, with the linear stratification of Eq. 3.5, the stratification will not be

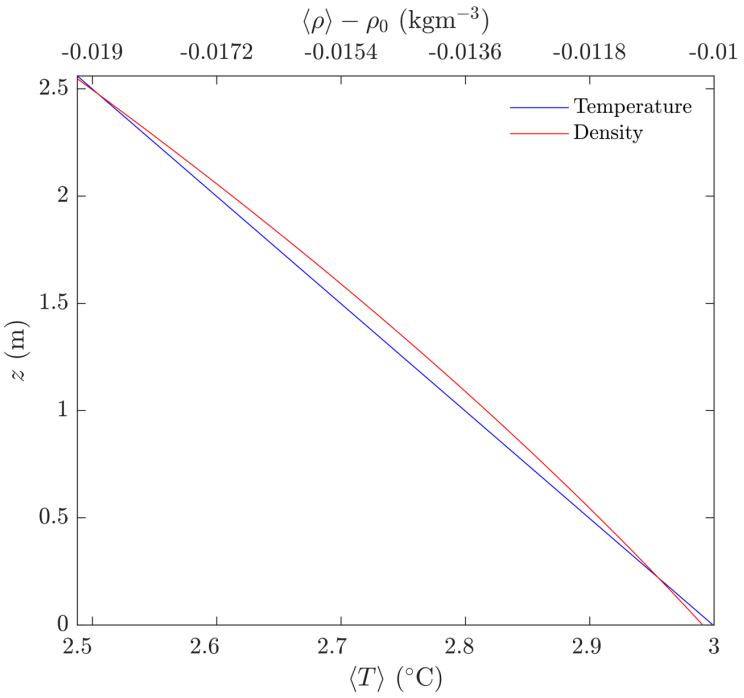

Figure 3.2: Comparison of the horizontally averaged initial conditions of temperature and density for the stratified cases presented in this chapter (see Table 3.1). The vertical axis gives the height of the domain. The bottom horizontal axis gives the temperature (blue) and the top horizontal axis gives the density perturbation (red) from the background, ρ_0.

immediately unstable. We can estimate the time where the stratification becomes unstable by considering the temperature evolution equation, Eq. 2.17, with $\vec{u} = 0$ and ignoring diffusivity

$$\frac{\partial T}{\partial t} = \frac{Q_0}{\lambda} \exp\Big(- \frac{L_z - z}{\lambda}\Big). \tag{3.6}$$

The following analysis is similar to the analysis presented in section 4(a) of (Farmer, 1975). Solving this simple equation for temperature and including the initial conditions, we have a background temperature profile written as

$$T_b(z,t) = \frac{Q_0}{\lambda} \exp\Big(- \frac{L_z - z}{\lambda}\Big)t + \frac{\Delta T}{L_z}(L_z - z) + T_0. \tag{3.7}$$

The question here is: when is the temperature gradient in z less than zero? We can find this by taking the gradient of Eq. 3.7 with respect to z, setting it to zero, and solving for

$L_z - z_s$, where z_s is the height of the transition from unstable to stable stratification. If we do that we find that

$$L_z - z_s = -\lambda \ln\left(\frac{\lambda^2 \Delta T}{t Q_0 L_z}\right). \tag{3.8}$$

This equation gives the depth below the surface where the stratification becomes stable. Here we are seeking the time in which the stratification first becomes unstable in the vertical. The form of the temperature forcing has temperatures increasing fastest at $L_z - z_s = 0$, hence, the temperature profile will become unstable first at the surface and the depth of this region will continually grow. By inspection, $L_z - z_s = 0$ occurs in Eq. 3.8 when the argument of the natural logarithm is unity. In other words,

$$t_s = \frac{\lambda^2 \Delta T}{Q_0 L_z}. \tag{3.9}$$

This equation is qualitatively consistent with our expectations of the system. A stronger solar forcing, captured by Q_0, results in a smaller time to instability. A stronger stratification has the reverse effect. Increasing λ - which is effectively increasing the water clarity and decreasing the rate of absorption with depth - increases t_s. Since solar radiation is absorbed more slowly, the temperature gradient in the vertical is smaller at all times. This change in t_s due to changes in λ is not linear and perhaps unsurprisingly as λ contributes to both the magnitude of the solar forcing and the shape of the Beer-Lambert law in Eq. 3.6.

t_s is an important time because Rayleigh Taylor instabilities cannot form before this time. However, for times only briefly following t_s, significant motion is still confined to a small layer near the surface. In the unstratified case, most of the temperature change occurs in the top $\lambda = 0.4$ m of the domain. Hence, another important time scale is when the left-hand side of Eq. 3.8 grows to $L_z - z_s = \lambda$, which occurs when

$$t_l = \frac{\lambda^2 \Delta T}{Q_0 L_z e^{-1}}.$$

$L_z - z_s = \lambda$ is somewhat of an arbitrary depth, other than it being equal to the attenuation length. However, it is a natural choice for a length scale of this problem. A nondimensionalization scheme for this system is presented in Chapter 4 and this length scale is used.

$t_s/t_l = e^{-1} \approx 0.36$ suggesting the time to reach an unstable region with depth λ is 3 times longer than it takes to develop an unstable stratification of any depth. We can

further understand why this is the case by finding the velocity of the height of the transition from unstable to stable by taking the derivative with respect to time of Figure 3.8 which becomes

$$\frac{\partial(L_z - z_s)}{\partial t} = \frac{\lambda}{t}. \tag{3.10}$$

For the time scales of interest, $t \gg \mathcal{O}(10^2 \text{ s})$. Eq. 3.10 is the velocity of the transition point between stable and unstable stratification. At early times, Eq. 3.10 will be larger than the typical velocity scales within the CL.

The above calculations will be considered in the results section, but not central to the results. However, they provide some important context when considering the differences between the stratified and unstratified cases.

3.2.4 Histograms

Average profiles (Eq. 2.23) are commonly used measures in fluid dynamics research. Profiles are convenient because they compress 2D or 3D data into a single line plot. However, the mean can leave out important information encoded in the full data. In this chapter, histograms are also used to analyze and quantify the differences between 2D and 3D. In 2D, histograms are typically less useful because of the fewer number of data points at every height.

By extending two dimensional simulations into a third dimension, we get N_y times more grid points. This naturally results in slower computations but more accurate physics. In this case, $N_y = 1024$. This reduction in points is responsible for the noise in $\langle wT \rangle$ in Figure 3.7(a) and Figure 3.10(a). In Section 3.3 histograms of wT in Figure 3.11 and of viscous dissipation (Eq. 2.19) in Figure 3.13 are given. The histograms are evaluated at each horizontal slice (fixed z) of the 3D simulation. Each discrete height in the 3D system has its own independent histogram. The colour of each pixel corresponds to the number of grid points with values in the range of the bin at fixed z. The shape of these histograms provide useful information about the dynamics, heat transfer and differences between 2D and 3D.

3.3 Results preamble

2D and 3D simulations subjected to volumetric heating generate convection towards the bottom, which can be classified as penetrative convection if the initial temperature profile

is stratified. This is shown in Figure 3.3 in the unstratified case and Figure 3.17 and 3.22 in the stratified case. Regardless of initial conditions, in both 2D and 3D, there is a solar radiation dominated phase where warming and motion is confined to a depth of $\lambda = 0.4$ m below the surface, followed by a convection dominated phase characterized by significant transport of heat in the vertical towards the bottom and a net cooling effect near the surface. The main difference identified between 2D and 3D convection - present with both unstratified and stratified initial conditions - is the difference in vorticity generation (Figure 3.5 and 3.25(a)) and the resulting lack of viscous dissipation in 2D. In Section 3.4, the unstratified cases are compared and analyzed, looking at full fields, domain averaged quantities and histograms. Similarly, in Section 3.5, for the stratified cases.

3.4 Constant temperature initial conditions

3.4.1 Temperature field

Figure 3.3 compares the temperature field at $t = 2100$ s in 2D and 3D using a single horizontal and vertical slice for the 3D case and the entire domain for the 2D case. The temperature fields shown in Figure 3.3 are presented in a mature state, well into the convection dominated phase[2]. In 2D (Figure 3.3(a)), the temperature field is dominated by large convective plumes, consisting of both downwelling warm fluid and upwelling cool fluid. The smaller features in the flow within the convective plumes are complex but also well connected in the sense that one can imagine tracing a line along features inside the warm convective plumes.

This is contrasted by the temperature field in a vertical slice (xz-plane) of the 3D simulation in Figure 3.3(b). This slice was chosen at the centre of y-dimension at $y = 2.56$ m. While there are variations between vertical slices, the one chosen here is on the whole representative of the entire domain. Features in the 3D temperature field are smaller scale and appear visually washed out, suggesting a higher rate of mixing compared with the 2D case. This is consistent with studies of the classical Rayleigh-Taylor instabilities (Young et al., 2001; Cabot, 2006), discussed further in 3.1. In addition, convective plumes at or near T_0 penetrate up into the CL in 2D but less than 1 m in 3D. The temperature field shown in Figure 3.3(b) can be divided into three horizontal layers. First, a warm, well-mixed layer confined to the top ≈ 0.5 m of the domain, essentially bounded by the

[2]The phases of convection are discussed in more detail in Chapter 4 in Section 4.4 and briefly further in this chapter.

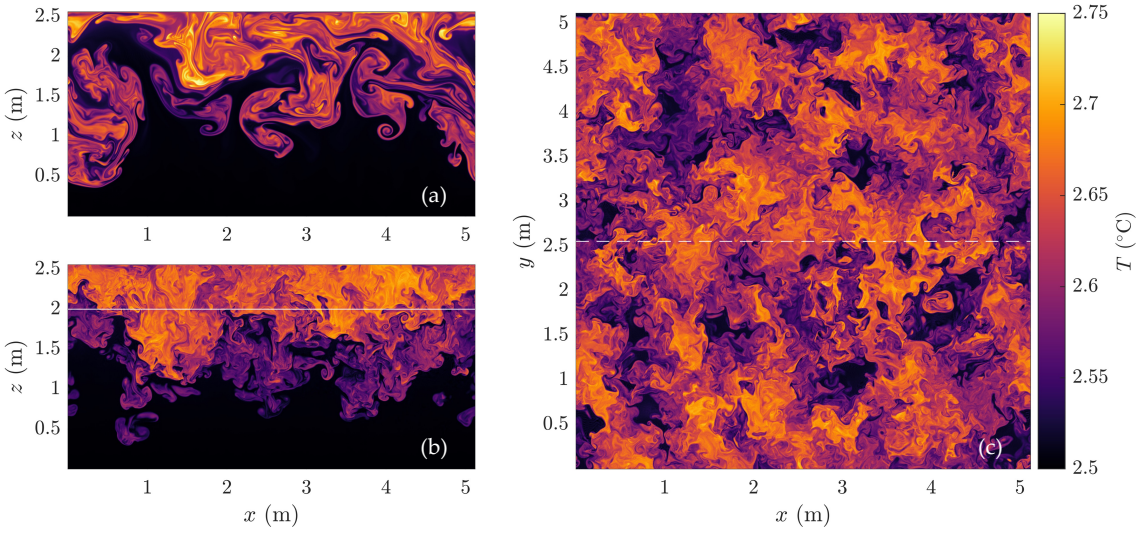

Figure 3.3: Temperature field slices at $t = 2100$ s for (a) 2D, where this slice is the entire domain, (b) 3D slice in the xz plane, and (c) 3D slice in the xy plane. The horizontal white line in panel (b) refers to the depth of the xy slice in panel (c) at $z = 2$ m. Similarly, the horizontal dashed line in panel (c) refers to the position of the vertical slice in panel (b) at $y = 2.56$ m.

horizontal white line. Second, a cool, ambient layer confined to the bottom ≈ 1 m of the domain - relatively unaffected by the temperature forcing - and, lastly, a narrow layer between them at an intermediate temperature and depth.

These three layers are relatively consistent at all times where significant convection is present. In 3D, temperature is nearly monotonically decreasing in the vertical with some small variations in each layer. There is no clear layering in the 2D temperature field, as shown in Figure 3.3(a). Temperatures are slightly warmer in a small region close to the surface, but temperatures in the interior of deep penetrating convective plumes are significantly warmer than the deepest penetrating convective plumes in 3D. If one selects a single profile at a random x position in 2D, the temperature is non-monotonic.

A horizontal slice at $z = 2$ m is given in Figure 3.3(c) that shows how the temperature field varies in the third dimension. This horizontal slice is on the whole representative of the variations in the temperature field within the active regions of the domain. In the vertical slice (Figure 3.3(b)) near the horizontal line (at the same depth as the horizontal slice), length scales of important features are small, especially above the line. Looking at the horizontal slice (Figure 3.3(c)), the same small length scales are observed in the warmer

regions. However, there is also a larger length scale associated with the patches between warm and cool regions. This shows two important things: (1) there is some variety in the penetration depth of upwelling cool plumes, and (2) the length scale of convective plumes - up and down, separately - is relatively consistent. Note that the temperatures at this depth are all at least 0.05 °C warmer than T_0, suggesting that some degree of mixing has taken place at this height. Contrast this to 2D (Figure 3.3(a)), where there are clear points at the same depth with temperatures at or very near to T_0 suggesting that the upwelling plumes in 2D are able to penetrate further towards the surface with less mixing.

3.4.2 Vorticity generation

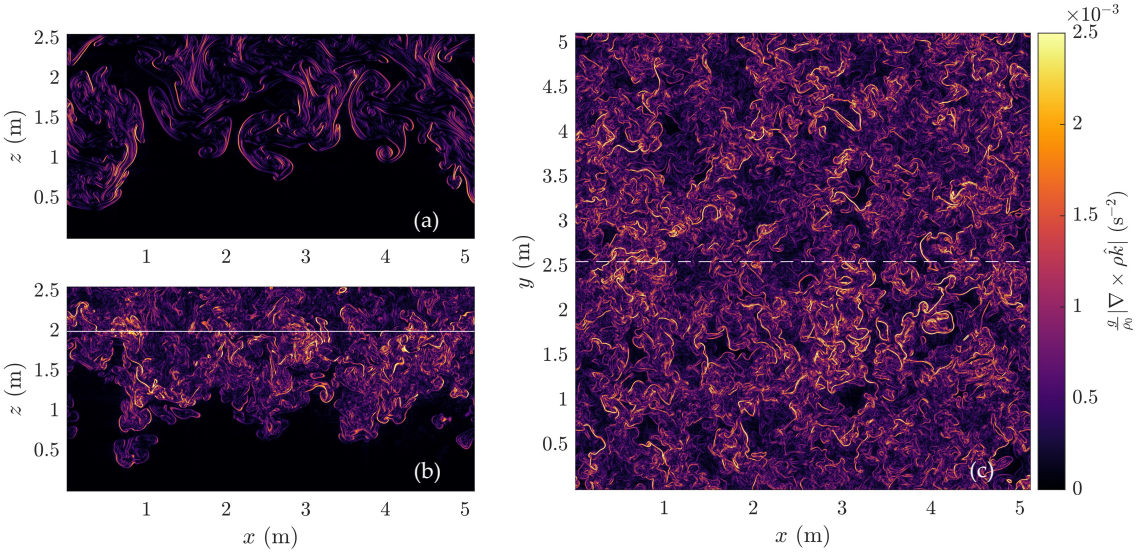

Figure 3.4: Baroclinic vorticity generation (See: Eq. 2.21) at $t = 2100$ s for (a) 2D, where a slice is the entire domain, (b) 3D slice in the xz plane, and (c) 3D slice in the xy plane. The horizontal white line in panel (b) refers to the depth of the xy slice in panel (c) at $z = 2$ m. Similarly, the horizontal dashed line in panel (c) refers to the position of the vertical slice in panel (b) at $y = 2.56$ m.

In Section 2.2.2, it was shown that differences between two and three dimensions - generally speaking - manifests clearly in the vorticity equation. In two dimensions, vorticity is only generated in the y-direction and the only mechanism to generate vorticity is through lateral differences in density via the baroclinic term in Eq. 2.21. In three dimensions, vorticity can be generated in the x and y direction by the baroclinic term, and in all

dimensions by the stretching and tilting term, to be discussed further below. The baroclinic vorticity generation field is compared between 2D and 3D in Figure 3.4.

In 2D, in Figure 3.4(a), the vorticity generation is maximized at the lateral boundaries of the convective plumes, which is where $\frac{\partial T}{\partial x}$ is maximized. There is non-negligible vorticity generation in the interior of the downwelling warm plumes. The upwelling, cool plumes are entirely irrotational in their interior. This is a consequence of these plumes advecting unheated fluid upwards, which as a result has no temperature differences to generate vorticity.

As discussed above about the 3D temperature field (Figure 3.3(b,c)), there are no up or downwelling plumes that span the entire depth of the CL in the temperature field as in the 2D case. This is reflected in the baroclinic vorticity generation field in Figure 3.4(b) and as a result, baroclinic vorticity is maximized in the interior of the CL and is not maximized at the boundary convective plumes (Figure 3.3(b)) because these boundaries are primarily horizontal. Further, the entire CL has some degree of baroclinic vorticity generation. This is in contrast to the 2D case (Figure 3.4(a)) where the cool plumes are irrotational and hence there is no possibility of dissipation, to be discussed further below. As with Figure 3.3(c), the baroclinic vorticity generation is also presented in a horizontal slice for the 3D case in Figure 3.4(c). From this perspective, it can be seen that the baroclinic vorticity generation is maximized at the boundary of the patchy features in the temperature field (Figure 3.3(c)). The patches of low, negligible or zero vorticity generation in the horizontal slice are consistent with the patches of cool fluid in the horizontal slice shown in the temperature field (Figure 3.3(c)). These patches do not generate significant vorticity compared to the rest of the domain but are comparatively small compared to the large regions in 2D (Figure 3.4(a)), which are irrotational.

For 3D systems, in addition to the baroclinic generation discussed above, there is the vortex stretching and tilting term in Eq. 2.21. Physically, this term says that vorticity changes due to gradients in the velocity along vortex lines. See Section 2.2.2 for more details. In 2D, the vortex lines are in and out of the page and, hence, no stretching and tilting is possible. This is vital to the differences between 2D and 3D, because vortex stretching and tilting is an essential process for breaking down vortices into smaller and smaller scales (as one would expect in classical turbulence). Figure 3.5 shows that not only is the stretching and tilting term non-negligible in 3D, it is inevitably several times larger in magnitude than the baroclinic term as shown by the inset of Figure 3.5. However, it should be noted that both are still comparable at all times considered here.

Also given in Figure 3.5 is the 2D mean baroclinic vorticity generation. At early times, when the baroclinic term dominates in 2D and 3D, there is more average baroclinic vorticity

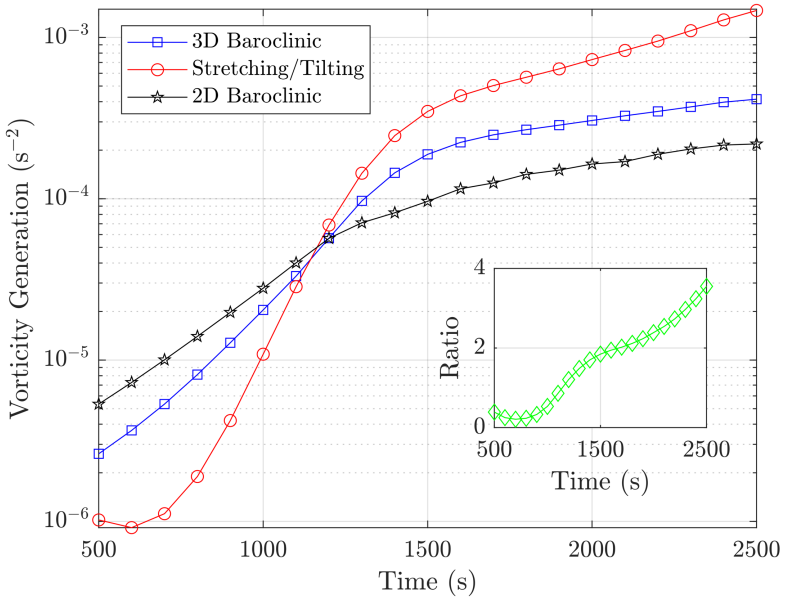

Figure 3.5: Mean vorticity generation on a base-10 log scale on the vertical axis and a linear scale on the horizontal axis. 3D baroclinic vorticity generation (blue squares), stretching and tilting (red circles) and 2D baroclinic vorticity generation (black stars). The inset shows the ratio of the mean stretching and tilting term to the 3D baroclinic vorticity term. Symbols represent the actual data points, while lines are guides to the eye.

generation in 2D than in 3D. One possible explanation for this is the dynamical differences between 2D and 3D and the slower rates of mixing. Another possible explanation is the fact that the filter is stronger in 3D compared to 2D (Section 2.4) and as a result, small scale velocity gradients are removed more effectively in 3D leading to smaller vortex generation rates. Whatever the cause, 3D is slightly delayed in its initial evolution compared to 2D as shown by Figure 3.9(a) (and again in the stratified case in Figure 3.21(a)). This initial phase prior to any significant vertical convection is dubbed the solar radiation dominated phase. At the end of the solar radiation dominated phase, the flow transitions into the convection dominated phase, and the baroclinic term is larger in 3D. The baroclinic term in both 2D and 3D are significantly smaller than the stretching and tilting vorticity generation after the transition to the convection dominated phase. Phase name convention is consistent with Chapter 3 and the associated paper (Allum et al., 2022). The phases are described and showcased in more detail in Section 4.4.

Figure 3.6 compares the baroclinic vorticity field to the stretching and tilting field in the same vertical slice as Figure 3.4(b). The magnitude of the stretching and tilting term (Figure 3.6(b)) is clearly larger than the baroclinic term (Figure 3.6(b) and 3.4(b)), consistent with Figure 3.5. The full field shows that at this mature stage, the largest values of the stretching and tilting term are concentrated on the interior of convective plumes instead of the boundary, as is the case for the baroclinic term in convective plumes in 2D (Figure 3.4(a)). The further break down of features in the flow to smaller scales is enabled by both the baroclinic and stretching and tilting term in 3D, but the largest effects are due to the stretching and tilting term.

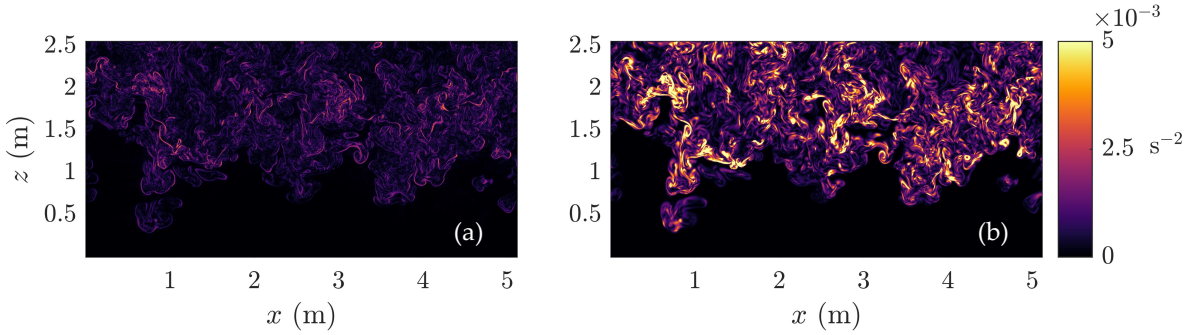

Figure 3.6: 3D slices in the xz plane at $t = 2100$ s. (a) Baroclinic vorticity generation, and (b) vortex stretching and tilting.

In both 2D and 3D, upwelling convective plumes of irrotational fluid exist. Both result in baroclinic vorticity generation on the boundary between the up and downwelling plumes. However, in 3D vorticity generation is comparable to that in the interior of the CL. In 2D, the vorticity generated in this way remains on the boundary and in the interior of the warm plumes. However, in 3D, vortex stretching and tilting, driven by variations in vorticity in the x and y direction, allows the upwelling plumes to breakdown.

3.4.3 Horizontally averaged vertical temperature flux

In the previous section it was established that in 2D, heat is transported by large, distinct convective plumes that are balanced by upwelling of large, cool, irrotational plumes. In 3D, there is a similar exchange between upwelling and downwelling plumes, but these plumes break down prior to penetrating deep into the CL. In this section, the average vertical temperature flux, $\langle wT \rangle$, is analyzed. The derivative of this quantity with respect to z is

found in the horizontally averaged temperature equation, 2.27, and represents the changes in average temperature due to fluid motion. Figure 3.7 compares $\langle wT \rangle$ between 2D (panel a) and 3D (panel b). Recall that angled brackets define a horizontal average, whether there are one or two horizontal dimensions Eq. 2.23. Each curve in either panel represents $\langle wT \rangle$ at 200 s time intervals starting at 800 s and ending at 2200 s, just prior to the CL reaching the bottom of the domain. The time of each curve is labeled in Figure 3.7. As time is increasing, the vertical extent of non-negligible $\langle wT \rangle$ increases, which corresponds to a deepening of the CL.

Figure 3.8 gives a typical shape of the $\langle wT \rangle$, as in Figure 3.7, but is not perfectly to scale. The purpose of this schematic is to give the reader physical intuition about the meaning of the sign of $\langle wT \rangle$ - and it's derivative with respect to z - has on the mean temperature change and temperature flux at each depth. Figure 3.8 shows three regions, each is assigned an arrow with a colour. The direction of the arrow indicates the direction of the mean flux and is inferred from the sign of $\langle wT \rangle$. For constant temperature initial conditions in both 2D and 3D, the mean flux is always towards the bottom because temperatures in the ambient are always smaller than in the CL. The colour of the arrow indicates whether the region is cooling (blue) or warming (red). Note that a negative $\langle wT \rangle_z$ corresponds to an increase in temperature because $\langle wT \rangle_z$ is negative in the mean temperature equation (Eq. 2.27).

The boundary between regions (a) and (b) in Figure 3.8 is where $\langle wT \rangle_z = 0$ and corresponds to the depth where the mean temperature changes are balanced but still net flux towards the bottom. Region (c) is not significantly distinct from region (b) since the mean temperature change and net flux is towards the bottom. However, the slope in region (b) is nearly constant - suggesting a nearly constant temperature change in this region - except near the boundary to region (a), with a rapid decline in slope to zero in region (c) at the boundary between the CL and the ambient.

At early times, $\langle wT \rangle$ develops similarly in 2D and 3D. The first three times shown in both panels (800 s - 1200 s) correspond to the solar radiation dominated phase that is characterized by a growth in the magnitude of the peak (measured left-to-right on the horizontal axis) and an increase in the magnitude of the slope, which remains negative. A larger, negative slope below the peak, implies an increase in the rate at which the CL descends into the water column. This phase is denoted by the blue arrow in Figure 3.7(a) and (b) pointing in the direction of increase of the slope of $\langle wT \rangle$ below the peak. In the solar radiation dominated phase, there is no clear CL and most of the increase in $\langle wT \rangle$ is due to changes in temperature.

The next phase is the convection dominated phase that is characterized by the descent

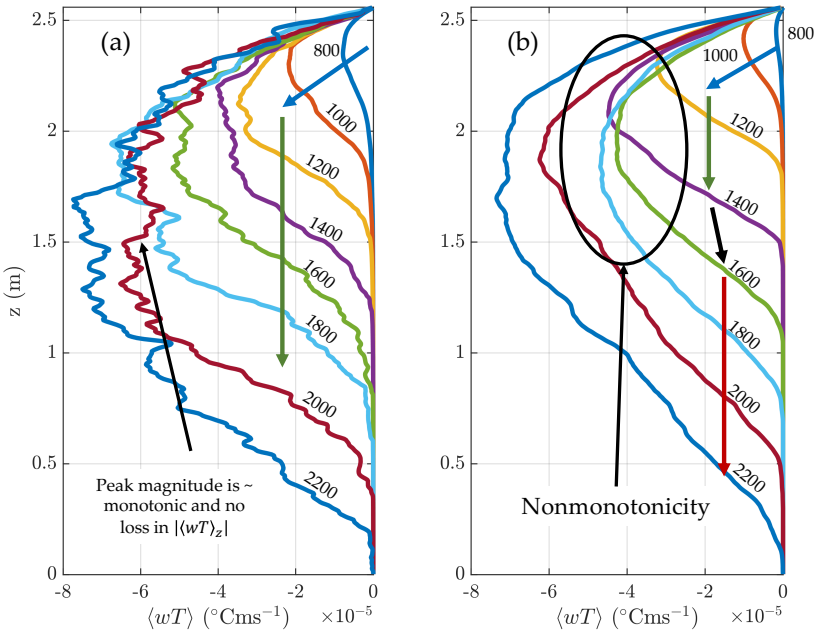

Figure 3.7: Horizontally averaged, vertical temperature flux - $\langle wT\rangle$ - in (a) 2D and (b) 3D prior to the CL hitting the bottom of the domain. Each curve is labeled by the simulation time in seconds. Arrows indicate the rate of change of $\langle wT\rangle$ below the peak in time. Towards the left indicates increasing magnitude, straight down is constant magnitude, towards the right indicates decreasing magnitude. The nonmonotonicity highlighted in panel (b) refers to the growth of the peak height.

of the CL. In 2D, this occurs near $t = 1000$ s. The solar radiation phase ends when the slope of $\langle wT\rangle$ below the peak stops growing (denoted by the arrows on Figure 3.7(a)). The transition is delayed in 3D to $t \approx 1300$ s At prior times, the region with $\langle wT\rangle < 0$ did not change in height. In 2D, there is no change in slope below the peak after this time. Recalling that $\langle wT\rangle_z$ is what changes temperature, a consistent slope of $\langle wT\rangle_z$ implies consistent convection and a consistent increase in temperature as the CL descends in the water column, neglecting diffusive effects. This consistent shape is denoted by the downwards pointing green arrow representing the constant $\langle wT\rangle_z$ below the peak. As the CL descends, the magnitude of the peak increases and its location decreases with height.

In 3D, however, the magnitude of the peak of $\langle wT\rangle$ in Figure 3.7(b) is non-monotonic with time and briefly decreases before increasing again in the range $t = 1400$ to 1800 s.

Further, the peak location remains close to a height of 2 m in 3D, compared to 2D where the height of the peak continues to descend with time. This corresponds to the boundary between regions (a) and (b) in Figure 3.8, which corresponds to the height where the change in temperature due to motion is balanced. This height descends more rapidly in 2D compared to 3D.

The non-monotonicity in the peak magnitude coincides with a decrease in slope of $\langle wT \rangle$ below the peak, suggesting a loss in the rate of increae of temperature at these depths, corresponding to region (b) in Figure 3.8. After this brief decrease, the slope below the peak remains constant as the CL approaches the bottom. This decrease in slope, despite an increasing magnitude of the peak, corresponds with a slight decrease in the rate of descent of the CL in 3D. This can be seen by comparing the rate of change of the minimum height of $\langle wT \rangle < 0$ between 1200-1400 s and 1600-1800 s. This change in slope during the convection phase does not happen in 2D. In this chapter, effects correlated to the non-monotonicity in the peak height of $\langle wT \rangle$ in 3D will be discussed. These effects are typically monotonic in time (but not the second derivative), however, the discussion of these related phenomenon will continue using the phrase "non-monotonic" for consistency.

Using $\langle wT \rangle$, the depth of the CL, h_{CL}, can be estimated. It is measured as a depth from the top of the domain, and is given in Figure 3.9 in 2D and 3D. h_{CL} approximately corresponds to the depth of the boundary between regions (b) and (c) in Figure 3.8. The method for obtaining the front position from $\langle wT \rangle$ is discussed in Section 3.2.2. As shown in Figure 3.9(a), $h_{CL} \propto t^{7/4}$ for $t = 1500$ to 2300 s in the 3D case. The time $t = 1500$ s is chosen because it is consistent with the timing of the non-monotonicity of $\langle wT \rangle$ - highlighted by the arrow - and including points further back in time reduce the quality of the fit. No fit is provided for the 2D case as the CL front position is less consistent with time and, as it is shown later in 3.2.3, 2D front position is much harder to identify due to the increased variation in $\langle wT \rangle$ values. Consistent with Figure 3.7, the 2D case is faster initially and at some intermediate time, h_{CL} is quite similar between 2D and 3D. At the front approaches the bottom, the rate of change of h_{CL} slows as the free slip boundary conditions and the incompressibility condition convert the downward momentum into horizontal momentum along the boundary.

The effect of the non-monotonicity is clearer in u_{rms} in the interior of the convective layer, and is plotted as a function of time in Figure 3.9(b). u_{rms} is defined in Section 3.2.2. At all times, u_{rms} is larger in 2D than in 3D further showcasing the effect of reduced dissipation in 2D. After the period of non-monotonicity observed in $\langle wT \rangle$ (Figure 3.7(b)) in 3D, the rate of change of u_{rms} gradually increases again before the CL reaches the bottom of the domain. In 2D, the rate of change of u_{rms} is also not constant with time or one consistent shape, however, these changes were not linked to any specific behaviour of $\langle wT \rangle$

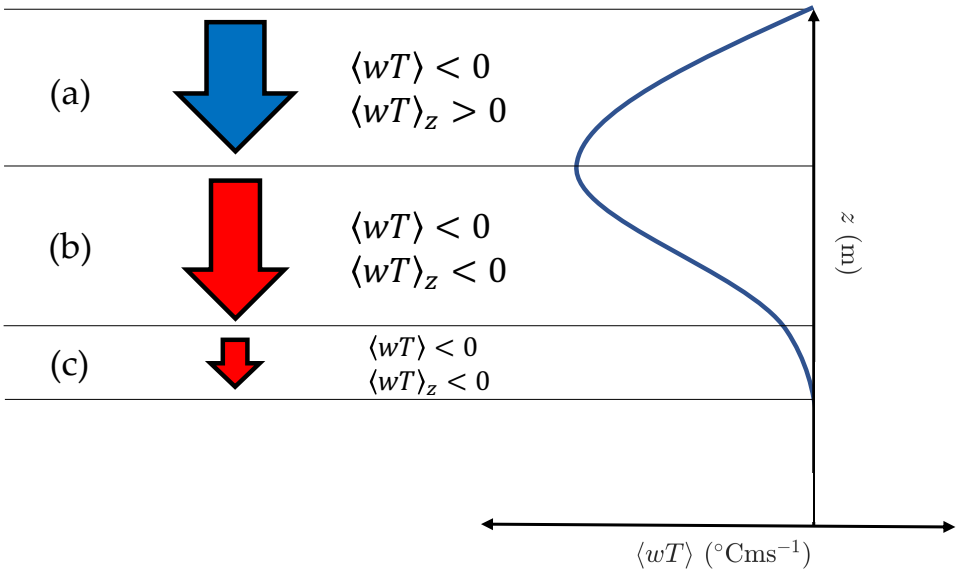

Figure 3.8: Schematic of the horizontally averaged vertical temperature flux. The shape of $\langle wT \rangle$ is consistent with late time behaviour in 3D as in 3.7(b). The vertical is divided into three regions and assigned an arrow denoting whether the region is cooling (blue) or warming (red), as well as the direction of the net flux, denoted by the direction of the arrow. This schematic only describes effects to temperature and flow due to convection. For example, (a) has a blue arrow pointing downwards indicating that this region is cooling with a net downwards flux.

and are potentially a result of the unreliability of averages using 2D data compared to 3D.

Up until now, we have not considered dynamics after the CL reaches the bottom of the domain. In Figure 3.10, we look at $\langle wT \rangle$ for 4 times in intervals of 400 s after the CL reaches the bottom. A more realistic bottom might have no slip boundary conditions but we are not concerned with the dynamics in the boundary layer, which is likely $\mathcal{O}(1$ cm). The dynamics after reaching the bottom are important because there are simulations in the literature carried out in 2D and include the bottom boundary, namely Ref. Ulloa et al. (2022) and (Ulloa et al., 2019). It is important to note that these simulations use embedded boundary conditions, where the fluid velocity is effectively set to zero along the boundary and as a result, less vertical momentum is transferred to horizontal momentum upon the CL reaching the bottom of the domain.

Ref. Ulloa et al. (2022) considers a 2D lake subjected to surface cooling at temperatures

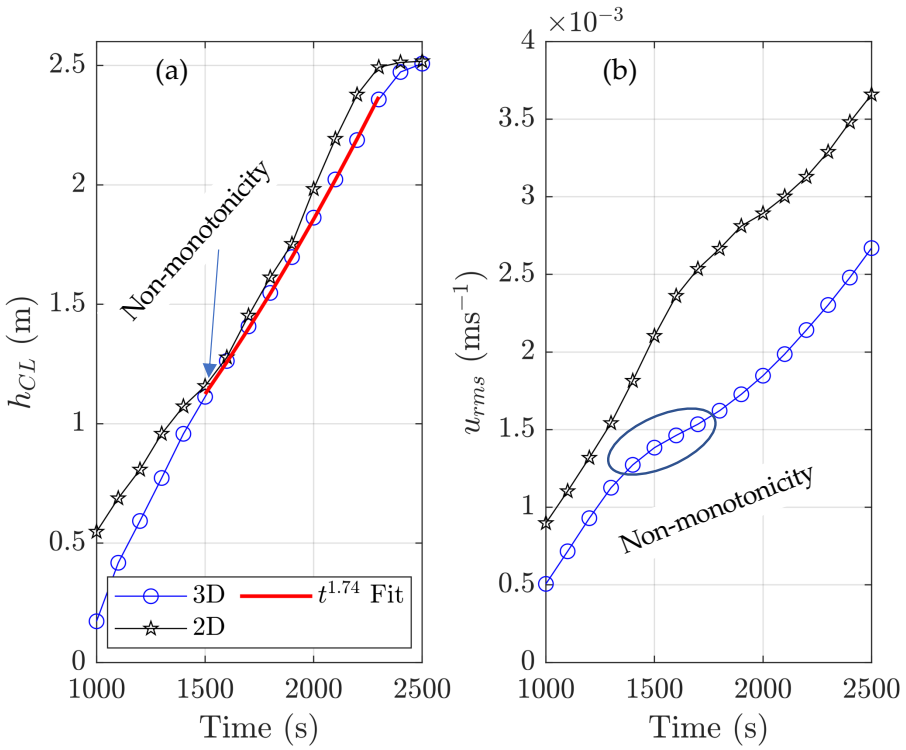

Figure 3.9: h_{CL} in 2D and 3D for the stratified initial condition. (a) h_{CL} versus time with a power law fitted to the 3D data. This fit is obtained after an initial growth phase from $t = 1000$ to 1500 s that appears visually similar but is not consistent with later times. The exponent of the power-law is approximately 7/4 (1.74). (b) h_{CL} versus u_{rms} within the convective layer. The label of 'non-monotonicity' refers to the discussion of Figure 3.7(b), where peak height is non-monotonic with time.

above the temperature of maximum density with non-uniform bathymetry. The differences in depth generate circulation near the shallow regions as shown in Fig. 2 in Ref. Ulloa et al. (2022). Prior to the onset of significant lateral circulation, convection is characterized by large convective cells that extend from the top to the bottom of the domain in the shallow regions, and from the top to a stratified layer at the bottom in the deeper regions. These convective cells are also typical at later times, in the simulations presented here, with horizontal length scales that increase gradually with time due to the constant heating rate. This circulation pattern appears despite the use of free slip boundary conditions in the simulations presented in this thesis, as a result we do not think the boundary layer effects have a significant impact on the dynamics we observe at late times.

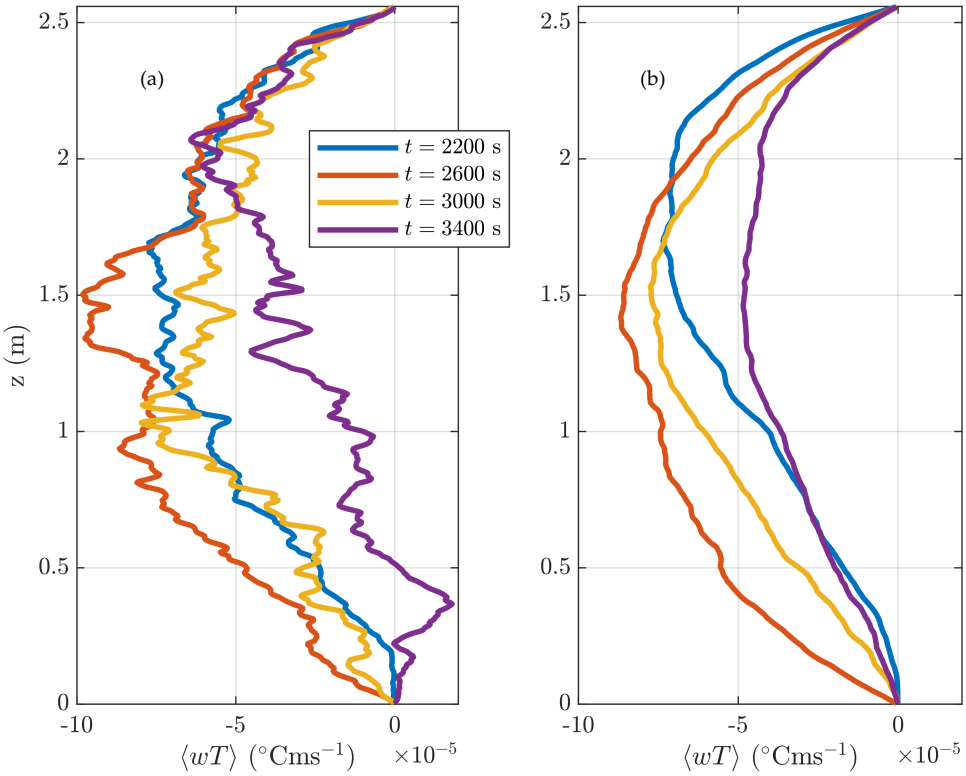

Figure 3.10: Horizontally averaged, vertical temperature flux - $\langle wT \rangle$ - in (a) 2D and (b) 3D after the CL hits the bottom of the domain.

The schematic in Figure 3.8 still applies at late time, however, region (c) is gone because

the CL now extends the entire domain. In 2D, Figure 3.10(a), after reaching the bottom there isn't a significant change in $\langle wT \rangle$. The peak in $\langle wT \rangle$ is already near the midpoint of the water column. $\langle wT \rangle$ above $z = 2$ m is consistent in the times shown, with significant variation in $\langle wT \rangle$ below $z = 2$ m. This is contrasted by the 3D case, Figure 3.10(b), where the peak is close to a height of $z = 2$ m when the CL reaches the bottom ($t = 2200$ s) and descends to below the midpoint shortly after at $t = 2600$ s before settling closer to the mid point. At the final time shown, $t = 3400$ s, $\langle wT \rangle$ is smaller at effectively all depths than the other times shown here. There is some similarity to the 2D case at the same time where the curve is smallest below $z = 2$ m in Figure 3.10(a). The decrease in $\langle wT \rangle$ after the CL reaches the bottom is most likely the result of convective cells circulating and transfering warm fluid upwards. Previously, prior to the CL reaching the bottom, most of the fluid advected upwards was near $T = T_0$.

Figure 3.7 and Figure 3.10 show that at a glance $\langle wT \rangle$ is quite similar in 2D and 3D, suggesting that on average in 2D the CL increases in depth in a similar manner to 3D. The solar radiation dominated phase is quite similar. There are, however, some minor differences that should be considered when researchers decide between using a 2D or a 3D simulation in the study of convection in the cold water regime. Further, 2D generally provides less precise information in the form of horizontal averaging due to noise. One could extend the horizontal domain significantly, which does reduce the noise observed in $\langle wT \rangle$, at which point it would be better to simply run a simulation in 3D.

3.4.4 Histograms of 3D data

For both Figure 3.11 and Figure 3.13, there are four panels for the following times: (a) $t =$ 1500, (b) 2100, (c) 2700 and (d) 3300 s. Each of these times correspond to different parts of the convection dominated phase, panel (a) and (b) of both figures show the histograms before the CL reaches the bottom. Panel (c) shows the CL in progress of crashing into the bottom boundary and panel (d) well after the CL has reached the bottom of the domain.

The wT histograms (Figure 3.11) have a bin width of 5×10^{-5} °Cms^{-1}, covering a range of -1.4×10^{-2} °Cms^{-1} to 1.4×10^{-2} °Cms^{-1}. Notice that the mean value is an order of magnitude smaller, shading the wide range of motion, hidden by the mean. The curves in Figure 3.7 and 3.10 correspond to the average value of these distributions, which are $\mathcal{O}(10^{-5} - 10^{-4})$ °Cms^{-1}. The range of Figure 3.11 compared to Figure 3.7 and 3.10 shows that these distributions are nearly symmetric about zero, with a slight positive skew. Figure 3.11(b) and (d) both have horizontal lines that correspond to the depth of slices in the wT field given in Figure 3.12. Figure 3.12(a) and (b) gives wT at $z = 2$ m and $z = 1$ m

in Figure 3.11(b), prior to the CL reaching the bottom boundary. Figure 3.12(c) and (d) gives wT at $z = 2$ m and $z = 1$ m in Figure 3.11(d), after the CL has reached the bottom boundary.

The equivalent 2D wT histograms are too difficult to interpret on account of having 3 orders of magnitude fewer data points compared to the 3D data. They do communicate some similar information but are not worth including here. When we increased the width of the 2D simulation it did have the effect of decreasing the noise in $\langle wT \rangle$ and in histograms of wT. However, there still was significant noise and any further increases to L_x would render any remaining advantages of 2D - namely, faster compute times - moot.

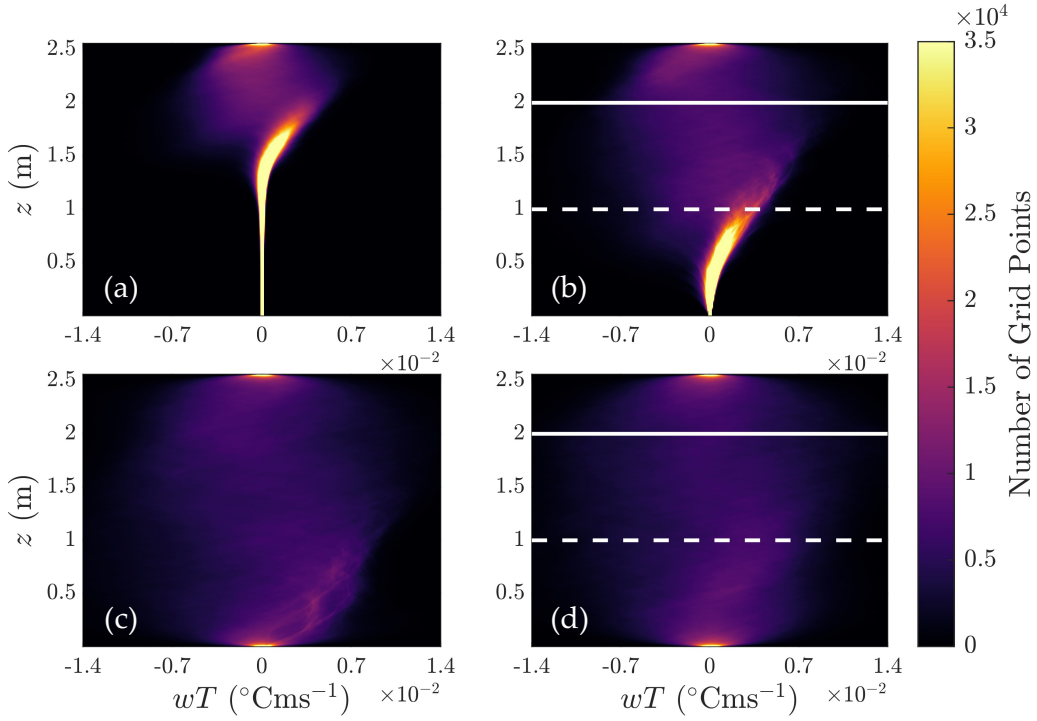

Figure 3.11: Histograms of the vertical temperature flux in 3D at four different times at each depth. (a) $t = 1500$ s, (b) 2100 s, (c) 2700 s and (d) 3300 s. Colour bar and colour in each panel indicates the number of grid points with the value on the horizontal axis. The bin width is 5×10^{-5} °Cms^{-1}.

The form of these distributions have some consistent features prior to the CL reaching the bottom of the domain (Figure 3.11(a,b)). Near the surface - excluding the portion in the top 5 cm of the domain - the distribution is positively skewed. On the negative side of

the distribution, the wT values are clustered closer to zero and on the positive side there are many comparatively large values of wT. Near the surface, upwelling fluxes have more space to move upwards and as a result build up speed producing some larger wT values. In Figure 3.12(a), we can see some evidence of the upwelling plumes with larger wT (slightly damped by the cooler temperatures) and by comparing with the temperature field at the same depth (Figure 3.3(c)) we can connect the patches of large positive wT to patches of temperatures closer to T_0, such as at $(x, y) = (3.5, 3.25)$. This shows that the regions of cool and warm temperatures further up or down in the vertical in Figure 3.3(b,c) are indeed upwelling and downwelling plumes.

Slightly below the CL, $z \approx 1.25$ to 2 m in Figure 3.11(a) and $z \approx 0$ to 1.5 m in Figure 3.11(b), the histograms are negatively skewed with much more intense clustering near zero than in the histograms near the surface and a much longer tail. This is because in this region convective plumes are penetrating into the motionless background so large portions of the area are small in both w and T. Whereas the downwelling plumes, the few that have reached this depth, have comparatively larger w values than the motionless ambient. We can see this in Figure 3.12(b) that shows a large area of small and positive wT values balanced by a small area of larger wT values. In this case, the downwelling plumes are transporting higher temperatures at larger speeds.

In between these two regions - near the surface and below the CL - is a very small region in Figure 3.11(a) and from $z \approx 1.5$ to 2 m in Figure 3.11(b), the histograms are nearly completely symmetric but as shown in Figure 3.7(b) they are not symmetric about zero but a value to the left of zero. In this region, the net temperature flux is towards the bottom but there are both small and large values of wT. If histogram of w values were symmetric, most fluid parcels with $w < 0$ would have a temperature larger than the mean and most fluid parcels with $w > 0$ would have a smaller temperature. This imbalance means that we should expect a distribution that is slightly positively skewed, which is what the curves in Figure 3.7(b) suggest.

At later times, Figure 3.11(c,d), the clustering near zero has mostly disappeared near the surface and, since the CL has reached the bottom, there is no longer an ambient. We can see that both slices in Figure 3.12(c,d) show comparable area and magnitude of down and upwelling fluxes. However it should be noted that the fluxes generally are larger in the slice at $z = 2$ m (Figure 3.12(c)). This is consistent with Figure 3.10(b), that shows that while the peak at $t = 3400$ is near the centre, it is not symmetric about the midpoint and there are clearly larger values on average above the midpoint. This occurs as heat is still continually being pumped into the upper layer of the domain and hence we expect the temperature and the resulting temperature fluxes to be on the whole larger than closer to the bottom.

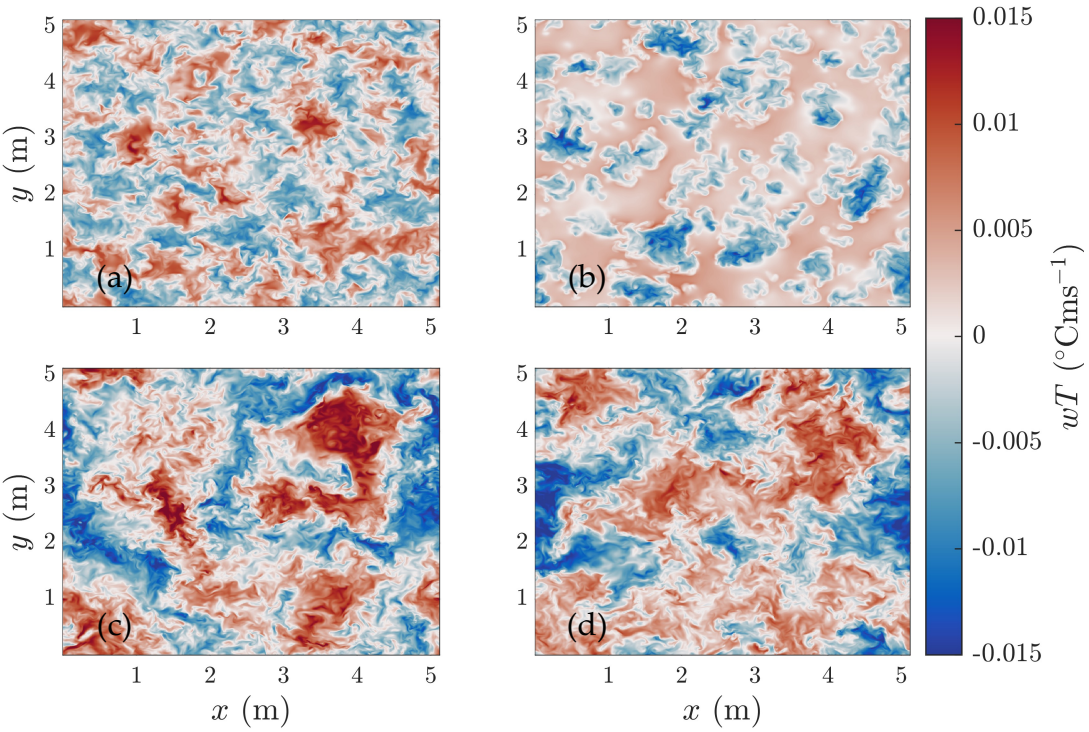

Figure 3.12: Horizontal slices in the vertical temperature flux in 3D at four different times at each depth. (a) $z = 2$ m and $t = 2100$ s, (b) $z = 1$ m and $t = 2100$ s, (c) $z = 2$ m and $t = 3300$ s, and (d) $z = 1$ m and $t = 3300$ s.

Early in this section we discussed briefly the fact that the upwelling plumes in 2D are irrotational while in 3D there are no irrotational plumes, up or downwelling. It was suggested that this implies that there are regions with no dissipation since rotation is essential for viscous effects (Kundu and Cohen, 1990). In the following we consider histograms of the viscous dissipation in 3D in Figure 3.13 and compare to a 2D histogram of the dissipation at a single depth in Figure 3.14.

The same times are chosen for each of the panels in Figure 3.13 as Figure 3.11. Early in the convection dominated phase (Figure 3.13(a)) inside the CL, the histograms have a large peak near 1×10^{-6} m^{2}s^{-3} with a small tail. Suggesting a large number of nonzero - but small - dissipation values. As we decrease z at fixed time, the magnitude of this peak increases, its height decreases, and the tail extends as larger values of ϕ, the viscous dissipation, are possible. Later in the convection dominated phase, before the CL reaches

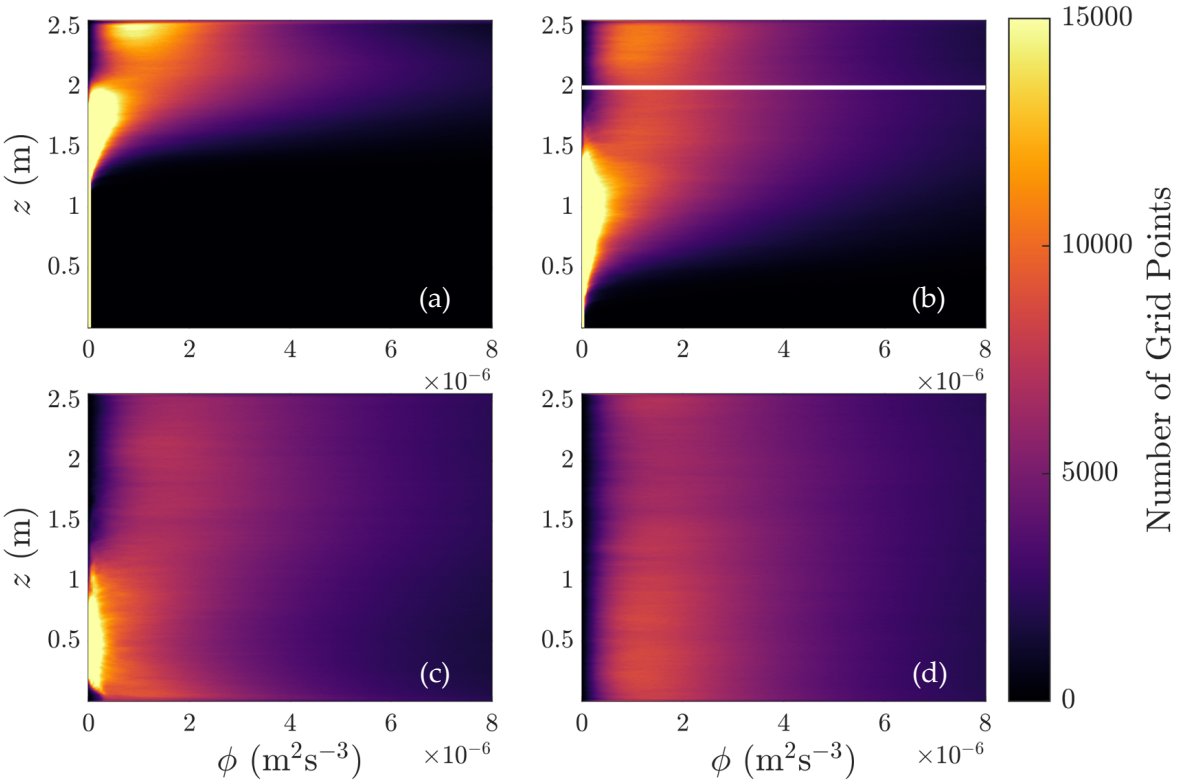

Figure 3.13: Histograms of the viscous dissipation in 3D at four different times. (a) $t = 1500$ s, (b) 2100 s, (c) 2700 s and (d) 3300 s. Colour bar and colour in each panel indicates the number of grid points with the value on the horizontal axis.

the bottom (Figure 3.13(b)), the magnitude of the peak near the surface is much smaller and the width of the histograms in the CL are nearly uniform.

At the bottom of the CL we see a histogram that is peaked at zero, a mix of fluid parcels with $\phi = 0$ and some larger values. This is a result of the features observed in Figure 3.12(b) where downwelling plumes intrude into a nearly motionless and irrotational ambient. In 3D, this only happens below the CL but in 2D as we can see in Figure 3.3(a) and Figure 3.4(a) that there are upwelling plumes in the CL, which are irrotational.

This is confirmed in Figure 3.14 where we compare the histogram at a single depth in 3D (Figure 3.14(a)) to the same depth at $t = 2100$ s in 2D (Figure 3.14(b)). The histogram for the 2D simulation is peaked at zero and falls off rapidly. The equivalent 3D histogram does not peak at zero and has many larger values of dissipation, past the peak. Evidently,

prior to the CL reaching the bottom there is significantly more dissipation occurring within the CL. 2D simulations of convection are thus not properly capturing dissipative effects in the interior (away from the boundaries).

When the CL reaches the bottom, the 3D case begins to lose any fluid parcels with zero dissipation and as we reach the latest time shown, the histograms are nearly uniform with depth, with negligible fluid parcels with zero dissipation.

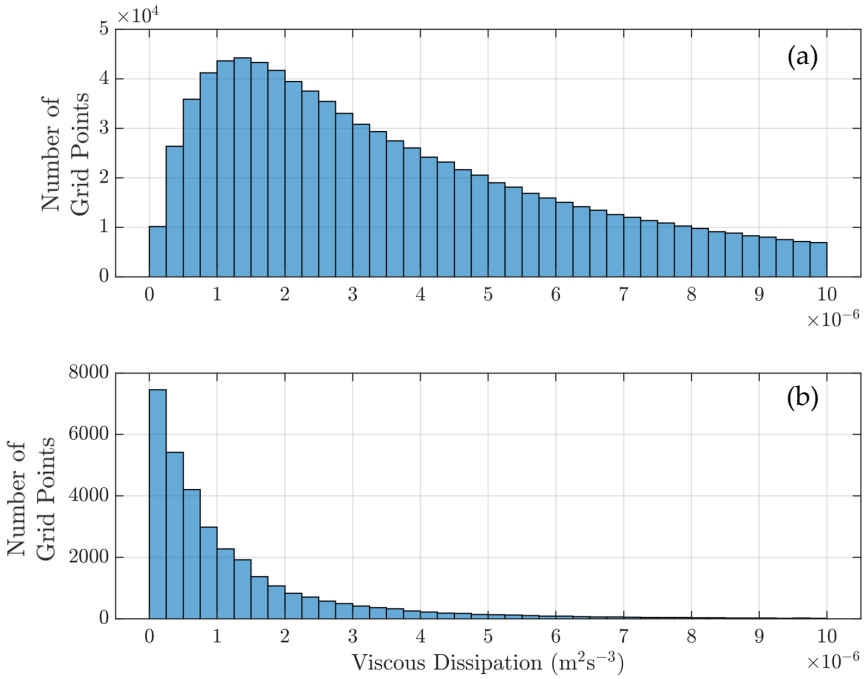

Figure 3.14: Histograms of the viscous dissipation at a height of $z = 2$ m in (a) 3D and (b) 2D at $t = 2100s$. Panel (a) is the histogram in Figure 3.13(b) at the depth of the horizontal white line.

3.4.5 Dissipation

In Figure 3.14, we showed that there are fundamental differences between 2D and 3D in the way that mechanical energy is dissipated into heat (neglected in the temperature equation in the boussinesq approximation (Kundu and Cohen, 1990) and as a result not included in

2.17). The differences manifest in the frequency of the largest dissipation rates (height of the histograms away from zero) and the location of the peak.

This is confirmed by Figure 3.15(a), which gives the full viscous dissipation field in 2D at $t = 2100$ s. As previously mentioned, the upwelling plumes in 2D are irrotational, shown again here due to the lack of dissipation in those regions in Figure 3.15(a). This is supported by Figure 3.4(a), which shows that the cool upwelling plumes do not generate vorticity. This explains why there are significant contributions to the histogram of dissipation near or at zero in 2D (Figure 3.14(b)). What cannot be inferred from the distribution alone is that dissipation inside the warm, rotational plumes does not manifest in the same way that it does in 3D (Figure 3.15(b,c)). In 3D, The dissipation field consists of small filaments whose widths are $\mathcal{O}(1$ cm) with a variety of lengths. At this depth it is quite similar to the structure of dissipation in fully turbulent Rayleigh-Bénard Convection at a Reynolds number greater than 4000 (Schumacher et al., 2014) suggesting that we are at least in a transitional state. Not only is dissipation in 2D significantly smaller in magnitude, it is quite dissimilar to that which is observed in fully turbulent convection.

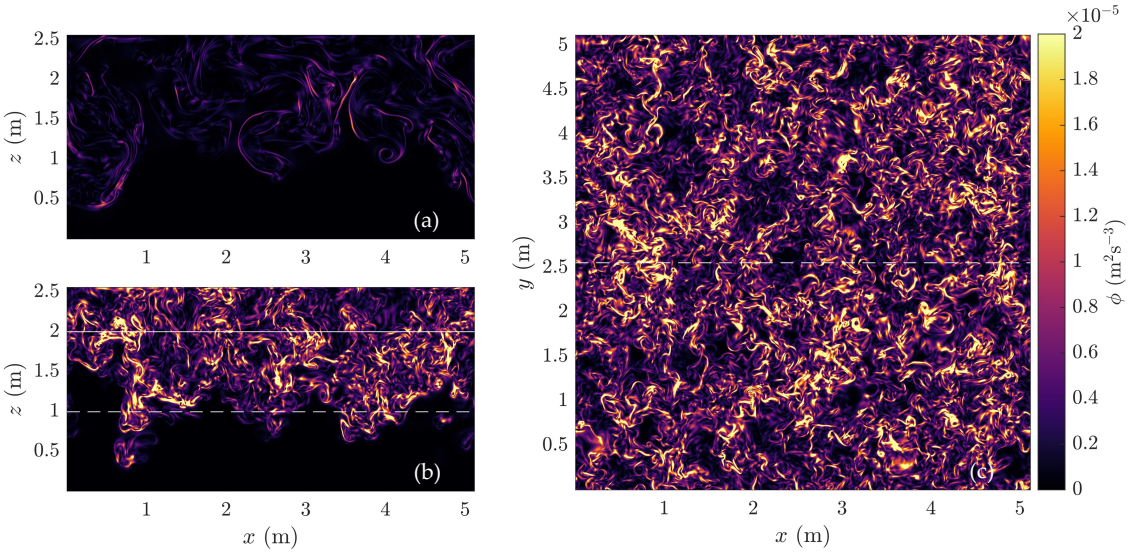

Figure 3.15: Viscous dissipation field (Eq. 2.19) slices at $t = 2100$ s for (a) 2D, where a slice is the entire domain, (b) 3D slice in the xz plane, and (c) 3D slice in the xy plane. The solid white line in panel (b) refers to the depth of the xy slice in panel (c) at $z = 2$ m and Figure 3.16(b). The dashed white line in panel (b) refers to the depth of the xy slice in Figure 3.16(a) at $z = 1$ m. Similarly, the horizontal dashed line in panel (c) refers to the position of the vertical slice in panel (b) at $y = 2.56$ m.

From Figure 3.15(c), $z = 2$ m, it is difficult to distinguish this system from fully turbulent motion in some scenarios (Schumacher et al., 2014). At a lower depth of $z = 1$ m (Figure 3.16(a)), we see a combination of convective plumes (moving into the page) of warm fluid with dissipative filaments as in Figure 3.15(c) and 3.16(b). But we also see large regions of irrotational fluid that are pulled upwards (out of the page) to balance the downward convection. Further, At this depth, the majority of viscous dissipation is in the interior of the warm plumes and not at the boundary. This is the reason for the depth variation of the CL as observed in Figure 3.15(b), 3.3(b), 3.6, and 3.4. However, these upwelling irrotational plumes eventually break down, which does not occur in 2D (Figure 3.15(a)). Evidence of these upwelling plumes after breakdown are visible in Figure 3.16(b) in patches of dissipation that are darker on length scales of $\mathcal{O}(1m)$.

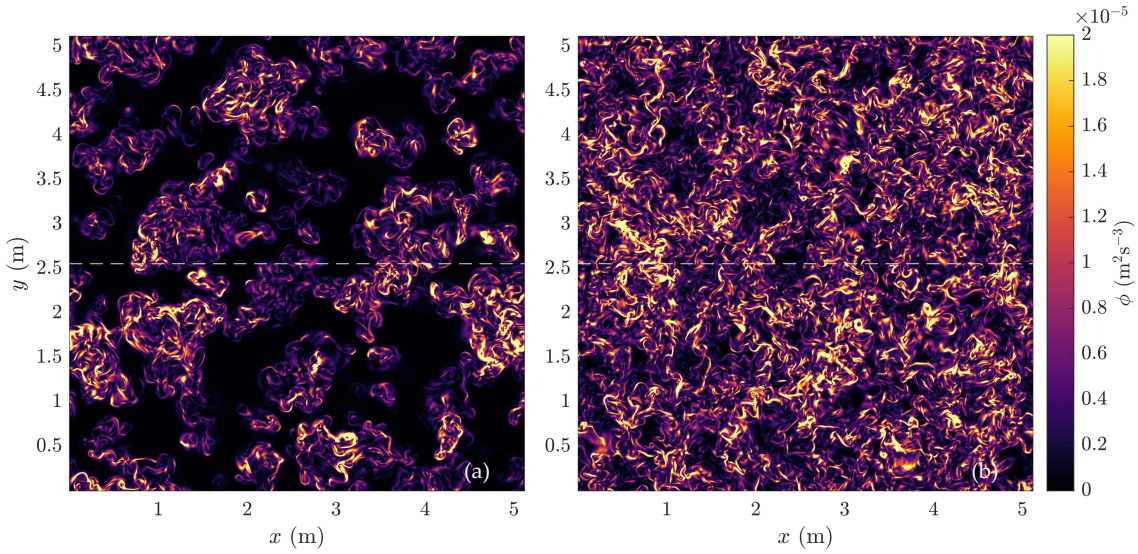

Figure 3.16: Horizontal slices of the viscous dissipation field at $t = 2100$ s for (a) 3D at $z = 1$ m corresponding to the white dashed line in Figure 3.15(b), and (b) 3D at $z = 2$ m, a copy of Figure 3.15(c) for comparison. The dashed white line in both panels refers to the y position of Figure 3.15(b).

3.5 Stratified temperature initial conditions

3.5.1 Systemic changes due to the stratification

Initially, the temperature profile is equal to the background stratification defined in Eq. 3.5, prescribed to the system as part of the initial conditions. The temperature and density stratifications are compared in Figure 3.2. This linear temperature stratification generates a density stratification that is strongest at the surface and weakest at the bottom as temperatures approach the temperature of maximum density. Figure 3.2 shows that - at least qualitatively - that the stratification is nonlinear but the non-linearity is at most a second order effect. Hence, discussing this system in terms of temperature is an adequate proxy as this region of the equation of state is monotonically increasing with increasing temperature.

The background stratification introduces some important systemic changes to the way that convection will develop. First, in the stratified case the temperature profile is stably stratified and remains stable until $t = t_s = \lambda^2 \Delta T / Q_0 L_z$ (derived in 3.2.3). Using the values in Table 3.2 and 3.1, $t_s \approx 440$ s here. This means that Rayleigh-Taylor instabilities will not start to develop until after this time.

Second, even when some part of the water column is unstably stratified, it is not the entire domain as in the unstratified case. After $t = t_s$, a region of depth $L_z - z_s$ (3.8) is unstable. z_s is labeled for $t = 800$ s on $\langle T \rangle$ for the stratified case in 3D (Figure 3.17(b)) and lines up with the actual transition between stable and unstable in $\langle T \rangle$. At later times, a transition point between stable and unstable is identifiable. However, this depth is typically deeper than that predicted by z_s, which is unsurprising because fluid motion, and hence convection, is neglected in the derivation of z_s in 3.8. Substituting in $t = 5600$ s into Eq. 3.8, we find z_s is equal to ≈ 1.5 m, whereas in Figure 3.17 at $t = 5600s$ the transition from unstable to stable in the mean temperature profile is at $z \approx 1$ m. It is clear that z_s is not an accurate proxy because it neglects convective effects but it does capture the initial development of $\langle T \rangle$.

The unstable layer in the stratified case is, by construction, significantly smaller than in the unstratified case. However, the temperature difference across the unstable layer is also smaller. To more accurately compare how unstable $\langle T \rangle$ is between the unstratified and stratified cases is to look at the ratio of the temperature change across the unstable layer to the bottom of this layer.

If we take the depth of the unstable layer in the unstratified case to be half the vertical domain, or ≈ 1 m and noting that the temperature difference is ≈ 0.1 °C. The ratio of

the temperature change to the depth of the unstable layer is approximately 0.1 °Cm^{-1}. If we repeat this for the unstable layer in the stratified case, noting that the change in temperature is of order 0.01 °C and the depth is of order 0.1 m, the ratio is approximately 0.1 °Cm^{-1}. This simple calculation shows that the temperature gradient in the unstable layer in the stratified layer is comparable to the temperature gradient in the unstratified case prior to the transition to the convection dominated phase.

Finally, in the unstratified case, while the entire domain is unstably stratified, most of the change in temperature is in the top half of the domain. In the bottom half, the temperature is nearly constant. This represents the largest difference between the stratified and unstratified cases where just beneath the unstable layer in the stratified case is a stable stratification. So while it is clear the temperature gradient is comparable in the unstratified and stratified cases at the same time, the transition to the convection dominated phase, characterized by the transfer of heat in the vertical, is slowed by the stratification until much larger temperature differences are achieved.

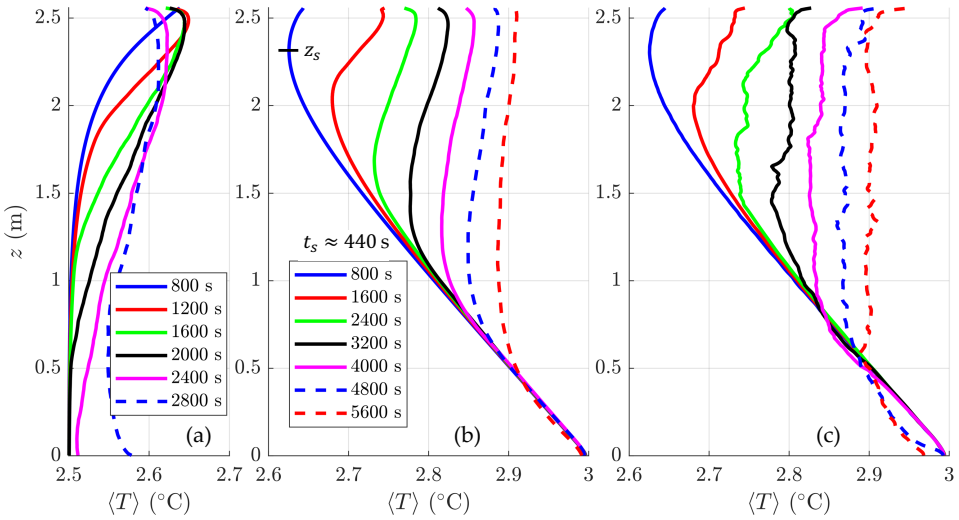

Figure 3.17: $\langle T \rangle$ for (a) 3D with no initial stratification, (b) 3D with an initial stratification, and (c) 2D with stratification. The differences in width between panel (a) and panels (b) and (c) are to emphasize the difference in temperature range between cases with and without an initial stratification. In panel (b), z_s is given for $t = 800$ s and t_s for the set of parameters for these simulations (see Table 3.1 and 3.2).

We transition into the convection dominated phase shortly before $t = 1600$ s. This transition is made clear by the fact that at earlier times, $t = 800$ s, $\langle T \rangle$ is smoothly and

slowly varying. Whereas at later times the transition between unstable and stable is more sharp, at the boundary of convective plumes penetrating into the background stratification. This is emphasized further in 2D where the region with significant convection is more noisy in $\langle T \rangle$. In this phase, temperatures grow more rapidly at the surface unlike in the unstratified case (Figure 3.17(a)) where temperatures are relatively constant before CL reaches the bottom of the domain. This implies that in the unstratified case, downward heat flux is nearly exactly balanced by incoming solar radiation. With the addition of a stratification the downward heat flux is slowed and hence temperature builds at the surface. The same effect is observed in 2D where the temperatures near the surface continually increases with time.

One small difference between 2D and 3D occurs in a small region near the surface. In 3D, in the convection dominated phase (with or without an initial stratification) $\langle T \rangle$ decreases at the surface and peaks just below. This magnitude of this decreases softens with time and is least pronounced at $t = 5600$ s. However, in 2D there is a slight increase in temperature at the surface and its magnitude exceeds the magnitude of the decrease observed in 3D. It is difficult to prescribe exactly the cause of this but it represents another way in which 2D departs from 3D. Due to the free slip boundary conditions and the lack of a thermal boundary layer, which complete simulations of ice-covered lakes would require, dynamics this close to the surface may not be relevant.

At later times, temperatures at the bottom of the CL in the stratified case (Figure 3.17(b)) - characterized as the depth where $\langle T \rangle$ converges to the background stratification - begin to heat more rapidly. Meanwhile, temperature continues to increase near the surface but this increase gradually slows with time. $\langle T \rangle$ approaches the uniformity one would expect in the interior of a CML (Farmer, 1975; Mironov et al., 2002; Bouffard and Wüest, 2019). This general behaviour of less heating near the surface and advanced heating near the bottom of the CL is similar to what we observe in the unstratified case after the CL reaches the bottom (Figure 3.17(a) for $t = 2400$ and 2800 s). This suggests that the bottom of the domain is having a similar effect on the mean temperature profile as the stratification in the stratified case. The difference being is that in the stratified case, convection penetrates into the stratification and increases the depth of the CL. In both cases, reaching a barrier (physical wall in the unstratified case and a pseudo barrier in the stratified case) has the effect of enhancing heat transport towards the bottom from the surface.

$\langle T \rangle$ given in Figure 3.17(b) for the 3D stratified case might suggest that at $t = 4800$ s convective plumes have not penetrated past a height of 0.5 m. This is supported by the fact that the temperatures below this height appear to match the background stratification that was present at early times. It turns out that this is only a deception of the mean.

Convective plumes indeed penetrate past the point where $\langle T \rangle$ matches the background stratification but is removed by taking the average. We will revisit this in more detail later in section Section 3.5.2. At the latest time shown, $t = 5600$ s, in Figure 3.17(b), we begin to see a small deviation in $\langle T \rangle$ from the background stratification.

This effect is amplified in 2D (Figure 3.17(c)) where the two latest times ($t = 4800$ and 5600 s) both are noticeably cooler than the background stratification. It is also noticeable at $t = 4000$ s but a much smaller deviation. This means that in 2D, temperatures at the bottom of the domain are colder than in 3D. Caused by a combination of (a) the lack of mixing due to the smaller values of viscous dissipation shown in Figure 3.14 and 3.15, and (b) entrainment of cool fluid towards the bottom, discussed in more detail in Section 3.5.2.

Before moving on it should be noted that stratified cases are examples of penetrative convection, which is often defined as a turbulent fluid penetrating into an ambient that is stably stratified (Deardorff et al., 1969; Farmer, 1975). The classical example is Ref. Deardorff et al. (1969) that presented measurements of penetrative convection in a laboratory setting. In this experiment they measured the temperature inside the tank at several times (Figure 4 and 5 in Ref. Deardorff et al. (1969)). In this experiment, water temperatures were far above the temperature of maximum density and, hence, as temperatures increased - as a boundary condition, rather than a body forcing - the instabilities were generated at the bottom and the convective layer propagated upwards. The temperature profiles presented in Ref. Deardorff et al. (1969), other than being inverted, evolve nearly identically to those presented in Figure 3.17(b,c). The largest difference is at the earliest times in Figure 3.17(b) that is likely a result of the shape of the Beer-Lambert law forcing. The cooling of $\langle T \rangle$ compared to the background stratification at later times observed in Figure 3.17(b,c) is also observed in Ref. Deardorff et al. (1969). This suggests that penetrative convection, after an initial growth phase, evolves independently of a Beer-Lambert law forcing or boundary condition, assuming that the domain height, L_z, is sufficiently larger than λ. In the limit of $L_z \gg \lambda$, these forcings are virtually identical after the initial development phase.

Quantifying the development of the convective layer

We can further compare how the CL develops by looking at $\langle wT \rangle$ for the 3D stratified case and comparing it to the 3D unstratified case, Figure 3.18(b) and (a), respectively. The solid lines in Figure 3.18(a) refer to times also given in Figure 3.18(b), separated by 800 s. Dotted lines in Figure 3.18(a) correspond to $\langle wT \rangle$ at intermediate times between solid lines. This allows us to visually compare the differences in time scales but also see the

intermediate behaviour in the unstratified case. For the unstratified case, we have given $\langle wT \rangle$ in more detail in Figure 3.7(b).

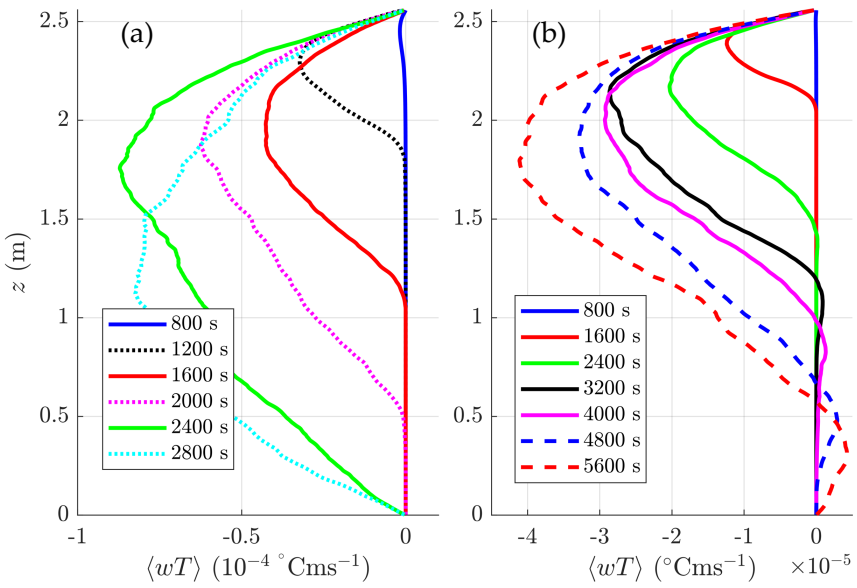

Figure 3.18: Horizontally averaged, vertical temperature flux, $\langle wT \rangle$ in (a) 3D with no initial stratification, and (b) 3D with an initial stratification. We do not include $\langle wT \rangle$ for the 2D stratified case because there is too much noise as a result of the narrow domain. Solid lines with the same colour correspond to the same time in both panels (e.g. solid blue line is $t = 800$ s for both panels) with a time interval of 800 s. Dotted lines in panel (a) correspond to mid points between sequential solid line times, times that do not appear in panel (b).

As for the unstratified case, a schematic is given in Figure 3.19 that represents the shape of $\langle wT \rangle$ at later times when $\langle wT \rangle > 0$ in a region at the bottom of the CL. This schematic shows that a positive mean corresponds to net upwards flux of temperature. This occurs when temperatures in the CL are comparable to, or smaller than, temperatures in the stratification beneath the CL. As a consequence, $\langle wT \rangle$ in the unstratified case, there was, of course, significant upward temperature flux in the ambient, as shown in Figure 3.11, but the mean temperature flux was still negative because the temperatures in the ambient were smaller than those in the CL. This is why at early times there is no region (c) and (d) in $\langle wT \rangle$ in the stratified case. The stratification near the bottom of the CL consists of temperatures cooler than those in the interior of the CL and in the interior of

convective plumes. At later times, temperatures in the stratification are comparable to and even exceed the temperatures in the CL and hence, wT values are much larger.

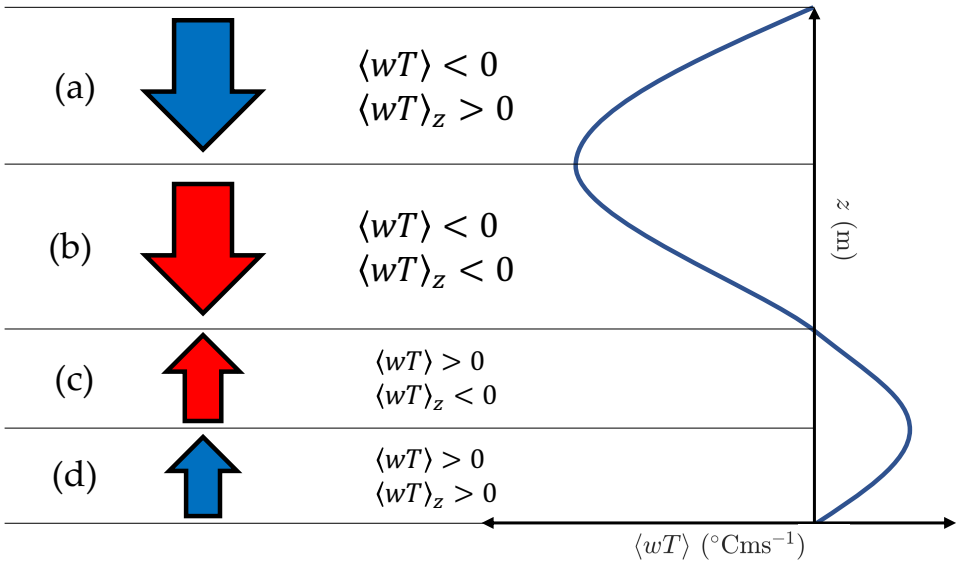

Figure 3.19: Schematic of the horizontally averaged vertical temperature flux. The shape of $\langle wT \rangle$ is consistent with late time behaviour in 3D as in Figure 3.18(b). The vertical is divided into four regions and assigned an arrow denoting whether the region is cooling (blue) or warming (red), as well as the direction of the net flux, denoted by the direction of the arrow. This schematic only describes effects to temperature and flow due to convection. For example, (a) has a blue arrow pointing downwards indicating that this region is cooling with a net downwards flux. Relative magnitude of the example $\langle wT \rangle$ curve in regions (c,d) compared to (a,b) is exaggerated.

Some key similarities between the stratified and unstratified cases are demonstrated by Figure 3.18. First, fluxes are initially confined to a small region near the surface. The height of the peak - boundary between regions (a) and (b) in Figure 3.19 - decreases with time. The magnitude of the peak and as well as the magnitude of the slope of $\langle wT \rangle$ below the peak, gradually increase. In the analysis of the unstratified case, comparing 2D and 3D, non-monotonicity of the peak location and magnitude was identified in 3D between $t = 1400$ and 1800 s in Figure 3.7(b). This non-monotonicity is not as apparent in Figure 3.18(a) because few times are shown. However, there is clearly some degree of non-monotonicity in the peak height and location in the stratified case between $t = 3200$ and

4000 s. A feature that was lacking in 2D and is present in 3D with or without stratification. Two time periods that exhibit some degree of non-monotonicity in the stratified 3D case are shown in Figure 3.20.

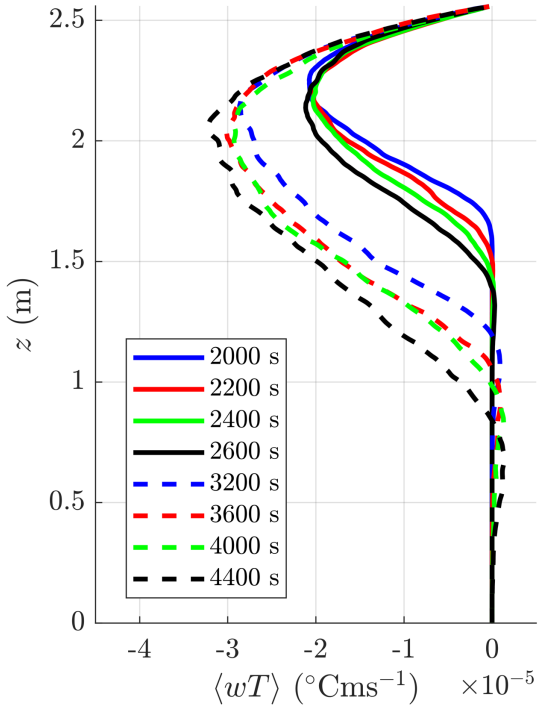

Figure 3.20: Horizontally averaged, vertical temperature flux, $\langle wT \rangle$ in 3D with an initial stratification highlighting the time periods of non-monotonicity of the peak magnitude.

These time periods are approximately $t = 2000$ to 2600 s and $t = 3200$ to 4400 s. The behaviour presented in Figure 3.20 is inconsistent with growth observed during other time periods. Neither the 2D stratified or unstratified cases showed any periods of non-monotonicity and generally consistent growth of mean quantities like $\langle wT \rangle$. In the 3D unstratified case, only one such period is identified as mentioned above.

There are also some key differences between the stratified and unstratified cases apparent in $\langle wT \rangle$ in Figure 3.18. First, beginning around $t = 2400$ s, at the bottom of the CL there are positive values of $\langle wT \rangle$ that indicate an upwards flux of temperature from the stratification into the interior of the CL, which has have a warming effect on the CL. The effect of the stratification is to slow development of the CL and through these upward

fluxes, the CL is able to descend further into the water column. In the unstratified case, there are also upwelling fluxes, however, the temperatures are much cooler than the downwelling fluxes. As a result the mean remains below zero and the net effect is to cool the CL. Recalling the histograms of wT in Figure 3.11, there are many small but positive values of wT at the base of the CL that correspond to the upwelling of the constant temperature ambient. This cooling effect is enhanced in 3D where there is more dissipation and mixing. The calculation of the mean temperature profile as in Figure 3.17 does not capture the lack of mixing and as a result $\langle T \rangle$ is quite similar between 2D and 3D.

In the stratified case, after $t \approx 2400$ s, the temperatures in the ambient are warmer than those in the CL and instead mixing with the ambient results in warmer temperatures. However, not all this fluid is immediately mixed and the kinetic energy imparted to the background stratification is converted to available potential energy (Winters et al., 1995, 2019) that will be converted back to kinetic energy as the fluid will be denser than its surroundings. This is discussed further in the analysis of the full fields in Section 3.5.2. The histograms for the stratified case develop similarly to those in the unstratified case in Figure 3.11. The only difference is that the clustering near the positive side of zero at the bottom of the CL is lessened as the T part of the wT product is marginally increased and that part of the histograms has a larger tail towards the positive wT values.

The total heat flux is another quantity presented in Ref. Deardorff et al. (1969) with some key similarities and differences to $\langle wT \rangle$ presented in this thesis, namely that it includes the diffusive heat flux. Recall that in Ref. Deardorff et al. (1969) the domain is inverted in the vertical due to their experiments using temperatures above the temperature of maximum density. In Figure 7, 8 and 9 in Ref. Deardorff et al. (1969), near the boundary where the CL meets the stratified background, $\langle wT \rangle$ crosses zero as is does in the stratified case presented here in Figure 3.18(b) at the bottom of the CL. One clear difference however is that at the bottom of their domain (the analogy to the top of the domain used in this chapter) the total heat flux does not converge to zero at all times. This occurs because the heat flux at the bottom boundary in Ref. Deardorff et al. (1969) is nonzero.

Further, $\langle wT \rangle$ at later times intersects with earlier times, also near the bottom. In Figure 3.18(b), $\langle wT \rangle$ only intersects itself at different times at the bottom of the CL after $\langle wT \rangle$ crosses zero. In Figure 7 and 8 in Ref. Deardorff et al. (1969), the intersections occur on both sides of $\langle wT \rangle = 0$. The fact that $\langle wT \rangle$ does not intersection below the peak, above the crossing of zero, indicates that the change of temperature is consistent as a function of time. Whereas in the cases presented in Ref. Deardorff et al. (1969), the change in temperature due to penetrative convection is not consistent with time. This shows a clear quantitative difference in how penetrative convection is sensitive to the form

of the temperature forcing. In this case, a boundary forcing (Ref. Deardorff et al. (1969)) and a body forcing (this thesis).

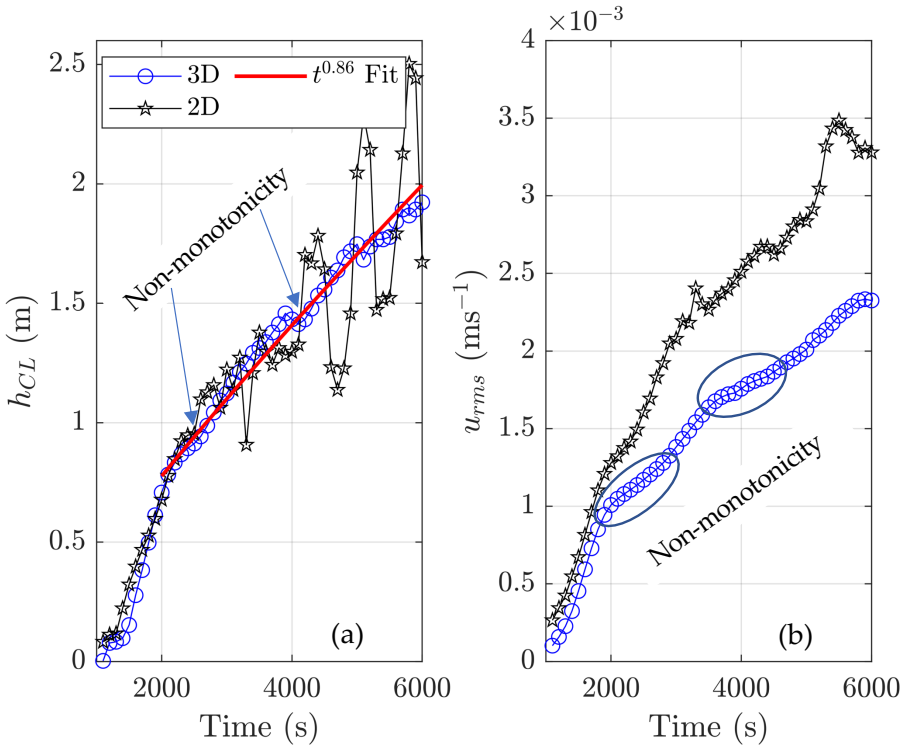

Figure 3.21: h_{CL} in 2D and 3D for the stratified initial condition. (a) h_{CL} versus time with a power law fit. This fit is obtained after an initial growth phase from $t = 0$ to 2000 s. The exponent of the power-law is approximately 6/7 (0.86). (b) h_{CL} versus u_{rms} within the convective layer. The label of 'non-monotonicity' refers to the discussion of Figure 3.20, where peak height is non-monotonic with time at two instances.

As in the unstratified case, h_{CL} is estimated using $\langle wT \rangle$ (Figure 3.21(a)). The way it is calculated is described in Section 3.2.2 and is similar to the approach used for the unstratified case. h_{CL} is then used to define u_{rms} (Figure 3.21(b)). h_{CL} has an initial growth phase in 2D and 3D as a function of time (Figure 3.21(a)), just as it did in the unstratified case, before transitioning to a new phase with generally slower growth. These two phases are the solar radiation and convection dominated phases. Here, the growth of h_{CL} in the convection dominated phase obeys a sub-linear power-law fit in time with an exponent approximately equal to 6/7. The fit was obtained only using the 3D data but

also fits the 2D data well, qualitatively, despite the variance in h_{CL} at late time in 2D. The variance in h_{CL} in 2D comes from $\langle wT \rangle$, which is extremely noisy in 2D. For this reason, it was not included in Figure 3.18. As in the unstratified case, u_{rms} in the interior of the CL is smaller in 3D than in 2D despite the fact that h_{CL} evolves nearly identically. In contrast to the unstratified case, u_{rms} is much closer in magnitude between 2D and 3D in the solar radiation dominated phase in the stratified case. Transitioning into the convection dominated phase, u_{rms} grows much more rapidly.

The non-monotonicity that is apparent in $\langle wT \rangle$ in 3D in 3.20, also effects h_{CL} and occurs very close to the transition between the solar radiation and convection dominated phases. The magnitude of the effect on h_{CL} is quite difficult to spot in Figure 3.21(a), even with the arrows as a guide. The non-monotonicity here appears as a brief decrease in the growth rate in the first period of non-monotonicity, and a decrease in magnitude of h_{CL} in the second period. The effect of the non-monotonicity is more apparent in u_{rms} (Figure 3.21(b)). In 3D, the non-monotonicity results in a decrease in the growth rate of the h_{CL}, followed by an increase in the growth rate. These periods are highlighted by the ellipses in Figure 3.21(b) and affect u_{rms} for more time than the h_{CL}, which appears to recover quickly. In 2D, u_{rms} exhibits a similar decrease in its growth rate during the first period of non-monotonicity, immediately followed by a similar increase in the growth rate. However, it is notably shorter when compared to 3D and does not have a detectable effect in $\langle wT \rangle$ due to the variations in $\langle wT \rangle$ in time.

The existence of two periods of non-monotonicity suggests some unique dynamics in 3D is occurring more than once when a stratification is introduced. One hypothesis is that the first bout of non-monotonicity is related to the transition from the solar radiation dominated phase to the convection dominated phase. The second one could be related to when the CL has descended to a depth where temperatures in the background stratification begin to exceed the temperatures at the bottom of the interior of the CL. As of yet, no specific mechanism has been identified.

3.5.2 Analysis of the full fields

In this section, the full temperature field is examined, rather than an average as in the previous section. In the previous section, it was shown that, in the stratified case, $\langle T \rangle$ evolves similarly in 2D and 3D, from a purely solar radiation dominated curve, to one with a nearly constant temperature CL that gradually eats away at the background stratification. Further, the mean depth of the CL evolves at a very similar rate after an initial phase where 2D evolves more rapidly. Some differences were also identified, namely, temperatures in 2D

were generally warmer in the CL and cooler further below, as shown in Figure 3.17(b,c). Similar to the unstratified case, motion within the CL was generally slower in 2D compared to 3D. The full temperature field will reveal the mechanisms behind these key differences and the similarities between the stratified and unstratified cases.

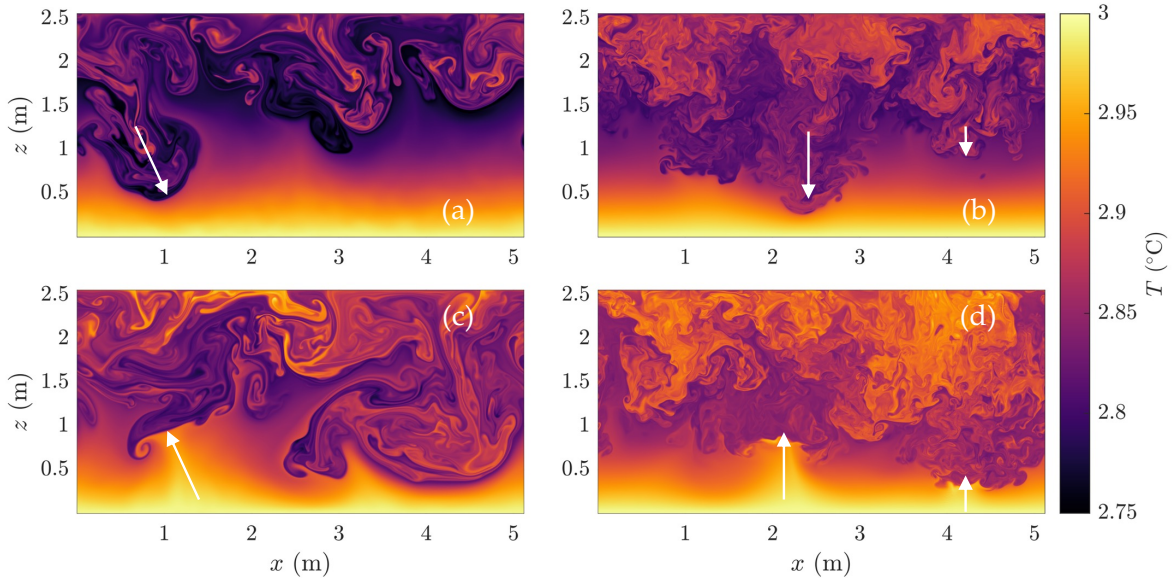

Figure 3.22: Temperature field slices for the stratified case for 2D and 3D at four different times. (a) 2D at $t = 3400$ s, (b) 3D at $t = 4200$ s, (c) 2D at $t = 4400$ s, and (d) 3D at $t = 5000$ s. The 3D slices are taken at $y = 2.56$ but is generally representative. White arrows indicate the approximate direction of propagation of convective plumes.

In Figure 3.22, panels (a) and (c) correspond to 2D at $t = 3400$ and 4200 s and panels (b) and (d) correspond to 3D at $t = 4200$ and 5000 s. The times presented in Figure 3.22 were chosen carefully to highlight an important effect that occurs when convective plumes reach the warmer stratification. In both 2D and 3D, convective plumes that penetrate deep into the stratification are gradually slowed and their kinetic energy is converted into potential energy, mostly reversibly. Inevitably, these convective plumes bounce off the stratification and are launched back into the interior of the CL. This occurs in both 2D and 3D as shown by Figure 3.22.

In the top row of Figure 3.22, downward flowing convective plumes penetrate into the stratification, highlighted by the arrows. At these earlier times, most of the convective plumes - save for the deepest penetrating plumes - have temperatures which are comparable to the background stratification at the same depth. At earlier times (not shown), this

effect is exaggerated and as a result the evolution of the convective plumes is not dissimilar to the unstratified case. During this earlier stage, the kinetic energy in the plumes is still increasing. Figure 3.22(a,b) approximately corresponds with times when convective plumes first begin to penetrate into a warmer background, converting their kinetic energy, gradually, into potential energy.

In the bottom row of Figure 3.22, in both 2D and 3D, these exact plumes have bounced off the stratification. This occurs when all of the kinetic energy in the convective plumes is converted into potential energy, mostly reversibly. This bounce entrains significant fluid from the stratification into the CL showing exactly the strongest mechanism for eating away at the stratification and as a result, contributing to the growth of the CL.

At earlier times (Figure 3.22(a,b) and earlier), before the convective plumes have turned around, most perturbations to the stratification are confined to the boundary of convective plumes. Due to the larger size of the convective plumes, and the increased entrainment of cool fluid towards the bottom, in 2D (Figure 3.22(a,c)), the perturbations are larger than in 3D (Figure 3.22(b,d)). In both 2D and 3D, at the later times (Figure 3.22(c,d)), the stratification has mostly repelled the advancing CL front. Only a small stratified layer remains at the bottom. Recall here the use of free-slip boundary conditions in both cases and, hence, the remaining stratified layer cannot be a boundary layer, resisting motion.

The upwards entrainment of the background stratification has the effect of heating the CL. At the times shown in Figure 3.22(c,d), visually, the CL might decrease in depth briefly. Indeed, a small decrease in h_{CL} at $t = 5000$ s, can be seen in Figure 3.21(a). This change is small compared to the change in depth of the convective plume in Figure 3.22(d) because it is inferred from an average and the rest of the CL during this time does descend. The net effect over time will be to increase the depth of the CL because of the upwards entrainment of warm fluid into the interior of the CL.

An important difference between 2D and 3D is that most of the upward entrainment is entirely in the vertical in 3D (Figure 3.22(d)) and occurs at an angle in 2D (Figure 3.22(c)). There are also clear differences in downward entrainment. In the 2D unstratified case, the largest temperature differences were on the boundary of convective plumes. This was because the interior was warm and the exterior was the cool ambient (Figure 3.3(a)). In the 2D stratified case, the temperature differences are still largest at the boundary of convective plumes but not because of a large temperature difference between the interior of the plumes and the ambient, but because of entrainment of cooler fluid downwards with the convective plumes (Figure 3.22(a,c)). This cool fluid at the boundary of convective plumes likely originates in the upper portion of the background stratification prior to the time of Figure 3.22(a). This entrainment likely also occurs in the 2D unstratified

case, but is impossible to see in the temperature field because the entrained fluid is the same temperature as the ambient. In 3D, there are no clear signs of entrainment of fluid cooler than the interior of the convective plumes towards the bottom. Temperatures at the boundary are comparable to temperatures in the interior and temperatures outside of the convective plumes are typical of the background stratification at these depths (Figure 3.22(b,d)).

This difference in entrainment is mostly responsible for the differences in $\langle T \rangle$ in 2D compared with the background stratification (Figure 3.17(c)). Other causes were identified in Section 3.4, including a lack of mixing demonstrated by the dissipation histograms at fixed depth (Figure 3.15) and the magnitude of the vorticity generation (Figure 3.5 and 3.4). The effect of the entrainment - or lack thereof - on the distribution of temperatures in Figure 3.23 in 2D and Figure 3.24 for 3D is evident.

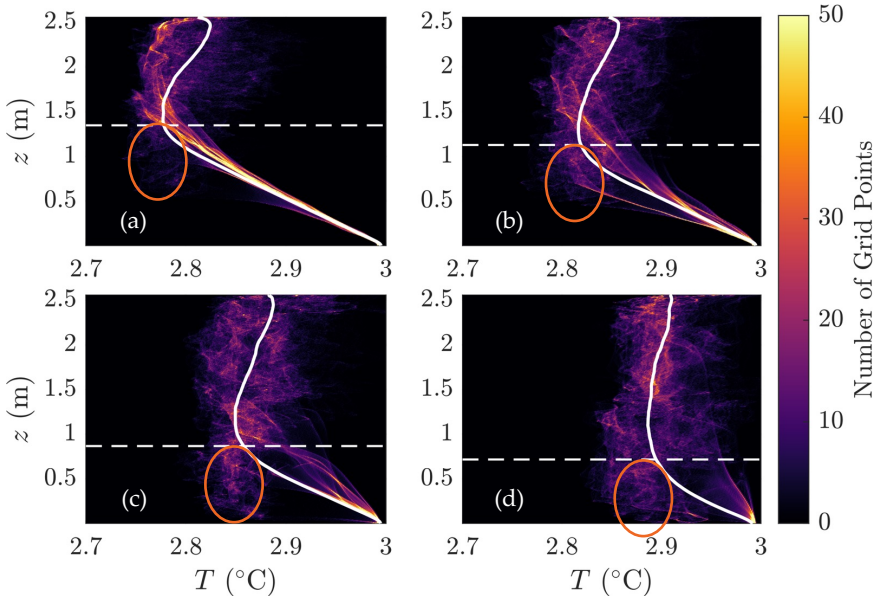

Figure 3.23: Histograms of temperature in 2D at four different times. (a) $t = 3200$ s, (b) 4000 s, (c) 4800 s and (d) 5600 s. Colour bar and colour in each panel indicates the number of grid points with the value on the horizontal axis. Solid white line is $\langle T \rangle$ and is also given in Figure 3.17(c). Dashed white line indicates the approximate depth of the CL given in Figure 3.21(a) using the 3D curve to avoid the noise observed in 2D, estimated using $\langle wT \rangle$ in Figure 3.18(b). The orange ellipses highlight an important feature discussed in the text and are also given in the same place in Figure 3.24 for comparison.

The four times shown in Figure 3.23 and Figure 3.24 are well after the CL has formed (exact times are in the caption). There are 3 important features of interest that evolve gradually in both 2D and 3D. (1) Temperatures cooler than the mean below the CL (below the dashed line, highlighted by the ellipse), (2) temperature range inside the CL (above the dashed line), (3) temperatures warmer than the mean below the CL.

Starting with the first feature, at all times there is a significantly larger concentration of grid points at temperatures colder than the mean in 2D, highlighted by the orange ellipse in each panel of Figure 3.23. A similar, but smaller and warmer, feature is also present in 3D (Figure 3.24). Note that the ellipses in Figure 3.23 and 3.24 are in the same location on each panel for easy comparison.

This feature in both cases is the result of convective plumes slowly penetrating into the background stratification, and is enhanced in 2D by the entrainment of cool fluid (Figure 3.22(a,c)) and the lack of viscous dissipation (Figure 3.15(a)). Despite this, the depth of a clear CL is still quite comparable between 2D and 3D, as shown in Figure 3.21(a). The difference in flow speed in the CL is demonstrated in Figure 3.21(b) where a similar CL depth corresponds to much large speeds in the CL interior.

The range of temperatures in the CL - the second important feature - is notably larger in 2D compared to 3D, further emphasizing the decreased mixing in 2D. At the earliest time shown, there is a larger concentration of warmer temperatures near the surface in 3D compared to 2D (Figure 3.24(a) 3.23(a)) in the $L_z = 2.56$ to 2 m range, whereas in 2D the distribution is widest in the 2 to 1.5 m range. As time progresses, the width of the distribution in the interior of the CL decreases in both 2D and 3D, this decrease is more pronounced in 3D as a result of the increased rate of mixing.

The last important feature are temperatures above the mean, below the CL. Clearly, at all times shown the distribution of temperatures is wider below the CL in 2D. This increased width compared to 3D does affect the mean, hence, the decrease in temperature near the bottom of the domain at late times in 2D in $\langle T \rangle$ (Figure 3.17(c)). This cool patch in 2D is partially, but not completely, offset by the warm, unmixed fluid in the interior of down welling convective plumes, present in both the stratified case (Figure 3.22(a,c)) and unstratified 2D case (Figure 3.3(a)). As it has mentioned time and time again in this section, this is the result of the lack of mixing in 2D that results in the transport of warm fluid towards the bottom with minimal mixing.

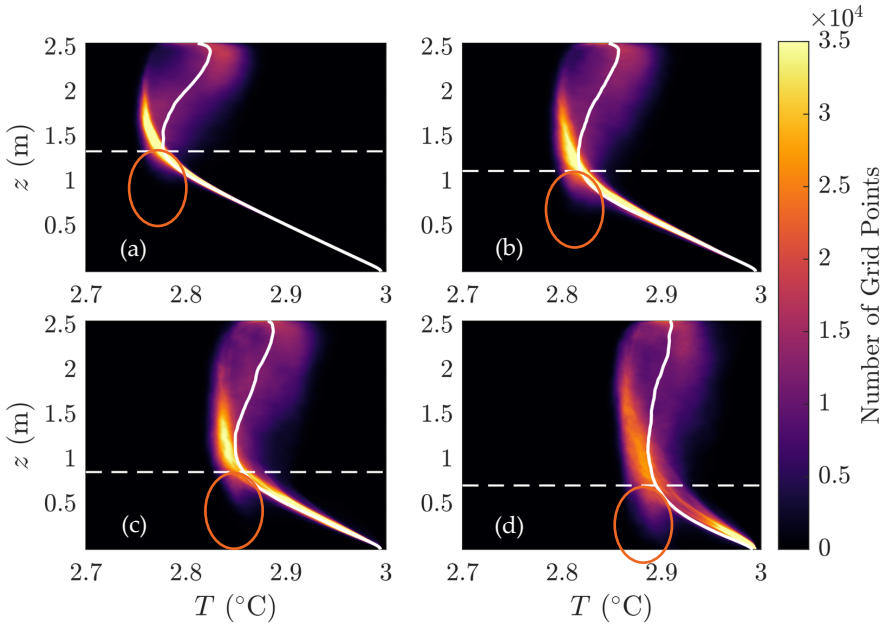

Figure 3.24: Histograms of temperature in 3D at four different times. (a) $t = 3200$ s, (b) 4000 s, (c) 4800 s and (d) 5600 s. Colour bar and colour in each panel indicates the number of grid points with the value on the horizontal axis. Solid white line is $\langle T \rangle$ and is also given in Figure 3.17(b). Dashed white line indicates the approximate depth of the CL given in Figure 3.21(a), estimated using $\langle wT \rangle$ in Figure 3.18(b). The orange ellipses highlight an important feature discussed in the text and are also given in the same place in Figure 3.23 for comparison.

3.5.3 Bulk quantities

For the unstratified cases, the components of the vorticity generation are compared. Baroclinic in 2D and baroclinic and stretching and tilting in 3D in Figure 3.5. A similar approach is taken here, and compare these quantities in the stratified case in Figure 3.25(a) with the unstratified components (a copy of Figure 3.5) in Figure 3.25(b) for easy comparison.

There are several similar features between the stratified and unstratified vorticity generation components. First, in the solar radiation dominated phase, the 2D baroclinic is larger than the 3D baroclinic and the stretching and tilting, as in the unstratified case. Possible causes for this difference are discussed in Section 3.4.2. The stretching and tilting term is so small because there is very little vorticity at this stage and the stretching and tilting term is proportional to the vorticity, unlike the baroclinic term, which depends only

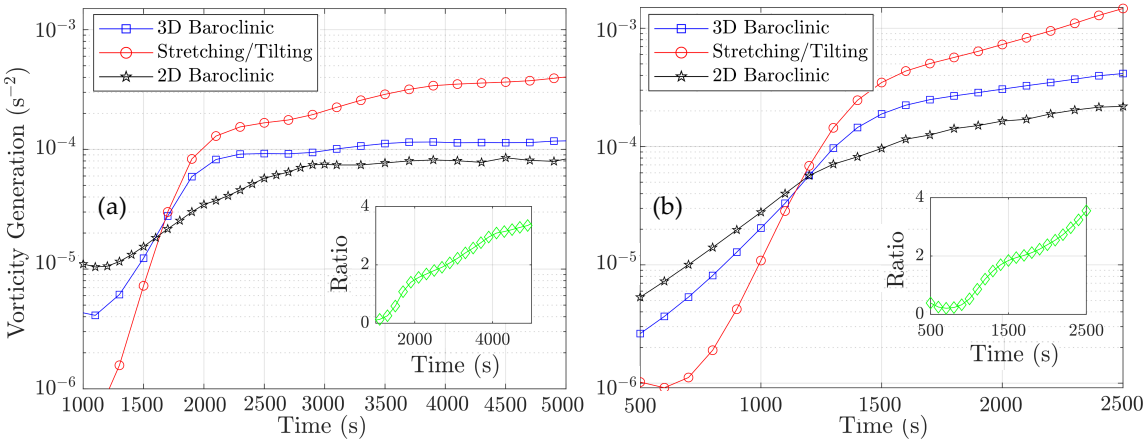

Figure 3.25: Mean vorticity generation on a base-10 log scale on the vertical axis and a linear scale on the horizontal axis. (a) Cases with stratified initial conditions, and (b) Cases with constant temperature initial conditions and a copy of Figure 3.5 for comparison. In both panels, 3D baroclinic vorticity generation (blue squares), stretching and tilting (red circles) and 2D baroclinic vorticity generation (black stars). The inset of each panel shows the ratio of the mean stretching and tilting term to the 3D baroclinic vorticity term. Symbols represent the actual data points, while lines are guides to the eye.

on lateral density gradients. Second, as the flow transitions to the convection dominated phase, in both the stratified and unstratified cases, the order reverses. The stretching and tilting term is the largest, enabling the breakdown of upwelling instabilities, the 3D baroclinic term is in the middle and the 2D baroclinic term is smallest in magnitude. In both the stratified and unstratified cases, the mean stretching and tilting term continues to grow for the duration of the simulation.

There are also several notable differences between the stratified and unstratified cases. First, only the vortex stretching and tilting term appears to grow in the stratified case in Figure 3.25(a). The baroclinic generation in 3D does grow slightly over the time period shown, but is very small on a log-scale. The baroclinic generation is effectively constant after $t = 3000$ s. In the unstratified case (Figure 3.25(b)), all three quantities have an initial growth during the solar radiation dominated phase and transitions to a smaller growth in the convection dominated phase. Given that the vertical axis is a log scale and the horizontal axis is linear, and the curves after $t = 1600$ s are approximately linear, each of these terms are growing approximately exponentially in the unstratified case (Figure 3.25(b)). While there is clearly an initial growth in the solar radiation dominated phase in the stratified case (Figure 3.25(a)), the transition is no longer consistent between the 2D baroclinic term and the 3D baroclinic and stretching and tilting terms.

The inset of both panels of Figure 3.25 give the ratio of the stretching and tilting term to the 3D baroclinic term. In the unstratified case, Figure 3.25(b), there is an initial growth, followed by a bump near $t = 1500$ s, followed by further growth. Note that this time $t \approx 1500$ s coincides with the non-monotonicity identified using the location and magnitude of the peak of $\langle wT \rangle$ in the unstratified case in Figure 3.7(b). This time is shortly after the start of the convection dominated phase, which starts at $t \approx 1300$ s, identified using the arrows on Figure 3.7(b) suggesting that this non-monotonicity that is apparent in Figure 3.7(b) and Figure 3.25(b) is a separate phenomenon. Note that while this effect was first presented in $\langle wT \rangle$ in Figure 3.18(b) where the peak height and magnitude were non-monotonic in time, the vorticity generation terms are clearly monotonic. However, the rate of change is non-monotonic. The term non-monotonic will be continued to be used to describe this phenomenon even as the quantities we use are monotonic in time, but their derivatives are non-monotonic.

In the inset of the stratified case on Figure 3.25(a), there are instead two bumps in the ratio of the stretching and tilting term to the 3D baroclinic term that coincides very closely with the two points of non-monotonicity identified in Figure 3.21. These bumps can also be seen in the 3D baroclinic and stretching and tilting terms in Figure 3.25(a), albeit with less detail. Evidently, the non-monotonicity in Figure 3.7(b) and Figure 3.18(b) is accompanied by a decrease in the growth of the vorticity generation terms.

The non-monotonicity can be further explored, which is a non-monotonicity in the rate of change of the vorticity generation, by comparing the average kinetic energy, KE_{avg} (Figure 3.26(a)), to the average enstrophy, $|\vec{\omega}|^2_{avg}$ (Figure 3.26(b)), in the stratified case. The enstrophy nearly flattens during the periods of non-monotonicity, meanwhile, the growth KE_{avg} slows slightly during the periods. The effect on the enstrophy is much stronger. The decrease in the enstrophy growth is consistent with the decreases in the growth of the stretching and tilting term in Figure 3.25(b). The slight decrease in the baroclinic term likely contributes but to a lesser degree.

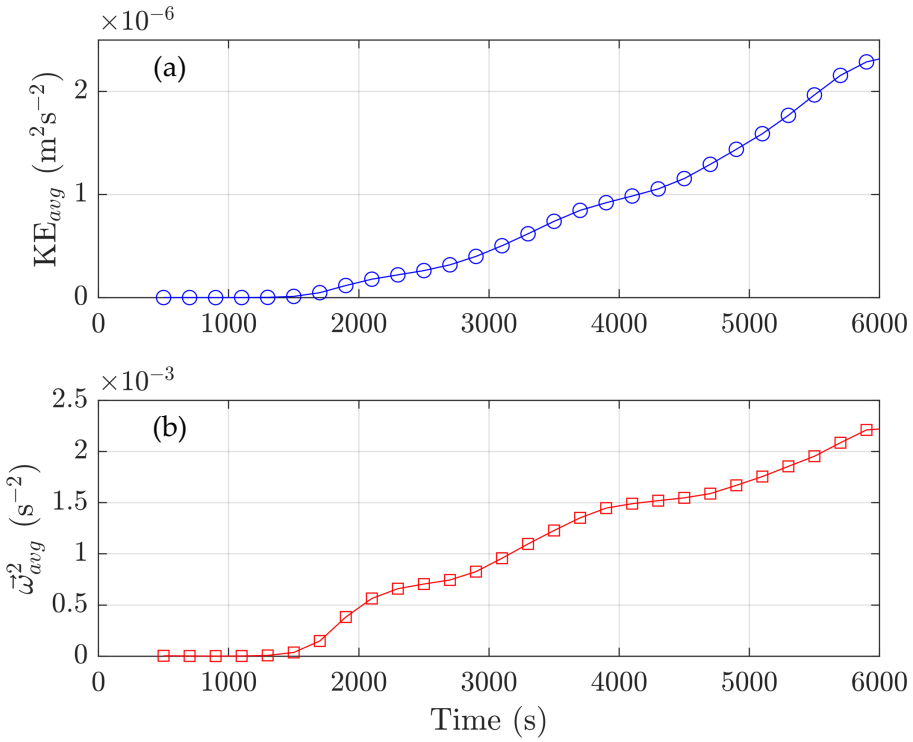

Figure 3.26: Comparison of KE and Enstrophy averaged over the domain according to Eq. 2.26. (a) KE_{avg} and (b) Enstrophy or $|\vec{\omega}|^2_{avg}$.

Figure 3.26 gives the magnitude of KE_{avg} and $\vec{\omega}^2_{avg}$ and Figure 3.27 gives the rate of change with respect to time of both of these quantities. $\partial \mathrm{KE}_{avg}/\partial t$ clearly decreases at each of the periods of non-monotonicity, however, after each dip in $\partial \mathrm{KE}_{avg}/\partial t$ the next peak is larger than the last. The KE growth rate is continually increasing, despite the brief decrease during the periods of non-monotonicity. The final decrease in $\partial \mathrm{KE}_{avg}/\partial t$

is associated with the CL reaching the bottom after having eaten away at most of the background stratification.

$\partial|\vec{\omega}|^2_{avg}/\partial t$ instead is largest at the onset of the first non-monotonicity period, which elapsed from $t = 2000$ to 2500 s. $\partial|\vec{\omega}|^2_{avg}/\partial t$ reaches a local minimum at the end of each of these periods and decreases rapidly near the end of the time period shown as the CL eats away at most of the background stratification, as in $\partial \mathrm{KE}_{avg}/\partial t$. The enstrophy growth rate oscillates with a nearly constant amplitude while the KE growth rate continues to increase with each oscillation.

In Figure 3.27, vertical lines are drawn connecting features of interest in $\partial \mathrm{KE}_{avg}/\partial t$ (panel a) to $\partial|\vec{\omega}|^2_{avg}/\partial t$ (panel b). The first two lines - from left to right - show that the local minima in $\partial \mathrm{KE}_{avg}/\partial t$ proceeds the local minima in the enstrophy. This suggests that if a casual relationship exists between these two quantities, it is the loss in KE growth that enables the loss of enstrophy growth. The final line connecting the two panels also shows that the location of the final peak $\partial \mathrm{KE}_{avg}/\partial t$ appears first again suggesting a loss of KE leads to a loss in enstrophy.

3.6 Conclusion

In this chapter, the results of four simulations were presented, two with constant temperature initial conditions and two with an initial stratification defined according to Eq. 3.5, subjected to volumetric heating - analogous to solar radiation - resulting in radiatively driven convection. One of each initial condition type is in 2D and the other in 3D. In the case of the stratified initial conditions, the convection is typically classified as penetrative convection. On the whole, convection in both 2D and 3D is an effective mechanism to transport heat in the vertical direction. However, the manner in which the transport is carried out and the manner in which heat is exchanged with the ambient is different in a few key ways. Convective plumes, both downwelling and upwelling, do not break down in 2D. As a result, we have large, irrotational regions and low viscous dissipation in the regions with rotation. In 3D, both the upwelling and downwelling plumes are able to break down thanks to vortex stretching and tilting. This results in significantly more viscous dissipation which is more uniformly spread throughout the CL. Regions near the bottom of the convective layer do look similar to 2D, as in Figure 3.12(b) and Figure 3.16(a), with large regions of irrotational patches, which quickly break down. Further, in 3D, the CL increases its depth more uniformly with a nearly monotonic temperature field at each z-profile, while in 2D, the z-profiles are wildly non-monotonic.

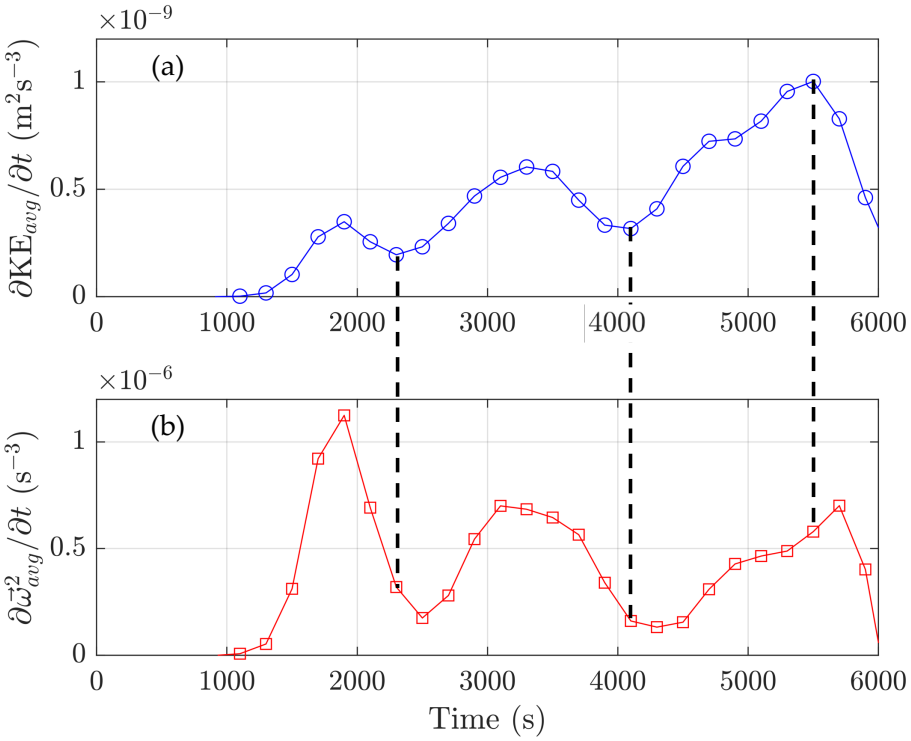

Figure 3.27: Comparison of the rate of change of KE and Enstrophy averaged over the domain according to Eq. 2.26. (a) $\partial \mathrm{KE}_{avg}/\partial t$ and (b) $\partial |\vec{\omega}|^2_{avg}/\partial t$. Vertical dashed lines connecting points in panel (a) to panel (b) are meant to highlight the offset in time of certain features of interest, which are expanded on in the text.

By comparing the mean of the magnitude of the baroclinic vorticity term to the mean of the magnitude of the stretching and tilting term in Figure 3.25 for both sets of initial conditions. It is established that the stretching and tilting term is not just absent from 2D systems but it is dominant in 3D in the convection dominated phase and modifies the propagation of convection into the ambient, constant temperature or stratified initial conditions. We also identified that the baroclinic vorticity is maximized in 2D at the boundary of convective plumes. It is also true for the 3D case but there is evidently more baroclinic contributions within the active layer compared to 2D, as shown in Figure 3.4. Figure 3.6 compares the baroclinic vorticity term to the stretching and tilting term in the same vertical slice as Figure 3.3(b) and 3.4(b) at $y = 2.56$ m. This figure shows clearly that the stretching and tilting in 3D (Figure 3.6(b)) is most active in the interior of the CL, contrary to the baroclinic term (Figure 3.6(a)). In both 2D and 3D, upwelling convective

plumes of irrotational fluid exist. Both result in baroclinic vorticity generation on the boundary between the up and downwelling plumes. In 2D, the vorticity generated in this way remains on the boundary and in the interior of the warm plumes. However, in 3D, vortex stretching and tilting allows the upwelling plumes to breakdown.

For the stratified cases, the initial stratification not only slows the development but also changes the manner in which it develops. Initially, the profile is stably stratified until $t = t_s$ after which it is unstable, confined to only a small region near the surface. This is contrary to the unstratified case where the mean profile is immediately unstable in the entire water column. As a result, penetration of convective plumes in the unstratified case will always result in an increase to the total kinetic energy (Eq. 2.19). Once the convection dominated phase begins, $\langle T \rangle$ gradually increases at the surface in the stratified case (Figure 3.17(b)), while remaining largely constant in the unstratified case (Figure 3.17(a)). The vertical temperature flux balances the solar radiation in the unstratified case but this is not the case in the stratified case. Once the CL reaches the bottom of the domain, the unstratified case $\langle T \rangle$ decreases at the surface and redistributes temperature towards the bottom. There is a similar, but muted, effect in 3D where the growth in $\langle T \rangle$ gradually slows as the CL penetrates further into the background stratification.

The stratified cases showed that on average, there are many similarities between 2D and 3D, especially highlighted by $\langle T \rangle$ in Figure 3.17(b,c). Generally, $\langle T \rangle$ is larger in 2D, consistent with the unstratified case where a lack of mixing allowed warmer temperatures to exist for longer. Another clear difference in $\langle T \rangle$ between 2D and 3D (Figure 3.17(b,c)) is that at late time in 2D, temperatures near the bottom are significantly cooler than the background stratification and compared to the 3D case at the same time. By analyzing the full temperature fields in Figure 3.22, it was shown that in 2D, there is significant entrainment of cool fluid towards the bottom. In 3D, the convective plumes do not entrain cool fluid towards the bottom and any cooling is achieved via an upwards entrainment of fluid back into the CL as convective plumes rebound off the background stratification (Figure 3.22). This bounce occurs in both 2D and 3D, but is the only mechanism for cooling the stratification in 3D, other than small amounts of mixing confined to the boundary of penetrating convective plumes. This bounce occurs because the temperatures in convective plumes are smaller than the background stratification and as a result most of the kinetic energy in the plume is converted into potential energy, reversibly, launching it back up into the interior of the CL.

As in the unstratified case, we identified non-monotonicity in the peak height and magnitude of $\langle wT \rangle$ (Figure 3.18). Here, we observed two time periods with some degree of non-monotonicity. This phenomenon was not present in the unstratified 2D case. In the stratified 2D case, $\langle wT \rangle$ had too much noise to show but we suspect it is also not

present in the stratified 2D case. The effect of this non-monotonicity was present in other quantities, namely, h_{CL} (Figure 3.21(a)), u_{rms} (Figure 3.21(b)), the mean stretching and tilting term (Figure 3.25(a)), the domain averaged KE (Figure 3.26(a) and 3.27(a)), and the enstrophy (Figure 3.26(b) and 3.27(b)). The first period of non-monotonicity, is quite close to the transition between the solar radiation dominated phase and the convection dominated phase, in both the stratified and unstratified cases, suggesting that the first period is linked to this transition. The second period is correlated with the point in time where temperatures in the interior of convective plumes are comparable to or cooler than temperatures in the stratification. The bounce phenomenon, observed in Figure 3.22, occurs over a time period that is similar to the period of decreased enstrophy growth in (Figure 3.27(b)), suggesting a relationship. However, both the transition to the solar radiation dominated phase and the bounce phenomenon both occur in 2D. Further, u_{rms} in 2D does exhibit some similar loss in growth rate during the first period of non-monotonicity. While the exact cause of the non-monotonicity is unclear, it is easy to identify in 3D and relate to other quantities.

Overall, in 2D bulk quantities like $\langle wT \rangle$, $\langle T \rangle$ and h_{CL} are well captured. Further, the bounce phenomenon where convective plumes reflect off the background stratification and entrain warmer fluid into the interior of the CL is present in both 2D in 3D (although the timing is slightly offset and occurs at an angle relative to the z-axis in 2D). However, quantities like dissipation, u_{rms} and the shape, composition and scale of plumes in the CL are not well captured in 2D. 2D simulations should be largely used for faster results to test hypotheses but should not be used to validate or test theories.

Chapter 4

Spatially heterogeneous solar radiation intensity with constant temperature initial conditions in two dimensions

4.1 Introduction

While there are many arctic lakes with perennial ice coverage (Mueller et al., 2009; Leppäranta, 2014), and multi-year ice is also possible on proglacial lakes (Leppäranta, 2014), most lakes with any period of ice-cover have an ice-free summer with freezing and break up dates at the start and end of winter (Magnuson et al., 2000; Leppäranta, 2014; Karetnikov et al., 2017; Hewer and Gough, 2019). Even for perennially frozen lakes and lakes past the freezing date, 100% ice-coverage is not always expected (Magnuson et al., 2000; Duguay et al., 2003; Karetnikov et al., 2017; Hewer and Gough, 2019). Climate Change is predicted to continue the observed trend of reducing the time between freezing and break-up dates, as well as increasing the number of break-ups between the freezing date and the break-up date (Magnuson et al., 2000; Woolway and Merchant, 2019). In addition, the number of lakes with perennial ice-coverage is decreasing (Mueller et al., 2009). Incomplete ice-cover is present in many inland lakes at different stages of winter and must be considered for a complete understanding of lake dynamics. There are two main consequences of incomplete or variable ice-cover: (1) shear wind stress in areas of no ice-cover and (2) horizontal variations in incoming solar radiation. In this chapter, we neglect any wind forcing effects and focus entirely on horizontal variations in solar radiation and the effect it has on temperature distributions in a lake environment.

4.1.1 Known Sources of lateral motion in ice-covered lakes

It is well established that lateral variations in temperature - and therefore lateral buoyancy variations - drive lateral motion (Leppäranta, 2014; Ulloa et al., 2019; Ramón et al., 2021; Bouffard and Wüest, 2019). When solar radiation is the main driver of convection, as is the case in the late winter in ice-covered lakes, non-uniform bathymetry generates these lateral buoyancy gradients (Ulloa et al., 2019; Ramón et al., 2021). Heat deposited in shallow regions is not able to mix with cooler fluid beneath, as in the deeper parts of the lake. As a result, these regions heat faster. Further, reflection or absorption of radiation at the bottom may provide an additional source of heating not present in the deep regions.

Wind on ice-free lakes in the winter has also been shown to generate lateral circulation in basin scale simulations (Ulloa et al., 2020). Proper ice-free simulations on the basin scale are especially problematic because the turbulent fluxes between the air-water interface are difficult to resolve (Karetnikov et al., 2017), without even considering the additional complication of accurate simulations of a free boundary surface.

In Ref. Ulloa et al. (2019) and Ref. Ramón et al. (2021), 2D and 3D simulations showed that differential heating in the shallow regions of an ice-covered lake increased the deepening and heating rate of the CML. Ref. Ulloa et al. (2019) and Ref. Ramón et al. (2021) assume a system with $\approx 25\%$ of the domain with a maximum depth smaller than the photic depth. There are many ice-covered lakes where the shallow regions occupy a much smaller fraction of the lake and, hence, differential heating in shallow regions is expected to be less important and other mechanisms are needed to explain lateral motion under the ice (Ellis et al., 1991; Stefanovic and Stefan, 2002; Salonen et al., 2014; Bouffard et al., 2016; Cortés and MacIntyre, 2020).

Non-uniform intensity of solar radiation can also lead to horizontal buoyancy gradients that will generate lateral motion (Forrest et al., 2008; Leppäranta, 2014; Zhdanov et al., 2017). Ref. Forrest et al. (2008) attributes lateral temperature variations and circulation to lateral variations in optical properties and ice depth in a lake in British Columbia. Ref. Austin (2019) shows that heat content on lake superior is connected to the ice-coverage, suggesting that large lakes may also have potential to be impacted by non-uniform solar radiation. Other research that attempts to quantify lateral variations is rare. The need to explore non-uniform solar radiation intensity as a mechanism for lateral motion is mentioned briefly in a review on lake convection (Bouffard and Wüest, 2019). It is also mentioned in a paper on differential heating the near shore as an alternative mechanism for horizontal transport to bathymetry variations, which is the focus of Ref. Ramón et al. (2021). Existing research using high-resolution, non-hydrostatic simulations of ice-covered lakes does not consider the effect of horizontal variations in solar radiation (Ulloa et al.,

2019, 2020; Ramón et al., 2021), leaving a clear research gap to be explored in this thesis.

4.1.2 Gravity Currents

Gravity currents are a classical area of environmental fluid dynamics and a classic simple experiment and demonstration can be found in Ref. Simpson (1999). The set up in a laboratory is rather simple. Start with a tank of water with a solid barrier placed near one end, with dense fluid (e.g. salty) on one side and light fluid (e.g. fresh) on the other. Removing the barrier introduces a horizontal pressure gradient at the interface of these two regions. This is caused by the buoyancy difference between the two fluids, each exerting a different amount of pressure on the boundary. This is rectified by the dense fluid slipping underneath the light fluid that generates a current which propagates along the boundary of the tank.

This kind of gravity current involves two fluids of different – but uniform – densities. The early history of the study of gravity currents is nicely summarized in (Huppert and Simpson, 1980; Simpson, 1999). There is also a significant amount of research on the subject of gravity currents propagating into a stratified ambient (Simpson, 1999; Maxworthy et al., 2002; Ungarish and Huppert, 2002; Ungarish, 2006). In some cases, the density of the intruding fluid was such that - for bottom propagating currents - its density exceeded the density of the fluid at the bottom of the stratification and vice versa for gravity currents that propagate along the top boundary. In other cases, the intruding fluid was at an intermediate density and as a result propagated in the interior of the stratification, away from the boundary. A further complication is to introduce a turbulent ambient, which alters the development of a gravity current (Simpson, 1999). In Ref. Linden and Simpson (1986), it was shown that the turbulent ambient quickly mixes the current with the ambient, rapidly increasing the height of the intruding fluid as it propagates.

The dynamics to be presented in this chapter will consistent of gravity-current-like motion - which will be referred to throughout as an intrusion[1] - with a time varying stratified ambient that is unstably stratified (like the simulations presented in Chapter 3) leading to radiatively driven convection. The gravity current research cited above with a stratified ambient uses stable stratifications and none of the stratifications are time varying. The results in this chapter represent the first deep analysis on this type of motion using 2D simulations.

[1]Part of the reason the word 'intrusion' will be used in lieu of 'gravity current' is to be consistent with the paper that this chapter is based on, Ref. Allum et al. (2022). The other part is that we are concerned with the way that the intruding fluid 'intrudes' into the ambient that will develop similarly as the 2D simulations in 3.4.

4.1.3 Chapter Overview

The following chapter is structured as follows. The methods section in Section 4.2 describes the simulations to be presented, any important quantities used in the analysis, as well as the non-dimensionalization scheme for this system. Section 4.3 presents a comparison between a representative base case and a 2D unshadowed system. In Section 4.5, key parameters are varied and the resulting change is present. The effect of noise is briefly discussed in Section 4.6. The results are bookended by a short discussion section on measurements of the varied parameters in ice-covered lakes is given in Section 4.7.

4.2 Methods

In Chapter 2, 2.1.3, the equations of motion which are solved by SPINS are outlined that will be used in this chapter. The form of $F(x, z)$, which appears in the temperature equation in 2.17, is given in Section 4.2.1 below.

In Section 4.2.2, we present the equation of motion and initial conditions for two passive tracers that will be used for the unshadowed and shadowed cases to quantify horizontal transport due to the shadowed region.

This chapter's primary focus is on lateral circulation but it would be useful to also quantify how a shadowed region modulates motion of any kind. In Section 4.2.3, three bulk quantities are presented which will aid in further quantifying the differences between the shadowed and unshadowed cases.

4.2.1 System of interest

The system of interest is a subset of the interior of a shallow lake, sufficiently far from any sloping boundaries with complete ice-coverage that blocks any mechanical wind forcing at the surface. Initially, the entire domain is set to a constant temperature, T_0. The Coriolis force is neglected due to the relatively short time scale of $\mathcal{O}(10^3$ s) and length scales of $\mathcal{O}(1 - 10$ m) that are relevant to these simulations. A schematic of the system of interest is given in Figure 4.1.

We use a rectangular domain in the xz-plane with periodic boundary conditions in the horizontal and free-slip boundary conditions in the vertical. Other simulations of ice-covered lakes typically fix the temperature to 0 °C at the surface so that heat is lost via a diffusive boundary layer to the ice (Ulloa et al., 2019; Ramón et al., 2021). We do not

Parameter	**Description**	**Value**
L_x	Lake Width	16.384 m
L_z	Lake Depth	4.096 m
N_x	Horizontal Grid Points	8192
N_z	Vertical Grid Points	2048
x_s	Shadow Centre	$L_x/2$ m
ρ_0	Reference Density	1000 kg m^{-3}
ν	Kinematic Viscosity	10^{-6} m^2s^{-1}
κ	Temperature Diffusivity	1.43×10^{-7} m^2s^{-1}
κ_C	Tracer Diffusivity	1×10^{-6} m^2s^{-1}
Q_0	Magnitude of Solar Forcing	7.17×10^{-5} °Cms^{-1}
w_d	Shadow half-width	1 m

Table 4.1: System parameters used in this chapter that are unchanged between simulations. For parameters that are varied see Table 4.2. Units are given where appropriate.

Case Name	T_0 (°C)	A_l	λ (m)	α (10^{-5} °C^{-1})
T02	2.5	0.9	0.4	2.2
T0B	2.5	0	0.4	2.2
Al6	2.5	0.6	0.4	2.2
Al3	2.5	0.3	0.4	2.2
T01	1.5	0.9	0.4	3.6
T03	3.5	0.9	0.4	0.8
La2	2.5	0.9	0.2	2.2
La8	2.5	0.9	0.8	2.2

Table 4.2: Table of cases. For unchanged parameters between cases see Table 4.1. When referring to one of these cases in the text the case name in this table will be used. All values are exact except α which is rounded to one decimal place.

include this boundary condition in the present study as our focus is on the dynamics further below. However, it is an avenue for future work and is discussed in more detail in Section 6.2. The domain width, L_x, and height, L_z, are given in Table 4.1. There are many different lakes where the study of lateral motion has been conducted (Ellis et al., 1991; Stefanovic and Stefan, 2002; Colman and Armstrong, 1983). As such, the simulations presented within are not meant to represent a specific lake. Initially at constant temperature, this system is subjected to constant time solar forcing with spatial variations determined by

$$F(x,z) = \exp\Big(-\frac{L_z - z}{\lambda}\Big)\left[1 - A_l \exp\Big(-\frac{(x-x_s)^{8w_d}}{w_d^{8wd}}\Big)\right]. \tag{4.1}$$

The first z dependent factor is the shape of the Beer-Lambert law (Eq. 1.5) and determines the vertical distribution of heat added to the system (Leppäranta, 2014). The second term determines horizontal distribution of heat. This particular form creates a region with incoming radiation damped by a factor of Al centred at position x_s with width $2w_d$ as in Figure 4.1. The sharpness of the boundary is determined by the exponent $8w_d$. The sharpness of the boundary is an important system parameter because the spectral nature of the model requires $5-10$ grid points across the interface to fully resolve the shadow boundary. In practice, the high resolution of the simulations performed ensures this with no significant restriction on the results. The magnitude of Eq. 4.1 is Q_0/λ (see 2.17). Q_0 is given in Table 4.1 and is the same as the one used in Chapter 3 and 5. This value of Q_0 corresponds to solar radiation intensity of 300 W/m^2[2] and is on the same order of magnitude as certain measurements of downwelling solar radiation above ice-covered lakes (Bouffard et al., 2016, 2019). For simplicity, we neglect any effects of angled solar radiation as is typical at high latitudes in the winter. Including the effects of angled solar radiation - and therefore an angled shadowed region - will be considered in future work. The value of $\lambda = 0.4$ m was selected to match the value chosen in (Ulloa et al., 2019), which is a recent study on convection under ice-covered lakes in 2D and is a motivator for launching the study presented in this chapter.

For the remainder of this thesis, we will refer to the region with reduced solar radiation as the shadowed region and anywhere else as the unshadowed regions. The system parameters which are unchanged throughout this chapter are listed in Table 4.1. In Section 4.3, three system parameters are varied to probe the effect these parameters have on the resulting motion. All cases used in this chapter are presented in Table 4.2. The parameters we vary are (1) T_0, the initial temperature, (2) Al, the albedo under the shadow, and (3) λ, the attenuation coefficient that determines the vertical structure of Eq. 4.1.

[2]The value used in SPINS is precisely $\frac{300}{\rho_0 c_p}$, so although Q_0 is really a one-significant figure estimate, the value for c_p used has four significant figures at 4,184 J/(kg °C).

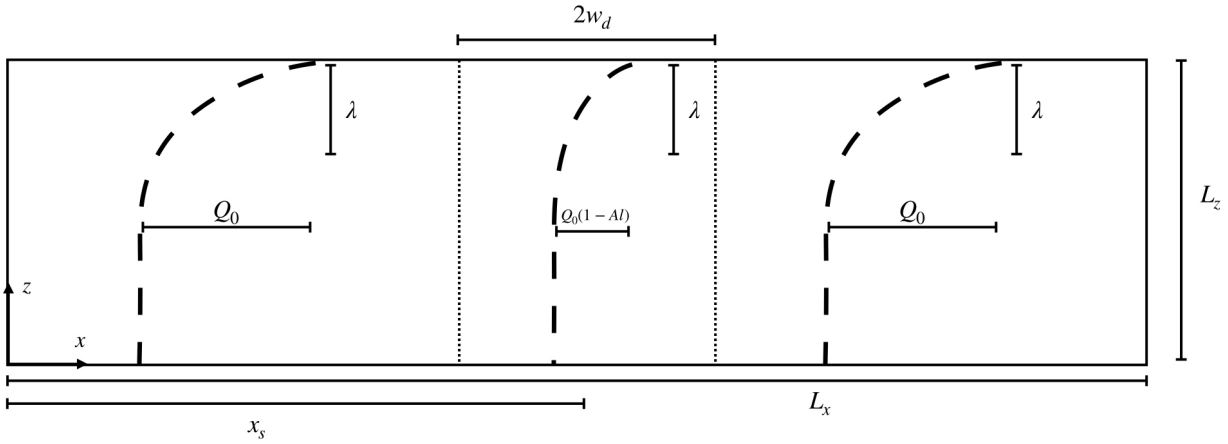

Figure 4.1: Schematic of the system used for the simulations in this chapter. The region between the vertical dotted lines, centred at x_s with width $2w_d$ is the shadowed region. The regions to the left and right of these dotted lines are referred to as the unshadowed regions. The dashed lines in each region denote the vertical shape of the solar forcing term in 2.17 in each region. λ is fixed between regions but the magnitude of the forcing at the surface is reduced by a factor of $(1-Al)$ in the shadowed region. z boundary conditions are free slip and the x boundary conditions are periodic. See Table 4.1 and 4.2 for parameter definitions.

There are two main features of interest that interact with the developing motion: (1) The horizontal density difference at the shadow boundary (determined by Al and the equations in Section 2.1) and (2) the vertical density gradient in the unshadowed region (determined by λ and Q_0). The vertical density gradient is immediately unstable because the initial temperature, T_0, of the domain is below T_{MD}. The magnitude of the vertical gradient will grow until the fluid begins to overturn via RT instabilities. However, the horizontal density difference will generate motion from the outset of the simulations (the amplitude of the motion will be small for early times). Like the vertical density difference, the horizontal density differences will grow over time due to the consistent solar forcing.

4.2.2 Tracers

A passive tracer, C, obeys the following equation of motion

$$\frac{DC}{Dt} = \kappa_C \nabla^2 C$$

where the left-hand side says that the passive tracer follows the fluid flow and the right-hand side represents the effects of diffusion. The tracer represents a dye used in lab experiments to visualize the fluid motion. The tracer diffusivity, κ_C was chosen to match the kinematic viscosity, ν. The effects of diffusion are minimal inside the intrusion and do not play a large role in its development, therefore, it can be thought of as loosely representing any particulates, dissolved matter or organisms which may be suspended in the water column. C has no effect on the fluid density (hence the label 'passive') and has no source or sink terms. In the context of this process study, the main purpose is to visualize the developing flow due to the shadowing. The units of C are chosen to be a concentration, where a value of 1 indicates maximum saturation and a value of 0 to indicate that no tracer is present. At $t = 0$, two passive tracers are initialized which do not interact with each other, nor the

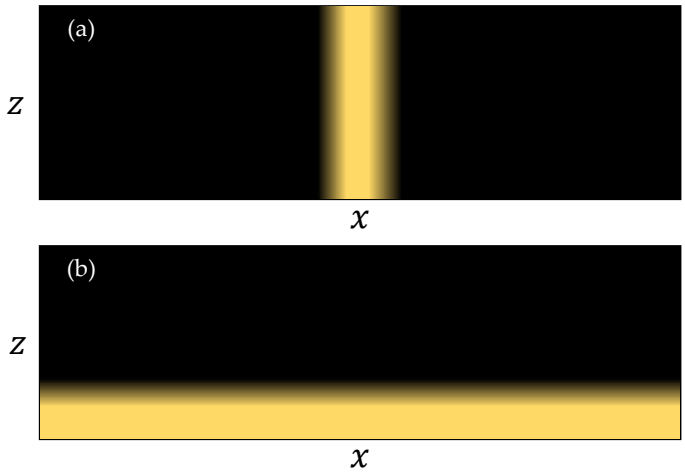

Figure 4.2: Initial conditions of the two passive tracers are presented here. (a) Tracer C_H initialized as a column at the centre of the domain with a maximum concentration of 1 at the centre. (b) Tracer C_V initialized in a region 1 m in height at the bottom of the domain with a concentration of 1 at the bottom.

fluid density. The first tracer - denoted as C_H - is arranged in a column at the centre of the domain (Figure 4.2(a)) with an initial width of $w_d = 2$ m, coinciding with the shadowed region. The column is assigned a concentration of 1, with sharp transitions on both sides to zero for the rest of the domain. We analyze this tracer using the vertical mean as a function of time. The purpose of $\langle C_H \rangle_z$ is to quantify the horizontal transport away from the centre.

The second tracer - denoted as C_V - is initialized in a region of width 1 m at the

bottom of the domain with a sharp transition from 1 to 0 at the top side (Figure 4.2(b)). This tracer is meant to quantify the vertical transport, and as such the evolution of the horizontal mean of C_V is of use. The purpose of $\langle C_V \rangle_x$ is to quantify the vertical transport up from the bottom.

4.2.3 Bulk motion

One approach to quantifying the bulk motion is to calculate the average kinetic energy per unit mass (KE_{avg}), which is an important quantity in the energy balance in ice-covered lakes (Winters et al., 2019). Define KE_{avg} as

$$\mathrm{KE}_{avg} = \frac{1}{2V} \int_V |\vec{u}|^2 dV. \tag{4.2}$$

KE_{avg} changes in time according to (Kundu and Cohen, 1990; Winters et al., 2019)

$$\frac{d\mathrm{KE}_{avg}}{dt} = -\frac{g}{\rho_0 V} \int_V \rho w dV - \frac{1}{\rho_0 V} \int_V \phi dV.$$

The first term on the right-hand side is the average vertical buoyancy flux per unit mass, which we will denote as Φ_{avg}. The negative sign reflects a decrease in KE_{tot} when there is a net upwards buoyancy flux. The second term is the average viscous dissipation (see Eq. 2.19) per unit mass, which we will denote as ϕ_{avg}. The negative sign reflecting that viscous dissipation always converts mechanical energy into heat.

KE_{avg} gives information about motion in the system but provides no point-wise information about the motion. We can isolate the horizontal and vertical components of the velocity vector by partitioning KE_{avg} into KE_{avg_x} and KE_{avg_z}. We can enhance this partitioning further by calculating the fraction of horizontal KE and the fraction of vertical KE, written as

$$\frac{\mathrm{KE}_{avg_i}}{\mathrm{KE}_{avg} + \delta} \tag{4.3}$$

where i is x or z. δ is a small parameter to avoid dividing by zero in the initial condition where KE_{avg} is zero. An alternative to Eq. 4.3 is the ratio between the horizontal and vertical root-mean-squared velocities, called the Flow Geometry metric presented in Ref. Ulloa et al. (2022). While these related quantities are algebraically different, we found that they were sufficiently similar for purposes of our analysis.

4.2.4 Density differences at the shadow boundary

It is the horizontal density differences across the shadow boundary which dictate the emergence of lateral circulation in the system discussed in this chapter and Chapter 5. The initial thickness of the shadow boundary is less important. The temperature changes due to the heating described by Eq. 4.1 are sufficiently small that we can use a linear equation of state in order to estimate an expression for the density difference across the shadow boundary

$$\rho(T) = \rho_0(1 + \alpha(T - T_0)). \tag{4.4}$$

We can then write the background temperature difference between the region under the shadow and the region away from the shadow. Here α is the thermal expansion coefficient that is a function of T_0 only. T_0 is chosen to match the initial temperature in each of cases described in Table 4.2. α is calculated as $\frac{1}{\rho_0}\frac{d\rho(T)}{dT}\big|_{T=T_0}$ for each case, using the same equation of state used in the simulations (Brydon et al., 1999). An approximate expression for α, which is quadratic in temperature, can be found in Ref. Bouffard and Wüest (2019). At early times, advection and diffusion terms in Eq. 2.17 are small compared to the forcing term. The temperature field is thus determined by the forcing alone and reads

$$T_b = \frac{Q_0}{\lambda}F(x, z)t + T_0. \tag{4.5}$$

Using Eq. 4.4 and T_b, we can calculate the density difference between the density at the shadow centre, x_s, and the density far from the shadow

$$\Delta\rho = \frac{\alpha\rho_0 Q_0 AlF(z)}{\lambda}t, \tag{4.6}$$

where $F(z)$ is equal to the z-dependent part of $F(x, z)$ (Eq. 4.1) alone.

T_0, Al and λ are varied in this chapter (Section 4.5) because they represent three different ways to alter the development of the lateral motion of interest. By varying T_0, we change the local slope of the equation of state. Changing the local slope, changes the development rate of RT instabilities and $\Delta\rho$ at the shadow boundary (Eq. 4.6). By varying Al, the temperature difference across the shadow boundary is modulated, but the instabilities away from the shadow will develop at the same rate. By varying λ, this changes the vertical distribution of temperature, $F(z)$, and the density difference across the shadow boundary. Unlike T_0 and Al, $\Delta\rho$ is inversely proportional to $1/\lambda$. The early time changes associated with horizontal density differences are captured by Eq. 4.6.

This quantity is used in Section 4.3 as a metric for understanding the development of motion as a result of the shadow. The time independent coefficient of $\Delta\rho$ is plotted as a function of z for each of the cases in Figure 4.3 (see Table 4.2 for list of cases). This shows how each of the relevant parameters change the vertical distribution of temperature across the shadow boundary. The coefficient of $\Delta\rho$ is linear in $\alpha(T_0)$ and Al, hence the difference of $\Delta\rho$ in each case is just a shift in log-10 space for changes to T_0 and Al. For La2 and La8, $\Delta\rho$ is inversely proportional to λ and so is the exponent of $F(z)$. As a result, the vertical structure and the magnitude at the surface are both modulated by changing λ.

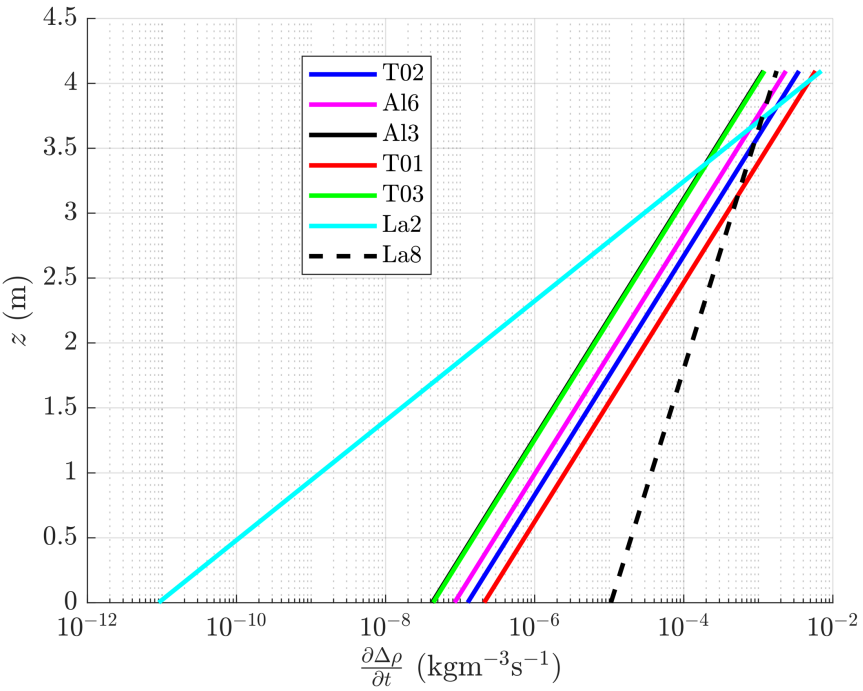

Figure 4.3: The coefficient of $\Delta\rho$ (Eq. 4.6) for each shadowed case (see Table 4.2 for full list). This coefficient is the rate of change of the density difference across the shadow boundary due to the background temperature alone.

4.2.5 Non-dimensional parameters

Using the parameters listed in Table 4.1 and 4.2 we use dimensional analysis (following (Grace et al., 2022), ignoring the shear flow aspects) to define a convective velocity scale

U and temperature scale θ as

$$U = (g\alpha Q_0 \lambda)^{1/3}, \tag{4.7a}$$

$$\theta = \left(\frac{Q_0^2}{g\alpha\lambda}\right)^{1/3}, \tag{4.7b}$$

using the linear equation of state, Eq. 4.4, unlike Ref. Grace et al. (2022) which uses a quadratic fit. U is the velocity scale set by the density differences within the flow. We scale the temperature as $T = \theta\tilde{T} + T_0$, and θ is the scale of the temperature away from the initial temperature. In other works, T is nondimensionalized as $T = \theta\tilde{T} + \bar{T}$, where $\bar{T}$ is the domain averaged temperature (Bouillaut et al., 2019; Grace et al., 2022). The maximum temperature differences observed in each of the cases considered are $\mathcal{O}(0.1\ ^\circ\mathrm{C})$ and therefore T_0 is a sufficient proxy for $\bar{T}$ for our purposes. Using these scalings, assuming an advective time scale of λ/U, we can nondimensionalize the system and define the following set of dimensionless parameters:

$$\mathrm{Gr} = \left(\frac{U\lambda}{\nu}\right)^2,\ \mathrm{Pr} = \frac{\nu}{\kappa},\ Al,\ \mu_1 = \frac{\lambda}{L_z},\ \mu_2 = \frac{w_d}{\lambda},\ \mu_3 = \frac{\lambda}{L_x} \tag{4.8}$$

Gr is the Grashof Number which is the relative strength of buoyancy and viscosity terms in the governing equations. Using Eq. 4.7a it can be written as

$$\mathrm{Gr} = \frac{(g\alpha Q_0)^{2/3}\,\lambda^{8/3}}{\nu^2}. \tag{4.9}$$

For the cases discussed in this thesis Gr is $\mathcal{O}(10^5)$-$\mathcal{O}(10^6)$. Variation of Gr is achieved through variations of α which depends on the initial temperature, T_0, in cases T01 and T03, and the attenuation length, λ, in cases La2 and La8.

Pr is the Prandtl number and defines the ratio of the momentum diffusivity to the temperature diffusivity. It is held constant at a value of 7 for all the cases considered in this study. This is a representative value for temperatures below T_{MD} and is used in studies of similar 2D non-hydrostatic simulations (Ulloa et al., 2019; Ramón et al., 2021). A Prandtl number of 10 has also been used in similar contexts (Grace et al., 2022, 2021).

Al is the albedo and is nondimensional by definition. The remaining three parameters are the relevant nondimensional length scales for this problem. μ_1 is the nondimensional attenuation length. μ_1 has been studied in similar contexts to those studied here which

showed experimentally that the magnitude of μ_1 determined the power-law relationship between the dimensionless vertical heat flux, the Nusselt number, and the Rayleigh number (Bouillaut et al., 2019). μ_2 is the ratio of the shadow width to the attenuation length and is the main aspect ratio of this system. μ_3 is the ratio of the domain width to the attenuation length. The attenuation length sets the horizontal scale of RT instabilities which are observed in this study. If μ_3 is too large then full RT instabilities are unable to form, disrupting the primary dynamics explored in our simulations. In the cases considered in this study $\mu_3 < 0.05$.

Analytical models exist which predict some aspects of the evolution of horizontal flow due to lateral buoyancy differences (Ulloa et al., 2019, 2022). Ref. Ulloa et al. (2022) studies lateral motion which emerges due to surface cooling and non-uniform bathymetry. The authors present a model which predicts three regimes (see Figure 2 in Ref. Ulloa et al. (2022)), the time scales of the transitions between regimes, and the velocity scales of the horizontal motion in each regime. Determining analytical expressions for the horizontal velocity and time scales in a similar fashion to Ref. Ulloa et al. (2022) is an avenue for future work but is not the focus of the present study.

Two other options to define a velocity scale are a buoyancy velocity $u_b = \sqrt{g'\lambda}$ and a convective velocity $w^* = (B_* h_{CML})^{1/3}$ (Deardorff et al., 1970; Bouffard and Wüest, 2019). This form of u_b was used in a numerical study of radially spreading gravity currents as the horizontal velocity scale in a rotating and non-rotating tank (Dai and Wu, 2016) and is also the form of the shallow water wave speed (Kundu and Cohen, 1990). $g' = g\frac{\rho_1 - \rho_0}{\rho_0}$ is the reduced gravity between two fluid layers, where ρ_1 is the denser fluid and ρ_0 is the less dense fluid. In our study, g' cannot be defined in terms of the initial conditions because the density is uniform everywhere. Instead we consider a representative temperature change of 0.3 °C and use it to estimate u_b for the three initial temperatures considered in this chapter (See Table 4.2). With this assumption we find that $u_b \approx 1 - 10$ mm s^{-1}, minimized for $T_0 = 3.5$ °C and $\lambda = 0.2$ m, and maximized for $T_0 = 1.5$ °C and $\lambda = 0.8$ m.

The typical vertical velocity scale within the CML is denoted by w^*, where h_{CML} is the depth of the CML (Bouffard and Wüest, 2019; Bouffard et al., 2016; Yang et al., 2021). w^* has also been linked to plankton settling rates using scaling arguments (Kelley, 1997). The simulations considered here do not have initial stratification, the primary balance against the deepening of the CML (Kirillin et al., 2012; Ulloa et al., 2019). In addition, we do not consider sufficiently long time scales to allow a CML to form as in (Ulloa et al., 2019; Ramón et al., 2021). As such w^* is not directly applicable to our set up. Nonetheless, it is an important velocity scaling in the study of convection forced by solar radiation. Following the calculation of B_*, the effective buoyancy flux, in Ref. Bouffard and Wüest (2019) we arrive at

$$w^* = \left(\alpha g Q_0 \left(\lambda e^{-h/\lambda} + h - \lambda\right)\right)^{1/3}.$$

There is no obvious choice for h_{CML} because there is no CML in our simulations. However, taking λ as h_{CML} we find

$$w^* = e^{-1/3} U \approx 0.72U,$$

where U is the velocity scale in Eq. 4.7a. The velocity scales in a CML whose depth is comparable to the attenuation length is similar in magnitude to U. In Ref. Ulloa et al. (2019), the smallest CML depth shown was ≈ 2 m and later expanded to ≈ 10 m. In the limit of $h \gg \lambda$, a more realistic relationship, we find

$$w^* = (\alpha g Q_0 h)^{1/3} = \left(\frac{h}{\lambda}\right)^{1/3} U.$$

4.3 Results preamble

We find that a shadowed region inevitably (as depicted in Figure 4.1) generates systematic lateral motion. This motion takes the form of a pair of lateral intrusions which flow outward away from the shadow near the surface and a return flow underneath. The return flow is strongest immediately below the intrusions and rapidly decays towards the bottom. The shadowed region also leads to earlier and enhanced vertical transport, compared to Rayleigh-Taylor (RT) instabilities alone. After describing an illustrative base case in Section 4.4, in Section 4.5 T_0, Al and λ are systemically varied, and in doing so we identify a qualitative relationship between the front position of the intrusion and each of these parameters. In all of these cases, noise is added to the initial temperature field in order to facilitate the growth of instabilities away from the shadowed region. In Section 4.6, noise is removed from and compared with the illustrative base case from Section 4.4 to quantify the effect of noise, and the resulting instabilities on the lateral motion.

To quantify the effect of the shadow, we employ case T02, or shadowed case with $T_0 = 2.5$ °C, $Al = 0.9$ and $\lambda = 0.4$ m. T02 is compared with T0B, the unshadowed case with $T_0 = 2.5$ °C, $Al = 0$ and $\lambda = 0.4$ m (see Table 4.2). The set of parameters chosen for T02 and T0B represent specific regions of their respective parameter space. In particular, $T_0 = 2.5$ °C is near the mid-point between the freezing temperature and T_{MD}. $Al = 0.9$ is representative of high albedo and, therefore, the largest density difference across the

shadow boundary and high potential for lateral motion. $\lambda = 0.4$ m is chosen to represent a lake of moderate clarity as in Ref. Ulloa et al. (2019, 2020).

4.4 Main comparison: shadowed versus unshadowed dynamics

The development of the temperature fields in T02 and T0B are compared in the two columns of Figure 4.4, T0B in the left column and T02 in the right column. Given the local linearity of the equation of state, the temperature is an adequate proxy for density. In T0B (Figure 4.4(a,c,e,g)) motion is generated exclusively via the development of RT instabilities, nearly identical to the unstratified 2D case in Chapter 3 except for the size of the domain and resolution. As the system is continually heated, the RT instabilities grow in both the vertical and horizontal. There are no signs of lateral motion on scales greater than the horizontal length scales of the RT instabilities. As mentioned in Section 3.2.2, we refer to the region of space between the surface and the mean RT instability depth as the convective layer (CL). The spatial scales of the instabilities are set by the magnitude of the vertical density gradient away from the shadow. At early times, the temperature gradient closely resembles T_b, Eq. 4.5. The parameters which control this gradient are λ, α and κ. In Section 4.5, λ and α are varied, the latter through the variation of T_0. Ref. Grace et al. (2022) used linear theory to show that increasing λ decreased the growth rate of instabilities while increasing the dominant length scale. Increasing the T_0 decreases the magnitude of the vertical density gradient at fixed time and, therefore, decreases the growth rate of instabilities. However, the dominant length scale does not appreciably change with T_0.

The CL develops through two distinct phases: (1) a solar radiation dominated phase where the mean temperature only deviates from T_b (Eq. 4.5) by small amounts (Figure 4.4(a,c)) and (2) a convection dominated phase where RT instabilities transport temperature deeper into the water column and as a result, decreases the mean temperature near the surface, overcoming the constant heating (Figure 4.4(e,g)). These phases are shown to exist in Figure 4.5. Left of the dashed line is the solar radiation dominated phase, characterized by a monotonically decreasing mean temperature profile in Figure 4.5(a) and a deviation from the background temperature (Eq. 4.5) of near zero in Figure 4.5(b). Right of the dashed line is the convection dominated phase, characterized by a non-monotonic mean temperature profile driven by RT instabilities transporting heat deeper into the water column. Figure 4.5(b) shows the regions in which convection has cooled or heated the mean profile. The depth of the CL is defined in Figure 4.5(a) as the maximum depth of

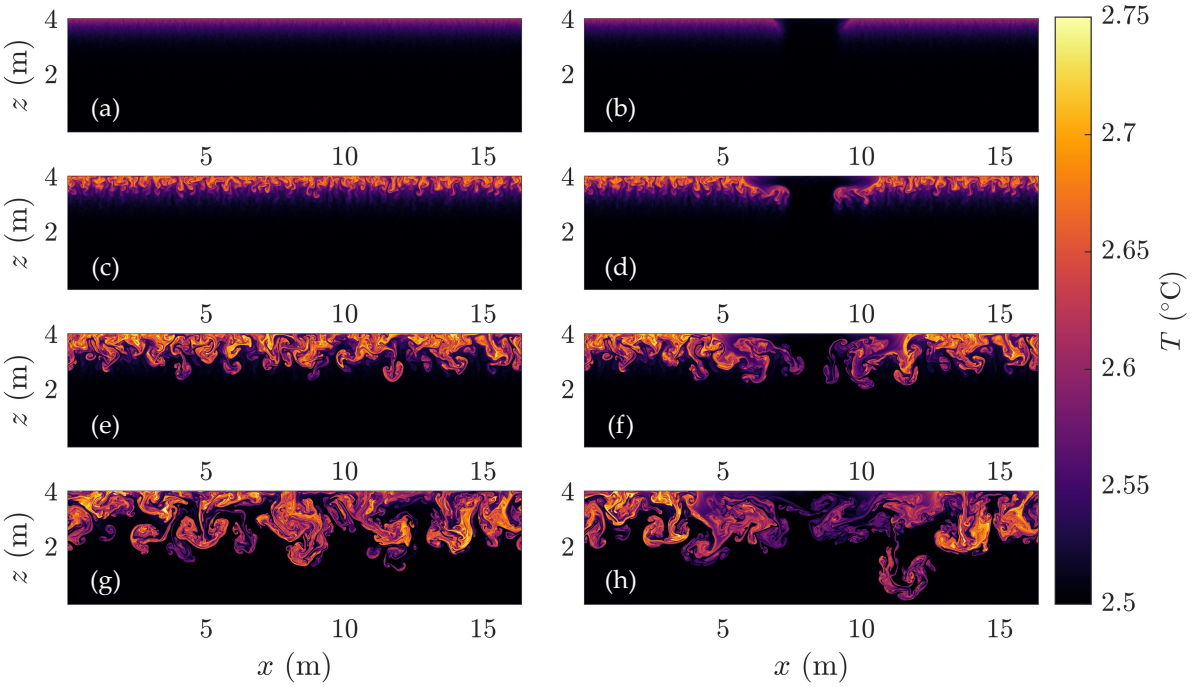

Figure 4.4: Snapshots of the temperature field for T0B (a,c,e,g) and T02 (b,d,f,h) at (a-b) 600s (c-d) 1200s (e-f) 1800s (g-h) 2400s. Both simulations use $T_0 = 2.5$ °C, $\lambda = 0.4$ m. T02 uses $w_d = 1$ m and $Al = 0.9$. T0B is entirely determined by the development of RT instabilities. T02 additionally has the shadowed region to generate systematic lateral motion.

fluid warmer than T_0 to the right of the dashed line. The CL is also visible in Figure 4.5(b) as the maximum depth of the region adjacent to the surface which is warmer than the background.

The shadowed region in T02, in contrast, creates systematic horizontal density gradients that are larger than those associated with individual RT instabilities in the CL (Figure 4.4(a,b)). As a result, lateral intrusions emerge, advecting RT instabilities near the shadow boundary, down and inwards (by Figure 4.4(d)) and upwards (by Figure 4.4(f,h)). The upwards motion of the return flow is evidence of an upwelling under the shadow from the intrusions that arises due to mass conservation as the intrusions propagate outward. The upwelling is found at the centre of the domain, under the shadow, and is discussed further in Section 4.4.1. As time progresses, the intrusions continue to flow outwards, disrupting

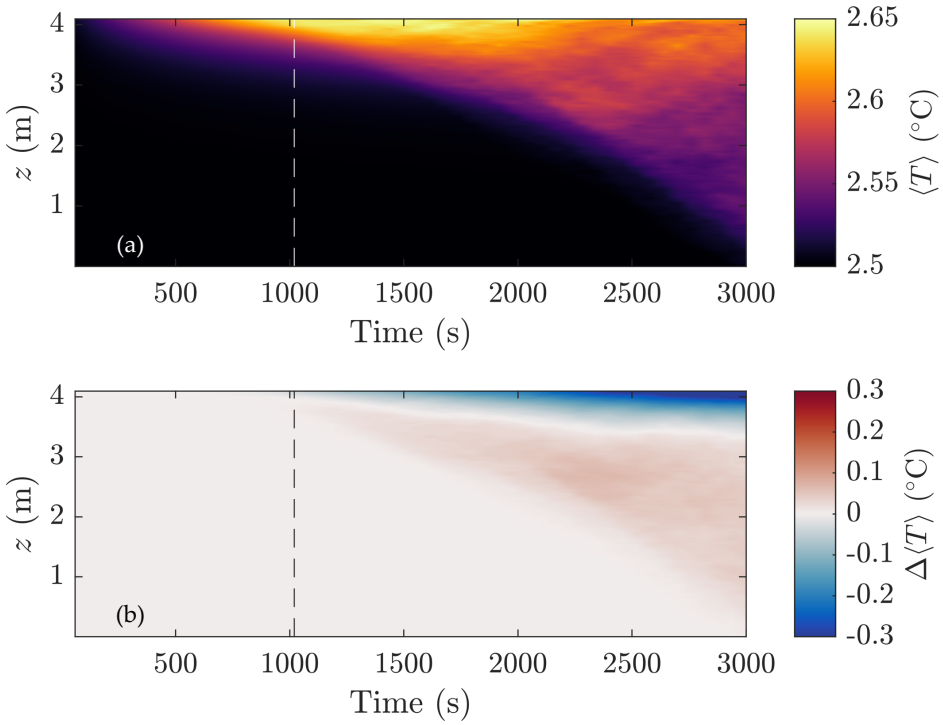

Figure 4.5: (a) Evolution of the horizontally averaged temperature field for T0B. Vertical dashed line is superimposed to indicate the approximate transition time between a solar radiation dominated phase and a convective dominated phase (defined in the text). (b) Deviation of the horizontally averaged temperature field from the background T_b (Eq. 4.5). The dashed black line retains the same meaning as in panel (a). Positive values indicate that the horizontally averaged temperature is warmer than just the background, negative values are colder than the background.

the CL near the surface. The return flow acts as a mechanism for distributing heat under the shadow but is insufficient to overcome the the damped heating in the shadowed region.

The intrusions themselves are similar to a classical gravity current. A tall current head with a narrow body propagating from a low density region to a higher density region (Figure 4.4(d)). However, there are some ways in which this diverges from classic gravity currents. The ambient is changing gradually with time and RT instabilities are transporting heat downwards and cool fluid upwards. After some time has passed, the intrusions are not always propagating into denser fluid, but instead propagating into an oscillating temperature field in space about the mean value shown in Figure 4.5(a). This oscillation is apparent in Figure 4.4(h) and somewhat in panel (f), where cool plumes reach the surface and, hence, the density difference at the front of the intrusions is oscillating in space, rather than constant. In Section 4.6, we identify that these changes at the front of the intrusion due to the growth of RT instabilities indeed have a small effect on the propagation speed of the intrusions.

4.4.1 Mean temperature flux

The development of the temperature field in Figure 4.4 demonstrates the effect of the shadowed region on the motion of the intrusions and the return flow immediately below the intrusion. The motion of the fluid under the shadow and closer to the bottom proceed due to the incompressibility assumption, however, due to the small temperature gradients at the bottom and under the shadow this motion doesn't manifest in the temperature field. Visualization of these features are quantified using the horizontally-averaged, horizontal temperature flux, $\langle uT \rangle_x$, and the vertically averaged, vertical temperature flux, $\langle wT \rangle_z$ (where these averages are defined in Eq. 2.23 and 2.24, respectively). $\langle uT \rangle_x$ is averaged over the left-half of the domain to avoid averaging out the motion of the intrusions.

In T0B, the unshadowed case, in Figure 4.6(a), mean horizontal fluxes develop in the CL (Figure 4.4(e,g)) and follow its descent to the bottom of the domain at later times. While there are nonzero mean fluxes in this system, there are no mechanisms for transport at depths below the CL or beyond the horizontal length scales of the RT instabilities, as shown in Figure 4.6(a). In addition, the mean fluxes at fixed depth are non-monotonic in time, suggesting a lack of systematic motion due to the random orientations of the convective plumes.

This is in contrast to the shadowed case, T02, where the fluxes near the shadow boundary dominate $\langle uT \rangle_x$ (Figure 4.6(b)). At all times, there is a large, increasing mean flux away from the centre ($\langle uT \rangle_x < 0$) at the surface, driven by the intrusion. Below this region

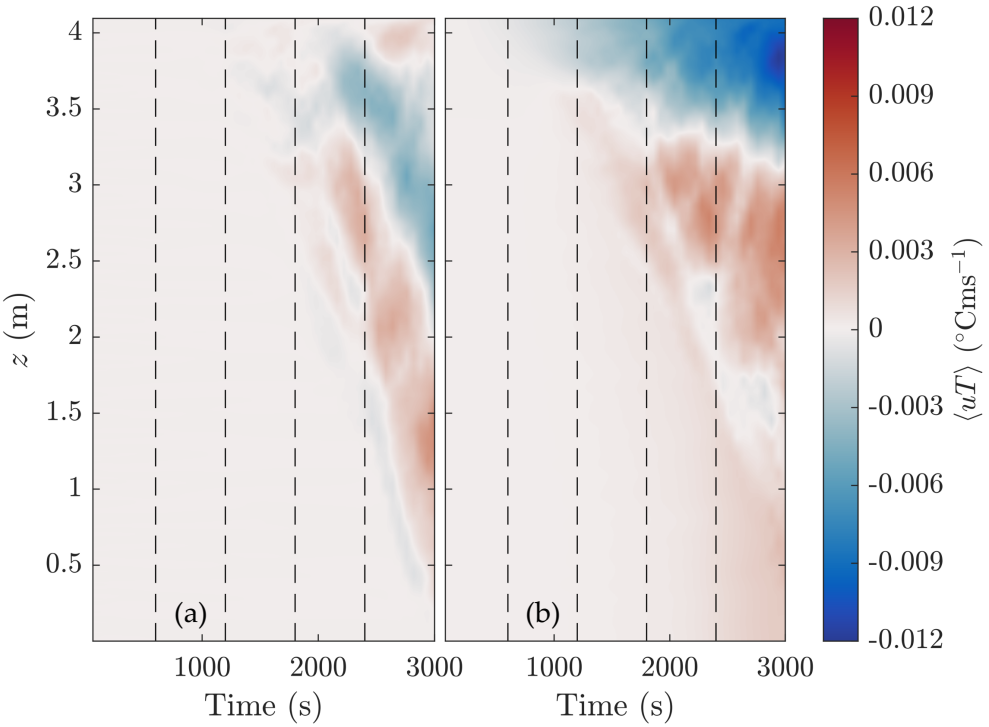

Figure 4.6: Horizontally averaged, horizontal temperature flux where $T_0 = 2.5$ °C for (a) T0B (unshadowed) and (b) T02 (shadowed). T02 in panel (b) is averaged over the left half of the horizontal domain to avoid cancellation of the lateral intrusion (See Figure 4.4(d,f) for signs of symmetry which would cancel in an average). Vertical dashed lines refer to the times corresponding to each row of Figure 4.4, in order of increasing value.

is a mean temperature flux towards the centre ($\langle uT \rangle_x > 0$) that extends to the bottom of the domain. After 2000 s the return flow dominates the mean at depths below the intrusions, even as the CL continues to develop. This is confirmed by comparing $\langle uT \rangle_x$ inside the CL for both Figure 4.6(a) and (b).

The fluxes near the bottom in the return flow are smaller in magnitude than those in the intrusions and the return flow immediately below the intrusion, but are systematic in a manner which does not appear in T0B (Figure 4.6(a)). The strength of these fluxes naturally will depend on the size of the domain, especially for shallow systems.

The depth of the boundary between motion toward and away from the centre in Figure 4.6(b) moves downwards in time, at a rate slower than the descent of the CL. This suggests

that the region effected by the intrusion also expands in the vertical in time. The ordered nature of $\langle uT \rangle_x$ in the shadowed case persists for the entirety of the time frame considered. Both the shadow and unshadowed case produce fluxes on the same order of magnitude, but in the shadowed case it is systematically stronger, more ordered, dominates more quickly, and effects the entire vertical domain before the descent of the CL.

The vertically averaged, vertical temperature flux in T0B (Figure 4.7(a)) evolves similarly to the CL. When the fluxes are small, appearing as thin streaks, as they are at early times in Figure 4.7(a) or in Figure 4.7(b) - away from the shadow - then the CL has yet to form and descend in the water column. When the fluxes are large - and irregular - at later times it is due to the presence of large convective cells that extend from the top to the bottom of the domain and interact with the top and bottom boundary at the later times.

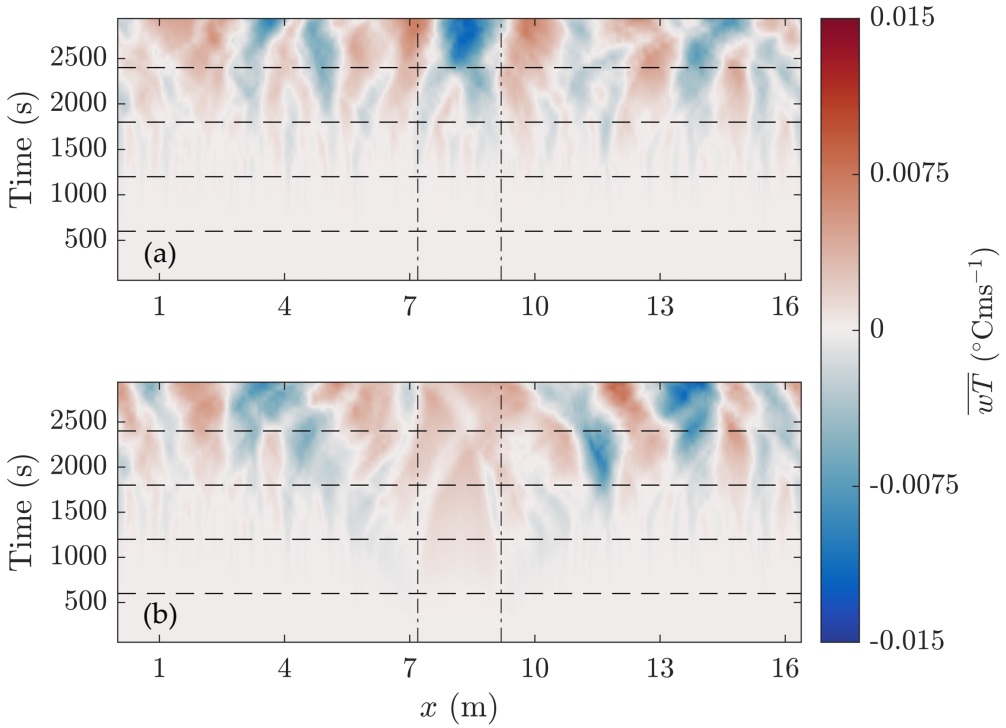

Figure 4.7: Vertically averaged, vertical temperature flux where $T_0 = 2.5$ °C for (a) T0B (unshadowed) and (b) T02 (shadowed). Vertical dot-dashed lines refer to the approximate edge of the shadow boundary. Horizontal dashed lines refer to the times corresponding to each row of Figure 4.4, in order of increasing value.

The shadow has the effect of introducing larger and more coherent vertical fluxes near and under the shadow at early times as seen at the bottom-half of Figure 4.7(b). The early enhanced fluxes near the shadow boundary are small compared to the fluxes at late times, but are relatively large compared to the fluxes away from the shadow at the same time. There is also a persistent effect of upwelling at late times on a larger scale than the RT instabilities at those times near the shadowed region. At early times, the region under the shadow shows a smooth, mean upward flux, free of any irregular features. This net vertical motion under the shadow is responsible for the motion towards the surface of the return flow immediately beneath the intrusion in Figure 4.4(d,f). On the boundary of the shadowed region is a mean downwelling of warmer fluid, showing signs of the RT instabilities which are pushed downwards in response to the horizontal expansion of the intrusions.

In the unshadowed case at later times, the patches of positive and negative fluxes in Figure 4.7(a) reveal the approximate horizontal length scales of the plumes at this stage. These are the opposing fluxes driven by the cool and warm plumes which propagate past each other, visible in Figure 4.4(e,g). Contrasting this to Figure 4.7(b), the region near the shadow is dominated by patches of positive (upward) fluxes, indicating that as the intrusion propagates outwards, the region of upwelling - initially confined to the shadow boundary - expands as well. $\langle wT \rangle_z$ in the shadowed case shows that a shadow enables vertical transport at an earlier time than the unshadowed case, which is driven by RT instabilities alone. Both of Figure 4.6(b) and Figure 4.7(b) show the potential for significant transport due to the shadow over length scales exceeding the RT length scales, and over time scales faster than the RT development timescale.

4.4.2 Vertical and horizontal tracer transport

The quantification of vertical and horizontal tracer transport is carried out using the two independent, passive tracers $\langle C_H \rangle_z$ and $\langle C_V \rangle_x$, respectively, with initial conditions as discussed in Section 4.2.2 and averages defined in Eq. 2.24 and 2.23. In Section 4.4.1, the locations of significant horizontal (Figure 4.6(b)) or vertical (4.7(b)) transport of temperature is quantified. Using $\langle C_H \rangle_z$ and $\langle C_V \rangle_x$, the amount of tracer transported and the distance of maximum transport over time can be quantified. The development of tracer $\langle C_H \rangle_z$ for shadowed and unshadowed cases are shown in Figure 4.8(a,b). The development of tracer $\langle C_V \rangle_x$ for shadowed and unshadowed cases are shown in Figure 4.8(c,d).

Despite the existence of horizontal temperature fluxes with similar magnitude in the unshadowed case (Figure 4.6(a)) and shadowed case (Figure 4.6(b)), the tracer C_H is

transported further from the centre in the shadowed case, with transport beginning earlier in time. Even at later times, when the mean fluxes have comparable magnitudes, the transport in the unshadowed case is unremarkable.

In the unshadowed case, averaging in the vertical eliminates most lateral transport in the first 1500 s. Significant net horizontal transport is only achieved when upwelling cool plumes or downwelling warm plumes reach the bottom or top boundary. In the shadowed case, the density difference is largest at the upper boundary (see Figure 4.3) and is immediately converted into lateral motion. C_H is transported earlier, further away and the maximum transported distance at each time is constantly increasing. At the latest times shown, any remnants of the initial conditions are almost completely destroyed by the horizontal fluxes in the shadowed case (Figure 4.8(b)), while the initial structure remains in the unshadowed case (Figure 4.8(a)).

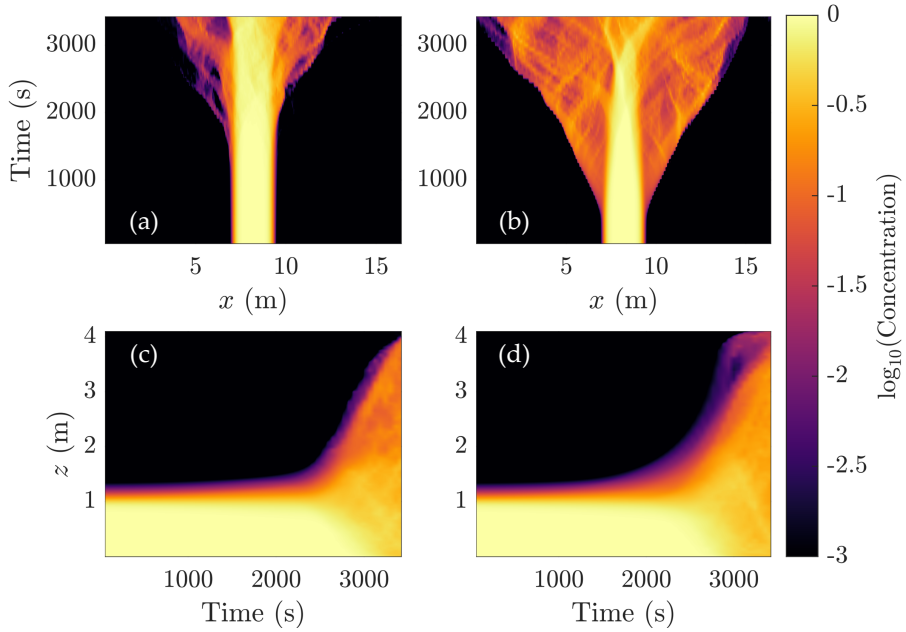

Figure 4.8: The horizontal and vertical mean of passive tracers highlighting enhanced transport due to the lateral motion generated by the shadowed region. Initial conditions given in Figure 4.2. (a-b) Tracer arranged in a column centred at the centre of the domain with width $2w_d$. Unshadowed case in panel (a) and shadowed case in panel (b). (c-d) Tracer aligned in a row at the bottom of the domain with a width of 1 m. Unshadowed case in panel (c) and shadowed case in panel (d).

The vertical transport from the bottom is not as significantly modified as the lateral transport (comparing Figure 4.8(c) to Figure 4.8(d)). However, there are some minor differences that can be identified: (1) The transition from smooth $\langle C_V \rangle_x$ to well mixed at later times happens sooner in the shadowed case but more gradually (2) $\langle C_V \rangle_x$ reaches the surface at an earlier time in the shadowed case.

4.4.3 Bulk motion

Figure 4.9 presents the average KE per unit mass for cases T01, T02 and T03 (See Table 4.2) and is nondimensionalized using the scalings presented in Section 4.2.5. The evolution of the average KE per unit mass (Figure 4.9(a)) on a logarithmic scale behaves as two linear regimes, with an initially shallow slope and a transition to a steeper slope at later times. The presence of the shadow does not effect the slope of either the pre- or post-transition curves. Instead, the shadowed cases transition earlier in time.

The time axes are labelled as tU/λ, where t is physical time (measured in seconds) and U/λ is the inverse of the advective time scale. The vertical axis in panel (a) is labelled as KE_{avg}/U^2 where $1/U^2$ is the inverse scaling of energy per unit mass. The vertical axes in panel (b) and (c) are nondimensional by definition. The key parameter in the comparison presented in Figure 4.9 is α, where $\lambda/U \propto \alpha^{-1/3}$ and $U^2 \propto \alpha^{2/3}$. This suggests that an increase to T_0 - which decreases α - increases the time scale and decreases the KE scale, with a stronger dependence on the KE scale. In Figure 4.9(a), the curves are initially separated by a vertical shift but collapse in both the shadowed and unshadowed cases after the transition, suggesting that a separate velocity scale is required for the early time evolution. In terms of dimensional variables, cases with different T_0 never collapse. This is also captured in the percentage difference between the shadowed and unshadowed KE shown in Figure 4.9(b). The horizontal offset in Figure 4.9(b) for $tU/\lambda < 5$ shows clearly that a different velocity scale exists during the growth of the lateral intrusions prior to the convection dominated phase.

The transition in the shadowed cases appears to begin at $tU/\lambda \approx 1$ where the KE_{avg} curves visibly diverge from their unshadowed counterparts with timing independent of T_0. The percent difference between KE_{avg} for the shadowed and unshadowed cases, for each T_0, reveals that this diverging behavior - or enhancement of KE_{avg} - in the shadowed case is growing from the onset of the simulation (Figure 4.9(b)). In physical time, the initial growth in the percentage difference collapses for all three cases suggesting that the growth rate in this phase is independent of T_0 (Figure 4.9(b)). The vertical offset is unchanged in terms of physical variables.

The transition in the unshadowed cases, however, is a function of T_0 and, therefore, α. The transition is the characteristic elbow of KE_{avg}, which is significantly sharper than in the shadowed cases (Figure 4.9(a)). It is also seen in the percentage difference between each pair of shadowed and unshadowed cases (Figure 4.9(b)), where the percent difference reaches its maximum for each T_0. In dimensionless time, as shown here, the transition time collapses to $tU/\lambda \approx 4$. In physical time, the transition time for the unshadowed cases is an increasing function of T_0, caused by the nonlinearity of the equation of state.

The rate of change of KE_{avg} is determined by the average buoyancy flux per unit mass, Φ_{avg}, and the average dissipation per unit mass, ϕ_{avg} (2.19). These quantities are presented in Figure 4.10 as dimensionless variables. ϕ_{avg} is comparable between shadowed and unshadowed cases (Figure 4.10(b)), in contrast to Φ_{avg} (Figure 4.10(a)), and so naturally the enhanced buoyancy flux dominates these results.

Comparing the times of the change in slope between Figure 4.9(a) and Figure 4.10(a) for each T_0 case, it is clear that the change in KE_{avg}, between the shadowed and unshadowed cases is driven entirely by the enhanced buoyancy flux generated by the shadowed region. Φ_{avg} is inevitably equalized at long times, resulting in a convergence of KE_{avg} between shadowed and unshadowed cases. As with Figure 4.9(a), the scalings from Section 4.2.5 are insufficient to correct the initial differences in Φ_{avg} at early times, but the curves collapse after the transition, further cementing that a different set of scalings is required for the early time behaviour.

While Φ_{avg} is a quantity calculated from the product of the vertical velocity and the density (Eq. 2.19), it is enabled in this system by the capacity to generate horizontal motion. This is captured in the ratio of the average KE per unit mass in the horizontal ($\mathrm{KE}_{avg_x} = 1/V \int_V u^2/2dV$) to the average KE per unit mass (Eq. 2.19). This ratio is given in Figure 4.9(c). The large increase in Φ_{avg} in Figure 4.10(a) in both the shadowed and unshadowed cases is correlated with an increase in the fraction of KE in the horizontal (Figure 4.9(c)). When the shadowed cases complete their transitions in KE_{avg}, $\mathrm{KE}_{avg_x}/\mathrm{KE}_{avg}$ is near 0.5. Similarly in the unshadowed cases, the transition is completed once KE_{avg_x} and KE_{avg_z} are comparable (Figure 4.9(c)). The unshadowed case catches up in terms of KE_{avg} and the buoyancy flux. This may occur because of the finite vertical domain but is not explored in this research.

4.5 Parameter variations

In the following sections, the parameters T_0, Al and λ are systematically varied to assess how they effect the lateral circulation and transport identified in Section 4.4. Justification

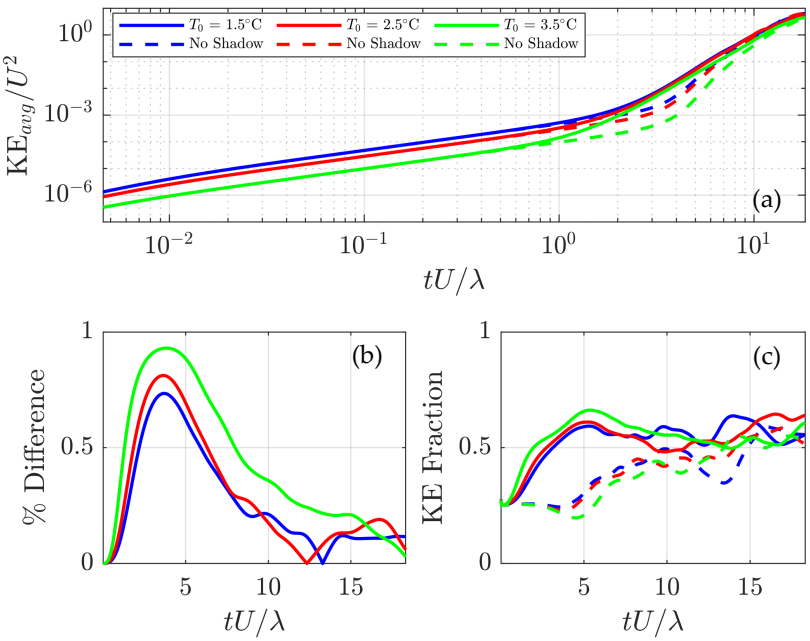

Figure 4.9: (a) Average kinetic energy per unit mass as a function of time for the three values of T_0 1.5, 2.5 and 3.5 °C. The average kinetic energy per unit mass is given for both the shadowed (Solid) and unshadowed (Dashed) case, for each T_0. Horizontal and vertical axes on logarithmic scales. (b) Percent difference between the shadowed and unshadowed KE_{avg}. (c) Fraction of horizontal KE (Eq. 4.3) in the shadowed (solid) and unshadowed (dashed) cases. All axes in each panel are dimensionless.

for varying these parameters is given in Section 4.2.4. Figure 4.11(a) shows the front position of the intrusion as a function of time associated with each simulation, to be discussed further for each parameter. The front position was identified using the propagation of the passive tracer C_H along the surface furthest from the shadowed region. Figure 4.11(b) gives the nondimensionalized front position, x/λ, as a function of the nondimensional time, tU/λ. In Figure 4.11(a), we see an initial acceleration phase followed by a period with nearly constant speed. Nondimensionalizing shows that apart from changes in albedo (cases Al3 and Al6) the speed of the intrusion collapses. Cases La2 and La8 are shifted vertically due to the change in λ.

In each section a common figure layout with 6 panels and two columns is used. Figure 4.12 for the T_0 variation, Figure 4.14 for the Al variation and Figure 4.16 for the λ variation.

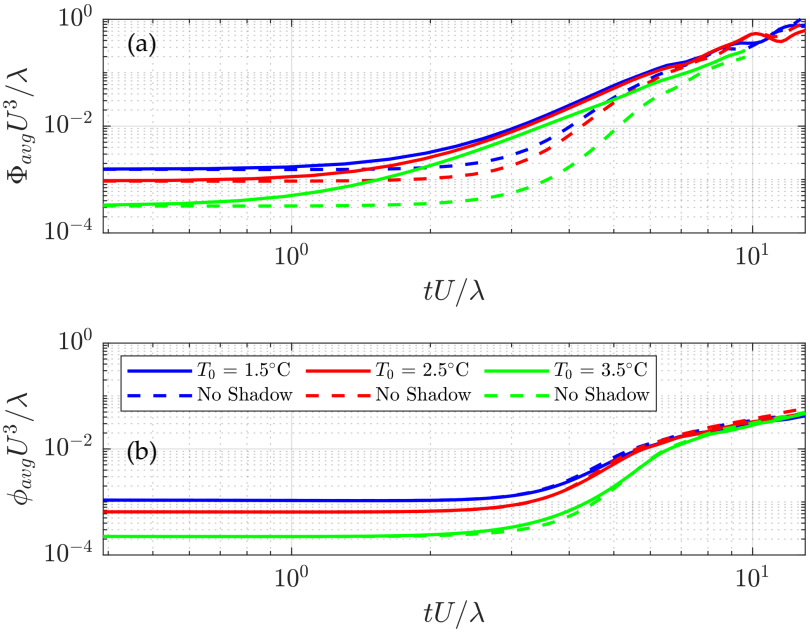

Figure 4.10: The rate of change of the average kinetic energy per unit mass with respect to time is a function of (a) the average buoyancy flux per unit mass, Φ_{avg} and (b) the average dissipation per unit mass, ϕ_{avg}. In both panels the quantity for both the shadowed and unshadowed equivalent are given. The legend in panel (b) also applies to panel (a). All axes in both panels are dimensionless.

The left column (subplot (a), (c) and (e)) is the mean temperature to a depth of λ below the surface. The right column (subplot (b), (d) and (f)) are snapshots of the temperature field at a time indicated by the horizontal, dashed line in the left column.

The left column has three important pieces of information encoded in it: (1) The large characteristic V-shape shows the horizontal extent (width) and speed (slope) of the intrusion as a function of time, (2) the solar radiation dominated phase is characterized by long, vertical streaks in the mean temperature field, and (3) the convection dominated phase, which immediately follows the solar radiation dominated phase, is characterized by branching of these streaks. The approximate transition time between the two phases is give by the solid white line. The purpose of the right column is to compare the progression of the intrusions in the full temperature field at fixed time.

There are two apparent phases to the front position: (1) The acceleration phase, where

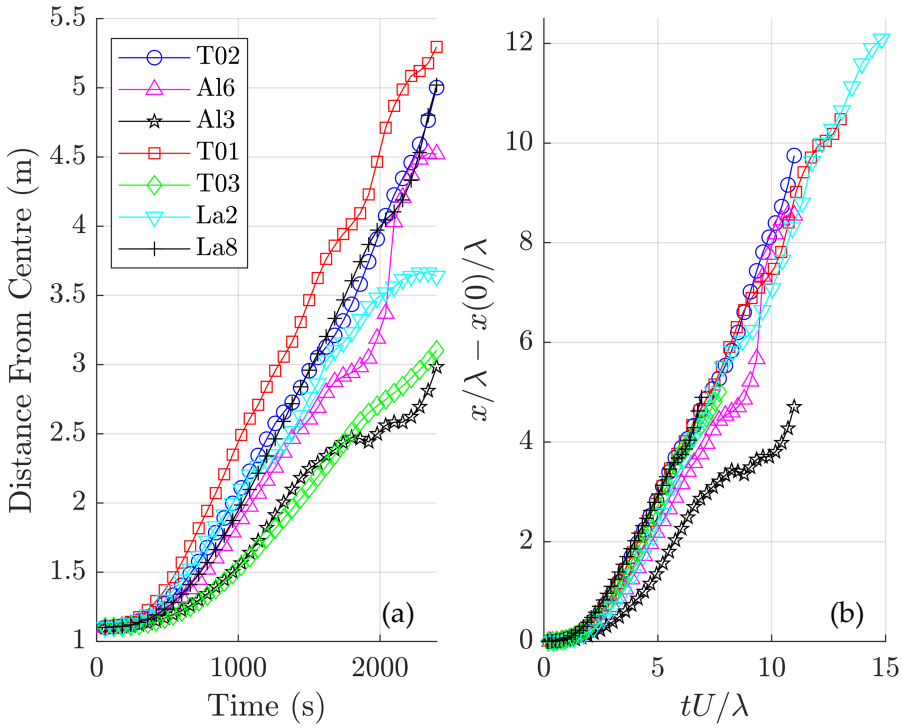

Figure 4.11: Position of intrusion front as a function of time at 60 s intervals for each case listed in Table 4.2 in both (a) dimensional and, (b) dimensionless variables. The front position is tracked using the tracer C_H defined in Section 4.2.2 with initial conditions defined in Figure 4.2(a). There is the main system T02, presented in Section 4.4, and two variations from this system for each parameter varied in Section 4.5: T_0, Al and λ.

the slope of the front position is increasing, and (2) the propagation phase, characterized by a nearly constant propagation speed. These front positions are estimated from the tracer C_H, defined in Section 4.2.2. The front position at later times are subjected to large plumes near the surface which means the front position is less coherent and harder to identify algorithmically at later times, but it often still easy to identify directly.

4.5.1 Initial temperature

In this chapter, the initial temperature is fixed to some $T_0 < T_{MD}$. In the main system, denoted as T02, $T_0 = 2.5\,^{\circ}\mathrm{C}$ and in this section (and Section 4.2.3) we also consider

$T_0 = 1.5, 3.5$ °C, or cases T01 and T03.

The slope of the equation of state approaches zero as $T_0 \to T_{MD}$ (top-to-bottom in Figure 4.12), and therefore larger changes in temperature are required to obtain similar $\Delta\rho$. As a result, the solar radiation dominated phase is prolonged (solid horizontal line in left column of Figure 4.12). The intrusion propagates approximately 2 m (indicated by the width of the V-shape) by the end of the solar radiation dominated phase, with only minor variations between each T_0 case.

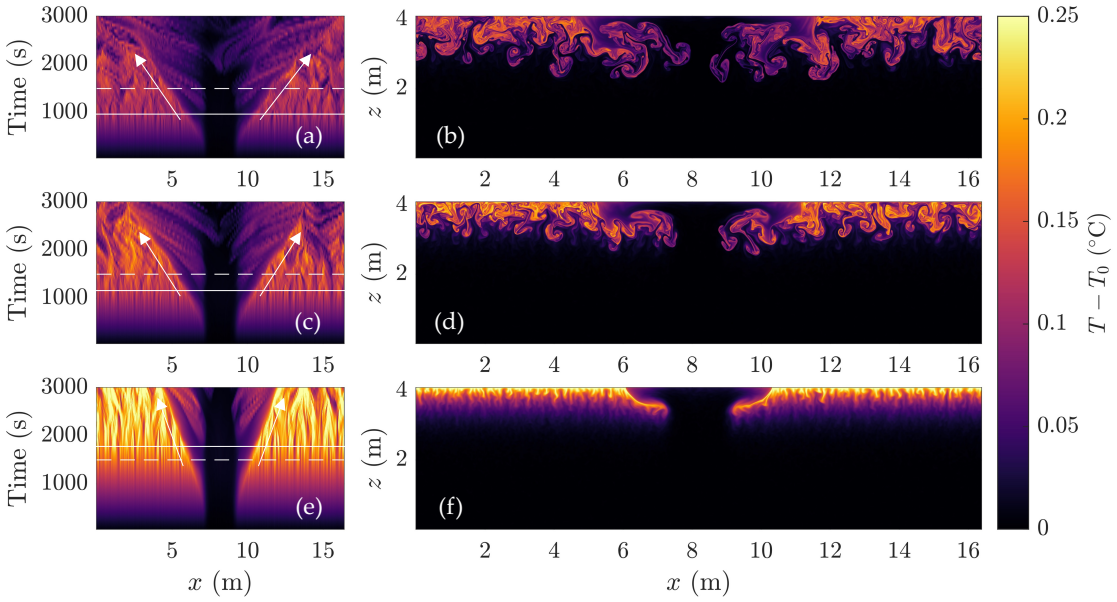

Figure 4.12: Averaged and full temperature fields for T01, T02 and T03. (a,c,e) Vertically averaged temperature field vs time. Vertical average evaluated from $z = L_z \to L_z - \lambda$. (b,d,f) Snapshots of the full temperature field at $t = 1500$ s for each value of T_0. Corresponds to the horizontal dashed line in (a,c,e). (a,b) $T_0 = 1.5$ °C (c,d) $T_0 = 2.5$ °C (e,f) $T_0 = 3.5$ °C. Solid horizontal line indicates the approximate transition time between the solar radiation dominated phase and the convection dominated phase of RT instability development. Solid arrows are a guide to the eye which indicate the bounds of the character V-shape discussed further in the text.

In the convection dominated phase, we observed a near constant front speed of the intrusion as indicated by the characteristic V-shape at the centre of Figure 4.12(a,c,e). The V is widest over the time period of interest when $T_0 = 1.5$ °C in Figure 4.12(a). The width of V shrinks with increasing T_0 in Figure 4.12(c,e). The change in width of the

V is not constant with T_0 and has a more extreme change between Figure 4.12(c) and (e), due to the non-linearity of the equation of state. The full temperature fields (Figure 4.12(b,d,f)) indicate the same trends. T01 and T02 are at similar stages of development of the RT instabilities and the intrusion, although T01 is more mature. The features in T03 are significantly less mature and the case is still in the solar radiation dominated phase at the time chosen.

Figure 4.13 compares the front position of the intrusion in T01 and T03 as a function of the front position in T02 (the base case). Over the first 2-2.5 metres, the separation between the T01 and T03 front positions and the T02 front position is increasing linearly, showcasing the differences in the growth rate of the intrusions in the acceleration phase. Following this initial separation in intrusion front position, T01 and T02 propagate at very similar rates (showcased by how the T01 curve is parallel to the diagonal). The T03 case propagates at a similar rate for a short duration (approximately 1 m) before slowing dramatically. At this stage of the simulation, temperatures near the surface are approaching T_{MD} and are likely causing the intrusion to rapidly slow.

As T_0 is moved further from T_{MD} (i.e. closer to 0), the duration of the solar radiation dominated phase is shortened. This speeds up the development of the intrusion, but does not significantly effect the distance traveled over the solar radiation dominated phase. In all three cases, over the time considered, the intrusion continues to propagate until the end of the simulation.

4.5.2 Albedo

In the following analysis we consider two smaller values of Al in addition to $Al = 0.9$ (T02) from the base case. The small values are 0.6 (Al6) and 0.3 (Al3). Unlike T_0, changing Al only changes the density gradients at the shadow boundary and has no effect on the growth rate of RT instabilities. Similarly to changing T_0, varying Al only results in a shift in $\Delta\rho$ (Figure 4.3), and with the right values can result in a very similar $\Delta\rho$. In addition to comparing the cases with varying Al, we can also compare the Al3 case to the T03 case, where $\Delta\rho$ is effectively equal.

By systematically varying Al, we can better isolate the lateral motion. Figure 4.14(a,c,e) gives the mean temperature field near the surface for decreasing Al from subplot (a) to (c) to (e). There are two main consequences of decreasing Al: (1) the width of the characteristic V-shape in Figure 4.14(a,c,e) decreases; and (2) the temperatures inside the V are larger.

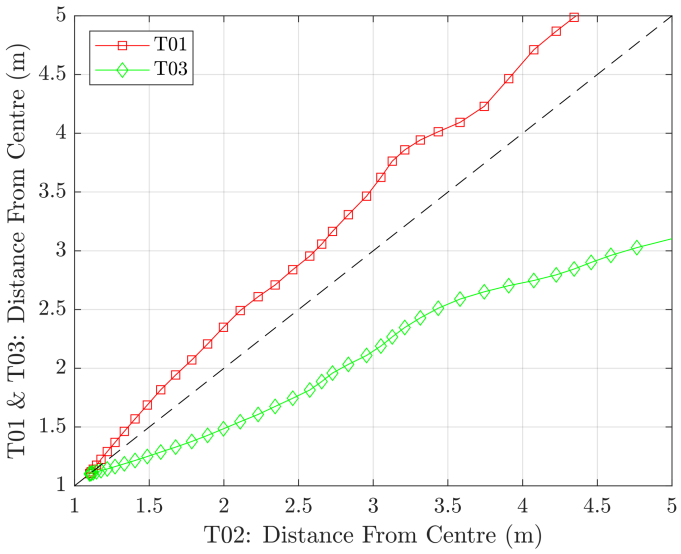

Figure 4.13: Intrusion front positions of T01 and T03 as a function of the intrusion front position for the main shadowed system (T02). Symbols are front positions extrapolated from SPINS output separated by a time interval of 60 s, connecting lines are a guide to the eye. If a curve is above the diagonal, dashed line, then it has propagated further than T02 up to that time. If it is below the diagonal line T02 has propagated further over the same time interval. Curves parallel to the diagonal are propagating at the same speed.

Consequence (1) is the result of decreasing the density difference at the shadow boundary (approximated by $\Delta\rho$) and therefore less lateral motion. Consequence (2) occurs because by decreasing Al, the temperature under the shadow increases more rapidly, even resulting in RT instabilities in Al6 and Al3. RT instabilities below the shadow are temporary before the upwelling below the shadow (Figure 4.7) is sufficiently large to overcome the temperature difference. These are seen clearly in the temperature field snapshots in Figure 4.14(d) and (f). At the same time, for $Al = 0.9$, no RT instabilities form. This suggests that below a certain threshold in Al the density differences under the shadow are sufficiently large to allow for some net downwards convection, for at least a short time.

As expected, a larger Al allows the intrusion to propagate further and more rapidly. Up to a propagating distance of 2.5-3 m, the front in Al6 propagates very closely to the T02 intrusion, as shown by Figure 4.15. The front in Al3 propagates even slower. At long times, T02 is able to continue propagating (Figure 4.11), whereas the speed of the intrusion in Al6 becomes more uncertain, possibly effected by cool plumes reaching the top

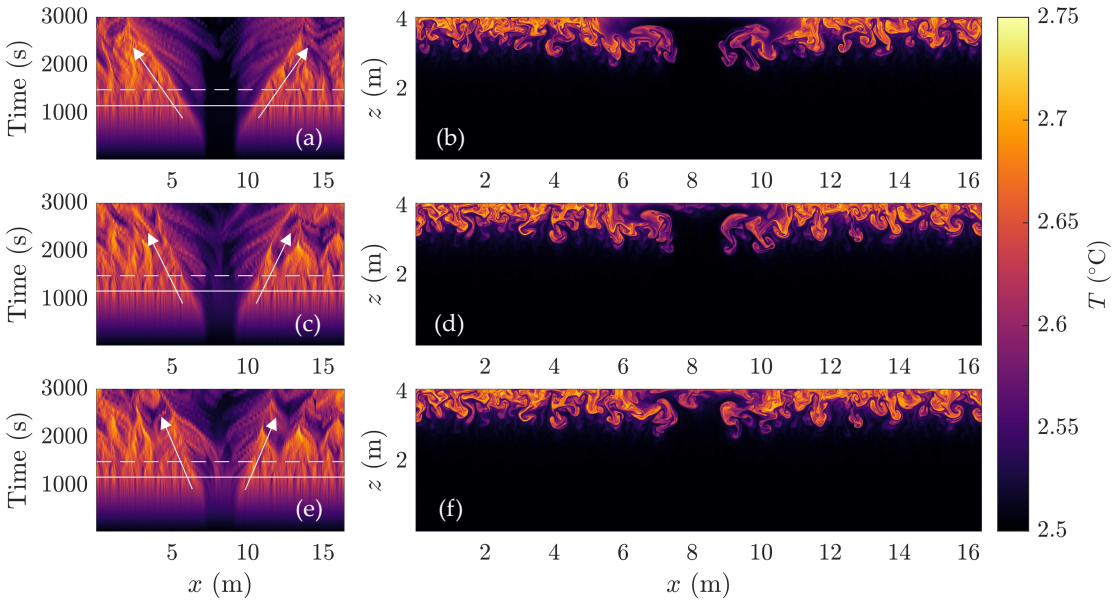

Figure 4.14: Averaged and full temperature fields for T02, Al6 and Al3 (a,c,e) Vertically averaged temperature field vs time. Vertical average evaluated from $z = L_z \rightarrow L_z - \lambda$. (b,d,f) Snapshots of the full temperature field at $t = 1500$ s for each value of T_0. Corresponds to the horizontal dashed line in (a,c,e). (a,b) $Al = 0.9$ (T02) (c,d) $Al = 0.6$ (Al6) (e,f) $Al = 0.3$ (Al3). Solid horizontal line indicates the approximate transition time between the solar radiation dominated phase and the convection dominated phase of RT instability development. Solid arrows are a guide to the eye which indicate the bounds of the character V-shape discussed further in the text.

boundary. In Al3, the intrusion slows dramatically, similar to the T03 case in the previous section.

4.5.3 Attenuation length

For variations of Al and T_0, there is a natural vertical length scale over which to average which is constant across each case: the attenuation length. For comparing La2 and La8 - where $\lambda = 0.2$ and 0.4 m, respectively - we continue to use the attenuation length as the depth over which we average the temperature in Figure 4.16, but this implies that the region we average over is different for each case. By increasing λ, as is done from Figure 4.16(a) to (c) to (e), we modify the RT instability growth rate in a new way. In T01,

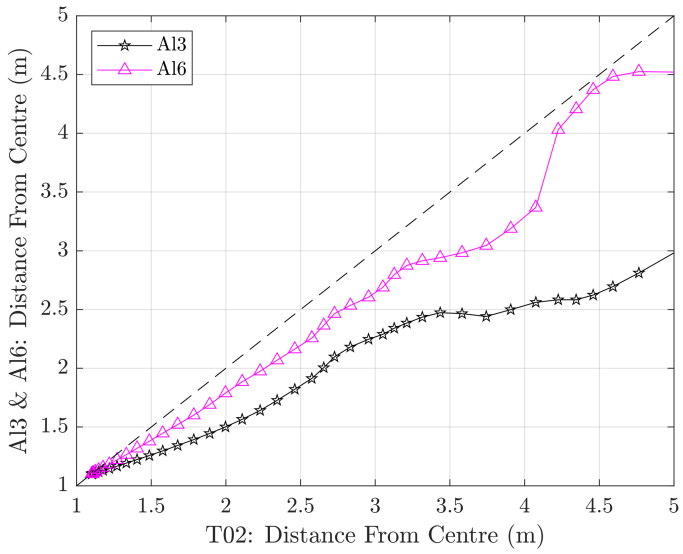

Figure 4.15: Intrusion front positions of Al3 and Al6 as a function of the intrusion front position for the main shadowed system (T02). Symbols are front positions extrapolated from SPINS output separated by a time interval of 60 s, connecting lines are a guide to the eye. If a curve is above the diagonal, dashed line, then it has propagated further than T02 up to that time. If it is below the diagonal line T02 has propagated further over the same time interval. Curves parallel to the diagonal are propagating at the same speed.

T02, T03, Al3 and Al6, the shape of the forcing term away from the shadow (Eq. 4.1) is independent of these parameters. For La2 and La8, not only is the magnitude of forcing at the surface changed, the shape of the Beer-Lambert law forcing is modified at all depths as it is set by the magnitude at the surface. This is illustrated by the dependence of $\Delta\rho$ on λ Figure 4.3.

In La2, the temperature forcing is the largest of all cases at the surface and weakest at the mid depths and below. In La8, the temperature forcing is weaker at the surface than all but Al3 and T03, but it is the strongest of all cases at the mid-depths and below. From this analysis, we can expect that RT instabilities should develop quickest in La2 and slowest in La8, forcing a shortened and prolonged solar radiation dominated phase, respectively.

The results are consistent with this analysis. The transition to the convection dominated regime is quickest in La2 (Figure 4.16(a)) and slowest in La8 (Figure 4.16(e)), with T02 at an intermediate transition time. This effect is especially clear in the right column

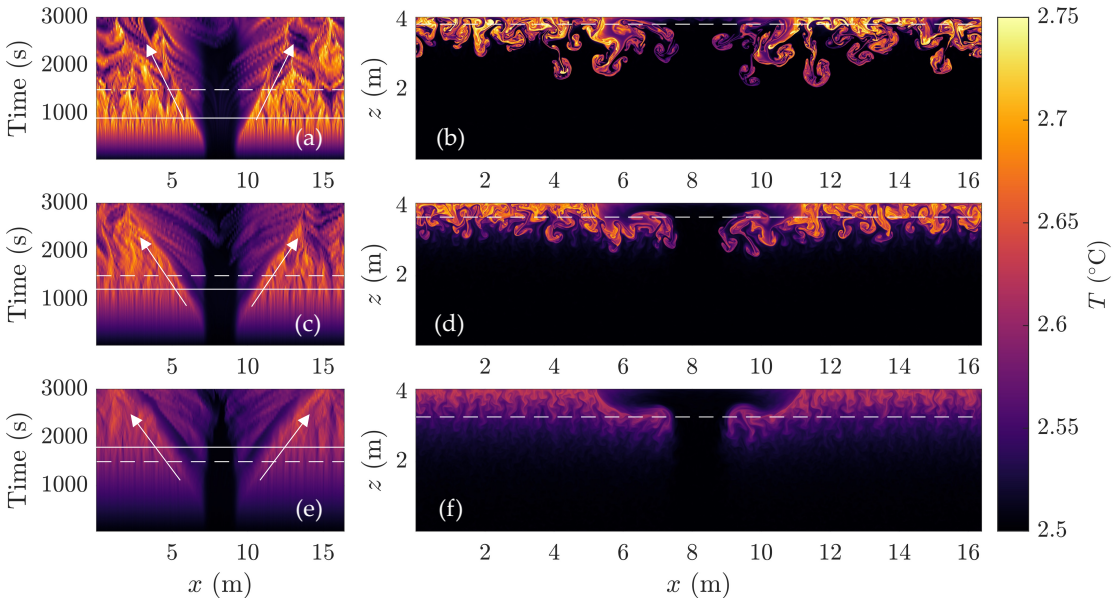

Figure 4.16: Averaged and full temperature fields for La2, To2 and La8. (a,c,e) Vertically averaged temperature field vs time. Vertical λ. (b,d,f) Is the full temperature field at the time indicated by the horizontal dashed line in (a,c,e). (a,b) $\lambda = 0.2$ m (La2)(c,d) $\lambda = 0.4$ m (T02) (e,f) $\lambda = 0.8$ m (La8). Solid horizontal line indicates the approximate transition time between the solar radiation dominated phase and the convection dominated phase of RT instability development. Solid arrows are a guide to the eye which indicate the bounds of the character V-shape discussed further in the text.

of Figure 4.16, where the boundaries of the RT instabilities are well defined in panel (b) and nearly non-existent in panel (f). A consequence of slower development of the RT instabilities is that the intrusion and return flow are much clearer in the temperature field (Figure 4.16(f)).

In addition, a change to λ only has a very small effect on the propagation of an intrusion compared to the other parameters variations in this section (Figure 4.17). La8 and T02 both consistently propagate for the entire simulation time and at nearly equal speeds. La2 propagates at a similar rate up to a distance of 3 m from the centre, but quickly slows to a stop. This suggests that a sharper gradient in the forcing can cause the intrusion to slow down dramatically. A sufficiently short attenuation length thus appears to be a mechanism by which the intrusion propagation can be arrested.

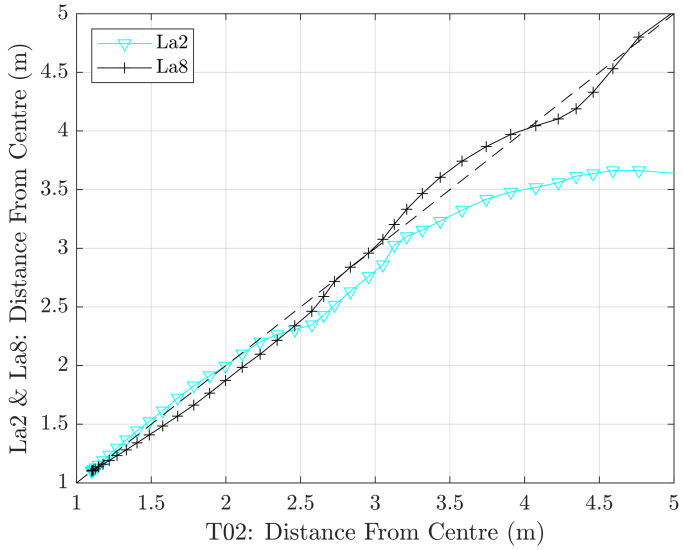

Figure 4.17: Intrusion front positions of La2 and La8 as a function of the intrusion front position for the main shadowed system (T02). Symbols are front positions extrapolated from SPINS output separated by a time interval of 60 s, connecting lines are a guide to the eye. If a curve is above the diagonal, dashed line, then it has propagated further than T02 up to that time. If it is below the diagonal line T02 has propagated further over the same time interval. Curves parallel to the diagonal are propagating at the same speed.

4.6 Effect of noise

Instabilities, including RT instabilities, which form due to unstable stratification require small perturbations to provide a seed that grows into macroscopic instabilities observed in simulations (see Section 4.3 or (Olsthoorn et al., 2019)). In nature, there are endless mechanisms which can generate perturbations: wind, cloud cover, and bathymetry are only a few examples. A low order numerical method introduces perturbations due to truncation error, which can be sufficiently large to grow into instabilities in the flow (Barad and Fringer, 2010). In a higher order method, such as that employed by SPINS, the numerical error introduced through the method is much smaller and therefore perturbations must be introduced artificially in order for instabilities to develop in a reasonable simulation time (Fringer et al., 2006; Xu et al., 2019; Grace et al., 2021). Perturbations can also be introduced via an external forcing as in (Lamb and Farmer, 2011; Passaggia et al., 2018). The perturbations can take the form of small variations in temperature or velocity. In the simulations presented in Section 4.3, by the nature of the initial conditions (T_0 is a constant) and the forcing (Eq. 4.1 is a smooth function), additive perturbations were introduced to the temperature field at the initial time.

Without artificial noise, RT instabilities will not develop away from the shadow on the time scale of the simulations, altering the conditions at the intrusion front. RT instabilities are a mechanism which transports heat deposited near the surface, towards the bottom. This is evident in the horizontally averaged temperature field in Figure 4.5. In addition, the RT instabilities generate motion near the surface. Unlike a typical gravity current experiment or simulation, the region into which the intrusion propagates is not static. The result of removing noise form the initial conditions is shown in Figure 4.18(a). The features of the intrusion on both sides of the shadow are symmetric. The shape of the intrusion front and the eddies generated by the return flow are clearly evident.

This is in stark contrast to the equivalent simulation with noise (Figure 4.18(b)). Noise is introduced to this simulation by assigning a temperature at each grid point randomly selected from a normal distribution with a mean of 2.5 °C and standard deviation of 0.035. This technique is used for all simulations included in this chapter and listed in Table 4.2. The result is a pair of intrusions which are significantly less prominent in the temperature field. Evidence of a significant return flow and a intrusion front are both diminished. The intrusion front position is not as sharply resolved and temperatures in the path of the intrusion are diminished compared in Figure 4.18(a).

Despite this shortcoming of the noisy simulations (Figure 4.18(a)), the front position is still identifiable and comparable with the noiseless case (Figure 4.18(b)). In Figure 4.19,

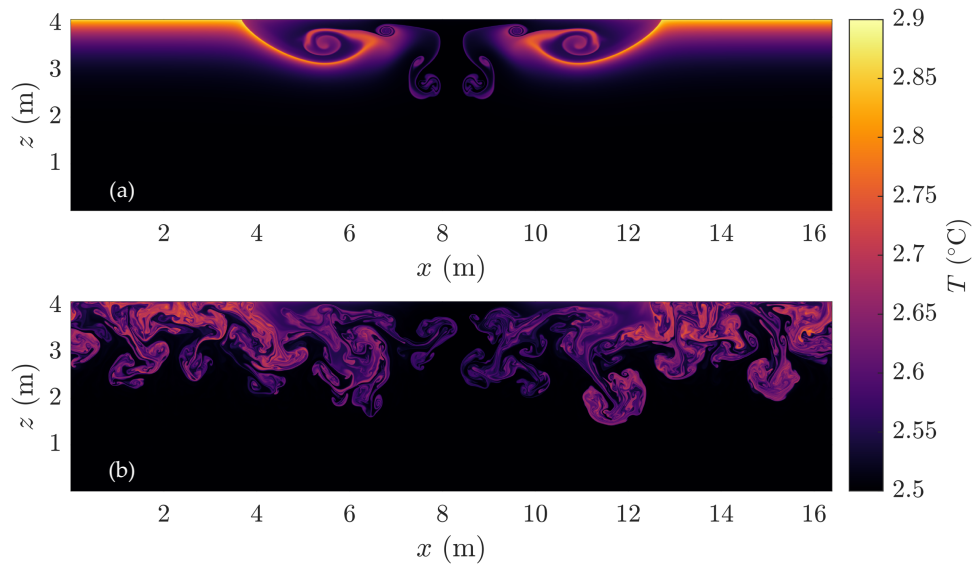

Figure 4.18: Intrusion in the temperature field for case T02 at 2100 s with (a) no noise in temperature field at the onset of the simulation; and (b) normally distributed noise in the temperature field at the onset of the simulation.

we compare the exact positions of the intrusions with and without noise using the same approach as in Section 4.3. For the first $\approx$ 1200 s, the front position evolves identically between the noisy and noiseless cases. After this period, the noisy case begins to slow compared to the noiseless case. However, the intrusion in the noisy case does not continue to slow down as one might expect. Instead, after a brief period of slow down, it resumes propagating at near the same speed as the noiseless case. The distance between the noisy and noiseless cases reaches a maximum at 1800 s of 0.4 m.

The significance of this result is that it shows that an intrusion at the surface due to lateral variations in solar radiation is robust despite changes in the conditions at the intrusion front and changes to the noise introduced at the onset of the simulation. It also demonstrates why finding an approximate front speed is perhaps not a useful approach as the front speed is gradually increasing (most evident in the noiseless case) in both cases as the mean temperature at the current front is increasing. In the noiseless case, temperatures at the intrusion front are warmer and the ambient fluid is motionless. In the noisy case, temperatures at the intrusion front are cooler on average than the noiseless case and there is fluid motion. These differences in temperature and motion are due to the development of the RT instabilities. Despite generally cooler temperatures in the noisy case (due to

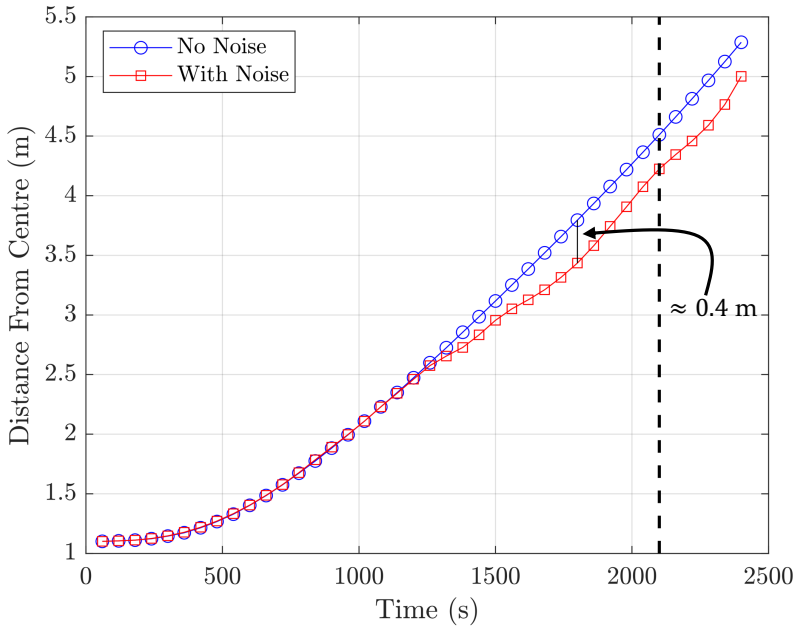

Figure 4.19: Position of the intrusion front versus time with and without noise (see legend). Vertical dashed line indicates the time corresponding to Figure 4.18. Approximate maximum difference between the intrusion position with and without noise is labeled by the vertical bar at $t = 1800$ s.

the mixing enabled by the RT instabilities), the mean density difference at the surface are comparable to the noiseless case. Despite the clear horizontal temperature differences in Figure 4.18(b) at the surface due to the formation of RT instabilities, the intrusion is able to propagate to nearly the same distance as the noiseless case. It is thus reasonable to expect that most buoyancy driven flows in an ice-covered, in-land lake would not be sufficiently large to disrupt lateral intrusions like those presented in this thesis.

4.7 Discussion

As shown in Eq. 4.6, there are four main parameters which modulate the strength of horizontal buoyancy differences:

1. The spatial variations in solar radiation intensity, determined by A_l.

2. The rate at which radiation is absorbed in the water column, determined by λ.

3. The position on the equation of state relative to the T_{MD}, determined by T_0.

4. The magnitude of the incoming solar radiation, determined by, Q_0.

The effect of the first three were explored in Section 4.5. In the following discussion, we present relevant measurements of the first three parameters in ice-covered lakes in order to situate the results in Section 4.3.

4.7.1 Albedo measurements

In this paper, the word albedo (and symbol A_l) was used to describe the magnitude of the spatial changes in solar radiation intensity at the top of the water column. Typically, albedo is reserved as a term for the fraction of radiation reflected at the surface. Due to attenuation inside the ice and snow layers above the water column, albedo - as recorded on ice-covered lakes - is insufficient to fully characterize the amount of solar radiation that reaches the water column. More accurately, A_l is the magnitude of the spatial changes in the transmissivity, the fraction of radiation that was not absorbed or reflected before reaching the water column. Measurements of the transmissivity ranged between 0.1 and 0.6 in Lake Vendyurshkoe and Lake Onega (Russia) (Leppäranta et al., 2010; Bouffard et al., 2016).

$A_l = 0.9$ was used in several cases (See Table 4.2) and the main system (Section 4.4) would correspond to a transmissivity of 0.1 of lake ice, adjacent to open water which typically has a transmissivity above 0.9. Cases Al3 and Al6 also fit into this parameter range, with weaker transmissivity on the ice-covered portion. Given that these simulations do not consider wind forcing, further research is needed to quantity the effect of nonuniform solar radiation coupled with wind forcing on the open parts of the surface.

Spatial changes in ice thickness could also have a meaningful effect on spatial changes in solar radiation intensity. However, to our knowledge the spatial variations in solar radiation intensity are seldom measured or linked to changes in ice thickness. The lakes mentioned above, had measured ice thickness ranging from 30-40 cm, with the surface mostly clear of snow (Leppäranta et al., 2010; Bouffard et al., 2016). In Ref. Leppäranta et al. (2010), in the second year data was reported, the transmissivity increased to the larger value of 0.6 in the late winter which corresponded with a near 40% loss in ice thickness.

Ref. Svacina et al. (2014a) showed that snow cover increased albedo measurements over lake ice from ≈ 0.4 to ≈ 0.8 after a snowfall. Spatial variations from clear ice to

snow-covered ice can have albedo differences near 0.4. This suggests that by changes in snow cover alone, we can expect significant transmissivity differences. Similarly, in Ref. Bouffard et al. (2019), mean measurements of transmissivity were ≈ 0.4 in 2015 and 2017 while the ice was clear of snow. The authors measured a transmissivity of < 0.1 in 2016, the year when the downwelling solar radiation was most intense (Bouffard et al., 2019). Ref. Bouffard et al. (2019) attributes most of the difference to a thin and patchy snow layer of up to 5 cm in depth. One might expect large spatial variations in transmissivity of ≈ 0.35 due to changes in snow cover alone. In Ref. Leppäranta et al. (2010), albedo measurements were reported for a wide array of cover: fresh snow (0.8), old snow(0.6), white ice (0.35), congelation ice (0.3) and water on the ice surface (0.15). This shows that by only considering changes in albedo, significant lateral variations in solar radiation intensity can be measured simply by variations in conditions at the surface.

4.7.2 Attenuation Length measurements

Water clarity is an important parameter in several sub-disciplines in the study of inland water bodies (Twiss et al., 2012; Ulloa et al., 2019; Yang et al., 2020). Irradiance incident on a clear lake will penetrate deep into the water column, with only a small fraction of the radiation absorbed per unit length. A turbid lake will have the opposite effect; a larger fraction of the incident radiation is absorbed per unit length. In this thesis, the absorption of incident radiation is modelled using Eq. 2.17 and 1.5, which assumes that all incoming radiation is absorbed at the same rate with a single attenuation coefficient. This simplifying assumption is appropriate for this process study and is used in other simulations which consider the effects of solar radiation in temperatures below T_{MD} (Ulloa et al., 2019; Ramón et al., 2021; Grace et al., 2022).

Lake Erie and Lake Onega are two large inland lakes with significant ice-coverage during the year where measurements of lake clarity and estimates of the attenuation length have been obtained (Twiss et al., 2012; Bouffard et al., 2019). Attenuation lengths were measured in Lake Erie at several specific wave lengths and as an average over the photosynthetically active radiation (PAR) range (approx. 400-700 nm) (Twiss et al., 2012). The attenuation in the PAR band was measured at four stations with an attenuation length as small as 0.6 m and as large as 1.3 m.

The light attenuation as a function of wavelength over the PAR band was also measured in Lake Onega (Bouffard et al., 2019). The attenuation lengths varied from as low as 0.2 m for ~ 440 nm light to as large as 0.8 m for ~ 700 nm light. The median attenuation length over the PAR band is approximately 0.32 m (See Fig. 5(a) in Ref. Bouffard et al. (2019), the median is a qualitative estimate and not reported in the paper).

In Section 4.4, we start our analysis with an attenuation length of 0.4 m matching the value used in other high resolution, non-hydrostatic simulations of ice-covered lakes (Ulloa et al., 2019; Ramón et al., 2021). In Section 4.5, we looked at one smaller value of 0.2 m and one larger value of 0.8 m. The parameter range considered here is comparable to those measured in lake Onega (Bouffard and Wüest, 2019) and typical of lakes more turbid than Lake Erie (Twiss et al., 2012).

4.7.3 Temperature measurements

Our goal in varying T_0 in this process study was to probe the effect of the non-linearity of the equation of state on the lateral intrusion that develops due to the shadowed region. Real ice-covered lakes in the late winter develop a stratification with three main layers (Kirillin et al., 2012; Bouffard and Wüest, 2019): (1) sharp diffusive layer immediately below the ice, (2) CML which is approximately spatially constant in temperature, and increasing in depth and temperature with time, (3) a stably stratified layer towards the bottom. The sharp diffusive layer comes from the ice cover forcing the top boundary to maintain a temperature of 0 °C and is neglected in this process study. The CML is nearly constant in temperature with depth and, therefore, is somewhat comparable to the simulations discussed in Section 4.3. CML temperatures in Lake Onega were measured in the range of 0.2 to 1 °C in March over several years, cooler than the simulations discussed in this paper which would result in higher potential for lateral motion, as suggested by Figure 4.12. The CML temperatures in Lake Pääjärvi were found to be significantly warmer, up to 2 °C, in April (Kirillin et al., 2012). In Ref. Cortés and MacIntyre (2020), the CML is nearly constant in density but not in temperature due to the influence of salinity. However, these measurements show that temperatures near T_{MD} develop near the surface as we approach ice-off (Cortés and MacIntyre, 2020).

4.8 Conclusions

In this chapter, simulations of a two-dimensional system initially at constant temperature subjected to temperature forcing via the Beer-Lambert Law, with a shadowed region, have been presented. At the centre of this region the solar radiation at the surface is reduced by a factor of Al. Shadowing leads to lateral buoyancy differences, and after some time, outward moving intrusions are generated at the surface, systematically transporting the cooler fluid under the shadowed region away from the shadow. In response to this outward motion along the surface, a return flow of warmer fluid forms. This fluid, largely consisting

of fluid trapped in the finite sized manifestations of RT instabilities, is transported back towards the shadowed region, where it is pushed upwards near the shadow boundary.

In addition to systematic lateral motion, vertical motion was also effected in a systematic way. The effect of the shadowed region on vertical motion was identified using KE_{avg} (4.2). KE_{avg} (Figure 4.9(a)) reveals two distinct regimes in both the shadowed and unshadowed cases, where the shadowed cases transition between regimes at earlier times than their unshadowed counterparts. This earlier transition is due to the enhanced vertical buoyancy flux generated by the lateral motion at the shadow boundary. This is apparent in by the average vertical buoyancy flux per unit mass shown in Figure 4.10(a). A shadowed region is a mechanism for lateral transport and transport of warmer fluid towards the bottom. In a system with no shadowed region, the lateral motion is not systematic and the development of RT instabilities is much slower at transporting warmer fluid towards the bottom. It should be noted that the average buoyancy flux per unit mass does eventually catch up to the shadowed case as shown in Figure 4.10(a).

The physical parameters which modify the development of the later intrusions are the albedo, Al, the attenuation length, λ, and the initial temperature, T_0. The short time effect of each of these parameters can be roughly quantified by the quantity $\Delta\rho$ (Eq. 4.6). $\Delta\rho \propto Al$ and a larger Al results in a faster and more robust intrusion along the surface. $\Delta\rho \propto \alpha(T_0)$, where α, the thermal expansion coefficient, is a decreasing function of temperature. As $T_0 \to T_{MD}$ the density differences for similar temperature differences are decreased resulting in slower development of an intrusion that is less robust.

The dependence on λ is more complicated. Increasing λ both decreases the magnitude of $\Delta\rho$ at the surface and increases the vertical extent of the solar forcing. This results in slower development and increased vertical extent of RT instabilities. Despite these quantifiable changes, the intrusions near the surface appear to develop at a similar rate initially, differing from the variations to T_0 and Al (see Figure 4.17, 4.15 and 4.13). Only the smaller $\lambda = 0.2$ m case produces an intrusion which slowed over the duration of the simulations. $\lambda = 0.4$ and 0.8 m remained similarly robust.

In terms of dimensional variables, we identified variations in the duration of the acceleration phase and the speeds of the intrusion during the propagation phase that depended strongly on Al, λ and T_0. In terms of dimensionless variables, the duration of the acceleration phase and propagation speeds collapsed to a single value, except for the cases where Al was varied (cases Al3 and Al6).

The numerical model we use, SPINS, is a high order pseudospectral model, and as such artificial noise is required in order to seed instabilities, such as the RT instabilities that form away from the shadowed region (see Figure 4.4). Naturally one expects that

the development of RT instabilities in the region away from the shadow would modulate the lateral intrusions with propagate outward, near the surface. A comparison between the front position of the intrusions in an identical simulation to T02 (see: Table 4.2) with the no initial noise revealed that the front position is not as strongly dependent on the development of RT instabilities away from the shadow as initially thought. In the solar radiation dominated regime, the effect of noise on the front position was negligible. The intrusion was slowed temporarily shortly after the transition into the convection dominated regime but propagated at a similar rate thereafter (Figure 4.19). This is despite the fact that the intrusion is barely recognizable in the temperature field as in Figure 4.18. This shows that the lateral intrusions are a robust feature which only depend very weakly on the surrounding RT instability set conditions.

In Section 4.7, measurements of transmissivity, albedo, attenuation length, and temperature in ice-covered lakes are reported to provide context to the simulations presented in this paper. We show that generally, the parameters presented in this paper are plausible in small, ice-covered lakes, but that this process should be further investigated via field experiments.

Chapter 5

Spatially heterogeneous solar radiation intensity with constant temperature initial conditions in three dimensions

5.1 Introduction

So far this thesis has looked at a comparison of radiatively driven convection between 2D and 3D simulations (Chapter 3) and intrusions generated by heterogeneous solar radiation intensity (Chapter 4), both in the cold water regime. The natural extension is to consider 3D simulations of heterogeneous solar radiation intensity, which is the focus of this chapter.

Gravity currents are a class of phenomenon that are often - at least initially - restricted to two dimensions: the direction of gravity and the propagation direction. However, as the current develops features along the head, at the contact boundary (in the case of no-slip boundary conditions) and at the interface between the intruding and ambient fluid develop much differently in 2D compared to 3D. As it was shown in Chapter 3, radiatively driven convection also evolves much differently in 2D and 3D and likely would impact the development of an intrusion in 3D. Dissipation is enhanced and convective plumes cascade into smaller features.

Lock-exchange gravity currents are a class of gravity currents that involve the removal of a physical boundary at the start of an experiment, where the physical boundary divides the ambient and intruding fluid (Simpson, 1999). In the lock-exchange literature, two configurations are most commonly studied: (1) the planar or two-dimensional gravity

current, and (2) the axisymmetric or cylindrical gravity current (Huppert and Simpson, 1980; Huppert, 1982, 2006; Cantero et al., 2007b; Dai and Wu, 2016; Inghilesi et al., 2018). These are convenient configurations primarily because they both can simulated and analyzed analytically as if they are in two dimensions, a planar current in the xz plane in Cartesian coordinates and an axisymmetryic current in the rz plane in Polar coordinates. It is then implicitly assumed that the current does not varying in the transverse (y for planar currents and θ for axisymmetric currents). Ref. Huppert and Simpson (1980) is an especially important paper that provides analytical solutions for the evolution of a planar and axisymmetric gravity current during the slumping phase (read about these phases in Chapter 12 of Ref. Simpson (1999) and (Cantero et al., 2007b)). There are two basic assumptions that are the foundation of this analysis. First, during this phase - where viscous effects are much smaller than buoyancy and inertia - the gravity current propagates through rectangles of equal area, implying that the total volume is unchanged and as the current stretches in the direction of propagation, it shrinks in the vertical to compensate. Second, the Froude number (the ratio of the gravitational forces to inertial forces) depends on the fractional depth of the gravity current compared to the domain depth. Using these two assumptions and empirically derived equations for the Froude number as a function of the fractional depth, the position of the current as a function of time is derived for both the planar and axisymmetric cases in the slumping phase. These equations matched well with experiments in the same paper. There is still some uncertainty about how to precisely define the Froude number at the head of the gravity current (Cantero et al., 2007b; Inghilesi et al., 2018), but nonetheless the derived expressions for the current front position are still considered an important step in gravity current analysis.

Gravity current studies that include axisymmetric 3D simulations, while less common compared to the rectangular case, are available in the literature (Cantero et al., 2007b; Dai and Wu, 2016; Inghilesi et al., 2018). Ref. Cantero et al. (2007b) compares 2D and 3D simulations of both planar and cylindrical/axisymmetric gravity currents. The two-dimensional axisymmetric current is simulated by solving the 2D Navier-Stokes equations in cylindrical coordinates. Both high Reynolds number (Re= 8950) and low Reynolds number (Re= 895) values were considered. The 3D cylindrical and planar currents remained largely 2D for the lower Re cases for the full duration of their evolution. It is reasonable to expect that 3D extensions of the simulations in Chapter 4 are at least initially two dimensional but should go 3D as the intrusion interacts with the convective ambient. Ref. Dai and Wu (2016) looked at cylindrical gravity currents subjected to a Coriolis force, finding significant azimuthal symmetry at all times in comparative non-rotating case and up to one-tenth of a revolution for slowly rotating cases. Ref. Inghilesi et al. (2018) generates an axisymmetric gravity current by placing a small opening in a large wall separating two fluids of different

densities. Fluid is exchanged symmetrically and then propagates outward radially from the opening, along the surface for the lighter fluid and along the bottom for the heavier fluids. To date, there do not exist simulations of 3D gravity currents in the cold water regime, although there have been several papers in 2D (Grace et al., 2021; Allum et al., 2022; Grace et al., 2023b)[1].

5.1.1 Chapter overview

In this chapter, we consider a rectangular shadow and a circular shadow (continuing with the language of Chapter 4) with constant temperature initial conditions. The former is a direct 3D analogy to the results in Chapter 4 and the classical planar gravity current. The circular shadow is unique as it will generate an intrusion that spreads outward and the length along the front edge will increase, which is constant in the rectangular case. The circular case is analogous to the axisymmetric case. This chapter is organized as follows: First a methods section in Section 5.2 where the system of interest is defined, the cases and relevant parameters are presented, and several quantities that are used in the results are defined. A summary of the results section is given in Section 5.3, followed by a summary of motion in all three cases in Section 5.4, then an analysis of the intrusion front and structure (Section 5.5), intrusion depth (Section 5.6), the effect of noise (5.7), and the long time behaviour (Section 5.8).

5.2 Methods

5.2.1 System of interest

In the previous chapter, due to the relatively small size of the individual simulations, it was possible to probe large portions of the parameter space. However, now we are considering 3D simulations and as a result the same computational resources produces a significantly smaller set of simulations, without making significant sacrifices to resolution or other factors. Instead of hoping to probe the entire parameter space, we instead consider a few common configurations typical to gravity current studies. To remain consistent with

[1] A recently accepted paper by a colleague does consider 3D gravity currents in the cold water regime, and is a 3D extension of Ref. Grace et al. (2021). Has not yet published at the time of writing. The title of this paper is 'Three-dimensional structure of cold-water gravity currents' and the lead author is Nico Castro-Folker.

the previous chapter we will continue referring to the motion as an intrusion while still noting similarities to gravity currents.

Further, in the previous chapter the shadow was placed in the centre of the domain with unshadowed regions on either side. This resulted in two intrusions that travelled in opposite directions along the surface away from the shadowed region. In order to maximize spatial resolution as well as the physical extent of the domain, in this chapter the shadowed regions are placed at the edge of the domain and only a single intrusion will be produced along the surface.

Case Name	Shadow Shape	Note
Corner	Quarter circle	-
Slat	Rectangular	-
No Noise	Quarter circle	Same as Corner case but without noise

Table 5.1: Table of cases. For the full list of parameters see Table 5.2. When referring to one of these cases in the text the case name in this table will be used.

There are three cases that we will consider in this chapter, listed in Table 5.1. The first case, called the Corner case, is a system subjected to solar radiation with a shadowed region and parameters similar to the T02 case in chapter 4. The physical and system parameters are given in Table 5.2. The shadow in the corner case is circular and is centred on the edge of the domain parallel to the z axis and passes through the origin. This means that this circular shadow is a quarter circle. A schematic for the side view and a to-scale, top-down view is given in Figure 5.1(a,b). The vertical shape of the solar forcing under the shadow region and away from the shadow region will continue to obey the Beer-Lambert law (4.1). In the Corner case, the lateral variations obey

$$\left[1 - A_l \exp\left(-\frac{(x^2+y^2)^{4w_d}}{w_d^{8wd}}\right)\right],$$

where the coefficient in the exponent is reduced from 8 to 4 due to a cancellation of a square root. In the bulk of gravity current research, the current generated using this geometry is called an axisymmetric or cylindrical gravity current (Huppert and Simpson, 1980; Huppert, 2006; Dai and Wu, 2016).

The only difference between the Corner case and the Slat case is the geometry of the shadow and the domain size. In the Slat case, the shadow is rectangular and extends the entirety of the y domain. This is typically referred to as two-dimensional spreading (Huppert and Simpson, 1980), or a current along a channel (Huppert, 2006). In the Slat

case, the symmetry is in the y dimension, rather than in the azimuthal direction as in the Corner case. As a result, the intrusion will propagate in the x direction and less horizontal extent (y direction) is required.

That being said, as shown in chapter 3, at later times large convective cells form. It follows that L_y, the length of the Y dimension, must be large enough to allow these cells to grow ahead of the intrusion. This means that while L_y can be decreased somewhat compared with the corner case, it must not be so small that connected cells are unable to form properly. In designing the simulation we chose a size that could fit at least two large convective cells between the walls at $y = 0$ and $y = L_y$ over the duration of the simulation. L_y was estimated qualitatively using the unstratified simulation from chapter 3. A schematic for the side view and a to-scale, top-down view for the Slat case is given in Figure 5.1(c,d). The lateral variations in the solar radiation intensity in the Slat case obeys

$$\left[1 - A_l \exp\left(-\frac{x^{8w_d}}{w_d^{8wd}}\right)\right],$$

which is very similar to the form used in Chapter 4 as in 4.1, but with the shadow starting at $x = 0$ m and ending at $x \approx w_d$.

In addition to these two cases we will also consider a single noiseless simulation, referred to as the No Noise case. A noiseless case was also discussed in the previous chapter, in 4.6. In the No Noise case, the geometry of the shadow is identical to that of the Corner case. While this kind of simulation is entirely fictitious - both the natural environment and the laboratory will have some degree of noise - it does provide interesting insight into where and when instabilities take over and breakdown the intrusion. In addition, it probes which features are due to the development of RT instabilities ahead of the intrusion or due to the nature of the intrusion itself. It also provides a point of comparison to estimate the effect of the growth of instabilities along the intrusion, in the return flow and at the intrusion front.

5.2.2 Richardson number and Kelvin-Helmholtz instabilities

A typical feature of gravity currents are Kelvin-Helmholtz (KH) instabilities generated by the shear interface between the current and the return flow. It can be shown, using the Taylor-Goldstein equations (Kundu and Cohen, 1990), that the Richardson number,

$$\mathrm{Ri} = \frac{N^2}{u_z^2}, \tag{5.1}$$

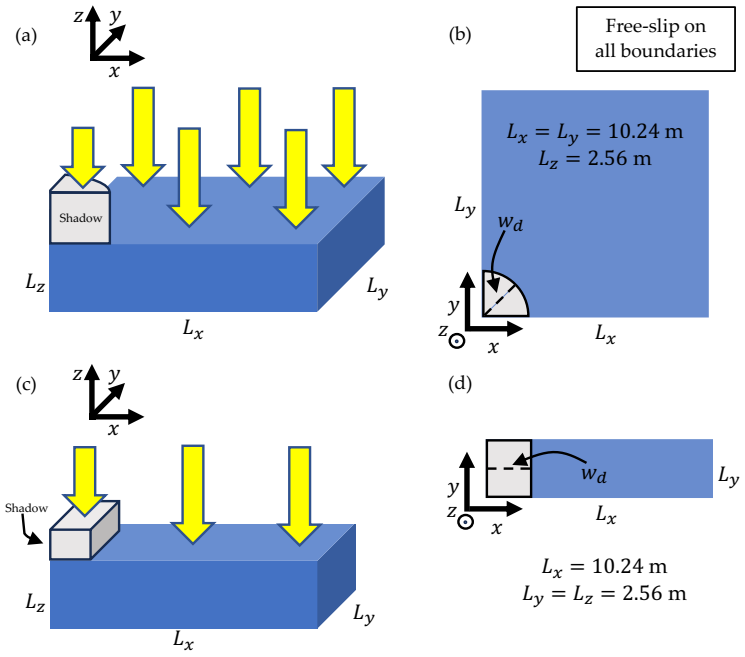

Figure 5.1: Schematic depicting the two main systems explored in this chapter. The first row (a,b) shows the schematic for the circular shadow, while the second row (c,d) illustrates the schematic for the rectangular shadow. In the first column (a,c), a 3D view of each configuration is presented. The shadowed region is depicted by the grey shape, and the incoming solar radiation is represented by the yellow arrows. The second column (b,d), gives a top-down view of both systems where the show and domain size are to scale. All cases have free-slip boundaries. Parameter values are listed in Table 5.2.

determines the stability of a shear interface to the growth of KH billows. $N^2 = -g\frac{\partial \rho}{\partial z}/\rho_0$ is the buoyancy frequency (Kundu and Cohen, 1990), and $u_z = \frac{\partial u}{\partial z}$ is the velocity shear across the interface. If Ri $> 1/4$, then the shear interface is said to be stable. In other words, above this threshold the stability of the density gradient resists the shear forces at the interface.

While the intrusions studied in this chapter are not classical gravity currents, they do exhibit several similar features including a shear interface between an intrusion flowing along the surface and return flow propagating in the reverse direction. Hence, KH billows are possible. Ri can be simplified by first assuming

$$\frac{\partial \rho}{\partial z} \approx \frac{\Delta \rho}{\delta z}, \tag{5.2}$$

Parameter	Description	Value
T_0	Initial Temperature	2.5 °C
λ	Attenuation Coefficient	0.4 m
ρ_0	Reference Density	1000 kg m^{-3}
ν	Kinematic Viscosity	10^{-6} m^2s^{-1}
κ	Temperature Diffusivity	1.43×10^{-7} m^2s^{-1}
Q_0	Magnitude of Solar Forcing	7.17×10^{-5} °Cms^{-1}
A_l	Albedo	0.9
w_d	Shadow Width	2 m

Parameter	Description	Corner	Slat
L_x	Lake Width	10.24 m	-
L_y	Lake Length	10.24 m	2.56 m
L_z	Lake Depth	2.56 m	-
N_x	X Grid Points	2048	-
N_y	Y Grid Points	2048	512
N_z	Z Grid Points	512	-

Table 5.2: Parameters used in this chapter. The upper table gives the physical parameters that do not change between configurations (See Figure 5.1). The lower table gives the domain size and resolution parameters, some of which do change between cases. A dash in the Slat column indicates that the parameter is the same as in the Corner case. No column is given for the No Noise case because it is identical to the Corner cases for all parameters listed.

and

$$\frac{\partial u}{\partial z} \approx \frac{\Delta u}{\delta z}, \tag{5.3}$$

where δz is the interface thickness. Another simplifying assumption is to evaluate the velocity difference between the intrusion and the return flow by assuming they are equal and equal to the buoyancy velocity, u_b. Under this assumption, Δu can be replaced with twice the buoyancy velocity[2]

$$2u_b = 2\sqrt{\frac{g\Delta\rho\lambda}{\rho_0}}, \tag{5.4}$$

[2]The buoyancy velocity can be found throughout the gravity current literature. A simple justification for its form can be found in Simpson (1999).

where λ is the effective depth of the fluid prior to release. In the dynamics described in this chapter, as well as the previous chapter, there is no standard intruding fluid and ambient fluid with a lock between them that is removed to produce a gravity current. However, the best analogy to a lock depth is the attenuation length. We use λ here with full knowledge that it is not the equivalent of a lock depth. Nevertheless, the goal here is to make an estimate about the stability of these intrusions to the growth of KH instabilities.

Using these approximations we arrive at

$$\mathrm{Ri} = \frac{\delta z}{4\lambda}, \tag{5.5}$$

and a stability criterion of

$$\delta z > \lambda. \tag{5.6}$$

In plain language, Eq. 5.5 and 5.6 effectively state that a thinner interface more easily generates KH instabilities, and a deeper gravity current resists the development of KH instabilities. The buoyancy velocity is a convenient choice for a velocity scale but is typically not exactly equal to velocity of a gravity current (Huppert and Simpson, 1980; Huppert, 2006; Cantero et al., 2007b). As a result, Eq. 5.5 and 5.6 should only be used as a guide for the relative interplay between the interface thickness and current depth.

Further, λ is equal for the Corner and Slat cases. Despite this, the depth of the interface is shown in Section 5.4 to be in variant between the two cases, the depth of the intrusion is effected by the differences in geometry (see Section 5.6.2). Instead, λ should be seen as a proxy for the interface depth in Eq. 5.5 and 5.6, which differs between the two cases.

5.2.3 Geometry of the systems of interest

The depth of a gravity current flowing along the top boundary is typically defined as the distance between the top boundary and the ambient in the z direction. This definition is possible to apply to the simulations discussed in this chapter at early times. However, after some time it can become difficult to define a proper transition point between the interior of the intrusion and the ambient due to the turbulent motion in the return flow and ahead of the intrusion.

In the study of gravity currents intruding into a motionless ambient, the height of the intrusion can be defined as follows. The fluid density is non-dimensionalized such that a density of zero corresponds to the ambient and a density of one corresponds to the density

of the intruding fluid (Cantero et al., 2007b). This approach assigned a weight to intruding fluid such that an intrusion height, $h(x, y, t)$ can be defined as

$$h(x, y, t) = \int_0^{L_z} \rho \, dz. \tag{5.7}$$

By construction, a column of fluid entirely consisting of the intruding fluid will have a height of L_z and a column of fluid consisting entirely of the ambient will have a height of zero. This definition is useful because it accounts for mixing along the interface between the gravity current and the ambient.

In this chapter, the focus is centred more on the transport of fluid from the shadowed region into the ambient. As a result, we use the following definition for the Corner case

$$F(z, t) = \frac{1}{L_C(t) - w_d} \int_{w_d}^{L_C(t)} \langle u_r \rangle_\theta dr, \tag{5.8}$$

where $F(z, t)$ is simply u_r averaged in the r and θ directions, and $L_C(t)$ is the intrusion front position. In the r direction, u_r is only averaged from the intrusion front position, $L_C(t)$ (see Section 5.2.4), to the edge of the shadowed region, w_d. The height is then determined by setting

$$F(z, t) = 0 \tag{5.9}$$

and solving for z.

A problem with Eq. 5.7 is that it does not account for the ambient gradually increasing in temperature and the interior of the intrusion gradually warming due to the external solar radiation forcing. It is possible to capture the net effect of the heat added to the system in the non-dimensionalization of the temperature as in (Bouillaut et al., 2019; Grace et al., 2023b). The temperature, T, is non-dimensionalized as

$$T = \theta \tilde{T} + T_{avg}(t), \tag{5.10}$$

where $\tilde{T}$ is the non-dimensional temperature, θ is the temperature anomaly away from the domain average temperature, $T_{avg}(t)$. $T_{avg}(t)$ is computed according to Eq. 2.26. Future work can consider a similar non-dimensionalization scheme.

5.2.4 Estimation of the location of the front position

The front position in both the Corner case and the Slat case is initially straightforward to identify in the temperature field, as in 2D in the previous chapter. And as with 2D,

the location of the front becomes more difficult to identify in the temperature field with time. For both the Corner and Slat case, the front position was initially identified as the maximum of $\langle T \rangle_\theta$ (Corner) and $\langle T \rangle_y$ (Slat) at $z = L_z$. Initially, the maximum temperature for these fields is located at the front position and extends down the parabolic leading edge. The boundary layer between the intrusion and the convective ambient is so thin that the temperature at the front is entrained by the intrusion and not well mixed, as well as continuously heated by solar radiation. Fluid further ahead of the intrusion is more easily mixed and slightly cooler.

After enough time had elapsed, the intrusion front position is no longer possible to identify using $\langle T \rangle_\theta$ or $\langle T \rangle_y$. This can be seen in Figure 5.5 or 5.6, in the left column of each figure. At later times, we instead use the same averages but applied to the velocity of the fluid parallel to the intrusion propagation direction. For the Corner case, this is the radial velocity, u_r, and for the Slat case this the x-velocity, u. Unlike $\langle T \rangle_\theta$ or $\langle T \rangle_y$ the maximum value of $\langle u_r \rangle_\theta$ or $\langle u \rangle_y$ is not located near the intrusion front, to be discussed in Section 5.4. Instead, the front position was identified as the edge of the region in $\langle u_r \rangle_\theta$ and $\langle u \rangle_y$ near the surface that is modified by the intrusion. In Section 5.4, it is shown that this edge is qualitatively obvious but still difficult to define rigorously. For these later times, the front position was chosen as the position that best aligned visually with the intrusion front in u_r and u, with both the average but also in conjunction with horizontal slices in the velocity field.

5.2.5 Temperature at the intrusion front

One of the main differences between 2D and 3D - beyond those which are apparent in the equations of motion (namely, Eq. 2.21 and 2.22) - is that variations along the intrusion front are possible. In 2D, the direction "along" the intrusion front does not exist and an intrusion must propagate through each convective cell, both upwelling and downwelling. In order to capture some of these temperature variations in 3D, in Section 5.5, a mean temperature near the intrusion front is presented at several times. This mean temperature is calculated by averaging the temperature in a region near the intrusion front. The region in the Corner case is depicted in Figure 5.2. This is written as an integral as follows

$$T_F(\theta, t) = \frac{1}{2\delta r \delta z} \int_{L_z - \delta z}^{L_z} \int_{L_C - \delta r}^{L_C + \delta r} \left[T(r, \theta, z, t) - \frac{2r}{\pi L_C} \int_0^{\pi/2} T(r, \theta, z, t) d\theta \right] dz dr \qquad (5.11)$$

where $T(r, \theta, z, t)$ is the temperature field in cylindrical coordinates, $\delta z = 0.1$ m is the height of the contributing layer, and $\delta r = 0.05$ m is the thickness of the region near the intrusion

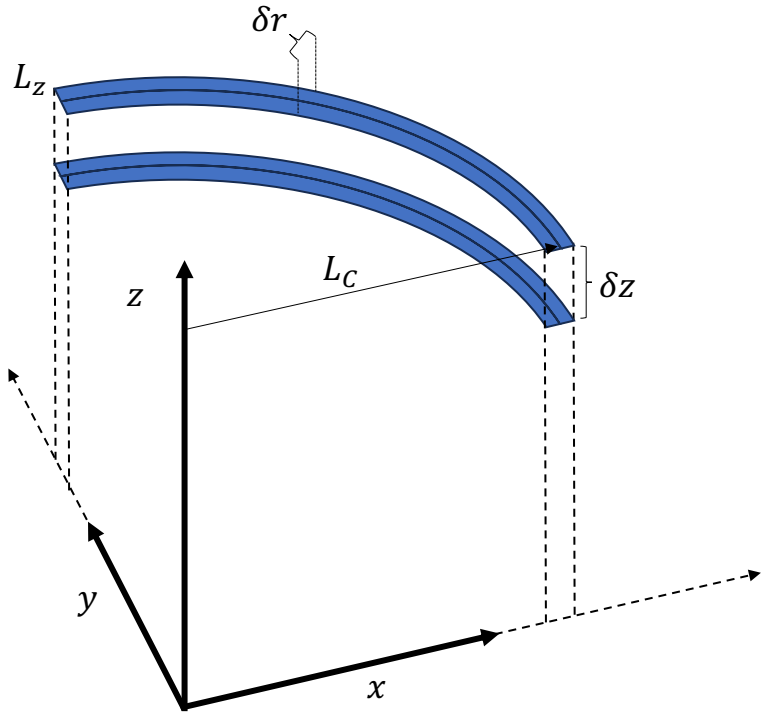

Figure 5.2: Schematic of the near-surface cylindrical shell for the calculation of $T_F(\theta, t)$ in the Corner case (Eq. 5.11). δr and δz are given in the text. L_C is the front position for the Corner case and is a function of time.

front. The second term[3] on the right-hand side of Eq. 5.11 is the average temperature over the entire cylindrical shell in Figure 5.2. The calculations performed by the model SPINS (Section 2.4) are done on a rectilinear grid. Therefore, in order to calculate $T_F(\theta, t)$ in the corner case, the temperature field must first be converted into cylindrical coordinates. By the very nature of this process it requires interpolating because some of the points are guaranteed to be misaligned with the grid. The interpolation was performed using the MATLAB function interp2 and the spline method, which is a cubic interpolation.

The new grid is obtained by requiring the same grid spacing as the original Cartesian grid of 5 mm. This was done by taking the front position, L_C, and determining the arc

[3]The purpose of subtracting some constant value is simply to eliminate the increasing temperature with time due to solar radiation. The purpose of T_F is to compare shape across times and not the magnitude. In Figure 5.10(a), T_F at each time is given an arbitrary offset for easy comparison, negating the importance of the exact form of the second term.

length

$$S = \frac{\pi}{2} L_C,$$

Then, S is divided by 0.005 m (or 5 mm) to find the number of points along the arc to maintain a grid spacing close to 5 mm. From this, we create a discrete set of points defining θ from 0 to $\pi/2$. The angle between grid points along this cylindrical shell is approximately equal to $\frac{0.005}{L_C}$. This calculation results in a 2D surface that is a function of θ and z only. Since Eq. 5.11 is an integral over r, as well as z, this means that several cylindrical shells must be calculated with radii both greater than and less than L_C. For simplicity of the mean calculation, the inner and out shells use the same θ and z grid as the shell with a radius of the intrusion front position. As a result, the arc length between grid points is larger than the grid spacing on the Cartesian grid for the shells ahead of the front position and smaller than the Cartesian grid spacing for the shells behind the front position. The mean is restricted to a small region near the surface of height δz and thickness $2\delta r$, as shown in Figure 5.2. The height restriction is to focus T_F on the intrusion front. A finite thickness, $2\delta r$ is used because the intrusion front position has a finite thickness. A thickness of $2\delta r$ likely exceeds the thickness of the intrusion front at early times but does not extend significantly into either the intrusion interior or the fluid ahead of the intrusion front position.

The calculation of T_F in the Slat case is similar to Eq. 5.11,

$$T_F(y,t) = \frac{1}{2\delta x \delta z} \int_{L_z-\delta z}^{L_z} \int_{L_S-\delta r}^{L_S+\delta r} \left[T(x,y,z,t) - \frac{2}{L_y} \int_0^{L_y} T(x,y,z,t)\, dy \right] dx dz. \quad (5.12)$$

Here the same values are given for δr and δz as for the Corner case. Noticed that the temperature field and T_F are not written in terms of cylindrical coordinates. This is because the propagation of the intrusion front is aligned with the grid.

5.3 Results preamble

In Chapter 4, a set of 2D simulations were presented in order to probe the parameter space of the intrusion. As we expand our interests to 3D simulations, while maintaining (1) the label of high resolution direct numerical simulations, and (2) the large vertical and horizontal length scales, a full analysis of the parameter space is less practical. Hence, this chapter will consist of the analysis of the three cases: Corner, Slat and No Noise, as listed in Table 5.1. The initial development of the intrusion in each of these cases is presented in

Figure 5.3 by using the temperature field (colour) and velocity field (arrows). We find that all three cases produce an intrusion that propagates away from the shadow region. The advance of the intrusion in the Slat case persists for longer and is generally deeper than the Corner or No Noise cases. Despite this, the intrusion in both the Corner and Slat cases propagates at approximately the same constant speed. In the no noise case, however, the speed of the intrusion gradually increases with time, consistent with Figure 4.19 from the previous chapter. By comparing the No Noise and Corner cases, we are able to see clearly the effects of the growing instabilities ahead of the intrusion.

5.4 Summary of motion

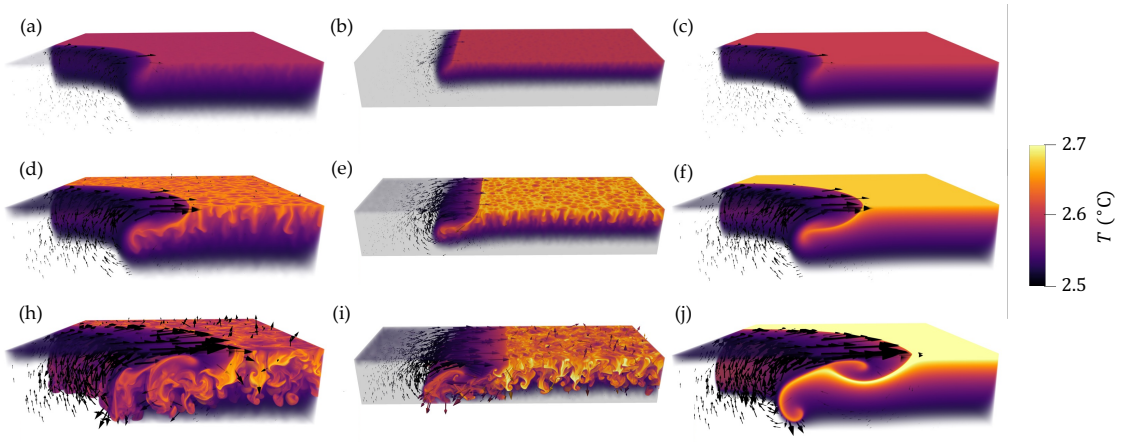

Figure 5.3: Initial development in intrusions for the (a,d,h) Corner case, (b,e,i) Slat case, and (c,f,j) the No Noise case at (a,b,c) $t = 600$ s, (d,e,f) $t = 1000$ s, and (h,i,j) $t = 1400$ s. Colour denotes the temperature field and the arrows denote the velocity field. There are 3000 arrows, randomly distributed, with sizes proportional to the velocity field and comparable between panels. All cases only show the top half of the domain. The Corner and No Noises cases have been truncated by 25% in both x and y. The Slat case is truncated in only x by 25%.

Figure 5.3 shows the development of an intrusion that propagates away from the shadowed region, as early as the solar radiation dominated phase (Figure 5.3(a-f)) and into the convection dominated phase (Figure 5.3(h,i,j)). A schematic of the flow as viewed from the side is given in Figure 5.4. Underneath the intrusion, a return flow develops with two

parts. Immediately below the intrusion the return flow is heated, a forms into a Rayleigh-Taylor-like instability. In the Corner and Slat cases, there are many features along the heated return flow, whereas, in the No Noise case, the heated return flow is smooth. The return flow extends to the bottom, consisting of cool, unheated ambient fluid with no discernible features. The return flow is generated by conservation of volume as the fluid under the shadow flows away from the shadowed region. The heated return flow initially propagates towards the shadowed region, but at a later time (Figure 5.3(h,i,j)) due to the shear interface (Labeled on Figure 5.4) the head of the heated return flow curls towards the surface, generating a large KH billow. KH billows are commonly observed in the tail of a gravity current with sufficiently large Reynolds number (Simpson, 1999; Cantero et al., 2007b,a).

The times shown in Figure 5.3, emphasize a period of time where the intrusion is still evident in the temperature field. In the previous chapter, it was shown that at later times in the simulations, the intrusion was mostly invisible in the temperature field, but remained evident in the velocity field and continued to propagate even to the latest times of the simulation. Indeed, the gradual breakdown of the intrusion in the temperature field also occurs in 3D but with much higher rates of mixing due to the differences in the way that convection develops in 2D and 3D, which was the focus of Chapter 3.

The development of the intrusion, from initial stages to collapse in the temperature field can be see clearly in the left column of Figure 5.5 for the Corner case and Figure 5.6 for the Slat case. The left column of both figures gives temperature field averaged in the transverse direction. $\langle T \rangle_\theta$, computed using Eq. 2.25 for the Corner case and $\langle T \rangle_y$ using Eq. 2.23 for only one horizontal dimension for the Slat case.

The right column of Figure 5.5 and Figure 5.6 gives the velocity in the direction parallel to the direction of propagation, $\langle u \rangle_y$ for the Slat case and $\langle u_r \rangle_\theta$ for the Corner case. These cases will be compared and contrasted side-by-side. In doing so, the terms 'outward' and 'inward' will be used in both cases to refer to motion away from and towards the wall at $x = 0$ m in the Slat case or the corner at $r = 0$ m (equivalently, $(x, y) = (0, 0)$ m).

The initial development for both cases is quite similar (Figure 5.5(a,b) and Figure 5.6(a,b)). The intrusion is only visible in a small region near the shadow boundary (r or $x = 2$ m, Figure 5.4). The horizontal density gradient generates vorticity along the shadow boundary, rotating the vertical temperature interface outward into the heated ambient (Figure 5.5(a) and 5.6(a)). This effect appears in $\langle u \rangle_{\theta/y}$ as a triangularly shaped region of outward flow towards the ambient. Flow velocity is strongest at the surface and weakest near a depth of λ where the horizontal temperature and density differences are smaller. In both cases, a region of weak flow towards the left is visible beneath the triangular region.

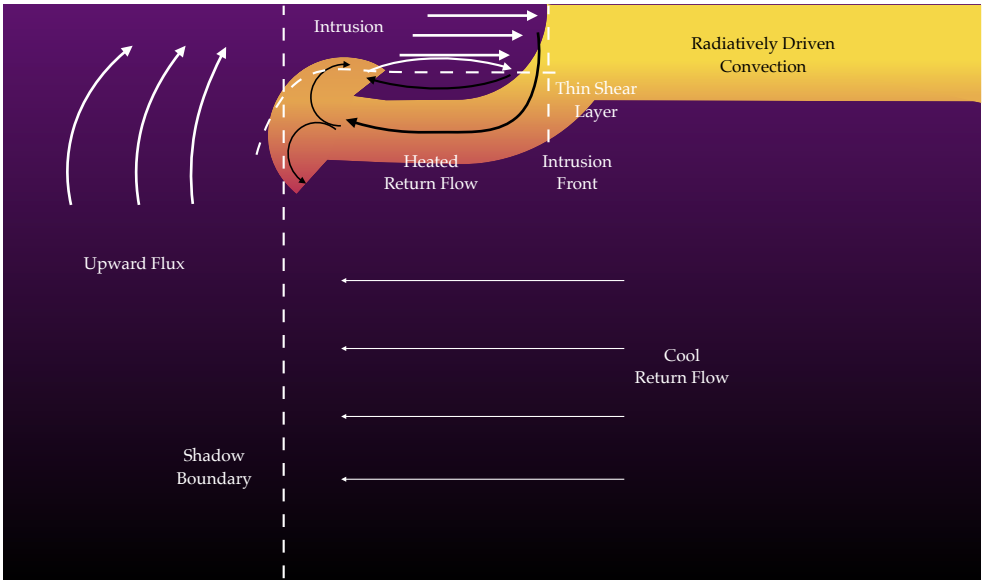

Figure 5.4: Flow schematic for the dynamics presented in this chapter, viewed from the side, focused on the intrusion. This stage of motion is representative of the temperature field $t \approx 1200$ s. Arrows indicate the mean direction of motion in this plane and are coloured to enhance contrast only.

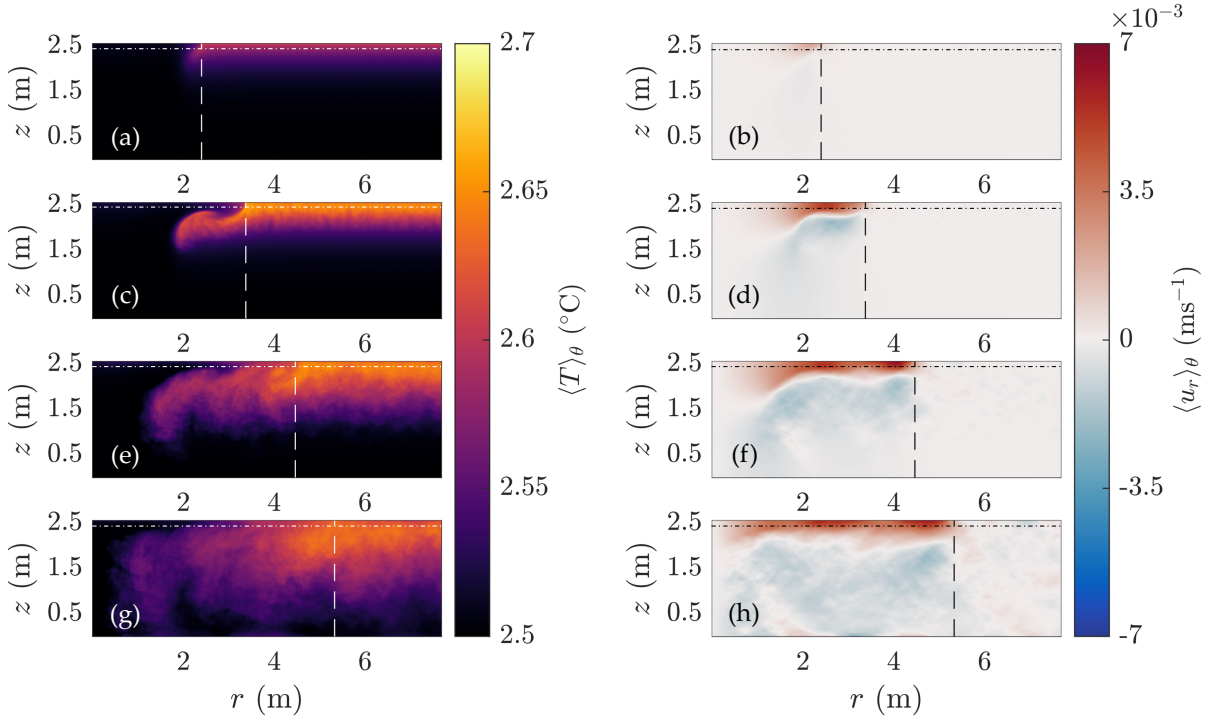

Figure 5.5: T and u_r averaged in the azimuthal direction for the Corner case. Azimuthally averaged (a,c,e,g) T and (b,d,f,h) u_r at (a,b) $t = 600$ s, (c,d) $t = 1200$ s, (e,f) $t = 1800$ s, and (g,h) $t = 2400$ s. The vertical dashed line in each panel gives the approximate front position as a function of time, given in full in Figure 5.9. The horizontal dot-dashed line in each panel gives the depth of the Slices in Figure 5.7 and Figure 5.8 for the Corner case.

As we will see later, this is the initial growth phase where the pace of the intrusion increases (in the first 600 seconds of each simulation).

At the next stage, Figure 5.5(c,d) and 5.6(c,d), the intrusion transforms into the shape of a classical gravity current typical of a free-slip surface with a parabolic shaped front edge (Härtel et al., 2000) consistent with the flow schematic in Figure 5.4. The intrusion at this stage is also consistent with gravity currents with no-slip boundary conditions at low Reynolds number (Re< 1)[4] (Huppert, 2006). The heated return flow underneath begins to resemble the typical mushroom shape of a Rayleigh-Taylor instability. Both the size of the head and the thickness of the neck of the return flow are smaller in the Slat case. This is possibly due to the fact that as the return flow propagates inwards, the volume is decreased towards the corner, forcing the heated return flow to expand downwards.

In both cases, $\langle u_r \rangle_\theta$ and $\langle u \rangle_y$ exhibits a consistent outward flow along the surface, a slightly weaker inward flow in the heated return flow, and a significantly weaker flow in the cool return flow towards the bottom towards. The shear layer is mostly horizontal except at the head of the heated return flow and at the intrusion front (Figure 5.4). The downwards angle of the shear layer bisects the head of the heated return flow from its neck. This is similar to the normal development of a Rayleigh-Taylor instability, where the velocity of the neck is in the direction of propagation and the velocity of the head is towards either side of the instability. At this stage of the motion, the velocity scales in the interior of the intrusion and return flow greatly exceed the velocity scales ahead of the intrusion.

At the third stage, Figure 5.5(e,f) and 5.6(e,f), the upper edge of the return flow has become a KH billow and has curled up into a vortex, which we will refer to here as the return flow vortex. Others will inevitably follow, but this vortex is crucial to the development and mixing of the intrusion in the temperature field. In both cases, the return flow vortex travels in the same direction as the intrusion as a faster rate. In the Corner case, the return flow vortex develops more rapidly and catches up to the intrusion front position at $t = 1800$ s (Figure 5.6(e,f). In the study of classical gravity currents, especially those bounded by a wall in the direction behind the current, an effect where the return flow catches up to the front of the current has been observed and well documented (Simpson, 1999). However, the return flow vortex is clearly generated by a KH instability along the shear layer between the heated return flow and the intrusion, and not an interaction with the return flow and a wall behind the intrusion.

[4]The flow presented in this chapter corresponds to Re$\gg 1$. The maximum Re can be estimated using a flow speed of 0.01 ms^{-1} and a length scale of λ, resulting in a Re of 4000. Most flow present in this work have speeds that are $\mathcal{O}(10^{-3}$ ms$^{-1})$ corresponding to a smaller Re but still much greater than 1.

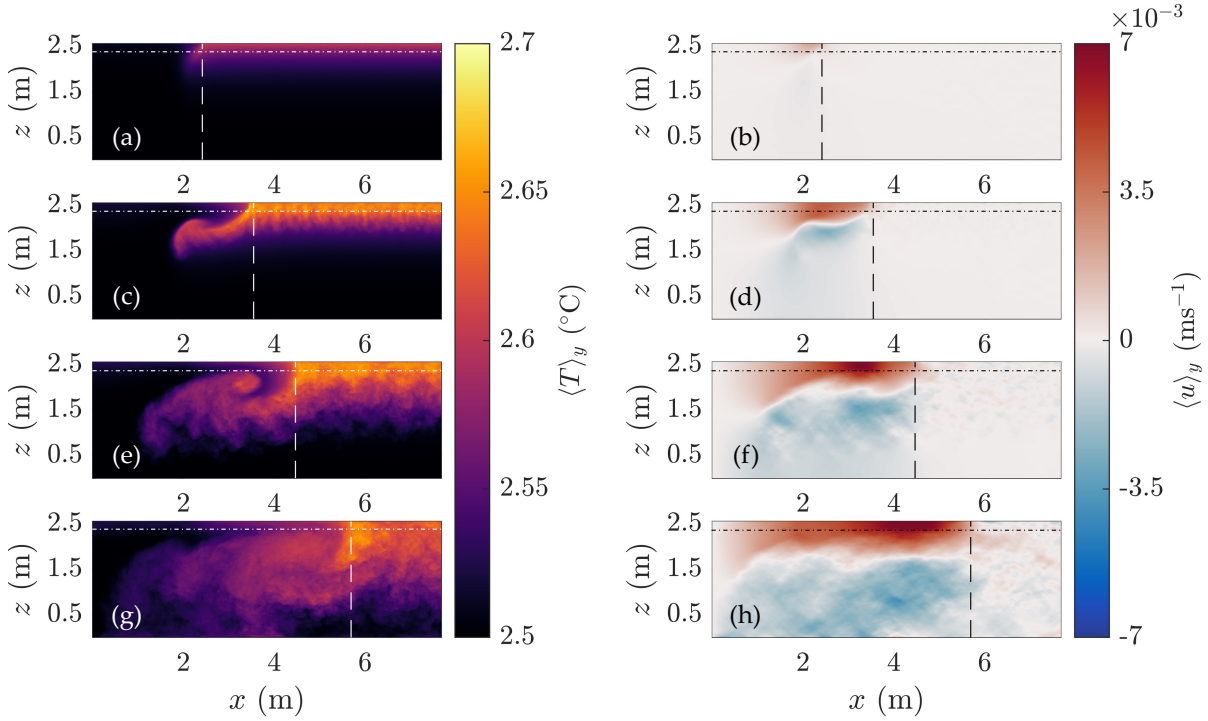

Figure 5.6: T and u averaged in the y direction for the Slat case. y averaged (a,c,e,g) T and (b,d,f,h) u at (a,b) $t = 600$ s, (c,d) $t = 1200$ s, (e,f) $t = 1800$ s, and (g,h) $t = 2400$ s. The vertical dashed line in each panel gives the approximate front position as a function of time, given in full in 5.9. The horizontal dot-dashed line in each panel gives the depth of the Slices in Figure 5.7 and Figure 5.8 for the Slat case.

The heated return flow inevitably dominates the cool return flow as the heated return flow falls as it propagates inwards. The collapse of the intrusion in the temperature field is apparent in the comparison between $\langle T \rangle_\theta$, in the Corner case, and $\langle T \rangle_y$ in the Slat case in Figure 5.5(e) and 5.6(e). The return flow vortex that is responsible for the collapse has reached the front of the intrusion in the Corner case by this time, but in the Slat case, the central axis of the vortex is nearly 4 m behind.

The likely source of the difference in timing is the difference in depth of the intrusion. The depth of intrusion in this case is defined as the mean depth of the shear interface between inward and outward motion in $\langle u \rangle_y$ in the Slat case and $\langle u_r \rangle_\theta$ in the Corner case. As shown in Ref. Cantero et al. (2007b), a gravity current spreading radially is typically thinner than a gravity current spreading as in the Slat case. Despite the fact

that radial and planar gravity currents are both studied heavily in the literature (Huppert and Simpson, 1980; Simpson, 1999; Huppert, 2006; Cantero et al., 2007b), both cases tend to be analyzed separately without much discussion and the exact differences are not well documented. In Section 5.6, a short analytical framework is established to explain the height different between the Corner and Slat case - as well as radially spreading and planar gravity currents, generally.

The mean depth of the intrusion is discussed in Section 5.6.1, which is defined in Section 5.2.3. There are clear variations in the depth of intrusion, defined as the transitional region between the intrusion and the return flow, called the shear layer. At early times, the shear layer is nearly constant in depth behind the head of the intrusion and ahead of the head of the heated return flow (Figure 5.5(d) and 5.6(d)). The variations at later times are apparent in $\langle u \rangle_y$ in the Slat case (Figure 5.6(f)) and $\langle u_r \rangle_\theta$ in the Corner case (Figure 5.5(f)) at $t = 1800$ s. The regions where the intrusion is thinnest aligns with the return flow vortex axis of rotation and the any subsequent KH billows. There are two such features in the Corner case in Figure 5.5(f) and one - the return flow vortex only - in the Slat case in Figure 5.6(f). The intrusion is deepest in the Corner case between the two features formed from KH instabilities. The velocity in the intrusion interior is maximized at the thinnest regions and minimized where the intrusion is thickest in the Corner case. This effect is less prominent in the Slat case, likely due to a combination of the increased intrusion depth and the relative size and position of the return flow vortex.

At the final stage, Figure 5.5(g,h) and 5.6(g,h), the KH billows in both cases have significantly disrupted the front edge of the intrusion. In the Corner case, at $t = 2400$ s, the front position and the vortex are no longer visible in $\langle T \rangle_\theta$ (Figure 5.5(g)). In the Slat case with development slightly behind the Corner case, at $t = 2400$ s, the vortex has nearly erased the front position in $\langle T \rangle_y$ (Figure 5.6(g)). However, there are clear differences beyond the time lag between the two cases. The return flow vortex in the corner case is restricted to the depth of the intrusion, whereas, in the Slat case, the return flow vortex appears to extend below the intrusion, suggesting the possibility for enhanced vertical motion in the Slat case that goes beyond the differences in intrusion depth.

In both cases, the sharp boundary separating the intrusion and the radiatively driven convection ahead of the front (Figure 5.4) is erased (Corner) or nearly erased (Slat). The original driving mechanism of the intrusion was a temperature differences across the shadow boundary. The width of the shadow boundary is approximately 1 m and a temperature difference at early times is of order 0.01 °C. This corresponds to an approximate temperature gradient of 0.01 °Cm^{-1}. At the latest time in both cases, (Figure 5.5(g) and 5.6(g)) there is a temperature change of approximately 0.15 °C but over approximately 6 m. This corresponds to a temperature gradient of approximately 0.025 °Cm^{-1}. The vorticity gener-

ation in the mean temperature field due to baroclinic effects is comparable to the vorticity generation at the shadow boundary at early times ($t < 1000$ s). However, as one might expect, the mean temperature field does not show the whole story. This is explored in more detail in Section 5.8.

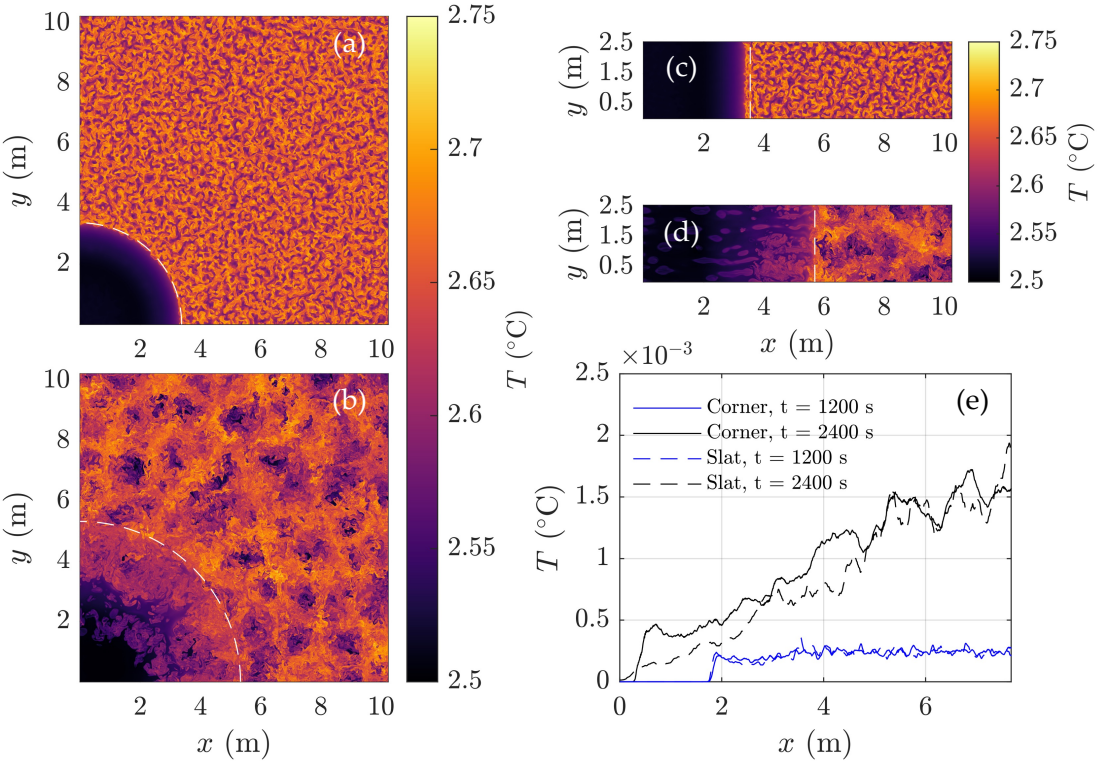

Figure 5.7: Slices in the temperature field for the (a,b) Corner and (c,d) Slat cases. (a,c) $t = 1200$ s and (b,d) $t = 2400$ s. Dotted lines in the slices give the front position at the time of the slice. (e) Variance in T along the direction of propagation. The horizontal axis represents r in the Corner case and x in the Slat case. Times and cases listed in the legend.

The averages given Figure 5.5 and 5.6 correctly demonstrate the general behaviour and evolution of the intrusion. However, they fail to capture the manner in which the intrusion develops in the transverse direction. Figure 5.7 and 5.8 give slices in the T and w fields, respectively, for both the Corner and Slat cases, as well as the variance in T and w at the same times, along the outward direction. The depths of the slices are shown in Figure 5.5 and 5.6 using the dot-dashed line. The depth was chosen to correspond to the approximate

mid depth of the intrusion at $t = 1200$ s, which is different between the two cases, hence, the slightly different depths sampled for Figure 5.7 and 5.8.

Both the Corner and Slat cases develop similarly in the initial stages of the motion (Figure 5.7(a,c) and 5.8(a,c)). A relatively smooth intrusion front with features smaller than the size of convective instabilities ahead of the intrusion is evident. The intrusion front is indicated by a sharp transition between convective plumes ahead of the intrusion and a smooth interior region. The convective plumes are the small patches of warm and cool fluid ahead of the intrusion in Figure 5.7(a-d). These plumes are randomly shaped, with rough features, oriented mostly in the vertical direction due to gravitation forces. At $t = 1200$ s, features along the intrusion front edge are visible that are comparable in length scale to the features ahead of the intrusion. This will be discussed further in Section 5.5. The shapes and sizes of the instabilities are apparent in both the T (5.7(a,c)) and w (Figure 5.8(a,c)) fields.

The temperatures in the interior of the intrusion are significantly smaller than those in the region ahead of the intrusion. The temperatures are smallest under the shadow, for radii less than 2 m in the Corner case and for x less than 2 m in the Slat case. Between the edge of the shadow boundary and the intrusion front, there exists a small gradient in temperature increasing in the direction of propagation, in both the Corner and Slat cases. This gradient is also apparent in $\langle T \rangle_\theta$ and $\langle T \rangle_y$ in 5.5(c) and 5.6(c,g), respectively. As the intrusion propagates away from the shadowed boundary, the interior is gradually heated at rate of Q_0/λ. The fluid closest to the intrusion front has been heated longer and as a result is warmer than fluid further behind the intrusion front. A sharp change in temperature of approximately 0.1 °C still persists at the intrusion front. Based on the rate of heating of Q_0/λ, an increase in temperature of 0.1 °C is obtained at approximately 600 s. Figure 5.5(a) and Figure 5.6(a) both show that at $t = 600$ s, the intrusion front is only barely away from the shadow boundary.

In the w slices at $t = 1200$ s (Figure 5.8(a,c)), the convective instabilities show the same rough and randomly oriented patches as in the T slices in Figure 5.7(a,c). The smaller temperatures correspond to positive w and vice versa. The intrusion front is similarly identified by transition between a smoothly varying region in the intrusion interior and the convective instabilities ahead of it, with small features along the front. The interior in both the Corner and Slat cases can be divided up into an upwelling region up to a distance of ≈ 2.2 m from the corner or wall, and a downwelling region from ≈ 2.2 to the intrusion front. The upwelling that occurs underneath of the shadow is due to conservation of mass as the intrusion propagates further out. The upward velocities peak near the shadow boundary. This peak occurs due to fluid forced upwards by the head of the return flow. The relative lengths of both of these regions is approximately the same in both the Corner and Slat

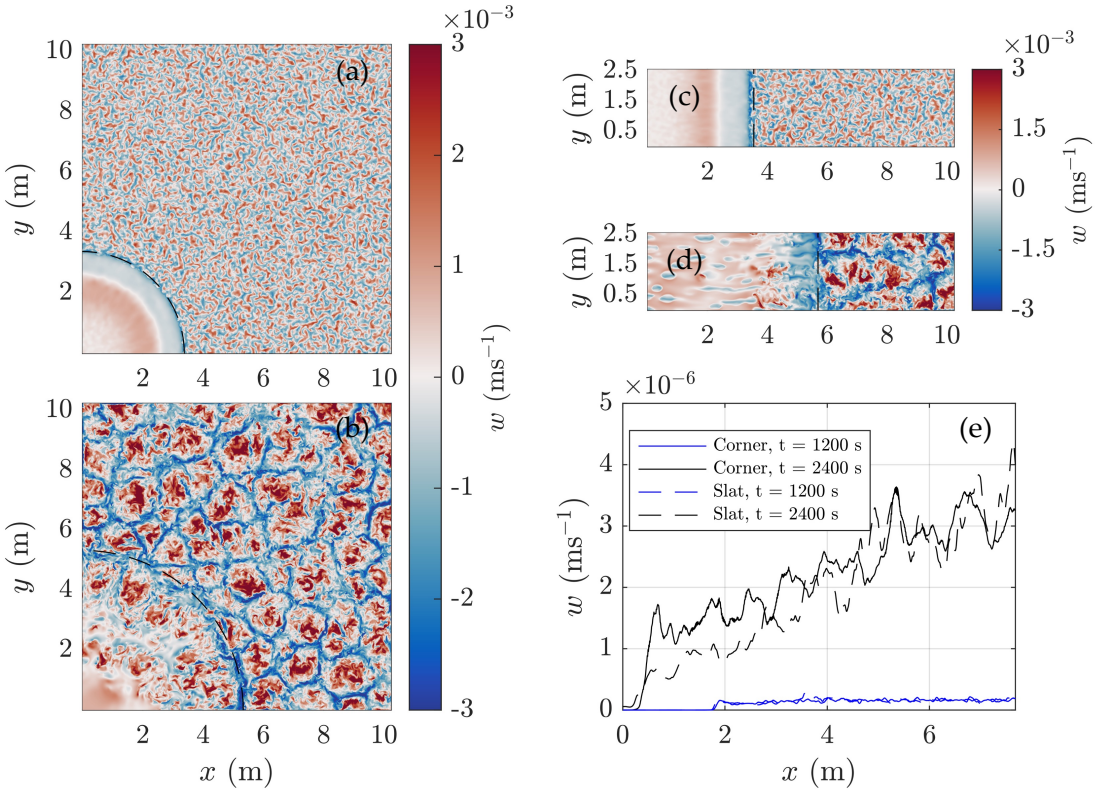

Figure 5.8: Slices in the vertical velocity field (w) for the (a,b) Corner and (c,d) Slat cases. (a,c) $t = 1200$ s and (b,d) $t = 2400$ s. Dotted lines in the slices give the front position at the time of the slice. (e) Variance in w along the direction of propagation. The horizontal axis represents r in the Corner case and x in the Slat case. Times and cases listed in the legend.

cases.

The variance in T and w (Figure 5.7(e) and 5.8(e)) along the direction of propagation at $t = 1200$ s is effectively identical for both cases, with a peak just before 2 m with nearly constant variance after to the end of the domain. Note that the location of the peak does not coincide with the front position. It instead corresponds to the head of the return flow (this can be verified by comparing with the return flow head location in Figure 5.5(c) and 5.6(c)). The largest variance in the temperature and vertical velocity occurs at the head of the return flow. Further evidence of the intensity of this variance (which includes information from both the transverse and vertical direction) in the azimuthal and

y direction is that above and below the return flow at $t = 1200$ s there are no (large) perturbations to the background temperature and vertical velocity field (not shown). This can be seen clearly in $\langle T \rangle_\theta$ and $\langle T \rangle_y$ in Figure 5.5(c) and 5.6(c) for the temperature. The variance in the intensity at the intrusion front must be so intense as to completely overwhelm the lack of variation above and below the return flow. While it is difficult to see any change in the variance at the front position for w at $t = 1200$ s (Figure 5.8(e)), there is a small dip for T at the same time (Figure 5.7(e)), with dips at r and x equals 2 m and 3.5 m (the latter is approximately the front position). The dip indicates that in the body of the return flow, there is less transverse variance in temperature compared to both the head of the return flow and the instabilities ahead of the intrusion. The lack of dip in the w variance may be because the heated return flow is propagating nearly entirely in the horizontal direction at this time.

At the next time ($t = 2400$ s) shown in Figure 5.7 and 5.8 in panels (d,b), there have been significant changes in both the T and w slices. The instabilities have grown into large convective cells with length scales $\mathcal{O}(0.1 - 1$ m). The length scales of these cells do not continue to grow appreciably after the CL away from the shadow reaches the bottom of the domain. The maximum cell size is likely set by λ/L_z but a more in-depth analysis is required to fully understand these cells and is not the focus of this thesis. Features along the intrusion front have grown, and the return flow has entered into the intrusion interior. There are also some differences that are identifiable between the Corner and Slat cases. The transition between the interior and exterior of the intrusion is less abrupt in the T slices for both the Corner and Slat cases. This is caused by the vortex generated by the interface between the return flow and the intrusion, visible near the front of the intrusion in $\langle T \rangle_y$ and $\langle T \rangle_\theta$ (see Figure 5.5(e,g) and 5.6(e,g)).

Focusing on the Corner case for a moment, the interior of the return flow vortex consists of small features (length scale < 1 m) in T (Figure 5.7(b)) and large upwelling convective cells in w (Figure 5.8(b)). The average temperature difference in the interior of the intrusion after interaction with the return flow are small. And unlike the convective cells ahead of the intrusion - which align somewhat with the features in T - there is generally less correlation between features in w and features in T behind the intrusion front. It's not so surprising because the convective cells form entirely due to buoyancy forces. Buoyancy forces clearly play a key role in the development of the return flow vortex, but buoyancy is not the reason for the break up in the return flow, visible only in the w slice in Figure 5.8(b), otherwise it would be visible in the T slice in Figure 5.7(b).

Shifting our focus to the Slat case, we can see that features visible in a slice are very different behind the intrusion front than in the Corner case. The reason for this is the difference in depth of the intrusion in the two cases. At $t = 1200$ s, the intrusion in

both the T and w slices (Figure 5.7 and 5.8) are similar in both shape and the stage of development, despite there being noticeable differences in intrusion depth. At $t = 2400$ s, the vortex from the return flow has removed the sharpness of the intrusion front in T in the Corner case at all depths. However, in the Slat case by $t = 2400$ s, some of the sharpness at the intrusion front remains in T (Figure 5.6(g) and 5.7(d)) due to the fact that the axis of rotation and the outer arms of the return flow vortex passes further below the surface compared to the Corner case. Figure 5.7(d) and 5.8(d) show that the return flow is able to penetrate close to the surface but not uniformly in y. This is contrasted by the Corner case which shows nearly uniform penetration in θ of the return flow into the upper slices (Figure 5.7(b) and 5.8(b)).

For the Slat case, in the regions where the return flow is not able to penetrate upward into the intrusion, there is an array of features with rounded edges and negative velocities in their interiors, shown in Figure 5.7(d) and 5.8(d). This pattern is typical of the bottom of the convective layer discussed in depth in Chapter 3 (see: Figure 3.12(b)). These features are RT instabilities that have grown slowly due to the continued supply of heat even in the shadowed region. Here, these features are more circular towards $x = 0$ m and become more oblate as x increases. This is likely due to the intrusion stretching these features in the outward direction. While there are similar velocities in the outward direction in the interior of the intrusion and under the shadow in both cases (Figure 5.5(h) and 5.6(h)), the fact that the return flow is unable to penetrate as far vertically into the intrusion in the Slat case allows new RT instabilities to form.

All of the features behind the intrusion front in the T slice correspond to the upwelling return flow. At earlier times (Figure 5.7(a,c) and 5.8(a,c)) there are discernible features beyond the temperature gradient behind the intrusion front because the return flow vortex has yet to approach the surface. Not only is the return flow in the Corner case able to penetrate closer to the surface, it is also able to penetrate further under the shadowed region (Figure 5.7(b) and 5.8(b)) compared to the Slat case (Figure 5.7(d) and 5.8(d)). The variance in T and w (Figure 5.7(e) and 5.8(e)) at $t = 2400$ s demonstrates this. The variance for both quantities s smaller under and close to the shadowed region ($r, x < 3$ m) in the Slat case. The difference in penetration towards the surface and under the shadowed region can also be seen in $\langle T \rangle_\theta$ ($\langle T \rangle_y$) and $\langle u_r \rangle_\theta$ ($\langle u \rangle_y$) in Figure 5.5(e-h) and 5.6(e-h).

The variance in the z and transverse direction in both w and T has changed significantly from earlier times at $t = 2400$ s in Figure 5.7(e) and 5.8(e). At this stage, the variance gradually increases with increasing distance from the shadowed region, even passed the intrusion front. This effect is not visually apparent from the w and T slices or in any of the averaged quantities discussed above shown in the section. We expect that the variance would be larger ahead of the intrusion front than behind it. We also expect that that

variance behind the intrusion should also increase with time as it interacts with the return flow. However, the gradual increase in the variance of w and T past the intrusion front suggests that the presence of the intrusion is affecting the convective cells nearest to the intrusion front (Figure 5.7(e) and 5.8(e)). Our expectation would be that past the intrusion front, the variance in w and T would quickly approach a constant value as it did at earlier times. The increasing variance with distance from the shadow implies that the convective cells closer to the intrusion front are affected by the intrusion, even if it is not visually apparent, compared to those further away. This is a surprising result that is not obvious from looking at the fields themselves, hence, it is revisited in Section 5.8.

Here we see one of the ways in which the intrusion is significantly different in 2D and 3D. In 2D, vertical temperature flux in the convection dominated phase leads to a landscape where temperature variations only exist ahead of the intrusion, but not in the transverse, by construction. However, in 3D the intrusion is able to follow the path of least resistance and pass between or around convective plumes.

5.5 Front position and structure

The front edge of the intrusion is clearly visible at early times in both the Corner and Slat cases. The location of the front edge is uniform in the No Noise case, analyzed in more detail in Section 5.7. The location of the front edge as a function of time is compared in Figure 5.9. The method for estimating the front position is outlined in Section 5.2.4. All three cases exhibit an initial growth phase in the first 600 seconds, where the rate of change of the front position with time increases (i.e. the front accelerates). The duration of the initial growth phase is identical to the one observed in 2D simulations discussed in the previous chapter (specifically, Figure 4.19). This shows that the initial growth is well captured in 2D. In the Slat and Corner cases, the next phase is characterized by an approximately linear slope. In the No Noise case, the slope of the front position in Figure 5.9 continues to increase with time. The No Noise case front position begins to diverge from Corner and Slat cases between near $t = 1500$ and 1800 s. This is discussed in more detail in Section 5.7.

In the previous section, it was shown that there are very clear similarities and differences between the Corner and Slat case. One such difference is the development rate and height of the KH billows generated at the top edge of return flow (comparing Figure 5.5 and 5.6). The resulting vortex catches up with the intrusion front and effectively erases it from the T field in the Corner case. The vortex in the Slat case develops similarly but at a lower height and more slowly. The manner in which it interferes with the intrusion front

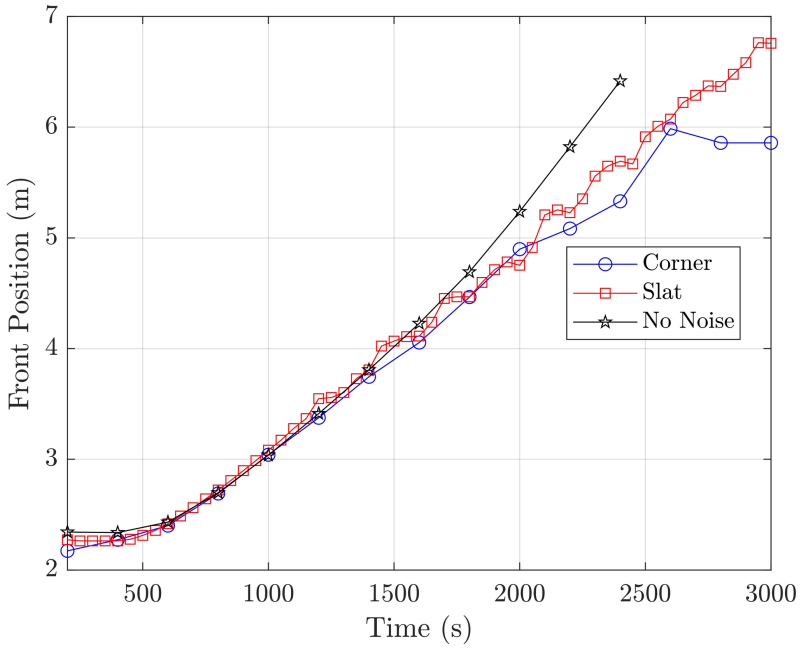

Figure 5.9: Front Position for all three cases listed in Table 5.1. The method of determining the front position is explained in detail in Section 5.2.4. Time resolution of curves is based on output frequency from each simulation, noting that the Slat case is 4 times smaller than the No Noise and Corner cases in terms of storage.

is also lessened, discussed in the previous section. Despite these differences, the location of the front edge of the intrusion is equal for both cases as a function of time, as shown by Figure 5.9. That is, however, until about $t \approx 2500$ s, where the leading edge of the intrusion stops progressing in the Corner case. The last time shown in Figure 5.5(h) is the last time in which the front position increases in the Corner case. This is perhaps not surprising because the mechanism for generating the intrusion is a temperature gradient across the shadow boundary. At later times the temperature gradient is smeared by the effects of the vortex crashing into the intrusion front. In Section 5.8, how the intrusion stops propagating in the Corner case but continues in the Slat case is discussed in more detail.

The location of the intrusion front position is well-defined during the solar radiation dominated phase in the temperature field, as shown by Figure 5.5(a,b), 5.6(a,b), and 5.7(a,c). However, as discussed in the previous section, it is difficult to define the edge

of the intrusion front. This is shown by Figure 5.7(b,d) and further emphasized by the variance taken along the transverse and z directions (Figure 5.7(e). There is a clear change in shape in the T variance near the intrusion front position, however, it is difficult to define algorithmically. This is also the case in the slices of T where there is clearly a region affected by the intrusion and region unaffected by the intrusion, but it is difficult to devise an algorithm to determine the intrusion front location.

The location of the intrusion front is more apparent in the w field, compared to the T field (compare Figure 5.8(b,d) to 5.7(b,d)). The leading edge at early times is a thin band of downwelling velocity, followed by a thicker region (about 1 m in length) of slower downwelling velocities in the interior of the intrusion. As the intrusion propagates forward, it forces the fluid ahead of the front rapidly downwards and into the heated return flow. Further behind the intrusion front is a region of entirely upward motion confined almost completely to the shadowed region. This is labeled on Figure 5.4 as 'upward flux' and exists due to the intrusion and supplies fluid for continued propagation.

At later times (Figure 5.8(b,d)), there is still a narrow region along the leading edge with strong downward velocities. It's width has grown and is no longer followed by a region of weaker, negative vertical velocities. Instead immediately behind this region is dominated by the upwelling return flow in the interior of the intrusion. As discussed earlier, in the Slat case the return flow does not penetrate uniformly in the y direction up to the chosen slice in Figure 5.8(d). Despite this, the narrow region of negative velocities at the intrusion front is still followed by a region of mostly upward velocities. This suggests that while the return flow vortex does not uniformly penetrate into the slice in Figure 5.7(d) and 5.8(d), the motion in the interior of the intrusion is still affected.

One of the features of interest in the study of 3D gravity currents is how instabilities form along the leading edge, one example being the lobe and cleft instability generated along no-slip boundaries (Simpson, 1999). As a result, features along the intrusion front are of interest. Profiles taken along the intrusion front[5], T_F, for the Corner and Slat cases are given at intervals of 200 s in Figure 5.10(a) and 5.11(a), respectively. T_F is the average profile along the front edge from a distance of 5 cm behind the intrusion front 25 cm in front of the intrusion front. Note that the horizontal axis in panel (a) of each figures has different between each case. For the Corner case the horizontal axis is θ, the azimuthal angle in radians, and for the Slat case it is y position in metres. As a result, it is difficult to compare T_F directly. Here, we will discuss them separately and subsequently contrast each of them. The spectra of T_F are given in panels (b,c,d) of Figure 5.10 and 5.11 at three

[5]A profile along the intrusion front refers to a curve that follows the path of the leading edge at fixed z and r for the Corner case, and fixed z and x for the Slat case.

selected times. Note that for both cases, a wavenumber of 30 corresponds to approximately 0.21 m. Therefore, for both cases, most of the weight on the spectra is on features with wavelengths of 0.21 m or larger.

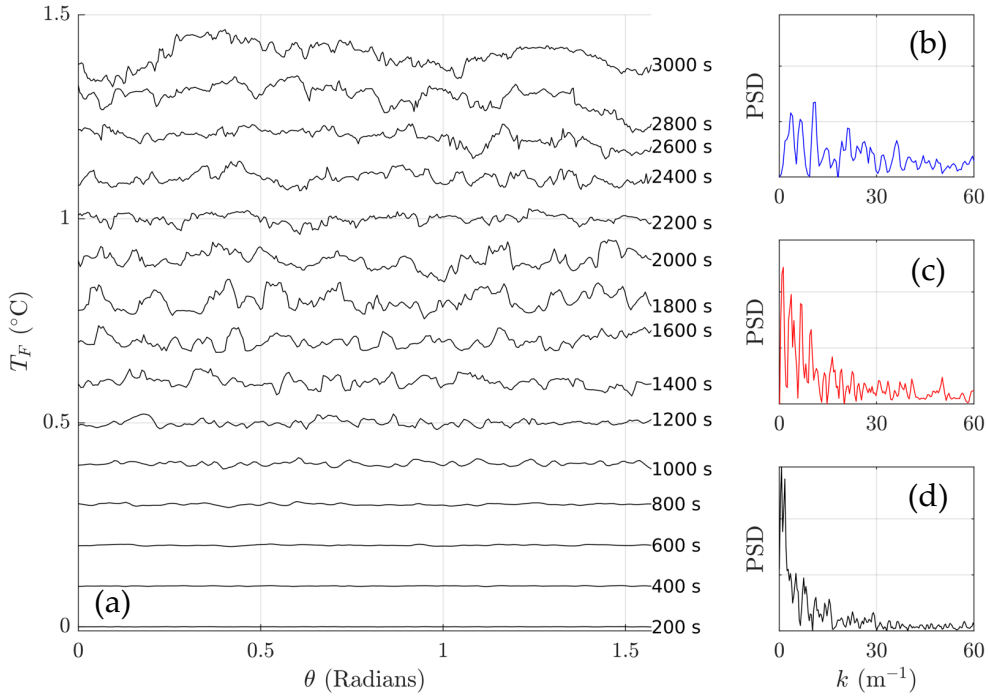

Figure 5.10: Mean temperature at the intrusion front (Figure 5.9), T_F, for the Corner case. (a) T_F with the mean value subtracted. Vertical offset for increasing time added artificially to show the differences. Times are given at given at the far right edge of this panel. Also shown are normalized spectra of T_F at (b) $t = 1200$ s, (c) $t = 2000$ s and (d) $t = 2800$ s.

Starting with the Corner case, recall that the horizontal axis in Figure 5.10(a) is the azimuthal angle, θ. Hence, the length of the azimuthal profile is not fixed as a function of time. For example, at $t = 0$ when the intrusion front is at the shadow boundary at $r = 2$ m, 1 m arc corresponds to an angle of $1/2$ radians. At $t = 1600$ s, when the intrusion front is at $r \approx 4$m, a 1 m arc covers an angle of $1/4$ radians.

The initial growth phase ($t = 0$ to 600 s) consists only of azimuthal profiles with negligible perturbations from the mean temperature. The time period with the largest acceleration unsurprisingly corresponds to the time period with the least development of

Rayleigh-Taylor instabilities ahead of the front of the intrusion. As shown in Figure 5.9, the velocity of the intrusion front increases until it reaches an approximately constant value at $t \approx 600$ s. Features begin to grow in T_F near the intrusion front during the solar radiation dominated phase, past the first 600 s. As shown by Figure 5.7(a), non-negligible features are present in the temperature field ahead of the intrusion front before the beginning of the convection dominated phase. The effect of these features is apparent in Figure 5.10(a). Figure 5.10(b) shows the spectrum of T_F at $t = 1200$ s. At this time, the spectrum has larger weight on smaller wave numbers but compared to the spectra at later times (Figure 5.10(c,d)) it has significantly more weight on larger wave numbers, indicative of the small scale features at and a head of the intrusion front in Figure 5.7(a).

Temperature differences are usually largest at the end of the solar radiation dominated phase, which for 3D cases is around $t = 1300$ s. The transition to the convection dominated phase is not evident in the intrusion front position (Figure 5.9; i.e., there is no change in slope or magnitude at this time). However, T_F does exhibit the growth of sharp and large amplitude features around this time. This is likely evidence of small convective plumes interacting with the intrusion front. Figure 5.7(a,c) shows that the length scale of features ahead of the intrusion at $t = 1200$ s are approximately $\mathcal{O}(1$ cm) and $\mathcal{O}(1$ m) at $t = 2400$ s. The size of the features in T_F immediately following $t = 1500$ s are $\mathcal{O}(0.1$ rad) - corresponding to an arc length of approximately half a metre - which falls nicely between the length scale of features in the temperature field at $t = 1200$ s and $t = 2400$ s. The spectrum at $t = 2000$ s in Figure 5.10(c) shows a clear shift in weight to smaller wavenumbers below $k \approx 10$ m^{-1}, compared to Figure 5.10(b). $k < 10$ m^{-1} corresponds to angles greater than 0.12 radians.

As the convection dominated phase continues, the sharpness of these features in T_F at $t = 1600$ to 2000 s decrease. As shown in Figure 5.7(a,b), the size of the features ahead of the intrusion front continue to grow, however, the length of the transitional region dividing convective plumes - consisting of warm temperatures - also grows. As a result, the sharpness of features at the intrusion front decreases as in Figure 5.10 from $t = 2000$ to 3000 s. The spectrum at $t = 2800$ s exhibits an even greater shift to smaller wavenumbers in Figure 5.10(d) for $k < 5$ m^{-1}. $k < 5$ m^{-1} corresponds to angles greater than 0.2 radians at this time. Indeed, this shift is most apparent in T_F at $t = 3000$ s where large wavelength oscillations, spanning nearly half of the intrusion front, are visible.

Shifting our intention to the Slat case (Figure 5.11(a)), where the length of the profile is always equal to $L_y = 2.56$ m. The initial growth phase ($t = 0$ to 600 s), matching the Corner case, has negligible perturbations to T_F. As we noted previously, most of the initial acceleration occurs when there are very few features at the intrusion front. As in the Corner case, small oscillations begin to grow with somewhat consistent amplitude and

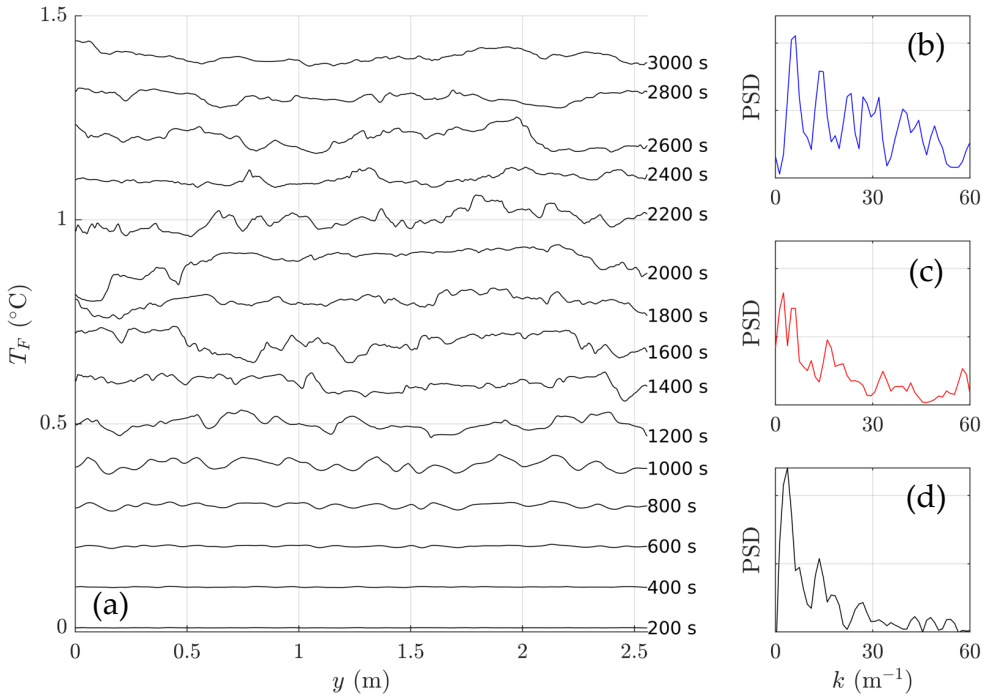

Figure 5.11: Mean temperature at the intrusion front (Figure 5.9), T_F, for the Slat case. (a) T_F with the mean value subtracted. Vertical offset for increasing time added artificially to show the differences. Times are given at given at the far right edge of this panel. Also shown are normalized spectra of T_F at (b) $t = 1000$ s, (c) $t = 2200$ s and (d) $t = 3000$ s.

wavelength, at least qualitatively. These features in T_F, as in the Corner case, gradually grow into larger scales with sharper edges, while still maintaining small features along the intrusion front. At later times, the sharpness of some of these features decreases, while the presence of large scale oscillations begin to become present in T_F.

The shift from a more uniform spread of weight on a variety of scales to more weight on large scales is reflected in the spectra at $t = 1000$, 2200 and 3000 s in Figure 5.11(b,c,d). Ignoring the initial growth phase, in both of the Corner and Slat cases there is a consistent shift from a wide variety of scales to mainly large scale features at later times. It should be noted that the length ratio of the intrusion front between the Corner and Slat cases at $t = 2000$ s is approximately 3, and as a result at later times the intrusion front is interacting with many convective plumes along its length in the Corner case (see Figure 5.7(b) and

5.8(b)). Whereas, in the Slat case the convective plumes nearly span the y dimension (see Figure 5.7(d) and 5.8(d)). Even if L_y were equal between the Corner and Slat cases, the length of the intrusion is always increasing in the Corner case and inevitably interacts with more convective plumes.

A larger y dimension would be necessary for better late time comparisons between the Corner and Slat cases.

5.6 Intrusion depth analysis

Figure 5.5 and 5.6 establish that there is a clear difference in intrusion depth between these two cases. As discussed in Section 5.2.4, we define the depth of the intrusion as the average depth of the shear layer (Figure 5.4) along the length of the intrusion starting at the shadow boundary and ending at the intrusion front position. Figure 5.12 gives the intrusion depth for all three cases considered in this Chapter. The first 1000 s are not shown as the intrusion depth by this definition does not produce useful results prior to this time.

5.6.1 Intrusion depth increase

The depth of gravity currents typically decrease with time (Cantero et al., 2007b; Simpson, 1999). Figure 5.12 clearly shows that the intrusion depth only decreases for the No Noise case. The turbulent mixing in the ambient and return flow in both the Corner and Slat cases increases the depth of the intrusion. An increase in gravity current depth due to a turbulent ambient has previously been observed and measured (Simpson, 1999).

The No Noise case here acts as a point of comparison. The intrusion depth remains constant until shortly after $t = 1500$ s. This time is close to the transition time between the solar radiation dominated phase and the convection dominated phase but there is no such transition in the No Noise case. However, around this time the return flow vortex approaches the intrusion front as shown in Figure 5.14(e), shortly after at $t = 1800$ s. After this point, the intrusion depth decreases in a manner that is consistent with the predicted shape in Figure 5.13(a).

Similarly, for the Corner case, there is a change in slope around the same time but instead it results in a increasingly positive rate of change in the intrusion depth. Immediately prior to this increase in slope, is a brief flattening of the intrusion depth between $t = 1600$

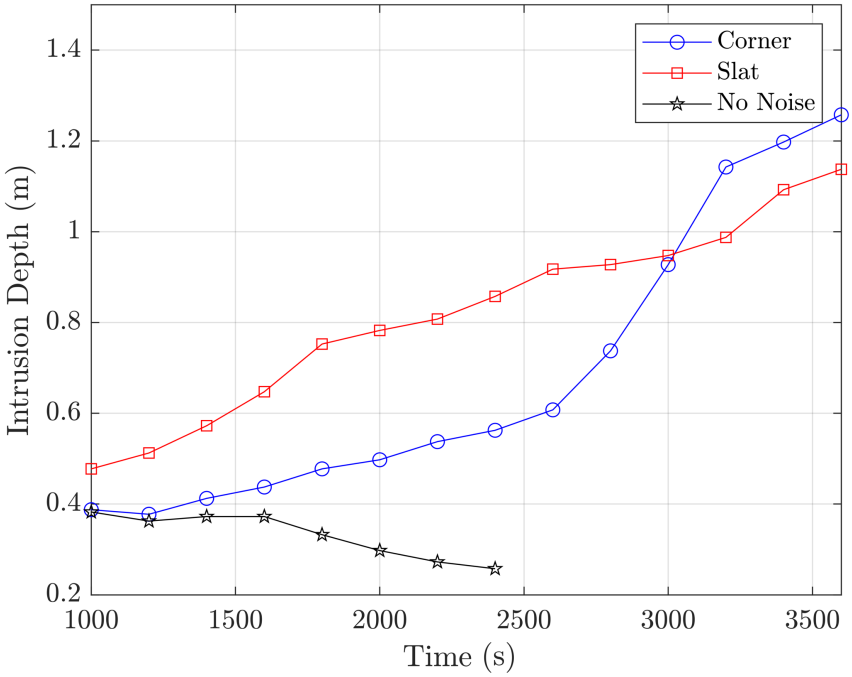

Figure 5.12: Intrusion depth defined as the transition between outward and inward motion in the u_r field (Corner and No Noise case) or u (Slat case).

and 1800 s, possibly due to the interaction between the return the vortex and the intrusion front. Evidently, the effect of the turbulent return flow is to increase the intrusion depth overtime, with a second increase in the rate of change shortly after the point in time where the outward flow of the intrusion ceases.

The slope of the intrusion depth versus time in the Slat case is nearly constant, with a small change near $t = 1800$ s. As shown by Figure 5.6, 5.7(b,d), and Figure 5.8(b,d), the return flow vortex leaves a gap of mostly undisturbed fluid near the surface in the interior of the intrusion. If the return flow vortex is indeed responsible for the change and slope in the Corner case, it is unsurprising that we observe less of a change in the intrusion depth in the Slat case, which is able to propagate further than the Corner case.

5.6.2 Conservation of volume and geometrical differences

Figure 5.12 shows that there is an initial vertical offset between the Corner and No Noise case and the Slat case, which can be explained by volume conservation and the geometrical difference between these cases.

The approach to this problem is similar to the classic idea that gravity current evolution - viewed from the side - can be approximated as a set of equal area rectangles with changing lengths and widths (Huppert and Simpson, 1980). As this problem is in three dimensions, the evolution is instead approximated by a series of equal volume cylinders (Corner and No Noise case) or cuboids (Slat case). This analysis neglects the variation in intrusion depth at the shadow boundary. This variation in depth is most apparent in $\langle u_r \rangle_\theta$ for the Corner case (Figure 5.5(b,d,f,h)), $\langle u \rangle_y$ for the Slat case (Figure 5.6(b,d,f,h)), and $\langle u_r \rangle_\theta$ for the No Noise case (Figure 5.14(b,d,f,h)).

For a radially spreading current (analogous to the Corner case), the initial volume is

$$V_{C,0} = \frac{\pi l^2 d}{4}, \tag{5.13}$$

where $l = w_d$ is the initial 'width' or radius of the intruding fluid and $d = \lambda$ the initial depth. The volume at some later time, t, has the same form as $V_{C,0}$ but with l replaced with the intrusion front position, $L_C(t)$, and d replaced with the intrusion depth, $D_C(t)$. It has the form

$$V_C(t) = \frac{\pi L_C(t)^2 D_C(t)}{4}. \tag{5.14}$$

Applying the constant volume constraint by equating Eq. 5.13 and 5.14 we obtain an equation for the intrusion depth

$$D_C(t) = \frac{l^2 d}{L_C^2}. \tag{5.15}$$

Following the same idea we can write down the initial volume in the Slat case as

$$V_{S,0} = L_y l d, \tag{5.16}$$

where L_y is the length of the y dimension, $l = w_d$, and $d = \lambda$. For some later time in the Slat case, the volume is

$$V_S(t) = L_y L_S(t) D_S(t), \tag{5.17}$$

where $L_S(t)$ is the intrusion front position and $D_S(t)$ is the intrusion depth in the Slat case. Equating Eq. 5.16 and Eq. 5.17 and solving for $D_S(t)$

$$D_S(t) = \frac{ld}{L_S}. \tag{5.18}$$

In the Slat case, the intrusion depth, D_S, is inversely proportional to the intrusion front position, L_S. In the Corner case, intrusion height, D_C, is inversely proportional to the square of the intrusion front position, L_C^2.

From Figure 5.9, L_C and L_S are approximately linear after the first 600 s in the Corner and Slat cases. Figure 5.13 gives D_S, D_C (panel a) and their respective rates of change with respect to time (panel b). Once with L_C and L_S from Figure 5.9 and again using a linear approximation of the form

$$L = ct + l. \tag{5.19}$$

The speed, c, is obtained by noting that the intrusions in the Corner and Slat cases advance 1 m in approximately 500 s according to Figure 5.9. This amounts to a speed of $c = 2 \times 10^{-3}$ ms^{-1}. Note that D_S and D_C - which use the front positions from Figure 5.9 - are not the truth intrusion depths, given in Figure 5.12. Instead, they are an expected depth assuming no mixing.

The predicted intrusion depth, calculated using the constant speed approximation, is shifted to start at $t = 600$ s for better comparison with the intrusion depth calculated using the measured intrusion front positions from Figure 5.9, where the intrusion in both cases transitions to a constant slope. Figure 5.13(b) shows that the majority of change to the intrusion depth without mixing with the ambient, heated fluid, occurs early on in its development and is the reason for the initial offset in Figure 5.12.

The predicted and measured intrusion depths initially exhibit a vertical offset, where the measured depth based on Eq. 5.15 and 5.18 is decrease compared to the predicted curve. However, the predicted and measured curves gradually converge. The initial vertical offset is likely generated by the nonlinear nature of the intrusion front position as a function of time early on in the simulation, as shown by Figure 5.9. As the front position becomes more linear, the measured depth using Eq. 5.15 and 5.18 converges with the predicted equivalent.

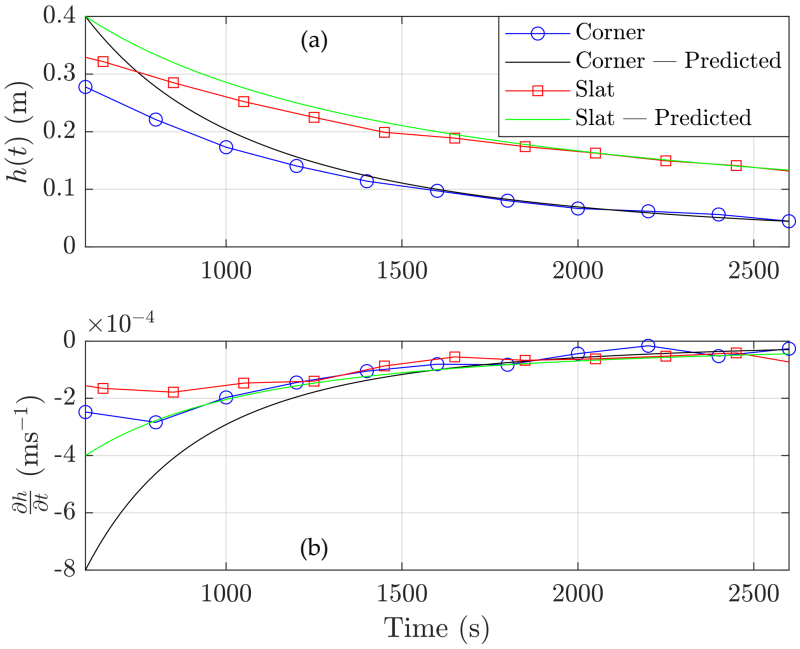

Figure 5.13: Intrusion depth calculated from Eq. 5.15 and 5.18 using the front position given in Figure 5.9 (Symbols) and using a constant speed approximation (Solid lines). (a) intrusion depth, and (b) rate of change of the intrusion depth with respect to time. The legend in panel (a) applies to both panels

5.7 The effect of noise and perturbations

The underlying methods to compute the velocity and temperature fields at each time step in SPINS are higher order (i.e. pseudospectral) methods. There's very little numerical error introduced into the simulations compared with a standard finite difference method (Boyd, 2000). As it was shown in Section 4.6, if SPINS simulations are not seeded with noise, instabilities that grow from small perturbations are only generated by errors at machine precision and due to the high order nature of the method, error propagates very slowly to generate macroscopic instabilities. In this section, we compare the No Noise case to the Corner case.

Other than the fact that the No Noise case does not have noise seeded in the initial velocity field, the initial conditions and the solar forcing are identical. Simulations with no noise seeded in the in the initial conditions are typically not considered to be physical

even though they are indeed correct solutions to the equations. This is because in the laboratory - let alone measurements in the field - controlling your flow to such degree that small perturbations are negligible is essentially impossible, except in steady flows or slowly varying laminar flows. However, that does not mean that the No Noise case has no utility. It presents an environment where we can analyze the intrusion without the net downward, vertical temperature flux ahead of the intrusion and away from the shadow and potentially quantify its effect (e.g., on front position and intrusion depth).

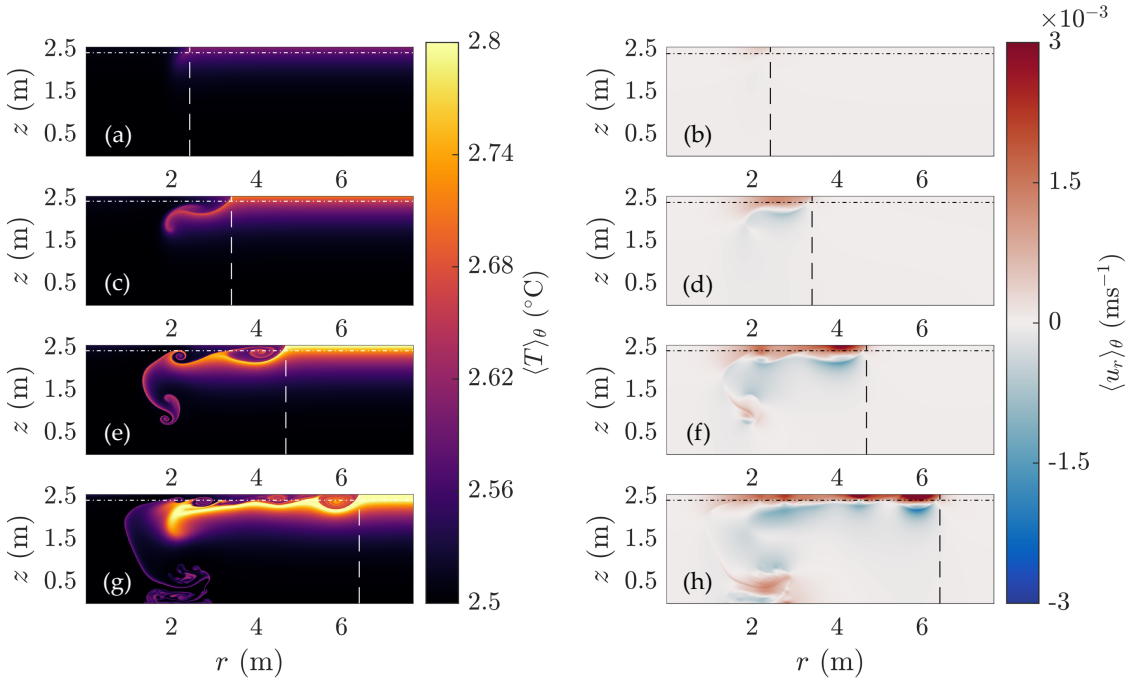

Figure 5.14: T and u_r averaged in the azimuthal direction for the NoNoise case. Azimuthally averaged (a,c,e,g) T and (b,d,f,h) u_r at (a,b) $t = 600$ s, (c,d) $t = 1200$ s, (e,f) $t = 1800$ s, and (g,h) $t = 2400$ s. The vertical dashed line in each panel gives the approximate front position as a function of time, given in full in Figure 5.9. The horizontal dot-dashed line in each panel gives the depth of the Slices in Figure 5.7(a,b) and 5.8(a,b).

To streamline the comparison between the Corner and No Noise cases, we will continue to refer to the solar radiation dominated phase and the convection dominated phase using the Corner case to define the transition. Recall that these phases are referring to the development of vertical temperature flux in regions far from the intrusion. The convection dominated phase starts at approximately $t = 1300$ s in 3D, as shown by the start of the transition in Figure 3.5 and the change in development of $\langle wT \rangle$ in Figure 3.7(b). This

transition is closer to $t = 1000$ s in 2D as shown by Figure 4.5 and 4.7. By distinguishing between the two phases of motion in the discussion of the No Noise case, the differences between it and the Corner case are emphasized.

The initial evolution of the intrusion in the No Noise case is quite similar to the Corner case and even the Slat case. This can be seen clearly by comparing the front position as a function of time between all three cases in Figure 5.9. All three cases exhibit the initial acceleration phase during the first 600 s, the early portion of the solar radiation dominated phase. Then is it immediately followed by a reduction in the acceleration of the intrusion front. For the Corner and Slat cases, this means a transition to a approximately linear regime, with constant velocity and no acceleration. This is similar to 2D from the previous chapter in Figure 4.11, as discussed in the previous section. The intrusion front position of all three cases follow very closely until the transition to the convection dominant phase. Again, similar to the comparison in 2D in Figure 4.19.

During the solar radiation dominated phase, shown in Figure 5.14(a-d). It is unsurprising that the No Noise and Corner cases are most similar prior to the onset in the convention dominated phase in the Corner case. The intrusion front is parabolic in shape. The head of the return flow is shaped like a Rayleigh-Taylor instability. The intrusion and return flow are generated from the unstable temperature differences across the shadow boundary, but they are not grown from small perturbations in the flow field since they appear in the No Noise case. Note the differences in temperature and velocity scale between the No Noise case (Figure 5.14) and the Corner case (Figure 5.5). Due to the lack of convection there is inherently no mixing ahead of the intrusion and temperatures continually increase with time. The velocities in the interior of the intrusion in Figure 5.14(d) are smaller than the Corner case at the same time (Figure 5.5(d)). Despite the fact that the speed of the advancing intrusion front is the same for the Corner, Slat and No Noise cases (Figure 5.9) during this time period. The peak velocity in the interior of the intrusion in the corner case is centred on the upper portion of the return flow at $t = 1200$ s, suggesting that at this stage the growth of instabilities enhances the growth rate of the return flow. The body of the return flow is noticeably thinner in the No Noise case compared with the Corner case. The increased thickness of the body of the return flow in the Corner case shows that the growth of instabilities into significant convection is also present in the solar radiation dominated phase. Since the return flow comes from the fluid ahead of the intrusion, the development of instabilities along its length are reflective of the development of motion ahead of the intrusion. However, it should be noted that the upper portion of the body of the return flow that is in direct contact with the intrusion is quite similar in appearance in both the $\langle T \rangle_\theta$ and $\langle u_r \rangle_\theta$ (Figure 5.5(c,d)), with instabilities only growing towards the bottom. Instabilities along the interface between the return flow and the intrusion are

smoothed out.

At later times - entering the convection dominated phase - the intrusion front position in the No Noise case begins to diverge from the Corner and Slat cases at around $t = 1600$ s (Figure 5.9). This is a notable time period during the development of the intrusion because it immediately follows the transition from the solar radiation dominated phase to the convection dominated phase for the Corner and Slat cases. It is at this point in time where the mean behaviour ahead of the intrusion begins to diverge between noiseless cases and cases with noise, and the resulting effect is for the intrusion front speed to gradually increase as the temperature difference between the intrusion and the ambient at the surface increases. In 2D, the intrusion front position begins to diverge closer to $t = 1000$ s, which is the end of the solar radiation dominated phase in 2D with the same parameters. The onset of the convection dominated phase has a slowing effect on the Corner and Slat cases.

The driving force behind the development and continued propagation of the intrusion is the temperature difference at the intrusion front that appears explicitly in the equations of motion through the baroclinic vorticity term Figure 2.21 and indirectly via the buoyancy term that is only present in the vertical momentum equation (Eq. 2.15a). The enhanced vertical temperature flux ahead of the intrusion - in the Slat and Corner cases - transports warm fluid downwards and cool fluid upwards, decreasing the mean temperature difference at the intrusion front. This transport, especially in 3D (see Chapter 3), generates mixing as well that further decreases the average temperature difference at the intrusion front. The return flow also catches up to the intrusion front at around this time, partly explaining the departure of the intrusion front position in the No Noise case form the Corner and Slat cases. The return flow vortex gradually breaks down in both the Corner and Slat cases, contributing to further differences between the Corner and Slat cases and the No Noise case.

One feature that is not obvious in the Corner case but is important in the No Noise case is the development of the lower half of the return flow. As the upper portion is pulled along by the intrusion, becoming KH billows, the lower portion continues to propagate towards the corner of the domain. This effect is visible, but washed out, in the Corner and Slat cases in Figure 5.5(e) and 5.6(e), respectively. In the No Noise case, this portion of the return flow turns downwards as it nears the back wall and then turns outward as it near the bottom of the domain, eventually propagating in the same direction as the intrusion. There is some evidence that something similar happens in the Corner case. Figure 5.5(h) has a small region of outward motion near $r = 2$ m at the bottom of the domain and could be caused by this feature suggesting that the head of the heated return flow can generate a second intrusion that propagates along the bottom of the domain, by interacting with the back wall or corner. There does not appear to be a similar effect in the Slat case visible in

Figure 5.6(f) or (h) as all the motion near the bottom of the domain is outward. This may be caused by the fact that the intrusion is deeper in the Slat case and the heated return flow is closer to the bottom of the domain, resulting in this feature being unable to develop in the same manner.

In the initial stages, prior to the onset of the convection dominated phase in the Corner case (Figure 5.14(a-d) and 5.5(a-d)), the depth of the intrusion is comparable between the Corner and No Noise cases. In Section 5.2.3,The the depth of the intrusionwas defined as the depth shear layer transitioning between inward and outward motion. As the intrusion continues to progress in the Corner case, its depth gradually increases as shown in Figure 5.12. However, in the No Noise case the depth of the intrusion is confined to a smaller and smaller layer near the surface, suggesting that, perhaps unsurprisingly, the role of boundary layer dynamics in a simulation with no slip boundary conditions becomes more important, because the boundary layer makes up a larger proportion of the intrusion. The effect of no slip boundary conditions on the development of the intrusion is not the focus of the present chapter, however, most gravity currents and ice covered lake simulations are studied with a no slip boundary condition at the surface and considering the potential impact of this boundary condition is important.

One final point to be made about the No Noise case is in the intrusion depth given in Figure 5.12. The shape of the depth versus time is identical to the shape determined by geometry alone assuming no mixing in Figure 5.13.

The comparison between the No Noise case and the Corner case through the azimuthal average clearly shows the effect of the growth of instabilities on the return flow and on the development of the intrusion. Without the growth of instabilities, the return flow vortex is unable to break down. As shown by Figure 5.7(b) the return flow has clear break down of symmetry behind the intrusion front. Figure 5.8(b) shows that the return flow consists of seperate upwelling plumes, rather than a single contiguous band as in the No Noise case. The break down is enhanced further by the interaction between the intrusion front and convective cells, as shown by Figure 5.10(a) at late times.

5.8 Long time behaviour

In the early stages of the simulations firmly in the solar radiation dominated phase the driving mechanism that generates the intrusion is the density differences at the shadow boundary. These density differences over a small region create a sharp increase in the baroclinic vorticity term in the vorticity equation. Figure 5.15 shows quite clearly that

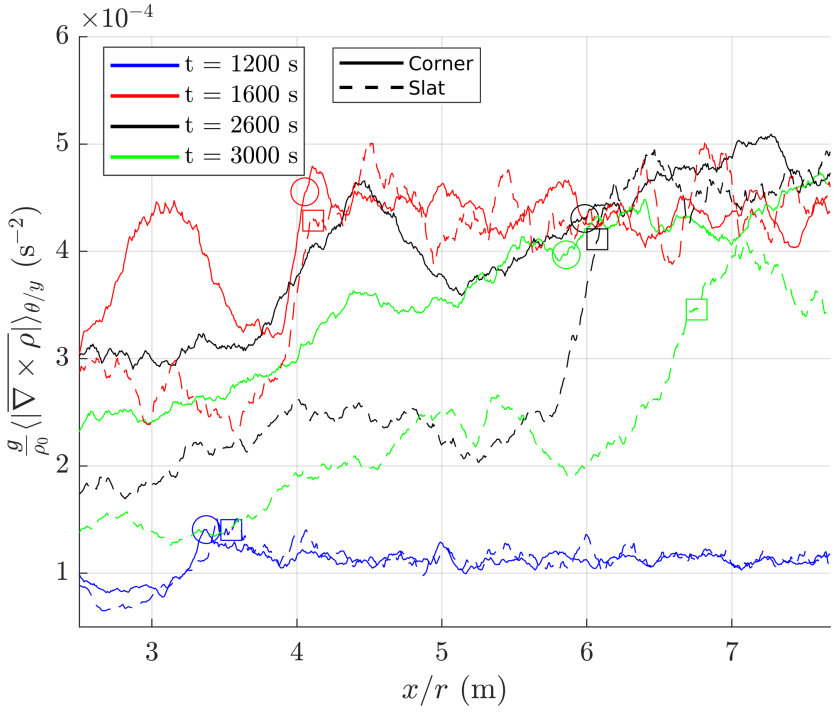

Figure 5.15: Baroclinic vorticity generation, averaged in the θ (Corner case - Solid lines) or y (Slat case - Dashed lines) direction and the top half of the z dimension. Times are indicated by a colour. The front position is indicated by a square (Slat case) or circle (Corner case) along each curve.

after the point in time that the intrusion in the corner case stops spreading ($t > 2400$ s) there is no longer a sharp change in the baroclinic term at the intrusion front. Meanwhile, in the Slat case the sharp increase at the intrusion front is still present and as a result the intrusion is able to continually propagate outward. It is not the convection ahead of the intrusion that arrests the motion and continued outward flow, but instead it is the destruction of the intrusion by the return flow vortex that softens and widens the horizontal density gradients at the intrusion front along the direction of propagation.

Figure 5.15 shows that as a result of the return flow vortex, the density gradients in the interior of the intrusion increase, approaching the gradients in the radiatively driven convection ahead of the intrusion. Even at earlier times, prior to the convection dominated phase, the magnitude of the baroclinic vorticity generation ahead of the intrusion front is comparable to the magnitude at the intrusion front, again implicating the sharp increase

at the intrusion front as the source of the continued motion.

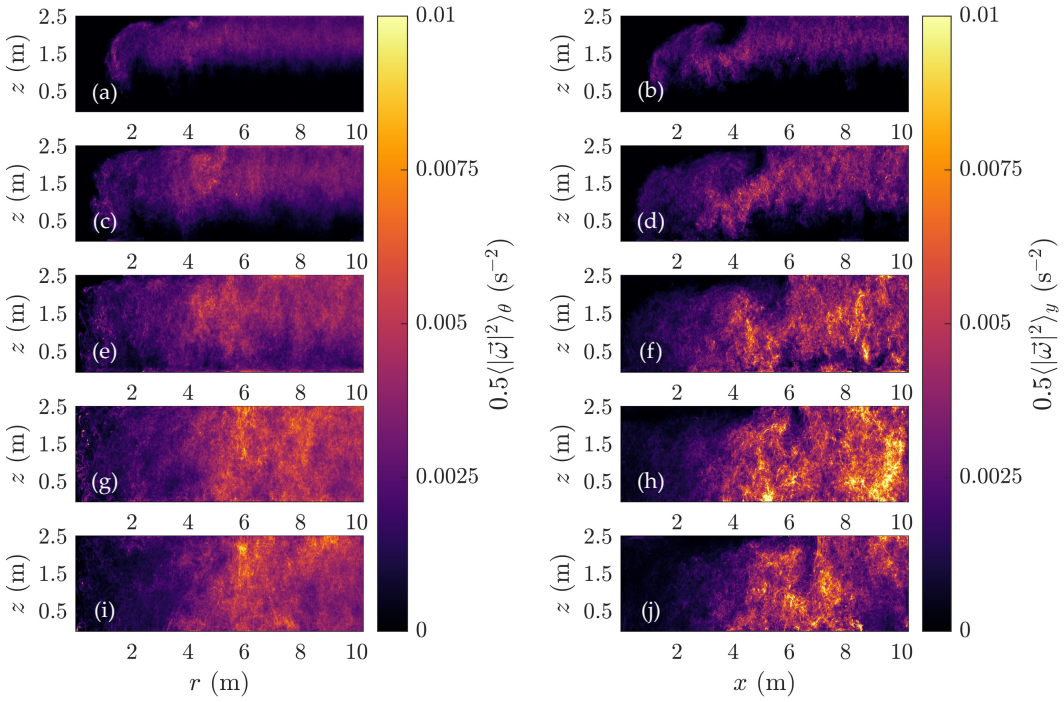

Figure 5.16: Enstrophy averaged in the azimuthal or y direction for the Corner and Slat cases. (a,b) t = 1800 s, (c,d) t = 2200 s, (e,f) t = 2600 s, (g,h) t = 3000 s, and (i,j) t = 3400 s. The first column (a,c,e,g,i) corresponds to the Corner case and the second column (b,d,f,h,j) corresponds to the Slat case.

It is the efficiency of the intrusion at introducing turbulent and heated fluid into the interior of the intrusion that arrests the continued outward flow of the intrusion. Geometric differences alone between the two cases explain how the Slat case continues to propagate outwards well after the Corner case stops propagating. It should be noted that the existence of an unmixed layer (Figure 5.16(f,h,j)) mostly unperturbed by the turbulent return flow vortex in the Slat case is likely parameter dependent, even if we expect that the Slat case will always result in a deeper intrusion due to conservation of volume (Section 5.6.2). If the initial vertical and horizontal length scales of the fluid underneath the shadowed region (namely λ and w_d) we're chosen to produce a smaller $V_{S,0}$ (Eq. 5.16), it is likely that a return flow would have the capacity to destroy the intrusion in the same way as in the Corner case and arrest they continued propagation of the intrusion front. In such

a scenario, the equivalent Corner case would mix with the return flow vortex and cease propagating more rapidly as well.

The evolution of the enstrophy, averaged in the transverse direction is given in Figure 5.16. The enstrophy, especially on small scales, is highly linked to dissipative effects as we showed in Chapter 3. At each time in Figure 5.16 (row by row), the stark difference is in the interior of the intrusion. In the corner case, non-negligible values of the Enstrophy is distributed throughout the domain. Unsurprisingly, the magnitude of the enstrophy behind the intrusion front is generally smaller than ahead of the intrusion front, with a positive gradient in the outward direction, reaching a maximum near $r = 6$ m at the intrusion front edge. The maximum value of the enstrophy is visible as a large mass behind the intrusion front (remnants of the return flow vortex) at $t = 1800$, 2200 and 2600 s in Figure 5.15(a,c,e). After the intrusion front ceases to continue propagating outwards, the enstrophy increases at the intrusion front (Figure 5.16(h,j)). The interaction between the intrusion - which is no longer flowing outwards - and the convective cells ahead of the intrusion generate a region of high enstrophy and enhanced mixing.

In the Slat case, a large pocket of low or negligible enstrophy is maintained near the intrusion front for all times shown, but modified by the return flow at later times. As we previously discussed in Section 5.4, the return flow is not able to destroy the intrusion front in the temperature field in the Slat case as in the Corner case. As the return flow vortex continues to increase in size with time, the pocket of low enstrophy is pulled downwards along the intrusion front at $t = 3000$ and 3400 s in Figure 5.15(h,j). As the intrusion front continues to propagate, no enstrophy enhancement is visible near the leading edge.

In both cases there is a significant amount of rotation on large scales behind the intrusion front. As we have just discussed, in the corner case this results in a pile up in enstrophy at the intrusion front (Figure 5.16(e,g,i)). In the Slat case, the intrusion continues to propagate outwards and the return flow vortex grows in both horizontal and vertical directions, gradually absorbing the irrotational fluid in the body of the intrusion. Vertical domain scale rotation is easily identified in $\langle w \rangle_\theta$ (Corner; Figure 5.17(a,c)) and $\langle w \rangle_y$ (Slat; Figure 5.17(e,g)), at $t = 2800$ s in Figure 5.17(a,b) and $t = 3400$ s in Figure 5.17(e,g), respectively. The rotation appears in the mean w field as a column of downward motion near the intrusion front, immediately adjacent and a rapid transition to a neighbouring column of upward motion, further behind the intrusion front (towards the left in Figure 5.17(a,c,e,g)).

There are two important features in this rotation that should be noted. First, this is an average and as shown by Figure 5.18(c,d) there is significant variations in w in the interior of the intrusion, close to the intrusion front. Second, in the corner case the column

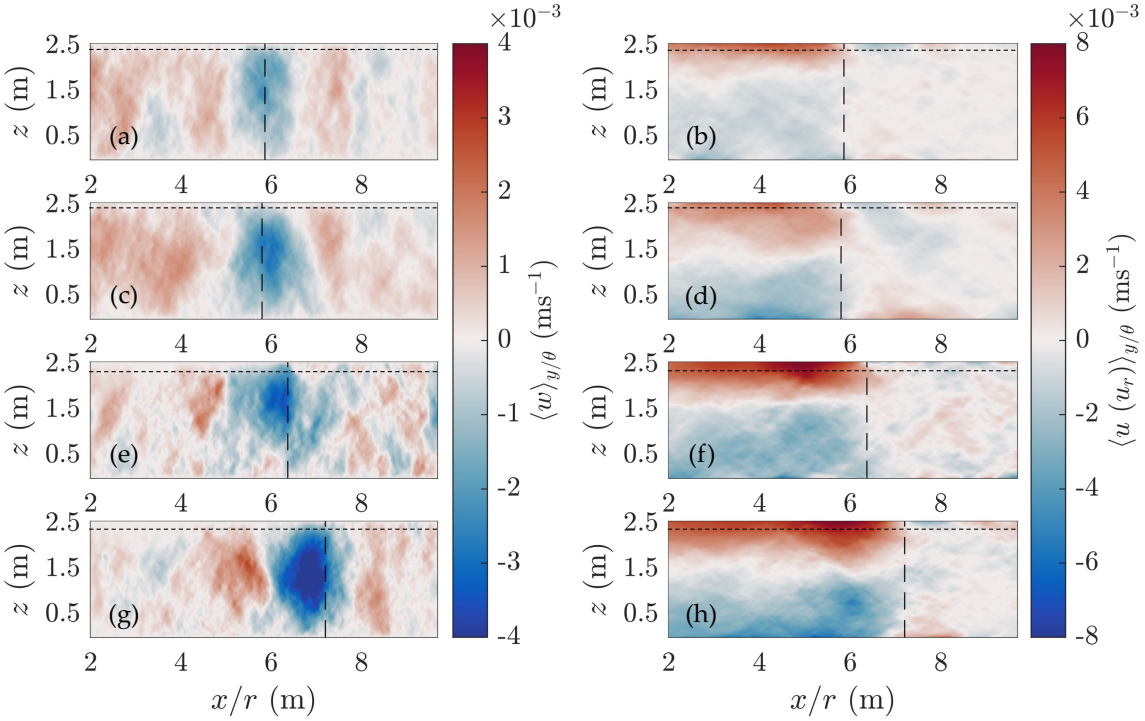

Figure 5.17: w (left column) and u or u_r (right column) averaged in the azimuthal or y direction for the Corner and Slat cases. (a,b) $t = 2800$ s for the Corner case. (c,d) $t = 3400$ s for the Corner case, (e,f) $t = 2800$ s for the Slat case, and (g,h) $t = 3400$ s for the Slat case. Vertical dashed line indicates the front position of the intrusion and the horizontal dashed line corresponds to the depth of slices in Figure 5.18.

of downward flow is centred on the intrusion front but in the Slat case this column is centred just behind the intrusion front. The relative position of the intrusion front and the convective downwelling cell indicates clear interactions between the intrusion and the convective cells ahead of the intrusion front. The layer of outward flow along the surface in $\langle u \rangle_\theta$ (Figure 5.17(b,d)) is directly connected to the return flow by the downwelling cell, through the convective region ahead of the intrusion front. Conversely, in the Slat case the intrusion and return flow interact behind the intrusion front.

There are many ways in which this interaction is apparent in the data. One way is the development of a vertical column of upward motion (again on average) in $\langle w \rangle_\theta$, clearly ahead of the intrusion front, in Figure 5.17(a,c). A similar effect is also clear at the later time of $t = 3400$ s in the Slat case in Figure 5.17(g). Connected columns of upwards or

downwards flow is not seen further ahead of the intrusion front in either case.

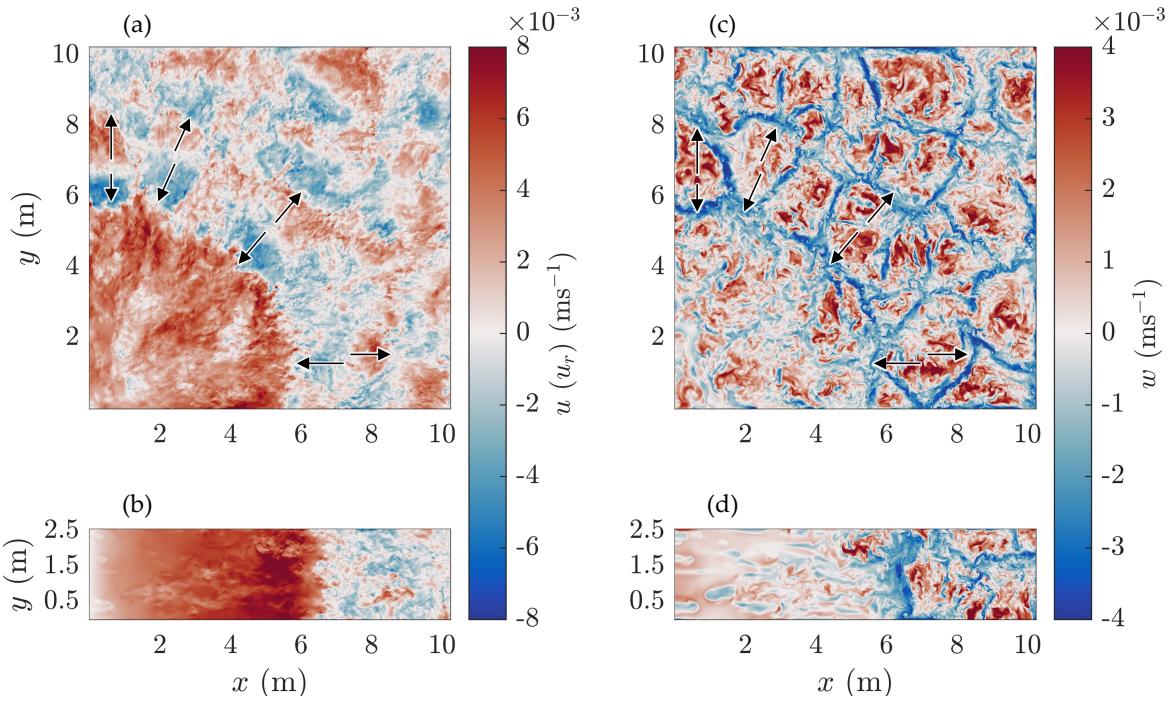

Figure 5.18: u or u_r (a,b) and w (c,d) slices for the Corner (a,c) and Slat (b,d) cases at $t = 3000$ s. Slices are taken at the depth shown by the horizontal dashed line in Figure 5.5 and 5.6.

The fields shown in Figure 5.17 are averages in the transverse direction. At the depths indicated by the horizontal dashed lines in Figure 5.17, slices of the w and u_r fields (u for the Slat case) are given in Figure 5.18. These slices paint a particular picture of the motion immediately ahead of the intrusion front, especially in the corner case (Figure 5.18(a,c)). Ahead of the intrusion, large convective cells develop. This convective cells are typical of Rayleigh-Bénard convection that has been previously studied in the context of radiatively driven convection (Bouillaut et al., 2019; Chand et al., 2022). Upward motion is a collection of large clumps bounded by this regions of downward motion, in a honeycomb pattern. As these convective cells approach the surface, the solid boundary forces the upward flow to move outwards.

The u_r slice (Figure 5.18(a)) shows that these clumps are bisected in the azimuthal direction at the approximate mid point in the radial direction. Arrows are drawn on the u_r slice and copied to the same location in the w slice (Figure 5.18(b)) to show the correlation

of flow towards the intrusion front. These convective cells are behaving like a fountain of water reaching its peak. Note that this inward flow due to the upwelling convective cells is not equally strong along the arc of the intrusion front. Inward flow ahead of the intrusion front is notably weaker for angles (as measured from the x-axis) less than 45 degrees.

Convective cells without arrows have notably weaker (or non-existent) inward flow than those that do. This emphasizes the variability along the intrusion front due to convection ahead of the intrusion. Convection ahead of the intrusion front in the Slat case is of similar strength in both the upward and downward direction (Figure 5.18(d)). However, flow in the negative x direction due to these upward convective cells is non-existent (Figure 5.18(b)). As it was just noted, this does happen in the corner case but only in small areas. Hence, the lack of significant in word flow in the Slat case could be a result of random variance and as a result a wider domain is necessary to fully analyze the inward flow generated up upwelling convective cells close to the surface.

5.9 Conclusion

In this chapter, three simulations are presented which examine the effect of heterogeneous solar radiation intensity extended into 3D. One simulation has a rectangular shadow (Slat case), another has a quarter circle shadow (Corner case), and the last one also has a quarter circle shadow but without noise seeded in the initial conditions (No Noise case) as a controlled point of comparison. Figure 5.3 and 5.4 shows the motion in the initial stages ($t = 600$ to 1400 s), mostly confined to the solar radiation dominated phase as defined in 3D in Chapter 3. An intrusion flows away from the shadowed region in all three cases, as in 2D. A heated return flow immediately beneath the intrusion and a cool return flow towards the bottom flow in the reverse direction. In all three cases, the head of the heated return flow forms into a shape similar to a Rayleigh-Taylor instability, bisected by the thin shear layer between the intrusion and heated return flow. Radiatively driven convection ahead of the intrusion is not sufficiently strong to significantly effect the propagation of the intrusion. Figure 5.3 shows that the velocity scale in the interior of the intrusion greatly exceed the velocity scales in the return flow and in the radiatively driven convection ahead of the intrusion. The front position at this stage for all three cases is identical (Figure 5.9).

There are two important structural differences prior to $t = 1400$ s. The first is between the No Noise and noisy cases (Corner and Slat) where there are features ahead of the intrusion and in the body of the heated return flow in the noisy cases and none in the No Noise case (by construction). The average taken in the transverse direction for each noisy case reveals the Rayleigh-Taylor-like shape at the head of the heated return flow (Figure

5.5(c) and 5.6(c)). The variations in the heated return flow in the transverse direction increase the height of the body of the heated return flow (Figure 5.3(h,i,j), 5.5(c) and 5.6(c)). The intrusion front, despite the features in the convection ahead of the intrusion, is comparatively smooth prior to $t = 1400$ s (Figure 5.7(a,c), 5.10(a), and 5.11(a)), likely to the difference in velocity scales between the intrusion and the convection ahead of the intrusion.

The second difference is in the intrusion height, defined as the depth of the shear interface between the intrusion and the heated return flow. Prior to $t = 1400$ s, the Slat case is noticeably deeper than both the Corner and No Noise cases. This difference can be entirely attributed to volume conservation. Assuming a fixed volume intrusion, in the Corner case the depth is inversely proportional to the square of the intrusion length. Whereas in the Slat case, it is inversely proportional to the length. It is shown in Figure 5.13 that most of the change in depth occurs rapidly at the onset of motion. Hence, even early in the simulation a difference in depth is noticeable.

As the intrusion continues to propagate, convection ahead of the intrusion begins to effect how the intrusion develops. The intrusion front position of the No Noise case begins to diverge from the Corner and Slat cases (Figure 5.9 past $t = 1500$ s and the depth of the shear layer gradually increases (Figure 5.12). Radiatively driven convection ahead of the intrusion front decreases temperatures compared to pure solar radiation. Figure 4.5(b) presents how the convection in 2D changes the background temperature. A similar effect is observed in 3D. This reduction in temperature ahead of the intrusion front reduces the magnitude of the baroclinic term in the direction of propagation, and hence, stops the intrusion front speed from continuing to increase. The depth of the shear layer gradually increases as a result of the convection at the intrusion front, contrary to classical gravity current set-ups where the gravity current depth gradually decreases[6] (Simpson, 1999; Cantero et al., 2007b). It has been shown that turbulence ahead of a gravity current causes its depth to increase (Simpson, 1999) and a similar effect is observed here and shown clearly by comparing u_r and u at later times (right column of Figure 5.17) to u_r and u earlier (right column of Figure 5.5 or 5.6).

The comparison between the Corner and Slat cases highlighted that the differences in geometry lead to differences in intrusion height. The main consequence of this difference is the manner in which the return flow vortex interacts with the intrusion. In both cases, the return flow vortex is generated along the shear layer and eventually catches up to the

[6]The depth of a gravity current is not exactly equal to the depth of the shear layer, especially near the current head, if the depth is defined as the transition between the intruding and ambient fluid. Nor are these two quantities equal for the intrusions discussed in this chapter (see Figure 5.5 or Figure 5.6 in the first or second row). However, it is an adequate proxy as a measure of the size of the intrusion.

intrusion front position. In the Corner case, the return flow vortex reaches the surface and erases the intrusion from the temperature field (Figure 5.5(g) and 5.7(b)), although a positive gradient in the radial direction remains. However, in the Slat case, the return flow vortex does not reach the surface, nor does it completely eliminate the intrusion from the temperature field (Figure 5.6(g) and 5.7(d)). Instead, the intrusion in the Slat case continues to propagate (Figure 5.9), allowing a thin and low enstrophy region to propagate further into the ambient (Figure 5.16(f,h,j)). It is then possible to speculate that the effect of increasing the intrusion depth, regardless of geometry, results in an intrusion which is able to propagate further. As shown by Figure 5.9, as a result of the return flow vortex reaching the surface, the intrusion almost suddenly stops propagating. This suggests that there exists a critical lifetime of an intrusion of this type, rather than a gradual slow down that one might expect of a classical gravity current (Simpson, 1999; Marino et al., 2005; Cantero et al., 2007b).

Chapter 6

Conclusions and future work

6.1 Concluding remarks

In this thesis, radiatively driven convection - extending to penetrative convection in the presence of a background stratification - is the focus of Chapter 3. This topic leads nicely to Chapters 4 where the simplest form of heterogeneous solar radiation is added and the resulting lateral motion along the surface presented. The key parameters A_l, T_0 and λ are varied in this process study. The natural extension of Chapter 4 is to extend these simulations to 3D and considering variations in geometry, as was the topic of Chapter 5. There, a rectangular and circular shadow are used, along with a single noiseless case. The main conclusions of each of these chapters are as follows:

Chapter 3: Radiatively driven convection on average shares many qualities between 2D and 3D. However, the manner in which heated fluid is transported is vastly different, especially concerning the viscous dissipation, which is drastically enhanced on all scales in 3D.

Chapter 4: A shadowed region generates a robust intrusion that propagates into the convection ahead of the intrusion in both 2D and 3D.

Chapter 5: Geometry of the shadowed region alters the lifetime, height and development rate of the intrusion and the heated return flow.

More detailed conclusions for each chapter are given in Section 3.6, 4.8 and 5.9. The research presented in this thesis adds to the growing literature on radiatively driven convection in ice-covered lakes at the late winter. It does this in several ways.

First, it challenges the accuracy of 2D simulations, which are common in the literature of buoyancy driven flows in the cold water regime (Ulloa et al., 2019; Grace et al., 2021; Allum et al., 2022), and quantifies the differences between 2D and 3D. Researchers using 2D instead of 3D should understand exactly what 2D captures well and what 2D is missing when they use these simulations for their research. The contents of Chapter 3 quantify these differences explicitly. The contents of Chapters 4 and 5 also compare 2D and 3D, but not directly.

Second, the broad research community has not, to date, considered horizontal variations in optical properties and their effect on the distribution of heat and the generation of currents. Clearly, from the work in Chapters 4 and 5, one can see such variations lead to the generation of robust horizontal currents, which we have referred to as intrusions in this thesis. These intrusions distribute cool fluid away from the shadowed region, even with less intense shadowing, and warm fluid under the shadow. This could potentially lead to faster melt rates in areas with shorter optical thicknesses (less radiation) and slower melt rates in areas with longer optical thicknesses (more radiation), which is contrary to what is expected. Further, these intrusions also provide a mechanism for distributing nutrients and other suspended materials laterally. Both Ref. Twiss et al. (2012) and Ref. Yang et al. (2020) documented the importance of the winter on spring blooms. Ref. Yang et al. (2020) showed specifically that upwelling convection in the late winter in a temperate lake keeps plankton in the photic zone, enabling primary production and increasing dissolved oxygen concentrations heading into the spring. The intrusions studied in this thesis present a mechanism to inject dissolved oxygen and other nutrients under ice and as well as earlier onset of vertical buoyancy fluxes to enable earlier primary production. Radiatively driven convection is mostly a vertical process with limited horizontal scales and by considering variations in optical properties - caused by ice thickness, clarity and snow cover - we have presented a mechanism for horizontal transport in small, ice-covered lakes.

Third, this thesis focused entirely on the transient state, transitioning from a quiescent background to a fully convective state typical of a CML which has been measured in many different locations under ice (Farmer, 1975; Kirillin et al., 2012; Bouffard et al., 2016; Bouffard and Wüest, 2019) and presented numerically and through experiments (Deardorff et al., 1969; Mironov et al., 2002; Bouillaut et al., 2019; Ulloa et al., 2019; Smirnovsky et al., 2023). None of these cited works focus on this transient state, which is exactly when the intrusions are most active.

The fourth and final way that the research contained in this thesis contributes to the body of literature is from a gravity current perspective. The analysis of gravity currents with time varying density differences did not exist in the literature (to the author's knowledge) prior to Ref. Allum et al. (2022) (the topic of Chapter 4). Horizontal variations in

solar radiation intensity with a quiescent background state - typically of ice-covered lakes in the morning and immediately after snow melts at the surface - represent a geophysically relevant example of a gravity current with time varying density differences driving motion. Another example could occur in ice over water bodies with high salinity, like the oceans. Melting ice freshens the water beneath it, and vice versa for freezing. If this occurs at the edge of a glacier or ice floe, density differences could drive a surface gravity current similar to the one studied in this thesis.

Taken as a whole, the research presented in this thesis should motivate experimentalists and researchers in the field to begin to focus on the ways that horizontal variations in solar radiation can impact the distribution of heat and suspended materials and the generation of lateral intrusions along the surface under ice-covered lakes.

6.2 Future work

The simulations presented in each of the results chapters (Chapters 3 through 5) were meant to represent a simplified under-ice lake environment. Many of the possible future projects include reintroducing certain elements of the ice-covered lake that were neglected for the studies considered here. A list of neglected components that are possible in SPINS include:

1. Varying bathymetry,
2. A background stable stratification,
3. $T = 0$ °C prescribed to the top boundary and No-slip boundary conditions at the vertical boundaries,
4. Time varying solar radiation intensity,
5. Fully 'turbulent' and CML before heterogeneous radiation,
6. Salinity,
7. Angled solar radiation intensity.

In the remainder of this section, I will outline the first three in some detail, whereas the others are left to an interested reader to explore.

6.2.1 Varying bathymetry

SPINS is capable of mapped domains and the mapping can be as complicated as the user would like, providing the new boundary is sufficiently smooth. SPINS was originally written specifically for mapped boundaries as adding mapped boundaries to a structured grid is more complicated than for an unstructured grid. More details can be found in Ref. Subich (2013). All lakes have some form of bathymetry variations along the bottom. As discussed in Section 1.1 and 4.1, differential heating in the shallow regions can generate gravity currents that propagate downslope (Ulloa et al., 2019; Bouffard and Wüest, 2019; Ramón et al., 2021). Ice-covered lakes are also expected to melt first in the shallow regions due to enhanced heating of and reflection off the bottom boundary providing a potential non-uniform solar radiation intensity. The focus in this case has typically been on the current that propagates downslope but no research to the author's knowledge has been focused on the the return flow along the surface, which would be similar to the intrusions discussed here.

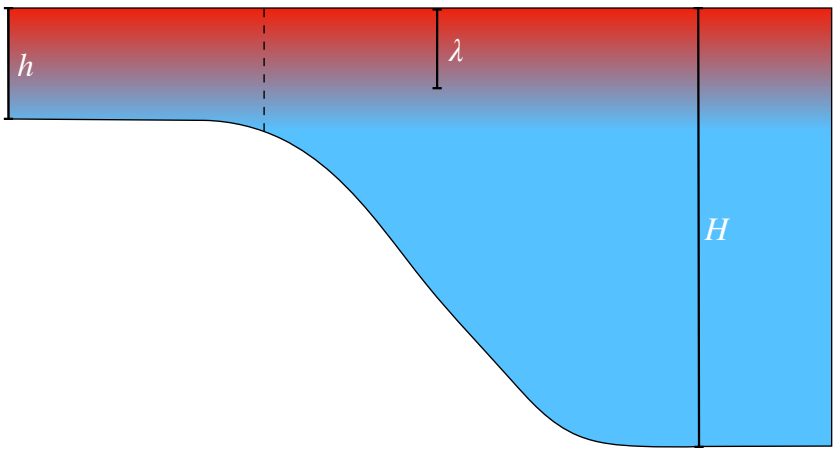

Figure 6.1: Possible configuration for varying bathymetry to induce downslope gravity current and surface return flow. λ is the attenuation length used in solar forcing (Eq. 1.6). h is the depth of the shallow region and H is the depth of the deep region. Vertical dashed line indicates the boundary between the shallow region and the rest of the domain.

One possible sloped boundary is the shape in Figure 6.1, with a shallow region of depth h and a deep region of depth H with a gradual transition between the two to simulate the sloped region. One potential project would be a process study where the following parameters are varied: the intensity of the solar radiation is progressively enhanced in the

shallow region (to the left of the dashed line), h/λ is varied above and below unity, and h/H is varied for values below unity. The first would model the effect of increased melt rate due to differential heating further increasing the penetration of solar radiation into the shallow region and how it would impact exchange between the shallow and deep regions. Variation of h/λ would model the effect of lake clarity on the resulting model. Variation of h/H could have a similar impact than h/λ but would have a sharper impact on differential heating, especially if solar radiation is homogeneous.

6.2.2 Intrusion with a background stratification

It is expected that at the end of Winter I (Ref. Kirillin et al. (2012) and described briefly in Section 1.3), the water column is stably stratified with very little motion under the ice as the heat added by sediment has been exhausted, solar radiation is weak and wind is blocked by the ice-cover (Kirillin et al., 2012; Bouffard and Wüest, 2019; Cortés and MacIntyre, 2020). Temperature gradients are weak compared to Winter II (Kirillin et al., 2012; Cortés and MacIntyre, 2020) but non-negligible. In Chapter 3, radiatively driven convection with a background stratification was analyzed, but in Chapters 4 and 5, a background stratification was not considered. A possible future project would involve simulations similar to those in Chapters 4 and 5 but with a background stratification.

As it was shown in Chapter 3, a background stratification slows the development of radiatively driven convection. But as it was discussed in Chapters 4 and 5 convection ahead of an intrusion has a slowing effect on the speed of the intrusion front, as shown conceptually in Figure 5.9 and 4.19 by comparing with the No Noise case (an admittedly extreme example). It can also be inferred by the variation of Al in Chapter 4. By decreasing Al, you are effectively altering the relative growth rate of the radiatively driven convection compared with the intrusion. For $Al = 0.9$, the largest value used in Chapter 4, the intrusion is able to travel much further at a faster speed, than for lower values. This suggests that the relative growth rates of the intrusion to the growth rate of the radiatively driven convection is an important parameter that could also be the focus of future research.

It was shown in Section 4.2.4 that the density difference across a the shadow boundary due to solar radiation alone, assuming a linear equation of state (which is reasonable for small temperature differences), is

$$\Delta\rho = \frac{\alpha\rho_0 Q_0 Al F(z)}{\lambda} t. \tag{6.1}$$

If this calculation is adjusted to include a background stratification, the background stratification cancels. A background stratification - using a linear equation of state - has no

effect on the temperature difference across the shadow boundary. Therefore, adding a background stratification that resists the development of convection ahead of the intrusion could result in a more robust intrusion that can propagate further with less mixing with the return flow.

In Figure 6.2, a schematic is given to compare the possible consequence of adding a background stratification. The fact that the stratification does not contribute to $\Delta\rho$ in Eq. 6.1 but clearly reduces the growth rate of radiatively driven convection (Chapter 3), the size of the intrusion would be unchanged but the depth of the convective layer, the magnitude of the convective velocities, and the size of features would be reduced at the intrusion front (compare Figure 6.2(a) to (b)).

It is important to consider nonlinear effects. In Eq. 6.1 and 4.6, the use of a linear equation of state is reasonable for small temperature variations. However, if we use a stratification similar to the one used in Section 3.5, the temperature below the surface would be closer to the temperature of maximum density and, hence, the density differences would be reduced. For a full understanding of this set up prior to running a simulation, one should consider re-calculating 6.1 and 4.6 with a nonlinear equation of state.

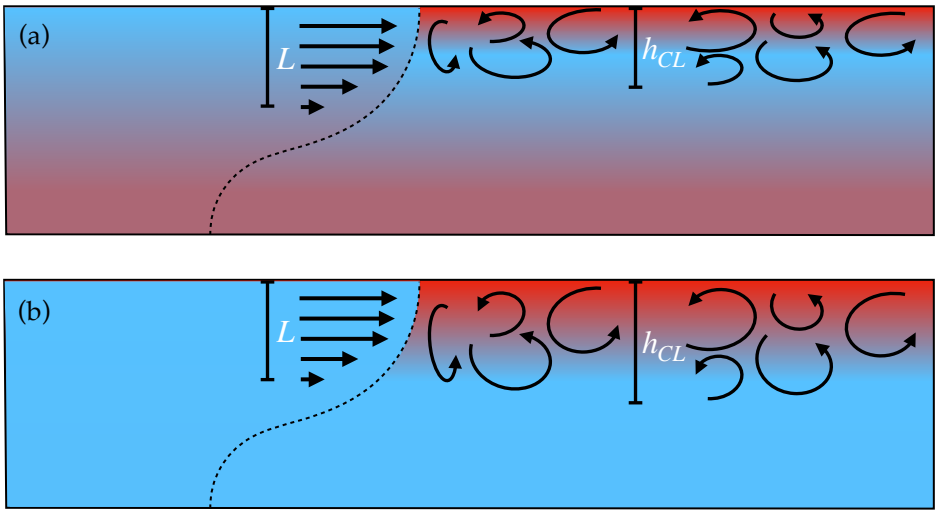

Figure 6.2: Schematic of an intrusion (a) with a background stratification and (b) without a background stratification.

6.2.3 Dirichlet temperature and no-slip velocity boundary conditions

In high-resolution, non-hydrostatic simulations of ice-covered lakes, ice is typically modelled using no-slip boundary conditions and by setting a Dirichlet temperature boundary condition to the top boundary at $T = 0$ °C (Ulloa et al., 2019; Ramón et al., 2021; Smirnovsky et al., 2023). Considering the present work of this thesis and the previous section, a natural next step would be to the include these more standard boundary conditions in simulations of ice-covered lakes. No-slip boundary conditions have always been standard in SPINS (Subich, 2013; Deepwell et al., 2017, 2021; Grace et al., 2021; Legare et al., 2021, 2023) but were neglected from Chapters 4 and 5 because (a) the increased computational cost of using a Chebyshev grid, which are required for no-slip conditions, and (b) the goal was to isolate the intrusion driven by spatially varying solar radiation and not on boundary layer effects. Very recently the capability to add Dirichlet temperature boundary conditions have been added to SPINS. Boundary conditions in SPINS requires that parallel boundaries have the same boundary condition applied. However, there is no such requirement that if Dirichlet boundary conditions are used that the top and bottom boundary must be held at the same temperature. One possible configuration is to set the top boundary to 0 °C and the bottom boundary to some larger temperature below or at T_{MD}.

As a consequence of this requirement that the top and bottom boundary conditions set to the freezing temperature and $T \leq T_{MD}$, respectively, a background stratification is required (discussed in the previous section). The temperature of the bottom boundary would consequently be set so that the background, vertical density gradient is comparable to a gradient typical of ice-covered lakes (Cortés and MacIntyre, 2020; Bouffard et al., 2016). At the end of Winter I (Ref. Kirillin et al. (2012) and described briefly in Section 1.3) the temperature profile is expected to be stratified with very little motion under ice, as a result, this set up is more consistent with the start of Winter II (once significant solar radiation enters the water column).

By simulating this system, the development of the thin boundary layer can be analyzed in detail for the first time. This boundary layer has been observed in ice-covered lakes between the ice and a convective mixed layer (Farmer, 1975; Bouffard and Wüest, 2019). A simulation like the one suggested in this section, with a shadowed region, would show the robustness of an intrusion in conditions that more closely resemble an ice-covered lake. Temperature differences will still develop similarly beneath the surface but will be modified closer to the top boundary, where the temperature differences were largest in this thesis.

One concern about this set up is the interaction of the CL with the bottom domain that would be held to a fixed temperature. In many small lakes the temperature profile in the

late winter consists of a CML that is constant in temperature, and a stably stratified layer beneath it (Farmer, 1975; Kirillin et al., 2012; Cortés and MacIntyre, 2020). However, in smaller lakes the depth of the CML could extend the entire vertical domain, similar to the penetration to the bottom of the domain shown in Chapter 3. As a result, the added heat at the bottom boundary could disrupt the simulations at long times.

References

S. I. Abarzhi. Review of theoretical modelling approaches of Rayleigh–Taylor instabilities and turbulent mixing. *Philosophical Transactions of the Royal Society A: Mathematical, Physical and Engineering Sciences*, 368(1916):1809–1828, 2010.

D. J. Allum, A. P. Grace, and M. Stastna. Two-dimensional simulations of flow in ice-covered lakes with horizontal variations in surface albedo. *Physical Review Fluids*, 7(10): 103501, 2022.

E. Andenæs, B. P. Jelle, K. Ramlo, T. Kolås, J. Selj, and S. E. Foss. The influence of snow and ice coverage on the energy generation from photovoltaic solar cells. *Solar Energy*, 159:318–328, 2018.

M. J. Andrews and S. B. Dalziel. Small Atwood number Rayleigh–Taylor experiments. *Philosophical Transactions of the Royal Society A: Mathematical, Physical and Engineering Sciences*, 368(1916):1663–1679, 2010.

H. Arst, A. Erm, M. Leppäranta, and A. Reinart. Radiative characteristics of ice-covered fresh-and brackish-water bodies. *Proc. of the Estonian Academy of Sciences, Geology*, 55(1):3–23, 2006.

J. A. Austin. Observations of radiatively driven convection in a deep lake. *Limnology and Oceanography*, 64(5):2152–2160, 2019.

M. F. Barad and O. B. Fringer. Simulations of shear instabilities in interfacial gravity waves. *Journal of Fluid Mechanics*, 644:61–95, 2010.

C. K. Batchelor and G. K. Batchelor. *An introduction to fluid dynamics*. Cambridge university press, 1967.

D. Bouffard and A. Wüest. Convection in lakes. *Annual Review of Fluid Mechanics*, 51: 189–215, 2019.

D. Bouffard, R. E. Zdorovennov, G. E. Zdorovennova, N. Pasche, A. Wüest, and A. Y. Terzhevik. Ice-covered lake Onega: effects of radiation on convection and internal waves. *Hydrobiologia*, 780(1):21–36, 2016.

D. Bouffard, G. Zdorovennova, S. Bogdanov, T. Efremova, S. Lavanchy, N. Palshin, A. Terzhevik, L. R. Vinnå, S. Volkov, A. Wüest, et al. Under-ice convection dynamics in a boreal lake. *Inland Waters*, 9(2):142–161, 2019.

V. Bouillaut, S. Lepot, S. Aumaître, and B. Gallet. Transition to the ultimate regime in a radiatively driven convection experiment. *Journal of Fluid Mechanics*, 861:R5, 2019.

J. P. Boyd. *Chebyshev and Fourier spectral methods*. DOVER Publications Inc., 2000.

D. Brydon, S. Sun, and R. Bleck. A new approximation of the equation of state for seawater, suitable for numerical ocean models. *Journal of Geophysical Research: Oceans*, 104(C1): 1537–1540, 1999.

W. Cabot. Comparison of two-and three-dimensional simulations of miscible Rayleigh-Taylor instability. *Physics of Fluids*, 18(4), 2006.

M. I. Cantero, S. Balachandar, and M. H. Garcia. High-resolution simulations of cylindrical density currents. *Journal of Fluid Mechanics*, 590:437–469, 2007a.

M. I. Cantero, J. R. Lee, S. Balachandar, and M. H. Garcia. On the front velocity of gravity currents. *Journal of Fluid Mechanics*, 586:1–39, 2007b.

N. Castro-Folker, A. Grace, and M. Stastna. Three-dimensional structure of cold-water gravity currents. *Physical Review Fluids*, 8(11):113901, 2023.

K. Chand, M. Sharma, and A. K. De. Effect of inclination angle on heat transport properties in two-dimensional Rayleigh–Bénard convection with smooth and rough boundaries. *Journal of Fluid Mechanics*, 950:A16, 2022.

S. Chandrasekhar. *Hydrodynamic and hydromagnetic stability*. Courier Corporation, 2013.

J. A. Colman and D. E. Armstrong. Horizontal diffusivity in a small, ice-covered lake 1. *Limnology and Oceanography*, 28(5):1020–1026, 1983.

A. Cortés and S. MacIntyre. Mixing processes in small arctic lakes during spring. *Limnology and Oceanography*, 65(2):260–288, 2020.

J. A. Curry and P. J. Webster. *Thermodynamics of atmospheres and oceans*. Elsevier, 1998.

A. Dai and C.-S. Wu. High-resolution simulations of cylindrical gravity currents in a rotating system. *Journal of Fluid Mechanics*, 806:71–101, 2016.

A. Dai, Y.-L. Huang, and Y.-M. Hsieh. Gravity currents propagating at the base of a linearly stratified ambient. *Physics of Fluids*, 33(6):066601, 2021.

S. Dalziel, P. Linden, and D. Youngs. Self-similarity and internal structure of turbulence induced by Rayleigh–Taylor instability. *Journal of fluid Mechanics*, 399:1–48, 1999.

S. B. Dalziel. Rayleigh-Taylor instability: experiments with image analysis. *Dynamics of Atmospheres and Oceans*, 20(1-2):127–153, 1993.

J. W. Deardorff, G. E. Willis, and D. K. Lilly. Laboratory investigation of non-steady penetrative convection. *Journal of Fluid Mechanics*, 35(1):7–31, 1969.

J. W. Deardorff et al. Convective velocity and temperature scales for the unstable planetary boundary layer and for rayleigh convection. *J. atmos. Sci*, 27(8):1211–1213, 1970.

D. Deepwell, M. Stastna, M. Carr, and P. A. Davies. Interaction of a mode-2 internal solitary wave with narrow isolated topography. *Physics of Fluids*, 29(7):076601, 2017.

D. Deepwell, C. Clarry, C. Subich, and M. Stastna. Vortex generation due to internal solitary wave propagation past a sidewall constriction. *Journal of Fluid Mechanics*, 913: A47, 2021.

A. Defant. *Physical oceanography*. 1960.

C. R. Duguay, G. M. Flato, M. O. Jeffries, P. Ménard, K. Morris, and W. R. Rouse. Ice-cover variability on shallow lakes at high latitudes: model simulations and observations. *Hydrological Processes*, 17(17):3465–3483, 2003.

C. R. Duguay, T. D. Prowse, B. R. Bonsal, R. D. Brown, M. P. Lacroix, and P. Ménard. Recent trends in Canadian lake ice cover. *Hydrological Processes: An International Journal*, 20(4):781–801, 2006.

C. R. Ellis, H. G. Stefan, and R. Gu. Water temperature dynamics and heat transfer beneath the ice cover of a lake. *Limnology and oceanography*, 36(2):324–334, 1991.

D. M. Farmer. Penetrative convection in the absence of mean shear. *Quarterly Journal of the Royal Meteorological Society*, 101(430):869–891, 1975.

I. Fer, U. Lemmin, and S. Thorpe. Observations of mixing near the sides of a deep lake in winter. *Limnology and oceanography*, 47(2):535–544, 2002.

H. Flanders. Differentiation under the integral sign. *The American Mathematical Monthly*, 80(6):615–627, 1973.

B. P. Flannery, W. H. Press, S. A. Teukolsky, and W. Vetterling. Numerical recipes in C. *Press Syndicate of the University of Cambridge, New York*, 24(78):36, 1992.

A. L. Forrest, B. E. Laval, R. Pieters, and D. S. Lim. Convectively driven transport in temperate lakes. *Limnology and Oceanography*, 53(5part2):2321–2332, 2008.

O. Fringer, M. Gerritsen, and R. Street. An unstructured-grid, finite-volume, nonhydrostatic, parallel coastal ocean simulator. *Ocean Modelling*, 14(3-4):139–173, 2006.

A. Grace. *Numerical simulations of convection and gravity currents near the temperature of maximum density*. PhD thesis, University of Waterloo, 2022.

A. Grace, M. Stastna, and F. J. Poulin. Numerical simulations of the shear instability and subsequent degeneration of basin scale internal standing waves. *Physical Review Fluids*, 4(1):014802, 2019.

A. P. Grace, M. Stastna, K. G. Lamb, and K. A. Scott. Asymmetries in gravity currents attributed to the nonlinear equation of state. *Journal of Fluid Mechanics*, 915, 2021.

A. P. Grace, M. Stastna, K. Lamb, and K. A. Scott. Numerical simulations of the three-dimensionalization of a shear flow in radiatively forced cold water below the density maximum. *Physical Review Fluids*, 7(2):023501, 2022.

A. P. Grace, A. Fogal, and M. Stastna. Restratification in late winter lakes induced by cabbeling. *Geophysical Research Letters*, 50(14):e2023GL103402, 2023a.

A. P. Grace, M. Stastna, K. G. Lamb, and K. A. Scott. Gravity currents in the cabbeling regime. *Physical Review Fluids*, 8(1):014502, 2023b.

T. Hanson, M. Stastna, and A. Coutino. Stratified shear instability in the cabbeling regime. *Physical Review Fluids*, 6(8):084802, 2021.

S. Harnanan, M. Stastna, and N. Soontiens. The effects of near-bottom stratification on internal wave induced instabilities in the boundary layer. *Physics of Fluids*, 29(1):016602, 2017.

C. Härtel, E. Meiburg, and F. Necker. Analysis and direct numerical simulation of the flow at a gravity-current head. Part 1. Flow topology and front speed for slip and no-slip boundaries. *Journal of Fluid Mechanics*, 418:189–212, 2000.

S. G. Hartharn-Evans, M. Carr, M. Stastna, and P. A. Davies. Stratification effects on shoaling internal solitary waves. *Journal of Fluid Mechanics*, 933:A19, 2022.

M. J. Hewer and W. A. Gough. Lake Ontario ice coverage: Past, present and future. *Journal of Great Lakes Research*, 45(6):1080–1089, 2019.

I. J. Hewitt. Subglacial plumes. *Annual Review of Fluid Mechanics*, 52:145–169, 2020.

W. Huang, B. Cheng, J. Zhang, Z. Zhang, T. Vihma, Z. Li, and F. Niu. Modeling experiments on seasonal lake ice mass and energy balance in the Qinghai–Tibet Plateau: A case study. *Hydrology and Earth System Sciences*, 23(4):2173–2186, 2019.

E. Hunke, W. Lipscomb, P. Jones, A. Turner, N. Jeffery, and S. Elliott. CICE, the Los Alamos Sea Ice Model, version 00, 5 2017. URL https://www.osti.gov//servlets/purl/1364126.

H. E. Huppert. The propagation of two-dimensional and axisymmetric viscous gravity currents over a rigid horizontal surface. *Journal of Fluid Mechanics*, 121:43–58, 1982.

H. E. Huppert. Gravity currents: a personal perspective. *Journal of Fluid Mechanics*, 554: 299–322, 2006.

H. E. Huppert and J. E. Simpson. The slumping of gravity currents. *Journal of Fluid Mechanics*, 99(4):785–799, 1980.

R. Inghilesi, C. Adduce, V. Lombardi, F. Roman, and V. Armenio. Axisymmetric three-dimensional gravity currents generated by lock exchange. *Journal of Fluid Mechanics*, 851:507–544, 2018.

L. H. Kantha and C. A. Clayson. *Small scale processes in geophysical fluid flows*. Elsevier, 2000.

S. Karetnikov, M. Leppäranta, and A. Montonen. A time series of over 100 years of ice seasons on Lake Ladoga. *Journal of Great Lakes Research*, 43(6):979–988, 2017.

G. E. Karniadakis, M. Israeli, and S. A. Orszag. High-order splitting methods for the incompressible Navier-Stokes equations. *Journal of computational physics*, 97(2):414–443, 1991.

D. E. Kelley. Convection in ice-covered lakes: effects on algal suspension. *Journal of Plankton Research*, 19(12):1859–1880, 1997.

G. Kirillin, M. Leppäranta, A. Terzhevik, N. Granin, J. Bernhardt, C. Engelhardt, T. Efremova, S. Golosov, N. Palshin, P. Sherstyankin, et al. Physics of seasonally ice-covered lakes: a review. *Aquatic sciences*, 74(4):659–682, 2012.

G. Kirillin, I. Aslamov, V. Kozlov, R. Zdorovennov, and N. Granin. Turbulence in the stratified boundary layer under ice: observations from Lake Baikal and a new similarity model. *Hydrology and Earth System Sciences*, 24(4):1691–1708, 2020.

P. K. Kundu and I. Cohen. Fluid Mechanics, Academic Press. *Philadelphia, Pennsylvania*, 1990.

K. G. Lamb and D. Farmer. Instabilities in an internal solitary-like wave on the Oregon shelf. *Journal of Physical Oceanography*, 41(1):67–87, 2011.

K. G. Lamb and V. T. Nguyen. Calculating energy flux in internal solitary waves with an application to reflectance. *Journal of Physical Oceanography*, 39(3):559–580, 2009.

E. Large and C. Andereck. Penetrative Rayleigh-Bénard convection in water near its maximum density point. *Physics of Fluids*, 26(9):094101, 2014.

S. Legare, A. Grace, and M. Stastna. Double-diffusive instability in a thin vertical channel. *Physics of Fluids*, 33(11):114106, 2021.

S. Legare, A. Grace, and M. Stastna. Double diffusive instability with a constriction. *Physics of Fluids*, 35(2), 2023.

S. Legg. Overflows and convectively driven flows. *Buoyancy-Driven Flows*, 203:239, 2012.

S. Lepot, S. Aumaître, and B. Gallet. Radiative heating achieves the ultimate regime of thermal convection. *Proceedings of the National Academy of Sciences*, 115(36):8937–8941, 2018.

M. Leppäranta. *Freezing of lakes and the evolution of their ice cover*. Springer Science & Business Media, 2014.

M. Leppäranta, A. Terzhevik, and K. Shirasawa. Solar radiation and ice melting in Lake Vendyurskoe, Russian Karelia. *Hydrology Research*, 41(1):50–62, 2010.

M. Lesieur. *Turbulence in Fluids*. Springer, 2008.

C. Li and F. Zeng. Finite difference methods for fractional differential equations. *International Journal of Bifurcation and Chaos*, 22(04):1230014, 2012.

P. Linden and J. Simpson. Gravity-driven flows in a turbulent fluid. *Journal of Fluid Mechanics*, 172:481–497, 1986.

D. Livescu. Turbulence with large thermal and compositional density variations. *Annual Review of Fluid Mechanics*, 52:309–341, 2020.

E. N. Lorenz. Available potential energy and the maintenance of the general circulation. *Tellus*, 7(2):157–167, 1955.

J. J. Magnuson, D. M. Robertson, B. J. Benson, R. H. Wynne, D. M. Livingstone, T. Arai, R. A. Assel, R. G. Barry, V. Card, E. Kuusisto, et al. Historical trends in lake and river ice cover in the Northern Hemisphere. *Science*, 289(5485):1743–1746, 2000.

B. Marino, L. Thomas, and P. Linden. The front condition for gravity currents. *Journal of Fluid Mechanics*, 536:49–78, 2005.

T. Maxworthy, J. Leilich, J. Simpson, and E. Meiburg. The propagation of a gravity current into a linearly stratified fluid. *Journal of Fluid Mechanics*, 453:371–394, 2002.

T. J. McDougall, D. R. Jackett, D. G. Wright, and R. Feistel. Accurate and computationally efficient algorithms for potential temperature and density of seawater. *Journal of Atmospheric and Oceanic Technology*, 20(5):730–741, 2003.

L. Middleton and J. R. Taylor. A general criterion for the release of background potential energy through double diffusion. *Journal of Fluid Mechanics*, 893, 2020.

F. J. Millero, C.-T. Chen, A. Bradshaw, and K. Schleicher. A new high pressure equation of state for seawater. *Deep Sea Research Part A. Oceanographic Research Papers*, 27 (3-4):255–264, 1980.

D. Mironov, A. Terzhevik, G. Kirillin, T. Jonas, J. Malm, and D. Farmer. Radiatively driven convection in ice-covered lakes: Observations, scaling, and a mixed layer model. *Journal of Geophysical Research: Oceans*, 107(C4):7–1, 2002.

P. Moin and K. Mahesh. Direct numerical simulation: a tool in turbulence research. *Annual review of fluid mechanics*, 30(1):539–578, 1998.

D. R. Mueller, P. Van Hove, D. Antoniades, M. O. Jeffries, and W. F. Vincent. High Arctic lakes as sentinel ecosystems: Cascading regime shifts in climate, ice cover, and mixing. *Limnology and Oceanography*, 54(6part2):2371–2385, 2009.

P. Müller. *The equations of oceanic motions*. Cambridge University Press, 2006.

V. Murty, Y. Sarma, D. Rao, and C. Murty. Water characteristics, mixing and circulation in the Bay of Bengal during southwest monsoon. *Journal of Marine Research*, 50(2): 207–228, 1992.

F. Necker, C. Härtel, L. Kleiser, and E. Meiburg. High-resolution simulations of particle-driven gravity currents. *International Journal of Multiphase Flow*, 28(2):279–300, 2002.

U. Obertegger, B. Obrador, and G. Flaim. Dissolved oxygen dynamics under ice: Three winters of high-frequency data from Lake Tovel, Italy. *Water Resources Research*, 53(8): 7234–7246, 2017.

J. Olsthoorn, E. W. Tedford, and G. A. Lawrence. Diffused-interface Rayleigh-Taylor instability with a nonlinear equation of state. *Physical Review Fluids*, 4(9):094501, 2019.

J. Olsthoorn, E. W. Tedford, and G. A. Lawrence. The cooling box problem: convection with a quadratic equation of state. *Journal of Fluid Mechanics*, 918:A6, 2021.

S. A. Orszag, M. Israeli, and M. O. Deville. Boundary conditions for incompressible flows. *Journal of Scientific Computing*, 1(1):75–111, 1986.

P.-Y. Passaggia, K. R. Helfrich, and B. L. White. Optimal transient growth in thin-interface internal solitary waves. *Journal of Fluid Mechanics*, 840:342–378, 2018.

F. Peeters, D. Finger, M. Hofer, M. Brennwald, D. M. Livingstone, and R. Kipfer. Deep-water renewal in Lake Issyk-kul driven by differential cooling. *Limnology and Oceanography*, 48(4):1419–1431, 2003.

G. Peng and W. N. Meier. Temporal and regional variability of Arctic sea-ice coverage from satellite data. *Annals of Glaciology*, 59(76pt2):191–200, 2018.

C. L. Ramón, H. N. Ulloa, T. Doda, K. B. Winters, and D. Bouffard. Bathymetry and latitude modify lake warming under ice. *Hydrology and Earth System Sciences*, 25(4): 1813–1825, 2021.

Rayleigh. Investigation of the character of the equilibrium of an incompressible heavy fluid of variable density. *Proceedings of the London mathematical society*, 1(1):170–177, 1882.

A. L. Robinson, S. S. Ariano, and L. C. Brown. The influence of snow and ice albedo towards improved lake ice simulations. *Hydrology*, 8(1):11, 2021.

K. Salonen, M. Pulkkanen, P. Salmi, and R. W. Griffiths. Interannual variability of circulation under spring ice in a boreal lake. *Limnology and Oceanography*, 59(6):2121–2132, 2014.

J. Schumacher, J. D. Scheel, D. Krasnov, D. A. Donzis, V. Yakhot, and K. R. Sreenivasan. Small-scale universality in fluid turbulence. *Proceedings of the National Academy of Sciences*, 111(30):10961–10965, 2014.

D. H. Sharp. An overview of Rayleigh-Taylor instability. *Physica D: Nonlinear Phenomena*, 12(1-3):3–18, 1984.

J. E. Simpson. Gravity currents in the laboratory, atmosphere, and ocean. *Annual Review of Fluid Mechanics*, 14(1):213–234, 1982.

J. E. Simpson. *Gravity currents: In the environment and the laboratory*. Cambridge university press, 1999.

A. Smirnovsky, S. Smirnov, S. Bogdanov, N. Pal'shin, R. Zdorovennov, and G. Zdorovennova. Numerical simulation of turbulent mixing in a shallow lake for periods of under-ice convection. *Water Resources*, 50(5):768–778, 2023.

E. Smith and G. Dent. *Modern Raman spectroscopy: a practical approach*. John Wiley & Sons, 2019.

N. Soontiens, M. Stastna, and M. L. Waite. Topographically generated internal waves and boundary layer instabilities. *Physics of Fluids*, 27(8):086602, 2015.

V. A. Squire. Ocean wave interactions with sea ice: a reappraisal. *Annual Review of Fluid Mechanics*, 52:37–60, 2020.

D. L. Stefanovic and H. G. Stefan. Two-dimensional temperature and dissolved oxygen dynamics in the littoral region of an ice-covered lake. *Cold Regions Science and Technology*, 34(3):159–178, 2002.

C. Subich. *Simulation of the Navier-Stokes Equations in Three Dimensions with a Spectral Collocation Method*. PhD thesis, University of Waterloo, 2013.

C. J. Subich, K. G. Lamb, and M. Stastna. Simulation of the Navier–Stokes equations in three dimensions with a spectral collocation method. *International Journal for Numerical Methods in Fluids*, 73(2):103–129, 2013.

N. Svacina, C. Duguay, and L. Brown. Modelled and satellite-derived surface albedo of lake ice–part i: evaluation of the albedo parameterization scheme of the Canadian Lake Ice Model. *Hydrological Processes*, 28(16):4550–4561, 2014a.

N. Svacina, C. Duguay, and J. King. Modelled and satellite-derived surface albedo of lake ice–part ii: evaluation of MODIS albedo products. *Hydrological Processes*, 28(16): 4562–4572, 2014b.

N. Svacina et al. Evaluation of the albedo parameterization of the Canadian Lake Ice Model and MODIS albedo products during the ice cover season. Master's thesis, University of Waterloo, 2013.

S. M. Taghavi, K. Alba, T. Séon, K. Wielage-Burchard, D. Martinez, and I. Frigaard. Miscible displacement flows in near-horizontal ducts at low Atwood number. *Journal of fluid mechanics*, 696:175–214, 2012.

S. Toppaladoddi and J. S. Wettlaufer. Penetrative convection at high Rayleigh numbers. *Physical Review Fluids*, 3(4):043501, 2018.

A. Townsend. Natural convection in water over an ice surface. *Quarterly Journal of the Royal Meteorological Society*, 90(385):248–259, 1964.

M. Twiss, R. McKay, R. Bourbonniere, G. Bullerjahn, H. Carrick, R. Smith, J. Winter, N. D'souza, P. Furey, A. Lashaway, et al. Diatoms abound in ice-covered Lake Erie: An investigation of offshore winter limnology in Lake Erie over the period 2007 to 2010. *Journal of Great Lakes Research*, 38(1):18–30, 2012.

H. N. Ulloa, K. B. Winters, A. Wüest, and D. Bouffard. Differential heating drives downslope flows that accelerate mixed-layer warming in ice-covered waters. *Geophysical Research Letters*, 46(23):13872–13882, 2019.

H. N. Ulloa, G. Constantinescu, K. Chang, D. Horna-Munoz, O. Hames, and A. Wüest. Horizontal transport under wind-induced resonance in stratified waterbodies. *Physical Review Fluids*, 5(5):054503, 2020.

H. N. Ulloa, C. L. Ramón, T. Doda, A. Wüest, and D. Bouffard. Development of overturning circulation in sloping waterbodies due to surface cooling. *Journal of Fluid Mechanics*, 930, 2022.

M. Ungarish. On gravity currents in a linearly stratified ambient: a generalization of Benjamin's steady-state propagation results. *Journal of Fluid Mechanics*, 548:49–68, 2006.

M. Ungarish and H. E. Huppert. On gravity currents propagating at the base of a stratified ambient. *Journal of Fluid Mechanics*, 458:283–301, 2002.

G. K. Vallis. *Atmospheric and oceanic fluid dynamics*. Cambridge University Press, 2017.

P. Verburg, J. P. Antenucci, and R. E. Hecky. Differential cooling drives large-scale convective circulation in Lake Tanganyika. *Limnology and Oceanography*, 56(3):910–926, 2011.

C. Verpoorter, T. Kutser, D. A. Seekell, and L. J. Tranvik. A global inventory of lakes based on high-resolution satellite imagery. *Geophysical Research Letters*, 41(18):6396–6402, 2014.

M. Visbeck, J. Marshall, and H. Jones. Dynamics of isolated convective regions in the ocean. *Journal of Physical Oceanography*, 26(9):1721–1734, 1996.

J. M. Wallace and P. V. Hobbs. *Atmospheric science: an introductory survey*, volume 92. Elsevier, 2006.

K. B. Winters and A. de la Fuente. Modelling rotating stratified flows at laboratory-scale using spectrally-based dns. *Ocean Modelling*, 49:47–59, 2012.

K. B. Winters, P. N. Lombard, J. J. Riley, and E. A. D'Asaro. Available potential energy and mixing in density-stratified fluids. *Journal of Fluid Mechanics*, 289:115–128, 1995.

K. B. Winters, H. N. Ulloa, A. Wüest, and D. Bouffard. Energetics of radiatively heated ice-covered lakes. *Geophysical Research Letters*, 46(15):8913–8925, 2019.

R. I. Woolway and C. J. Merchant. Worldwide alteration of lake mixing regimes in response to climate change. *Nature Geoscience*, 12(4):271–276, 2019.

A. Wüest and A. Lorke. Small-scale hydrodynamics in lakes. *Annual Review of fluid mechanics*, 35(1):373–412, 2003.

C. Xu, M. Stastna, and D. Deepwell. Spontaneous instability in internal solitary-like waves. *Physical Review Fluids*, 4(1):014805, 2019.

B. Yang, J. Young, L. Brown, and M. Wells. High-frequency observations of temperature and dissolved oxygen reveal under-ice convection in a large lake. *Geophysical Research Letters*, 44(24):12–218, 2017.

B. Yang, M. G. Wells, J. Li, and J. Young. Mixing, stratification, and plankton under lake-ice during winter in a large lake: Implications for spring dissolved oxygen levels. *Limnology and Oceanography*, 65(11):2713–2729, 2020.

B. Yang, M. G. Wells, B. C. McMeans, H. A. Dugan, J. A. Rusak, G. A. Weyhenmeyer, J. A. Brentrup, A. R. Hrycik, A. Laas, R. M. Pilla, et al. A new thermal categorization of ice-covered lakes. *Geophysical Research Letters*, 48(3):e2020GL091374, 2021.

Y.-N. Young, H. Tufo, A. Dubey, and R. Rosner. On the miscible Rayleigh–Taylor instability: two and three dimensions. *Journal of Fluid Mechanics*, 447:377–408, 2001.

D. L. Youngs. Numerical simulation of turbulent mixing by Rayleigh-Taylor instability. *Physica D: Nonlinear Phenomena*, 12(1-3):32–44, 1984.

A. Zhdanov, N. Granin, and M. Shimaraev. The generation mechanism of under-ice currents in Lake Baikal. In *Doklady Earth Sciences*, volume 377, pages 329–332. Pleiades Publishing, Ltd.(Плеадес Паблишинг, Лтд), 2001.

A. Zhdanov, R. Y. Gnatovskii, N. Granin, V. Blinov, I. Aslamov, and V. Kozlov. Variations of under-ice currents in Southern Baikal by data of 2012–2016. *Water Resources*, 44(3): 442–452, 2017.